Development of dual emissive adenosine analogs for nucleic acid labeling and life sciences

Hoang Ngoan Le

UNIVERSITÉ CÔTE D'AZUR

ÉCOLE DOCTORALE
SCIENCES FONDAMENTALES ET APPLIQUÉES

THÈSE DE DOCTORAT

Développement d'analogues d'adénosine à émission duale pour le marquage des acides nucléiques et les sciences de la vie

Hoang-Ngoan Le

Institut de Chimie de Nice

Présentée en vue de l'obtention du grade de docteur en Chimie
d'Université Côte d'Azur
Dirigée par : Pr Alain Burger
Co-encadrée par : Dr Benoît Michel
Soutenue le : 15/12/2020

Devant le jury, composé de :
Andrey Klymchenko, DR CNRS, Université de Strasbourg
Michael Smietana, Pr, Université de Montpellier
Frédéric Fages, Pr, Aix-Marseille Université
Véronique Michelet, Pr, Université Côte d'Azur
Alain Burger, Pr, Université Côte d'Azur
Benoît Michel, Dr, Université Côte d'Azur

Développement d'analogues d'adénosine à émission duale pour le marquage des acides nucléiques et les sciences de la vie

Development of
dual-emissive adenosine analogs
for nucleic acid labeling and life sciences

Jury :

Président du jury
Véronique MICHELET, Professeur, Université Côte d'Azur

Rapporteurs
Andrey KLYMCHENKO, Directeur de recherche CNRS, Université de Strasbourg
Michael SMIETANA, Professeur, Université de Montpellier

Examinateurs
Frédéric FAGES, Professeur, Aix-Marseille Université

Directeur de thèse
Alain BURGER, Professeur, Université Côte d'Azur

Co-directeur de thèse
Benoît MICHEL, Maître de Conférences, Université Côte d'Azur

Résumé

Les analogues fluorescents de nucléobases sont devenus des outils attractifs pour la chimie biologique des acides nucléiques. En règle générale, ces analogues ne doivent pas compromettre la capacité intrinsèque des bases complémentaires à s'associer. Ceux présentant des longueurs d'onde d'absorption et d'émission décalées vers le rouge, une bonne sensibilité et sélectivité, tout en conservant la capacité d'appariement des bases sont très recherchés. Parmi eux, les sondes fluorescentes à émission duale stimulent un grand intérêt en raison de leur émission ratiométrique permettant une auto-calibration du signal. Dans cette thèse, nous rapportons le développement d'analogues d'adénosine à émission duale auto-calibrée pour le marquage des acides nucléiques et l'étude de leur comportement au cours de processus biologiques associés. Tout d'abord, une série de conjugués à émission duale – composé d'un nucléoside 7-déazadéoxyadénosine (**d7A**) et d'un colorant de type 3-hydroxychromone (**3HC**) – ont été synthétisés en vue de réaliser leur caractérisation photophysique. Ces analogues présentaient le désavantage d'avoir de faibles rendements quantiques dans les milieux protiques polaires, tels que le méthanol. Cette extinction de fluorescence a laissé suggérer l'occurrence d'un mécanisme photoinduit de transfert d'électrons (PET). Ensuite, une étude détaillée de cette réaction de PET a été conduite sur des analogues de **d7A** et 8-aza-7-déazadéoxyadénosine (**8d7A**) connectés à une 3-méthoxychromone (**3MC**). Notre étude a révélé que les conjugués entre **d7A** et le colorant **3MC** formaient déjà des complexes à l'état fondamental à des concentrations de l'ordre du nM, favorisant le processus intermoléculaire de PET. L'annihilation du PET a pu s'effectuer soit en acidifiant la solution, soit en remplaçant dans le conjugué, la nucléobase **d7A** par son analogue 8-aza (**8d7A**).

Dans la continuité de ces observations, les sondes présentant un groupement 3-hydroxyle libre, **FC8A** et **TC8A** (conjugué entre une **8d7A** et une 2-(2-furyl)-**3HC** ou 2-(thiophèn-2-yl)-**3HC**, respectivement), ont été synthétisés puis caractérisés par photophysique. Ces fluorophores ont conservé deux bandes d'émission bien résolues et ont montré plusieurs améliorations par rapport à leurs parents **3HC**, telles qu'une absorption et une émission décalées vers le rouge, ainsi qu'une brillance supérieure. Parmi eux, **FC8A** a présenté les propriétés les plus appropriées pour une incorporation dans de l'ADN car la forte sensibilité à l'hydratation de son émission duale est corrélée de façon linéaire de 0 à 100 % d'eau. En conséquence, au moyen d'une synthèse sur support solide, le reporter **FC8A** a été incorporé de façon site-spécifique dans différentes séquences courtes d'ADN. La sonde a montré un effet marginal sur la structure et la stabilité des duplexes d'ADN marqués, tout en maintenant une émission duale avec une brillance appréciable et une bonne sensibilité à l'hydratation et au transfert d'électrons. En définitif, cette combinaison de sensibilité à l'hydratation et au transfert d'électrons ouvre de nouvelles voies pour détecter des évènements biologiques impliquant l'ADN.

Mots clés : Sonde à émission duale, analogue d'adenosine, transfert d'électrons au sein de l'ADN, sensibilité à l'hydratation, chimie des phosphoramidites

Abstract

Emissive nucleobase analogs have become attractive tools in the chemical biology of nucleic acids. As a rule of thumb, the analogs exhibiting red-shifted absorption and emission wavelengths, good sensitivity and selectivity, while maintaining the base-pairing ability are highly demanded. In this thesis, we report our study on the development of self-calibrated dual-emissive adenosine analogs for labeling nucleic acids and studying their related events. Firstly, a series of conjugates comprising 7-deazadeoxyadenosine (**d7A**) and 3-hydroxychromone (**3HC**) dye were synthesized for photophysical characterization. These analogs suffered from low quantum yields in polar protic media, such as methanol, due to a photoinduced electron transfer (PET) reaction. Secondly, a detailed study on the PET reaction was carried out on 3-methoxychromone (**3MC**) connected to **d7A** or its 8-aza analog (**8d7A**). Our investigations revealed that conjugates between **d7A** and **3MC** dyes already formed ground-state complexes at concentrations of the order of nM, which favor the intermolecular PET process. Quenching due to PET can be switched off whether by acidifying the solution or substituting **d7A** by **8d7A** in the conjugate. In continuation of these findings, the free hydroxyl dyes (conjugates between **8d7A** and **3HC**s) were synthesized for photophysical study. These fluorophores kept as their parent **3HC**s, a well-resolved dual emission but showed several improvements such as red-shifted absorption and emission, and superior brightness. Among them, **FC8A** exhibited the most appropriate properties for incorporation in DNA as its dual emission is strongly sensitive to hydration on a wide range of variation. As a consequence, using solid-phase synthesis, the new label was incorporated in different ODN sequences. The probe displayed a marginal effect on the structure and stability of the labeled DNA duplexes; while dual emission lighted up the DNA sequences with appreciable brightness and good sensitivity to hydration and electron transfer. Interestingly, combining sensitivity to hydration and electron transfer opens new routes for sensing DNA-related events.

Keywords: Dual-emissive probe, adenosine analog, electron transport in DNA, hydration sensitivity, phosphoramidite chemistry.

“Don't wish it was easier, wish you were better.”
Jim Rohn

Acknowledgement

First of all, I would like to express my appreciation to the University Côte d'Azur, especially the IDEX program, which has provided the financial funding for this work.

I am deeply grateful to Prof. Alain Burger for his leadership and supports for my thesis. I also appreciate the insightful discussions and learning opportunities that he has provided me individually. I am equally thankful to Dr. Benoît Michel for his essential supports to this thesis, especially in organic synthesis. I also received generous assistance from him with administrative issues. I want to thank Prof. Véronique Michelet and Dr. Maria Duca, members of my "Comité de thèse", for useful discussions and constructive comments on this work. I would like to express my gratitude to Dr. Rachid Benhida for the greetings, helps, and useful discussions during my stay in the MB group.

I want to show my appreciation to the members of my jury, Dr. Andrey Klymchenko, Prof. Michael Smietana, and Prof. Frédéric Fages.

I would like to thank all the permanent staffs of our group and ICN; in particular, Dr. Marc Gaysinski for the help in NMR spectroscopy, Dr. Lionel Massi for the help related to the mass spectrometry, Dr. Sandra Olivero for her support to cyclic voltammetry, Dr. Anthony Martin for his helpful advice, Dr. Nadine Martinet for her helps and efforts on my social integration, Prof. Nadia Patino, Dr. Audrey Di Giorgio for their greetings and useful discussions, Dr. Cyril Ronco, Dr. Pascal Dao, and Prof. Luc Demange for their advice and encourages. Prof. Uwe Meierhenrich and Dr. Cornelia Meinert are thankful for the greetings and recognition. I would also like to thank Dr. Thierry Darmanin for the advice and motivation from his productivity. I also want to thank Najiba for her assistance during my stay.

I would like to thank Dr. Jérémie Léonard and Dr. Johanna Brazard for our collaboration. I want to give special thanks to Guillaume and Steve for being my lab mates and sharing fruitful as well as painful

moments together. I am also thankful to Loïc, Samy, and Carolina for their help in conducting absorption and emission spectra. I want to thank Dr. Suman for the proofreading of my thesis.

Here are the places I would like to express my thanks to friends from ICN. I am in debt to Dr. Hanh for her supportive friendship and numerous funny discussions. I have greatly benefited from several discussions with Dr. Mauro and Rost. I am thankful to Lou, Sarah, Marie, Chloé, Sylvain, Zakaria, Mathilde, Maurine, and Céline for joyful talks. I want to offer my special thanks to the ancient ICNers for the advice and talks. I miss Dr. Tom, Dr. Alex, Dr. Sasha, Dr. Gabriela, Dr. Nelli, and Cécile.

Outside of ICN, I owe a very important debt to Dr. Bui Thi Buu Hue, Dr. Ton Nu Lien Huong, Dr. Nguyen Trong Tuan, and Nguyen Van Dat from Can Tho University, for the supports and provided opportunity. I would like to offer my special thanks to Dr. Vo Duc Duy, Dr. Dang Quoc Viet, and Dr. Quach Quang Huy for the useful advice and beautiful friendships. I appreciate Jim Rohn, Darren Hardy, and Brian Tracy for the wonderful ideas and motivation from their words.

I want to show my most tremendous appreciation to my parents and my parents-in-law for things that I would not be able to count.

Last but not least, I am thankful to Hong-Sen, Quang-Minh, and Thu-Han for their endless supports, joyfulness, and motivation; without whom, the work may not have accomplished.

December 2020

List of abbreviations

2AP – 2-aminopurine
3HC – 3-hydroxychromone
3HF – 3-hydroxyflavone
3MC – 3-methoxychromone
8vdA – 8-vinyldeoxyadenosine
Å – angstrom
a.u. – arbitrary unit
BRCA1 – breast cancer type 1 susceptibility
BDF – *base-discriminating fluorescence*
BPT – *back proton transfer*
c – speed of light
Cbz – carboxybenzyl group
CD – *circular dichroism*
cm – centimeter
CPG – controlled-pore glass
COSY – *correlation spectroscopy*
CPG – *controlled pore glass*
CV – cyclic voltammetry
D – Debye
DAPI – 4′,6-diamidino-2-phenylindole
DCM – dichloromethane
DIPEA – diisopropylethylamine
DMAP – 4-dimethylaminopyridine
DMF – dimethylformamide
DMSO – dimethylsulfoxide
DMT – 4,4’-dimethoxytrityl group
DNA – deoxyribonucleic acid
E – energy
EDTA – ethylenediaminetetraacetic acid
ESI – electrospray ionization
ESICT – excited state intramolecular charger transfer
ESIPT – exited state intramolecular proton transfer
Et – ethyl group
eV – electronvolt
EWG – electron-withdrawing group
ε – molar absorption coefficient
FC – Franck–Condon
FRET – fluorescence (Förster) resonance energy transfer
Fur – furyl group
h – Planck’s constant
H-bond – hydrogen bonding
HMBC – *heteronuclear multiple bond correlation*
HOMO – *highest occupied molecular orbital.*
HPLC – *high performance liquid chromatography*
HRMS – *high resolution mass spectrometry.*
HSQC – *heteronuclear single quantum coherence*
ICT – intramolecular charge transfer
IR – infrared
k_{nr} – non-radiative decay rate
k_r – radiative decay rate
ℓ – the light path length in a sample (cm)
LUMO – lowest unoccupied molecular orbital
Me – methyl group
N*/T* – intensity at the N* maximum over intensity at the T* maximum
nm – nanometer
nM – nanomolar
NMR – *nuclear magnetic resonance*
ODN – oligodeoxyribonucleotide
bp – base pair
PCR – *polymerase chain reaction*
PDB – *protein data bank*
Ph – phenyl group
Pyr – pyridine
RNA – ribonucleic acid
RT – *room temperature*
s – second
SNP – *single nucleotide polymorphism*

T*/N* – intensity at the T* maximum over intensity at the N* maximum
THF – tetrahydrofurane
TICT – twisted intramolecular charge transfer
TLC – thin layer chromatography
Tm – melting temperature
TMS – trimethylsilyl group
TOF – time of flight
Tol – toluoyl group
UHRF1 – Ubiquitin-like, containing PHD and RING Finger domains 1
UV – ultraviolet
VIS – visible

vs. – versus
Δf – Lippert's parameter
$\Delta\lambda_{SS}$ – *St*okes shift
λ – wavelength (in nm)
λ_{abs} (or abs) – absorption maximum
λ_{em} (or em) – emission maximum
μ_E and μ_G – dipole moments of the excited and ground states
π – pi electrons
σ_P – Hammett value
τ – fluorescence lifetime
Φ or QY – quantum yield
ν – wavenumber

Table of Contents

Table of Contents

Chapter 1. Bibliographical Review

1.1. DNA structure and function

1.1.1. Introduction to DNA

While proteins give cells structure and perform most of the cellular tasks, the information concerning how, when, and where to manufacture each kind of protein is carried in the DNA (*deoxyribonucleic acid*). DNA is like a hard drive of all living organisms on earth where genetic information is stored and read in due time. DNA is a polymer with its three-dimensional structure consisting of two long helical strands coiled around a common axis, forming a *double helix*. DNA strands are constituted of monomers called *nucleotides* (Figure 1). Each nucleotide comprises three primary components: *deoxyribose*, a *base* at position 1′ of the sugar, and a *phosphate group* joined to the sugar molecule from position 5′ (Figure 1). Four different nucleotides are differentiated by four nucleobases, abbreviated A, T, C, and G, and are joined end-to-end in a DNA strand, with the base parts projecting out from the helical backbone of the strand. Each DNA double helix has a simple construction: A pairs with T, and C pairs with G.[1]

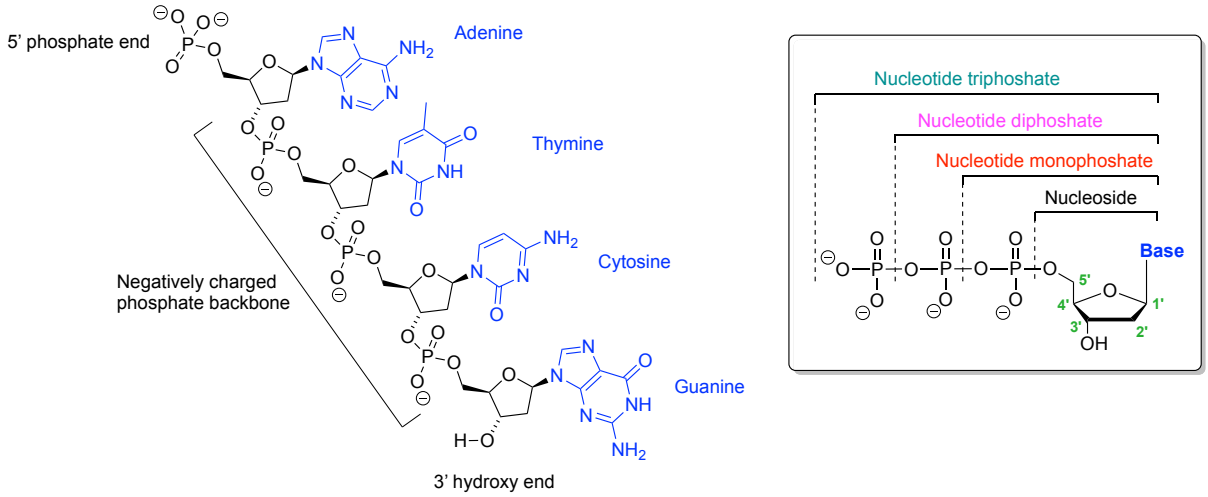

Figure 1. A single strand of DNA. The DNA chain is composed of the bases (A = adenine, T = thymine, C = cytosine, and G = guanine), the deoxyribose, and the phosphate groups. Each base is connected with a sugar moiety to make its corresponding nucleoside. The nucleosides are linked together through the phosphate groups connected between the 5′ carbon and the 3′ carbon of adjacent deoxyribose sugar molecules. The chain of DNA has a negatively charged phosphate backbone. The DNA chain has two chemically distinct ends: the 5′ end *(top)* with a phosphate group and the 3′ end *(bottom)* with a hydroxyl group. This sequence would be written 5′-ATCG-3′ or just ATCG.

The genetic information is carried by DNA residues in its sequence, the linear order of nucleotides along the DNA strand. The DNA's information-bearing portion is divided into

discrete functional units, the *genes*, which typically are 5000 to 100,000 nucleotides long. Most bacteria have a few thousand genes; humans, about 40,000. Each gene commonly contains two parts, a *coding region* and a *regulatory region.* The former specifies the amino acid sequence of a protein, while the latter controls when and in which cells the protein is made. The human genome consists of approximately 3 billion base pairs (*bp*), only about 2% of them are coding region and roughly 98% are noncoding region.[1]

A full copy of the genome is found in every eukaryotic cell's nucleus in extensively folded structures known as *chromosomes* (Figure 2). Each chromosome contains a single linear DNA molecule associated with certain proteins. In humans, each cell has the same 46 chromosomes. Half of these, and thus half of the genes, can be traced back to Mom; the other half, to Dad. Chromosomes are not always present; they form around the time cell divides, where the two copies of the DNA need to be separated. Every time a cell divides, a large multiprotein replication machine, the replisome, separates the two strands of double-helical DNA in the chromosomes and uses each strand as a template to assemble nucleotides into a new complementary strand. The outcome is a pair of double helices, each identical to the original.[1]

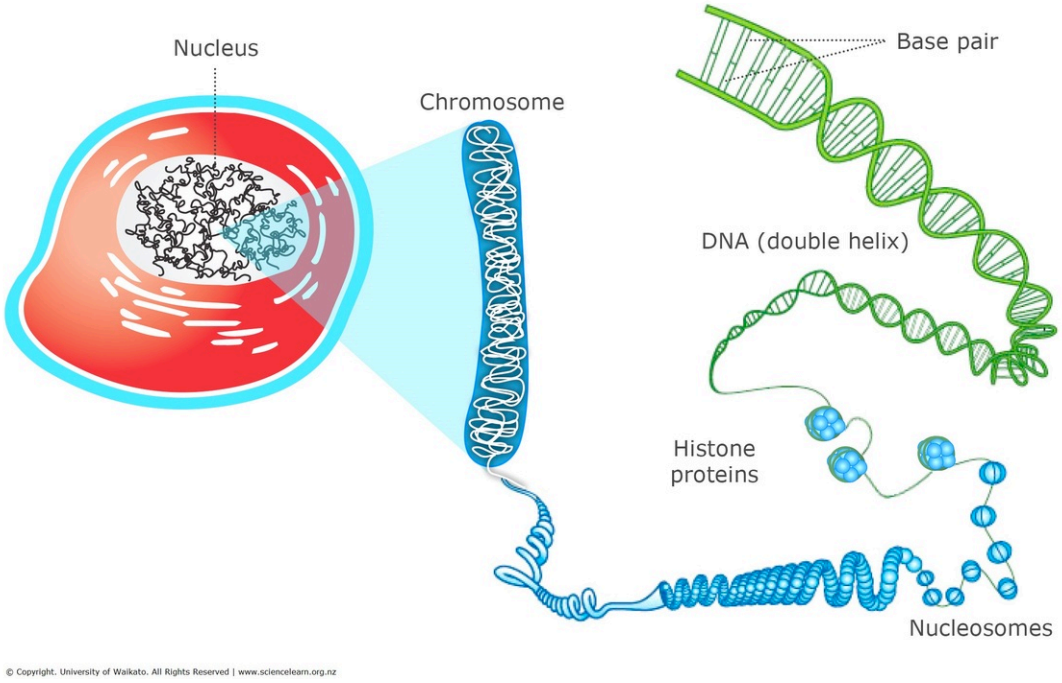

Figure 2. In the cell, DNA is wrapped up around histone proteins and then coiled up further into chromosomes. In eukaryotic cells, chromosomes are found in the nucleus. (From: https://www.sciencelearn.org.nz/images/198-cell-chromosomes-and-dna, 25/06/2020)

Cells use two processes in series, transcription and translation, to convert the coded information in DNA into proteins (Figure 3). All living organisms have ways to regulate when and where to transcribe their genes. For instance, almost every cell in our bodies contains the full set of the human genome. In each cell type, however, only a number of these genes are activated and used to produce proteins. That is why liver cells produce some proteins that are not produced by kidney cells and vice versa. Moreover, many cells can respond to the changes in external

conditions or external signals by turning specific genes on or off, thereby adapting their proteins' repertoire to meet current needs. Such control of gene activity depends on DNA-binding proteins called *transcription factors*, which bind to DNA and act as switches, either activating or repressing of particular genes (Figure 3).[1]

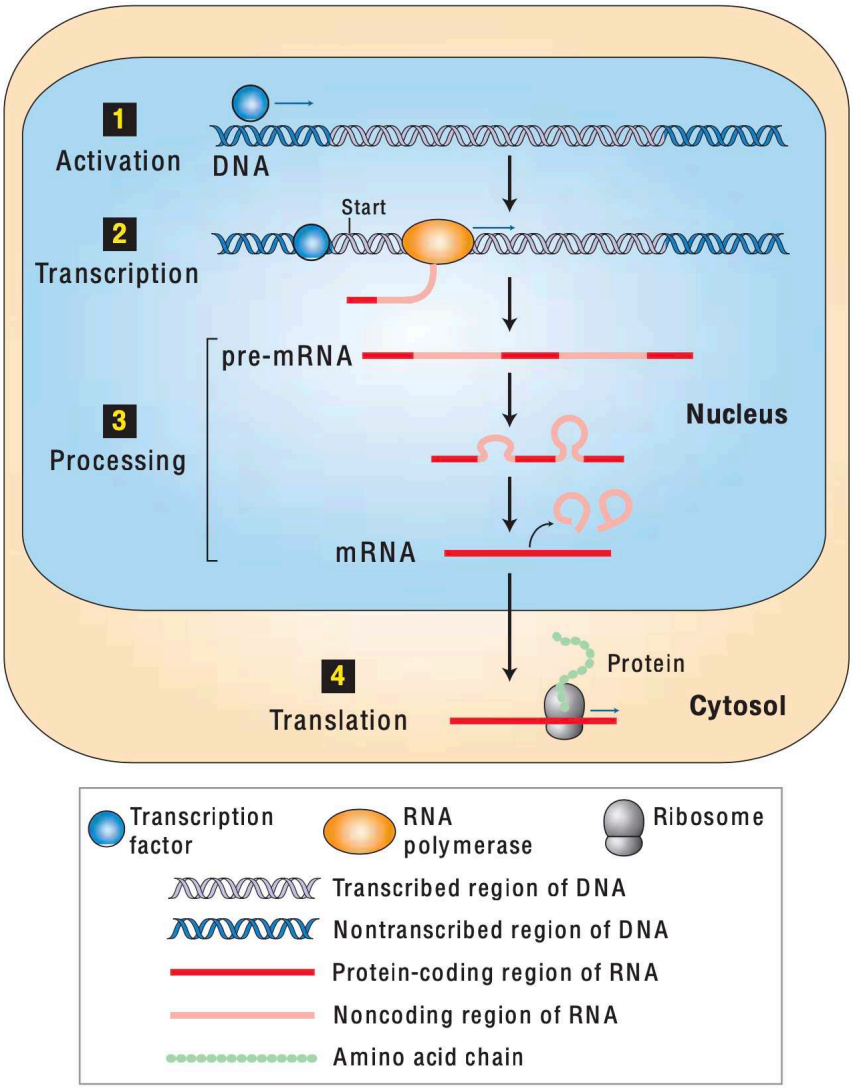

Figure 3. The coded information in DNA is transformed into proteins by a multistep process. Step 1: Transcription factors bind and activate the regulatory regions of the specific genes they control. Step 2: RNA polymerase transcribes the activated gene in its specific region. During this step, a single-stranded pre-mRNA is synthesized using the DNA strands as a template. Step 3: The pre-mRNA is processed to remove noncoding regions. Step 4: In a eukaryotic cell, the processed messenger RNA (mRNA) travels to the cytoplasm, where it is bound by the ribosomes that read its sequence and synthesize the corresponding protein. (From ref[1])

1.1.2. DNA base pairing – Helix Parameters

1.1.2.1. Watson and Crick base pair

The structure of the DNA double helix was first described by Watson and Crick in 1953 as a right-handed helix formed by two complementary DNA strands aligned in an *antiparallel* fashion.[2] To be more precise, one strand is oriented in the 5′→3′ direction and the other in the 3′→5′ direction. Two strands of DNA are held together and folded in its three-dimensional shape by *base pairing* (specific hydrogen bonds, *H-bond*s) and *base stacking*. As a rule of thumb, A base pairs with T (A•T) and G with C (G•C), with two and three H-bonds, respectively. The two base pairs are almost identical in dimensions allows each of the four combinations (A•T, T•A, G•C, and C•G) to substitute for any of the others without distorting the three-dimensional structure of the double helix.[3] G•C base pair has greater stability comparing to A•T due to an additional H-bond of the former with their free energy in an aqueous solution of −5.8 and −4.3 kcal/mol, respectively.[4] Base stacking is additional non-covalent interactions contributing to the folding of DNA helix and its stability. The bases are *stacked* near the center of the cylindrical helix, while the sugar and phosphate groups are located on the outside forming a "backbone" for the helix. There are about 10 base pairs per turn of the double helix. A representation of their model is shown in Figure 4.

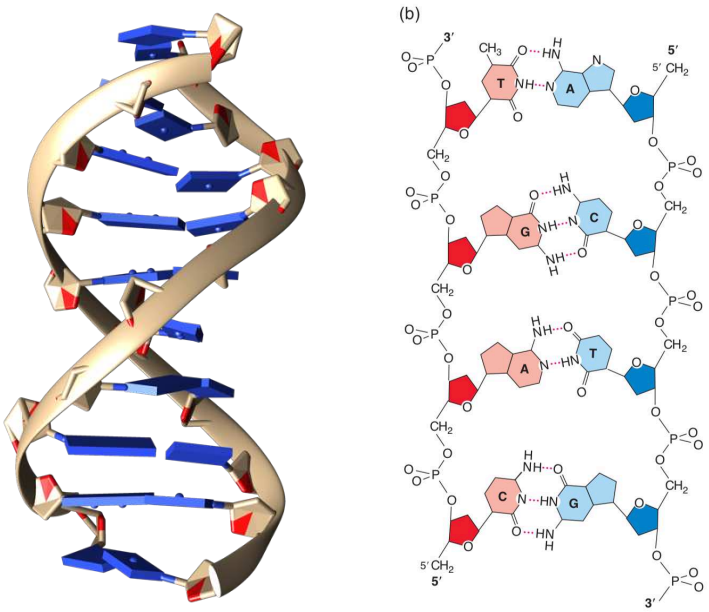

Figure 4. Structure of DNA double helix described by Watson and Crick. (Left) A three-dimensional structure shows base-stacking interactions and the phosphate sugar backbone of the DNA helix (PDB: 1zew). (Right) An extended schematic shows the two sugar-phosphate backbones and H-bond between the Watson–Crick base pairs, A•T and G•C. (From ref[1])

1.1.2.2. Other base pairs

Since the seminal report of Watson and Crick, other base pairs were also discovered. For example, Karst Hoogsteen discovered the pairing between 1-methylthymine and 9-methyladenine by using single-crystal X-ray crystallography.[5,6] In which, the analog of A was flipped 180° to form a unique set of H-bonds, at N6 and N7 atoms instead of the N1 and N6 atoms of the Watson-Crick base pair, with the analog of T (Figure 5B). Later, G was found to similarly base pair with a protonated C.[7] These base pairs were defined as the *Hoogsteen base pairs*. Later, the edge on purine nucleotide bearing groups that can form H-bond with the corresponding pyrimidine nucleotide was called the Hoogsteen edge (Figure 5A).[3] On the other hand, bases can also form *Wobble pairs*, in which the position of one base relative to its complementary base is shifted within the flat plane of the two bases and their H-bonds. A wobble G•T base pair is shown in Figure 5B. In addition to ionized mispairs, 5-bromodeoxyuridine (5-BrdUrd) and 2-aminopurine (**2AP** – Figure 23) can also form a wobble base pair.[8,9]

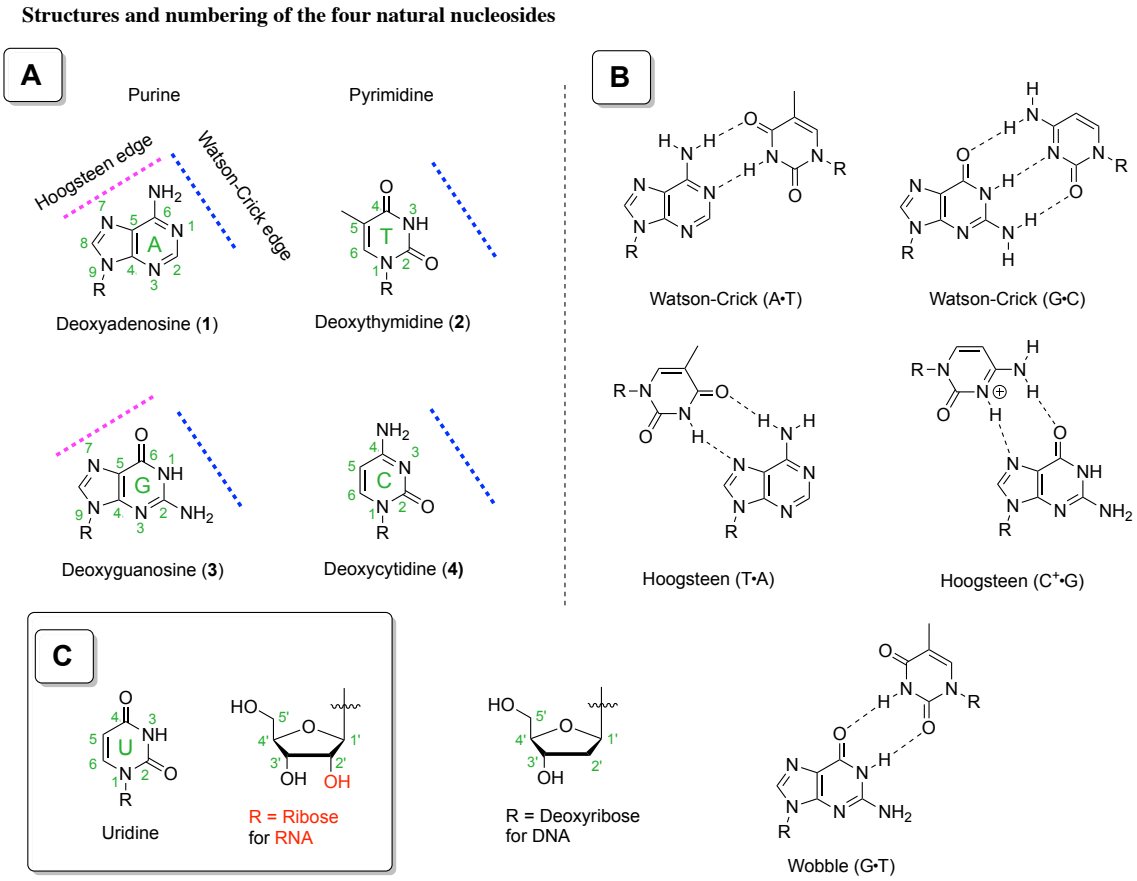

Figure 5. (A) Numbering and the base-pairing edge of the four natural nucleosides, Watson–Crick edges are depicted with blue dashed lines and Hoogsteen edge on purine bases with magenta dashed lines. (B) Representation of Watson–Crick, Hoogsteen, and Wobble base pairs. (C) Ribose nucleic acid, *RNA*, has its nucleosides bearing the ribose sugar instead of the deoxyribose in DNA; and the nucleobases of both types of nucleic acids are the same, except T in DNA is replaced by U in RNA.

1.1.2.3. Helix Parameters

The structure of DNA can be described by a number of parameters that define the helix. It is necessary to be familiar with these defined terms since this will facilitate understanding the structure of different DNA forms, which will be described later. Saenger and Sinden described these parameters in detail in their books.[10-12] The main parameters are illustrated in Figure 6.

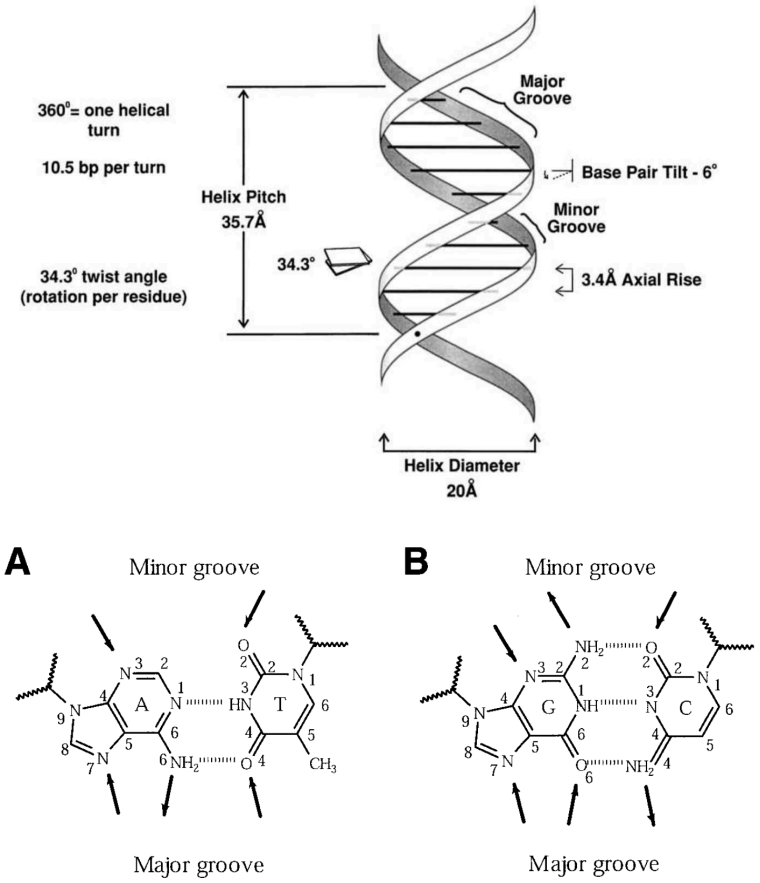

Figure 6. (Top) Structural parameters of DNA helix: Example of a Watson–Crick double helix (From ref[12]). (Bottom) Access to different functional groups from the major and minor groove of the helix. (From ref[13])

Helix sense refers to the helical turn of the double helix. DNA can fold in different forms (B-DNA, A-DNA, etc. which will be described later in this chapter). The canonical B-DNA is a right-handed (clockwise) helix. Most helical forms of DNA are right-handed.

Residues per turn refer to the number of base pairs in one helical turn. That is the number of bases required to complete one 360° rotation. The structure described by Watson and Crick contains about 10 base pairs per turn.

Axial rise is the distance between neighboring planar bases in the DNA double helix. In B-form DNA, the axial rise is about 3.4 Å.

Helix pitch is the length of a complete helical turn of DNA, which for B-form is 34 Å.

Base pair tilt refers to the angle of the planar bases regarding the helical axis. The tilt angle is measured by respecting the angle made by a line drawn through the two H-bonded bases relative to a line drawn perpendicular to the helix axis. In B-DNA, the bases are tilted by only −6°.

Diameter of the helix refers to the width in Å across the helix. The B-DNA diameter is 20 Å.

Rotation per residue, or *twist angle,* sometimes designated *h,* refers to the angle between two adjacent base pairs. Consider the angle between lines drawn through two adjacent base pairs. The rotation per residue is about 36° for B-form DNA.[11,12]

+ *Conformations of the nucleosides and sugar puckers*

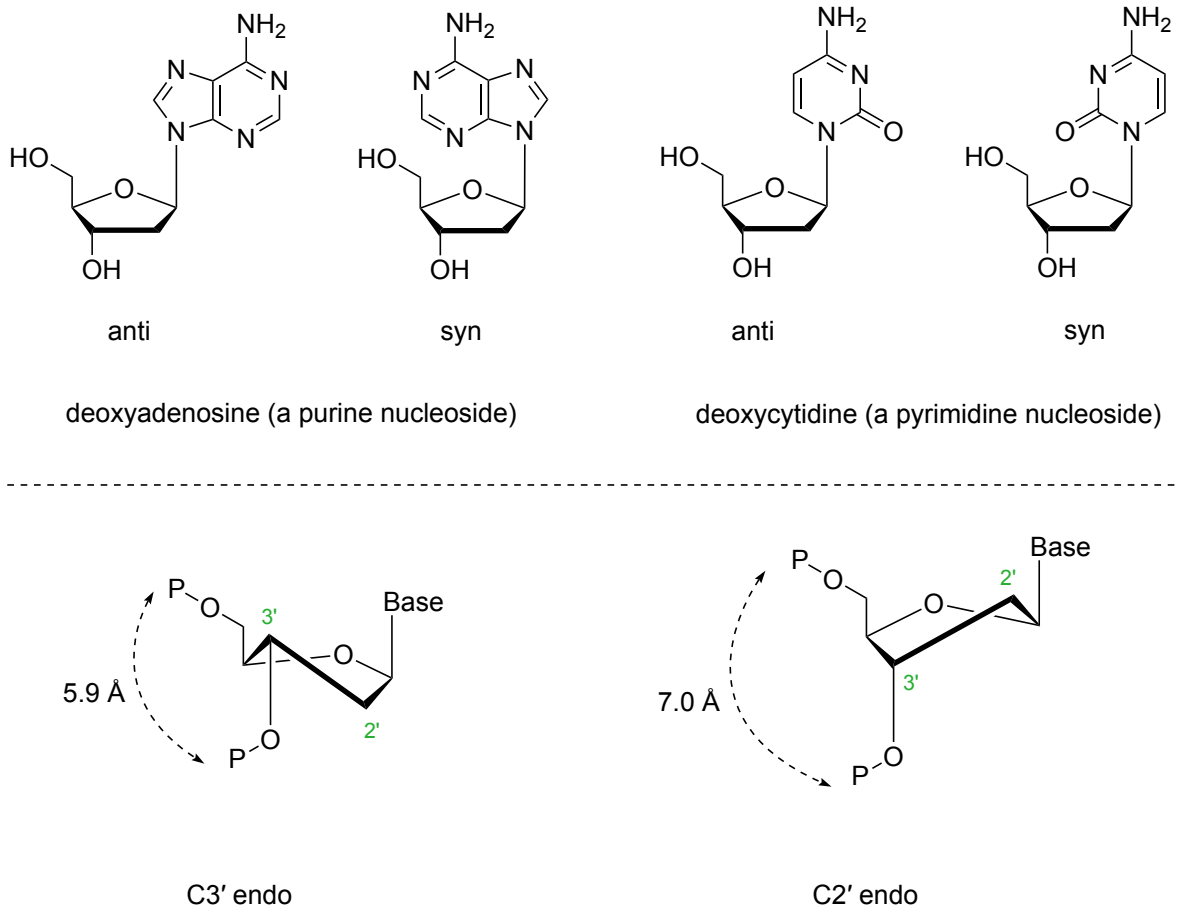

Figure 7. *Anti*- and *syn*- conformations of the nucleosides (top). C3′-*endo* and C2′-*endo* conformations of the deoxyribose (bottom).

One of the main reasons for the fact that DNA can adopt different forms is because the nucleosides can exist in different conformations. The bases can be *syn* and *anti* with respect to the sugar, and the sugar itself can exist in different conformations (mainly C2′-*endo* or C3′-*endo*) (Figure 7).[10] The *anti*-conformation is more stable than the *syn* orientation, especially for pyrimidine nucleosides. However, the *syn* conformation is energetically close to that of the *anti* for purine nucleosides. Both conformations are usually in equilibrium in solution at room temperature. A regular Watson–Crick base pair can be accomplished when the two

complementary nucleosides are in their *anti*-conformations. On the other hand, Hoogsteen base pairing requires the purine nucleosides in the *syn*-conformation. The sugar part of a nucleoside can adopt different conformations, where C3′-*endo* and C2′-*endo* are the most common. The C3′-*endo* and C2′-*endo* are defined when the corresponding C3′ and C2′ are placed upwards of the mean plane of the sugar ring. Noticeably, the C3′-*endo* conformation, with a shorter distance between the two adjacent phosphate groups than C2′-*endo*, can result in a more compact double helix. Sugar pucker is C2′-*endo* in a standard B-form DNA while it is C3′-*endo* for A-DNA (see also Table 1).

1.1.3. DNA hydration

Saenger[14] described DNA hydration in great detail. Herein, we would like to make a brief introduction based on the elegant book chapter and present some necessary updates based on recent research results.

In the cell, DNA exists in an aqueous environment containing other macromolecules, such as protein and different ions. In this case, water is not only playing the role of a medium to keep the solutes dissolved but also mainly responsible for stabilizing the secondary and tertiary structure of the macromolecules. For example, DNA phosphate–phosphate electrostatic repulsion is diminished by the high dielectric constant of water and hydrated counter-ions.[14] Moreover, DNA hydration has become an integral part of DNA conformation and its interaction with other molecules. In fact, relative water content and nature of the counter-ions affect the conformation of DNA. DNA undergoes a transition from A-form to B-form as the hydration is increased.[15-18]

The hydration is not homogeneous around the DNA and can be described in terms of two discrete layers representing primary and secondary hydration shells.[14] The first, consisting of approximately 20 water molecules per nucleotide, is impermeable to ions;[19] the second is permeable to ions and is not clearly distinguishable from bulk solvent. The bulk solvent beyond these two layers consists of water molecules that do not occupy fixed positions.[20] Hydration around DNA was studied by a number of techniques and further supported by the computational methods. For example, Howard et al.[21] reported contour maps showing relative hydration density around A•T and G•C base pairs (an example was shown in Figure 8). X-ray crystallography of oligonucleotides (*ODN*, a short single-stranded DNA sequence) has made it possible to explore the details of the fixed water positions around DNA. X-ray experiments have shown the existence of structural water molecules, particularly in the minor groove, illustrating a spine of hydration presented at the DNA minor groove. A chiral spine of hydration in the minor groove of DNA was also reported.[22]

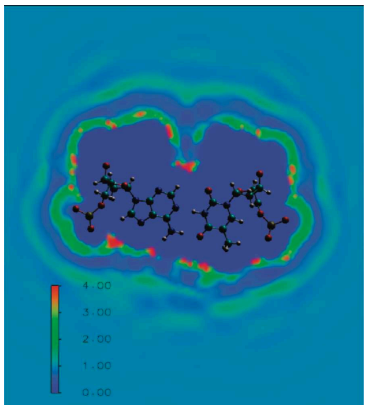

Figure 8. Volume slice through an A•T base pair. The slice is averages of the planes above and below the center plane with a range of ±0.47 Å. The color scale bar represents the density of water with a range of up to 4 times the bulk water. (From ref[21])

The roles of water in mediating interactions between drugs and nucleic acids are also of some interest. Water is displaced when a drug and nucleic acid bind to one another. If the water that is displaced originated from some well-ordered network that was totally disrupted, there would be a contribution to entropic stabilization.[20] On the other hand, the water may rearrange itself in such a way as to continue to play a structural role. For example, in the structures of complexes between daunomycin and dCGATCG,[23] or dCGTACG,[24] clearly defined water between the drug and the DNA were reported. In a recent study of the complex between berenil and dCGCGAATTCGCG, there existed a well-ordered water molecular bridge between the drug and the DNA, and some of the displaced water molecules were seen in the major groove around the phosphates.[25] A bridging water molecule had also been seen in the interaction of DNA with another groove binder, 4′,6-diamidino-2-phenylindole (DAPI).[10,20,26,27]

Overall, the water surrounding DNA consists of at least two layers, with the first layer bearing distinctive properties from bulk water. The hydration level of DNA is an integral part of DNA conformation. Moreover, water molecules around DNA play an important part in facilitating DNA–drug, DNA–macromolecules interactions. Ultimately, DNA hydration could become a vital channel for getting insight into DNA-related processes.[28]

1.1.4. DNA conformations

Local structural transitions from the canonical B-DNA into other complementary conformations can be functionally important. These transitions can occur within certain sequence elements of DNA and can play a key role in interactions with proteins involved in replication, gene expression, and recombination.[29] Typically, random DNA sequences can only form A-DNA or B-DNA. However, special sequences can form alternative structures such as left-handed Z-DNA, i-motif, or G-quadruplex.[12] An introduction to these conformations is presented in this part.

Table 1. Structural parameters of some conformations of DNA. (From: ref[11] and ref[29])

Structural Parameter	A-DNA	B-DNA	Z-DNA
Direction of helix rotation	Right handed	Right handed	Left handed
Residue per helical turn	11	10.5	12
Axial rise per residue	2.55 Å	3.4 Å	3.7 Å
Pitch (length) of the helix	2.82 Å	34 Å	44.4 Å
Base pair tilt	20°	−6°	7°
Rotation per residue	32.7°	34.3°	−30°
Diameter of helix	23 Å	20 Å	18 Å
Configuration **dA**, **dT**, **dC**	*anti*	*anti*	*anti*
of glycosidic bond **dG**	*anti*	*anti*	*syn*
Sugar Pucker **dA**, **dT**, **dC**	C3′ *endo*	C2′ *endo*	C2′ *endo*
dG	C3′ *endo*	C2′ *endo*	C3′ *endo*

1.1.4.1. B-DNA

The canonical B-DNA is a right-handed double helix made of two antiparallel strands that are held together via hydrogen bonds in the A•T and G•C base pairs (Figure 6). There are about 10.5 bp per helical turn. The ribose sugar is in its C2′ endo. The structural parameters of B-DNA are described in Table 1. A dominant feature of B-form DNA is the presence of two distinct grooves, a major and a minor groove, Figure 6. The two grooves have surfaces with different characters at which proteins can interact. For example, one DNA binding protein can have its domain of interaction at the major groove while other protein can bind to the minor groove. Certain chemicals and drugs can have specific interaction with either the major or the minor groove. From each groove, different functional groups on the bases can be accessible. For example, The Watson–Crick hydrogen bonding edges of the bases are not accessible to solvent or proteins since the functional groups on these edges are locating at the center of the double helix. So, the Hoogsteen hydrogen bonding edges of purines are accessible through the major groove (Figure 6). In B-DNA, the stacked base pairs form a central core surrounded by the phosphate backbone. The central core is a relatively chemically inert place to store genetic information.[11]

1.1.4.2. A-DNA

Similar to the B form, A-DNA is also a right-handed double helix made of two antiparallel strands (Figure 9). However, other structural parameters are different between the two forms. For example, one helical turn of A-DNA including 11 base pairs where the base pairs are tilted to about 20° with respect to the helical axis. Comparing to the canonical form, the grooves of A-DNA are not as deep, and the sugar pucker is C3′ endo instead of C2′ endo for B-DNA. A-DNA has its base pairs shifted to the helix periphery, which creates a 9-Å-hole in the helix center. The two forms of DNA have different stability conditions due to their different patterns of bound cations and water molecules.[30-32] B-DNA is stable under various conditions, whereas

A-DNA mainly observes under reduced water conditions and is somewhat sequence-specific. For example, A-form DNA was originally observed on DNA fibers at 75% relative humidity.[33] Runs of poly(dG)•poly(dC) are likely set up an A-like helix, characterized by circular dichroism (CD).[34] Therefore, it is reasonable to assume that specific regions of B-like DNA may exist in an A-DNA form.[11]

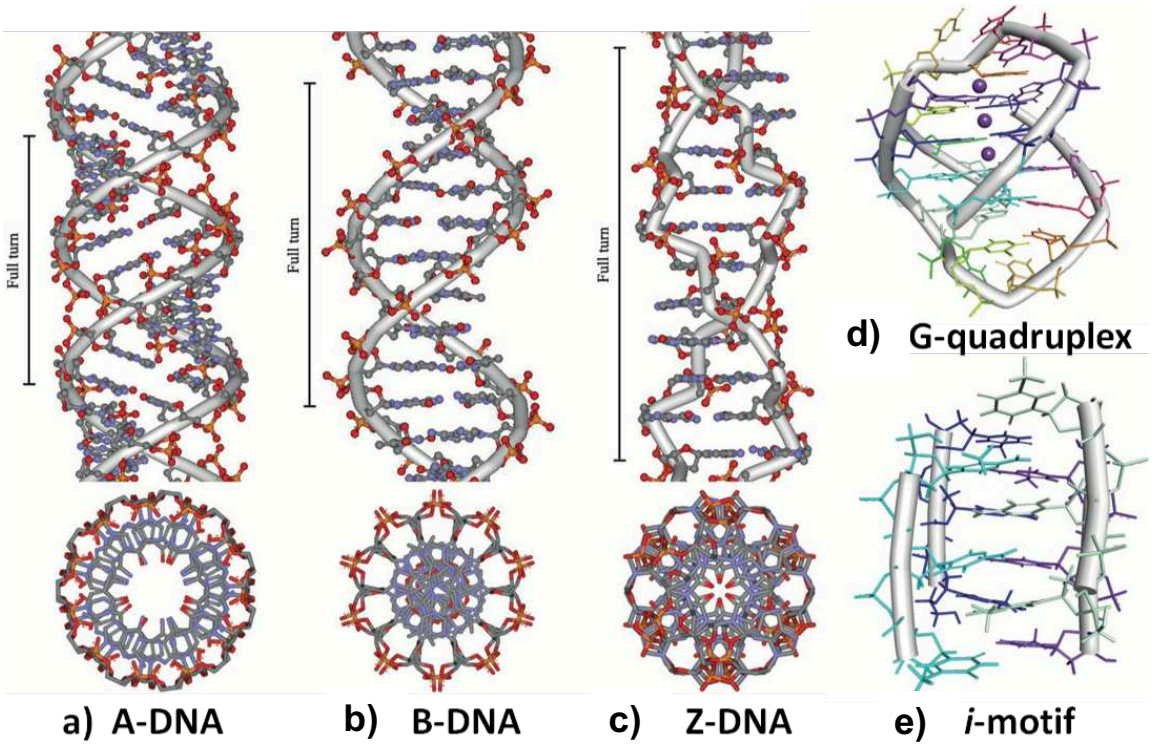

Figure 9. Models of various known DNA structures. (a), (b), (c), (d), and (e) corresponding to A-DNA, B-DNA, Z-DNA, G-quadruplex, and i-motif, respectively. (Adapted from ref[35])

1.1.4.3. Z-DNA

Z-DNA (Figure 9 and 10) is a left-handed helix which mostly found in alternating purine–pyrimidine sequences such as $(CG)_n$ and $(TG)_n$.[36] Z-DNA is thinner than B-DNA with 18 Å and 20 Å in helical diameter, respectively. Z-DNA has its base pairs shifted to the periphery of the helix and only one deep, narrow groove equivalent to the minor groove of the canonical structure. Z-DNA is characterized by 12 bp per helical turn, an average rise is 3.7 Å/bp, and a zigzag backbone. In Z-DNA, **dC**, **dT**, and **dA** have *anti*-conformation with the sugar pucker is C2′ endo; meanwhile, dG has *syn*-conformation and the sugar pucker is C3′ endo. Some negatively charged phosphate groups of Z-DNA are closer than that in B-DNA due to the zigzag backbone path. Therefore, Z-DNA is stabilized by high salt concentrations or polyvalent cations, which can help to shield the phosphate groups' electrostatic repulsion. The existence of Z-DNA *in vivo* has been suggested by several convincing pieces of evidence. First, Z-DNA forming sequences exist abundantly in the human genome.[37] Secondly, various Z-DNA binding proteins exist *in vivo*, suggesting the Z conformation may have certain roles inside the cell.[38-40] Moreover, a crystal structure of a junction between the right-handed B-DNA and left-

handed Z-DNA was reported. The junction was stabilized by numerous base pairings and stackings, thereby minimizing the energetic cost and facilitating the existence of Z-DNA in nature.[41,42]

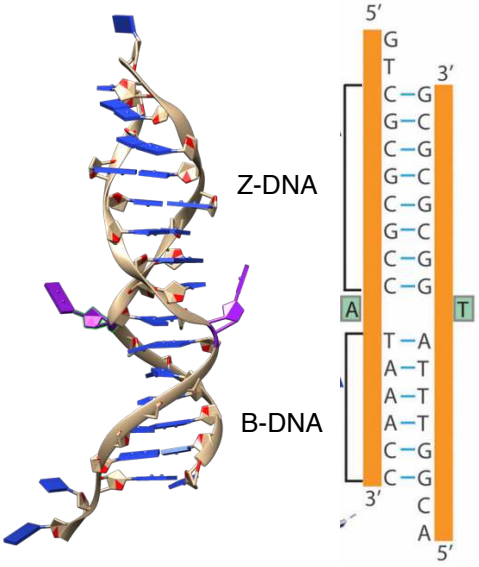

Figure 10. Crystal structure of the B–Z junction (PDB: 2ACJ and ref[42]). Adenine and thymine bases at the B–Z junction are flipped out of the helix. Base pairings and stacking are maximized in this structure.

1.1.4.4. i-Motif DNA (i-tetraplex)

The i-motif structure consists of two parallel-stranded DNA duplexes held together by cytosine–cytosine^{+} hemiprotonated base pairs that are intercalated in an antiparallel orientation (Figure 9 and 11).[43] The structure is formed from a cytosine (C)-rich strand at slightly acidic or even neutral pH.[44,45] C-rich sequences are found in G/C rich promoters and telomeric regions in DNA. Dissociation of a G/C rich double-stranded DNA produces two single G- and C-rich strands, which can fold in G-quadruplex and i-motif, respectively. The i-motif structures are greatly affected by the number of cytosine bases,[46] loop length,[47] environmental condition,[48] and attached or interacting material with the DNA strands.[42,49-51]

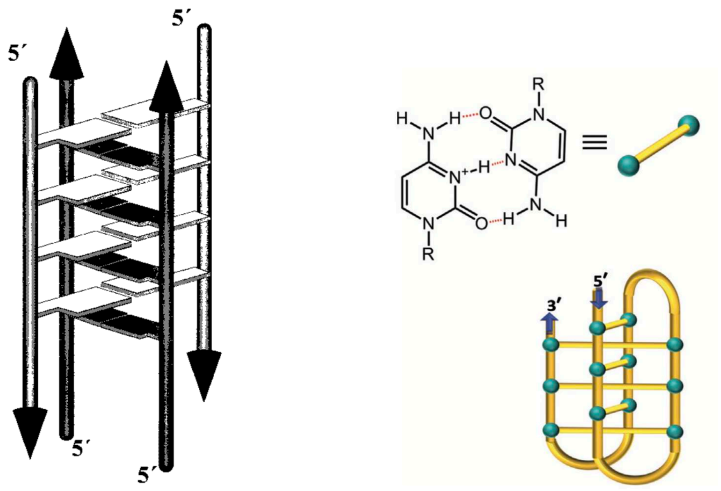

Figure 11. (Left) Representation of the base pairs of i-motif structure (From: ref[51] and ref[52]). (Right) Structure and orientation of i-motifs (From: ref[53]).

1.1.4.5. G-quadruplex

Guanine (G)-rich sequences can form G-quadruplex structures consisting of π–π stacking of planar G-tetrads. Each G-tetrads is constructed from four guanine bases, which cyclically bound to each other through eight hydrogen bonds, according to the Hoogsteen base pairs.[54,55] The G-tetrads is further stabilized by the coordination with mono- or di-valent cation at its center (Figure 9 and 12).[42] There are various G-quadruplex structures which depending on the nucleotide sequences, the orientation of the strands, the syn/anti conformation of guanosines, and environmental factors such as cations.[55-59] G-rich sequences are frequently observed in the promoter region of oncogene and human telomeric DNA, predicting the potential biological importance of the structures.[42,44,60,61] Moreover, recent evidence suggests their involvement in key genome processes, such as transcription, replication, and epigenetic regulation, as well as numerous connections to cancer biology.[62]

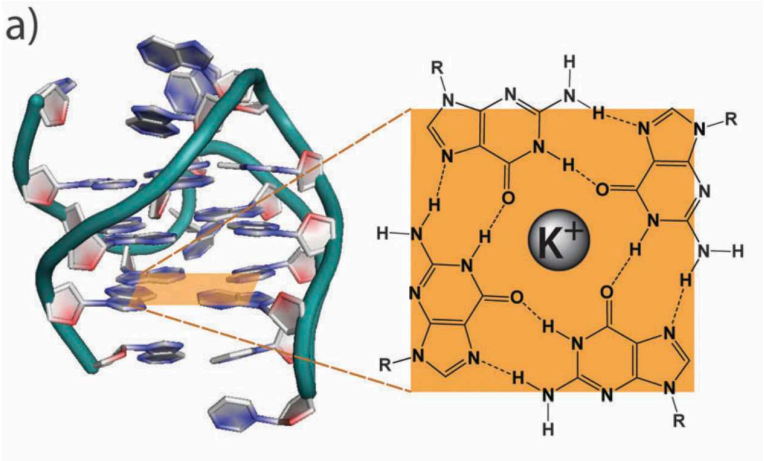

Figure 12. G-quadruplex (PDB id: 2KZD) and G-tetrads composed of four guanine bases (orange). (From: ref[42])

1.1.5. DNA–protein interactions

Transcription and translation of genes leading to protein formation are known as molecular biology's central dogma (Figure 3). The initial stage of this process, so-called "gene expression" – which involves chromatin modification and transcription complexes, is regulated by DNA binding proteins.[63] Precise regulated control, including activation and suppression of gene expression, is essential for proper growth, development, and subsequent maintenance of an organism. In general, transcription involves the binding of a specific group of proteins (called transcription factors, *TF*s) to local regions of DNA. The latter is then unzipped into two separate strands following by the synthesis of messenger RNA (mRNA) from one of the two strands. Apart from transcription, DNA recognition by proteins is crucial in other important processes such as the transfer of genetic information, cell differentiation, packaging, rearrangement, replication, and repair.[63] At the fundamental of all such is the binding of proteins to DNA sequences to form protein–DNA complex.[64] Therefore, it is essential to understand DNA–protein interactions as it is a stepping stone for understanding life's fundamental processes.[63]

DNA–protein interaction is accomplished by specific as well as nonspecific interactions;[13] and often accompanied by the conformational changes in either or both partners.[65-68] Specific interactions involve the hydrogen bonds network between a specific DNA sequence and amino acids of the protein as well as sequence-dependent deformation of DNA.[63,69-71] Nonspecific interactions include electrostatic interactions between the negatively charged phosphate backbone and protein, the van der Waals interaction, and water-mediated bonds.[13] The conformational changes should lead to a stabilization of the protein–DNA complex. DNA conformational changes can vary from smooth to drastic changes such as disruption of the base stacking, base flipping, or sharp bends.[63,72] An example of a protein–DNA complex is given in Figure 13.

Interestingly, it has been proposed that protein binds nonspecifically to DNA before sliding along to reach its specific binding site on DNA.[73-75] This is known as the "facilitated diffusion

mechanism", which has been proposed to explain the fast binding rate of protein to genomic DNA.[63]

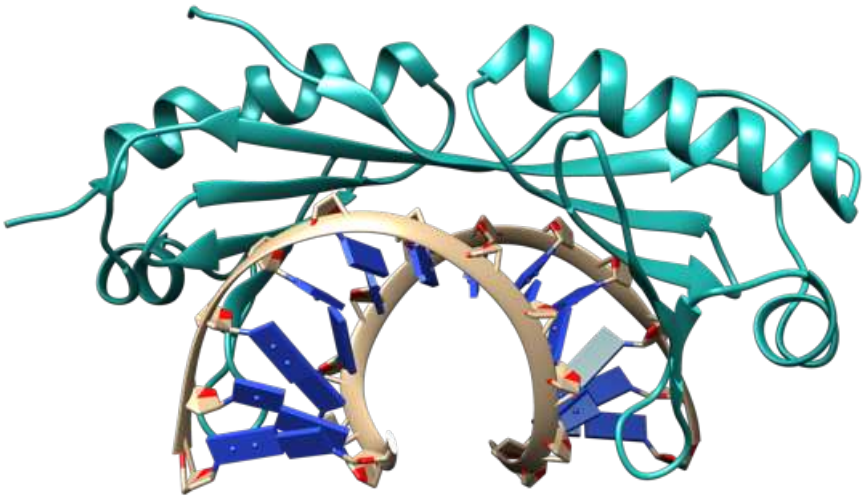

Figure 13. Crystal structure of a complex between TATA protein and its DNA sequence. (From PDB: 1TGH)

1.2. Introduction to light-related processes

There are several processes in which DNA is one of the central players in maintaining a living cell's function. New processes will continue to be discovered with the coming of time. At this moment, however, some of the most important processes are DNA–protein interactions, DNA conformational changes, and DNA modifications. Each process is not an isolated event; instead, one process could lead to a series of other processes and vice versa. For example, the binding of a protein to a DNA sequence could change the latter's conformation and/or lead to base modifications.

Since the above processes are at the heart of chemical biology, a better understanding of these processes could accelerate other research areas such as drug developments. This comes from the development of better tools and sensing approaches where a majority is based on light-related processes such as absorption and emission of light. For this reason, we would like to introduce some basics regarding the laters.

1.2.1. What is light?

The expression "light" used here is limited to the near-ultraviolet (UV, λ 200–400 nm) and visible regions (VIS, λ 400–700 nm) of the entire electromagnetic spectrum (Figure 14), which spans over 20 orders of magnitude.

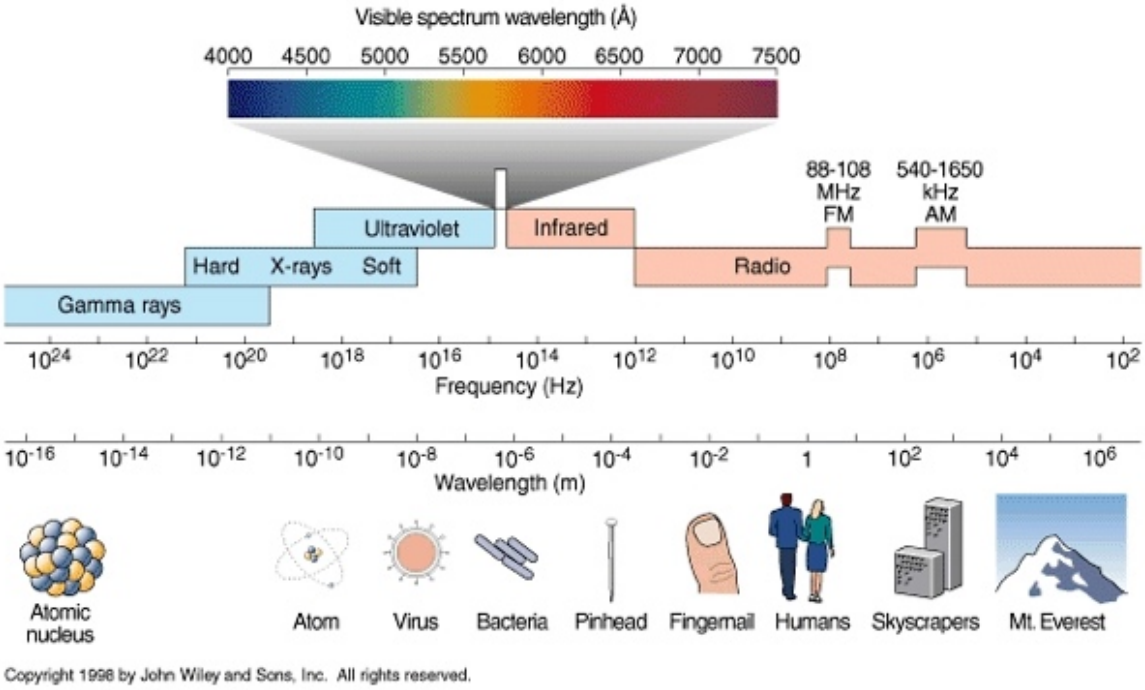

Figure 14. Representation of a full range of electromagnetic radiation and its energy. (From https://www.geo.arizona.edu/xtal/geos306/geos306-12.htm, on 29/07/2020)

According to quantum theory, light is quantized, which means only certain levels of energies are allowed. The absorption or emission of light (will be described later) occurs by the transfer of energy as *photons*. These photons have both wavelike and particle-like properties. Each photon has a specific energy, E, given by *Planck's law*:[76]

$$E = h\nu = hc/\lambda$$

Where,
h = Planck's constant (6.62607004×10^{-34} m^2 kg/s);
ν is the frequency of photon (Hz);
c is the speed of light (in vacuum c = $3x10^8$ m/s);
λ is the wavelength of photon (nm).

1.2.2. Absorption

Light absorption is a process in which light is absorbed and converted into energy. When light reaches an object, it can be absorbed, transmitted, or reflected. Absorption depends on the electromagnetic frequency (energy) of the light and the object's nature.

Similar to light, electrons in the matter have both wavelike and particle-like properties. The energy of matter is also quantized. Light can be absorbed by a matter if its photon having energy equal to the energy gap between two electronic states of the matter. Among the absorption of light, energy from absorbed photon becomes part of the total energy of the matter and is used to move an electron of the matter from the lower energy level to an upper one, producing an electronically-excited state.[76] Chemical functionalities that absorb light are termed *chromophores*.

Light absorption in the UV-vis region by an organic molecule generally involves the transition of an electron from π to π^* orbitals present in multiple bonds (C=C, C=X, C≡C, and C≡N bonds). The more multiple bonds a molecule has, the greater probability for light absorption by that substance. Meanwhile, the maximum absorption is moving to longer wavelengths (lower energy) as the amount of electron delocalization in the substance increases (Figure 15). Thus, the lowest energy transition in an organic molecule will be the HOMO → LUMO transition.

Transitions n → π^* are forbidden according to the symmetry selection rule. However, in practice, the band corresponding to the n → π^* transition can be observed in the absorption spectrum. If observable, this transition is often as a weaker band and at a longer wavelength compared to that of the $\pi \rightarrow \pi^*$ transition. The latter is due to a higher energy level of orbital n comparing to π orbital (Figure 15). In fact, n → π^* transition is weakly allowed due to *vibronic coupling*.

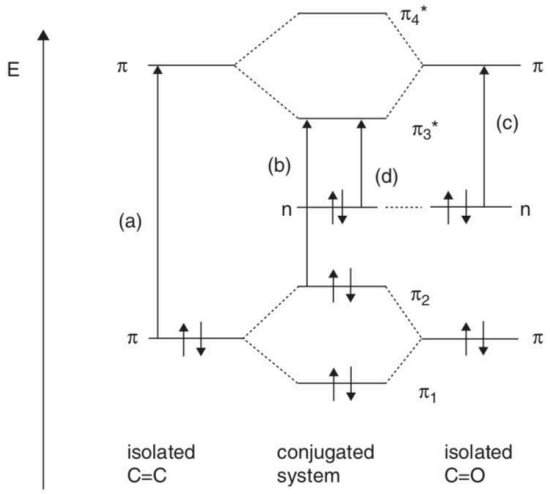

Figure 15. Interaction of a C=C bond and a C=O group in propenal. (a) Transition $\pi \rightarrow \pi^*$ of isolated C=C corresponding to a band at the shortest wavelength (highest energy). (b) The $\pi \rightarrow \pi^*$ transition of the conjugated system corresponds to a band at a longer wavelength and higher transition probability (larger absorption coefficient). (c–d) The $n \rightarrow \pi^*$ transitions occur at longer wavelengths but with lower probabilities. (From ref[76])

1.2.2.1. Beer–Lambert law

As light passing through a sample with a path length (ℓ), it is absorbed. The intensity of light entering the sample, I_{in}, is greater than that coming out of the sample, I_{out}. There is an exponential relationship between the relative absorption (transmittance, T) and the concentration (C) and path length (ℓ) of the absorbing substance.

$$T = I_{out}/I_{in} = 10^{-\varepsilon \ell C}$$

Taking logarithms to the base 10 gives us:

$$\log T = \log(I_{out}/I_{in}) = -\varepsilon \ell C$$

Thus:

$$-\log T = \log(I_{in}/I_{out}) = \varepsilon \ell C$$

The quantity of $\log(I_{in}/I_{out})$ is called *absorbance*, $\mathcal{A}$, and the linear relationship between absorbance, concentration and path length is known as the *Beer–Lambert law*:

$$\mathcal{A} = \varepsilon \ell C$$

Where,
ε is the molar absorption (or extinction) coefficient ($M^{-1}.cm^{-1}$);
ℓ is the path length (cm);
C is the concentration (mole/L).[76]

1.2.2.2. Franck–Condon (FC) Principle

FC principle states that because nuclei are much more massive than electrons (the mass of a proton is ca. 1000 times the mass of an electron), an electronic transition from one orbital to another takes place while the massive, higher-inertia nucleus is essentially stationary (From: page 123)[77] (Figure 16). It means that the most probable electronic transitions will occur between those states processing a similar nuclear configuration and vibrational momentum at the instant of an electronic transition. In other words, absorption of a photon often results in a *vertical electronic transition* (*Franck–Condon transition* or *vertical transition*), Figure 16.[76]

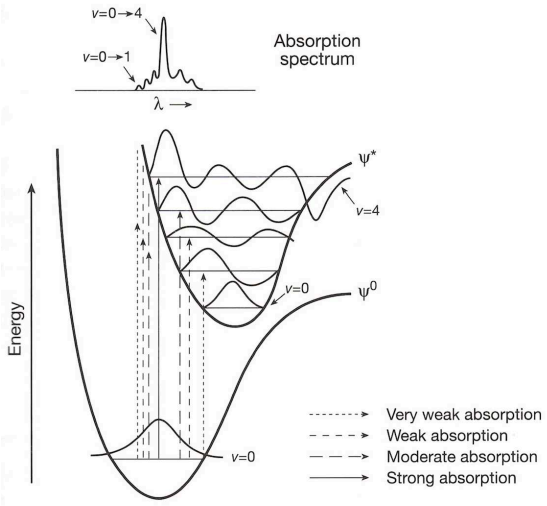

Figure 16. Representation of FC interpretation of the absorption of light. (From page 129 – ref[77])

1.2.3. Luminescence

1.2.3.1. Jablonski diagram

Photon absorption results in a molecule in the excited state which is excess in energy and is then following a number of pathways to come back to its ground state. Jablonski diagram (Figure 17) is widely used to represent these pathways. Understanding these decay processes lies at the heart of molecular photophysics. The following parts are dedicated to describe important processes and give some basics for elucidating photophysics that will go on later.

Vibrational Relaxation

FC transition usually results in an excited species with an excess of vibrational energy ($v > 0$ in Figure 17). Transition between a vibrationally-excited state ($v > 0$) and the $v = 0$ state within a given electronic state, for example $S_2(v = 5) \rightarrow S_2(v = 0)$, is called *vibrational relaxation*. Typically, this process happens within 10^{-13}–10^{-9} s timescale, and the excess vibrational energy is dissipated as heat.

Internal Conversion

Internal conversion is the relaxation from an upper excited electronic state such as S_2, S_3, etc. to a lower electronic excited state with the same multiplicity. For example, $S_2 \rightarrow S_1$ relaxation is an internal conversion. Typical timescale internal conversion between excited states is around 10^{-14}–10^{-11} s, and around 10^{-9}–10^{-7} s for conversion between S_1 and S_0.

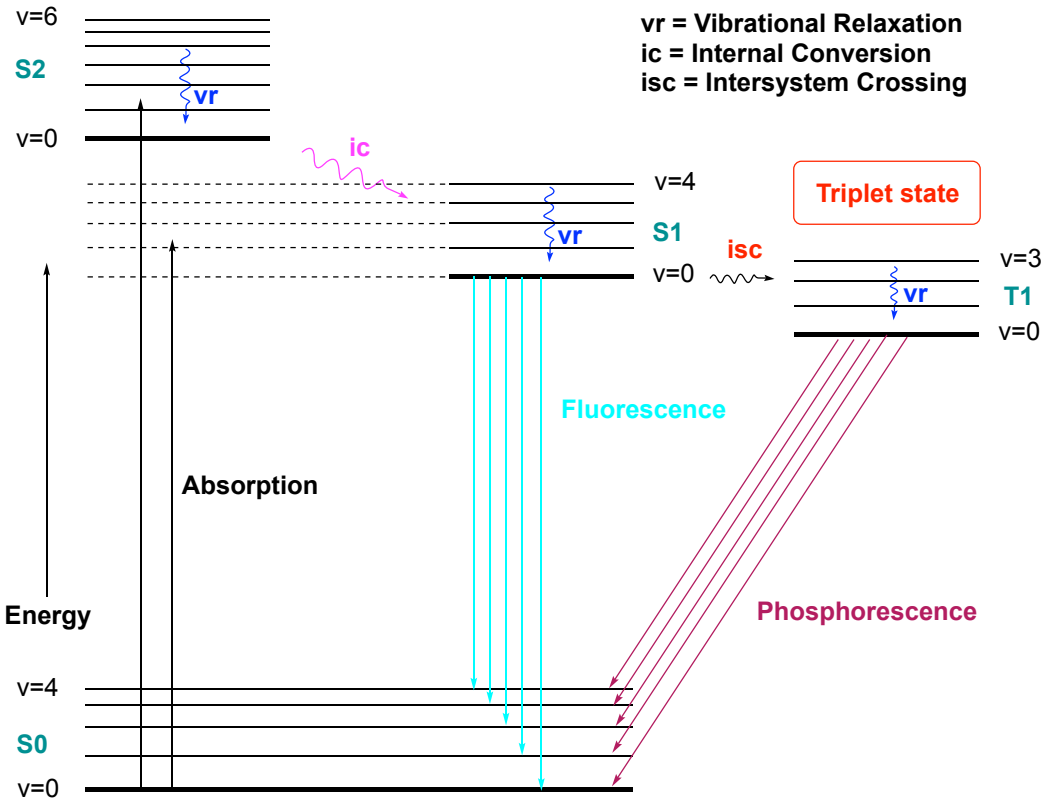

Figure 17. Jablonski diagram for an organic molecule, illustrating excited-state processes.

Intersystem Crossing

Intersystem crossing involves transitions between isoenergetic states of different multiplicity, for example $S_1(v = 0) \rightarrow T_1(v = n)$. These intramolecular radiationless transitions are spin-forbidden with a broad range of timescale around 10^{-11}–10^{-3} s.

Fluorescence involves a radiative transition (photon emission) between states of the same multiplicity (spin-allowed), usually from the lowest vibrational level of the lowest excited

singlet state, $S_1(v = 0)$. Typical timescales for fluorescence emission are of the order of 10^{-12}–10^{-6} s.

$$S_1 \rightarrow S_0 + h\nu$$

A molecule (or a part of a molecule) that has the ability to fluoresce is called a *fluorophore*. A fluorophore is also commonly called a *dye*. The difference in energy (wavenumber or frequency unit) between absorption and emission maxima of the same electronic transition is called *Stokes shift*. A fluorophore used to study biological samples is called a *probe*.

Phosphorescence is a spin-forbidden radiative transition between states of different multiplicity, usually from the lowest vibrational level of the lowest excited triplet state, $T_1(v = 0)$. Typical timescales for photon emission by phosphorescence are of the order of 10^{-3}–10^{2} s.

$$T_1 \rightarrow S_0 + h\nu$$

Luminescence

Luminescence is the spontaneous emission of light quanta upon excitation by any source of energy (sometimes except heat). The energy sources can be a chemical reaction (chemiluminescence), an electric current passed through a substance (electroluminescence), mechanical action on a solid (mechanoluminescence), light (photoluminescence). Photoluminescence is classified into two forms, fluorescence and phosphorescence, concerning the nature of the radiative transition (described previously).

1.2.3.2. Kasha's rule

Since the energy gap between S_1 and S_0 is generally much larger than that between any successive excited states, internal conversion between S_1 and S_0 occurs much slower than the internal conversions between excited states. This is the foundation of *Kasha's rule*, which states that because of a very rapid deactivation to the lowest vibrational level of the lowest excited state $S_1(v = 0)$ or $T_1(v = 0)$, luminescence emission and chemical reaction by excited molecules will always originate from the lowest vibrational level of S_1 or T_1. The outcome of this rule is that emission spectra are typically independent of excitation wavelength.[76,78]

Some exceptions to Kasha's rule were known where fluorescence is observed mostly from S_2.[79,80] Among them, the azulene family represents a well-studied case. The lack of normal fluorescence from azulene is due to a fast $S_1 \rightarrow S_0$ internal conversion as the result of a relatively small S_1, S_0 energy gap and the presence of a conical intersection crossing near the S_1 minimum.[77]

1.2.3.3. Lifetime and Quantum yield

The fluorescence lifetime and quantum yield are vital characteristics of a fluorophore. Quantum yield (QY, Φ) is the number of emitted photons relative to the number of absorbed photons. QY is proportional to the brightness, defined later in this part, of a fluorophore. The excited state's lifetime is defined by the average time the molecule spends in the excited state prior to return to the ground state. The lifetime is also important, as it could give useful information about interactions of a fluorophore and its environment.[81,82] QY (Φ) and lifetime (τ) are given by

$$\Phi = k_r/(k_r + k_{nr})$$

$$\tau = 1/(k_r + k_{nr})$$

Where: k_r is radiative decay rate; and k_{nr} is non-radiative decay rate (including ic and isc).

The lifetime of a fluorophore in the absence of non-radiative processes is called the intrinsic or natural lifetime and is given by

$$\tau_n = 1/k_r$$

Hence, the natural lifetime can be calculated from a measured lifetime (τ) and QY.

$$\tau_n = \tau/\Phi$$

The brightness of a fluorophore is proportional to its QY and extinction coefficient and is given by:

$$\text{Brightness} = \text{extinction coefficient } (\varepsilon) \text{ x Quantum yield } (\Phi).$$

1.3. Fluorescent nucleic acid base analogs

1.3.1. Introduction

Among important techniques for studying nucleic acid-containing systems, fluorescence is dominant. It comes from the fact that the technique is versatile, easily accessible, fast and straightforward, noninvasive, and especially extremely sensitive. Eventually, it has found enormous uses in single-molecule real-time dynamics, microscopy, nucleic acid detection, and nucleic acid–protein interaction measurements.[83] Specifically, fluorescence spectroscopy has found extensive uses in investigations such as nucleic acids conformational changes, nucleic acid–protein interactions as well as nucleic acid–small molecule complexes.[84-87]

Since the four canonical nucleobases have very low intrinsic emission, fluorescent reporters have to be introduced into nucleic acids, either noncovalently or covalently.[88-92] Well known for the former includes ethidium bromide, DAPI, SYBR Green, and Hoechst dyes. These dyes can bind noncovalently to nucleic acids by intercalation or along the grooves and can be used to visualize nucleic acids in cell microscopy or gel electrophoresis. Alternatively, nucleic acids can be fluorescently modified by attachment of a fluorophore to the phosphate backbone, sugar, or base. Derivatives of rhodamine, Alexa, and cyanine dyes, etc. are commercially available and are easy to use for such purposes.[93,94] In fact, they have found many uses in fluorescence experiments base on Förster resonance energy transfer (FRET), fluorescence anisotropy, and single-molecule fluorescence experiments.[95-101] However, the major problem is that these approaches often cause significant perturbations to nucleic acids' native structure. Hence, examples were found in which the probes were linked to ODNs via long linkers in order to decrease the perturbations.[102]

Fluorescent nucleobases are alternatives to overcome the above issues. They are analogs of the canonical (DNA and RNA) nucleobases that could maintain the biological functionalities such as base pairing, stacking, and enzyme incorporation and bring fluorescence properties to the nucleic acids under analysis. Hence, these molecules (probes) have emerged as extremely useful tools for understanding nucleic acid-containing systems at the molecular level. One of the most well-known examples is 2-aminopurine (**2AP**).[103] Typically, significant modifications to the structure of nucleobases are required to make them useful probes. These modifications can either be described as canonical or non-canonical, depending on the Watson–Crick-like pairing ability of the modified analogs.[104] Canonical nucleobase analogs, as defined by Kool et al., 2017 in their seminal review, are constrained by:[104] i) the purine or pyrimidine underlying architecture; and ii) retention of at least two Watson–Crick hydrogen-bonding groups. The latter allows the designed analogs to potentially base pair with a complementary base and maintain the structure and stability of the forming duplex.[104]

We limit ourselves here to describe some of the most important approaches in the class of canonical nucleobase analogs. The analogs will be classified into four main groups: substituent modification and isomorphic nucleobases, ring-fused systems, connecting the base with a fluorophore via a flexible linker, and extending the nucleobase's electronic system via a conjugated bridge. First of all, the general synthetical (modification, designing) approaches will

be presented. Then, within each group, some examples will be given along with a brief introduction about their photophysical characters and applications when necessary.

1.3.2. Design and synthesis

1.3.2.1. Design

As a rule of thumb, fluorescent nucleobase analogs are often desired to get their excitation and emission wavelengths shifted toward the red for *in vivo* applications. Achieving that helps avoid background emission of the cell and cytotoxicity arises from the excitation at ultraviolet wavelengths. Extension of the π-systems and incorporation of heteroatoms are typical routes to obtain red-shifted optical profiles. However, these modifications may affect the base pairing and/or helical structure of the duplex.[104] Thus, careful structural design is important to construct useful probes for such applications.

The architecture of the natural nucleobases offers various possibilities to make them fluoresce. However, there are some positions where modifications should be favored in order to obtain fluorescently canonical nucleobase analogs. In general, modifications at the base-pairing (WC) edge should be avoided since it may cause significant effects on the base pairing and the DNA structure. For the rest, a suitable position needs to take into account the DNA groove as well as the synthetical accessibility of the modification.

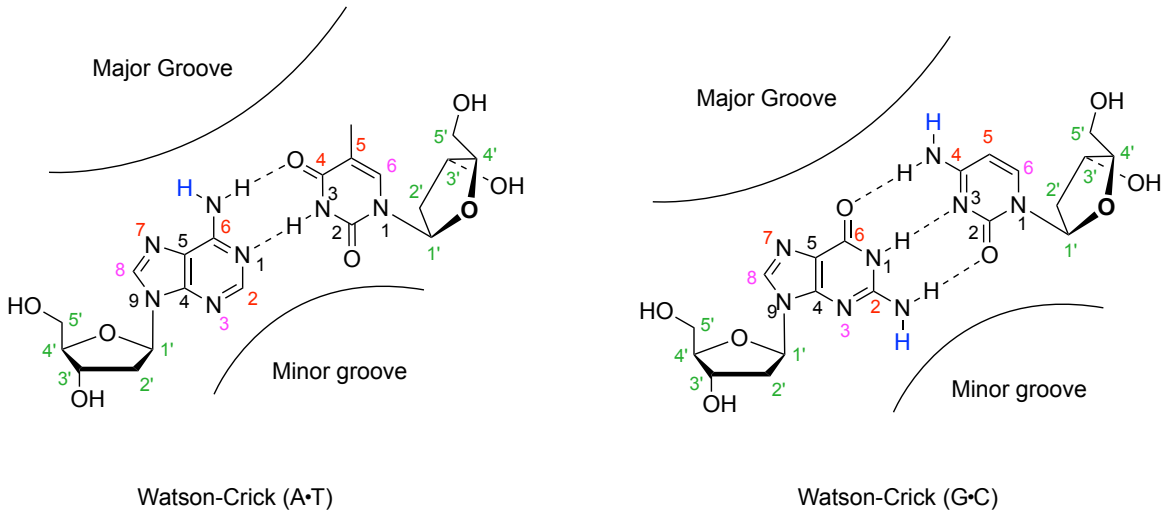

Figure 18. Representation of the structures and prospective positions for modifications of the four canonical nucleobases. Common positions are depicted in red, magenta, and blue.

For pyrimidine bases, it is clear to see that the 5 position is the most suitable (Figure 18). Substitution at this position not only exposes the substituent to the major groove of the DNA helix with wide space but also synthetically easy to achieve. Moreover, several examples using this approach have shown good biocompatibility. Eventually, it has become the best position for such purposes.

Purine nucleobases offer more possibilities to modify their structures such as the 8, 7, 6, 2, and 3 positions. Nevertheless, much fewer examples were reported comparing to that of pyrimidine ones. In terms of chemical synthesis, the 8 and 2 positions are the most easily accessible. The 8 position has become a dominant contributor to such modifications. In terms of biocompatibility, the 7 position is the most promising. However, modification at this position often requires the use of deaza analogs of purine bases, which are sometimes not commercially available. Table 2 outlines some advantages and disadvantages of modification at common positions of pyrimidine and purine bases.

Table 2. Different positions for modifications of nucleobases: Pros and cons.

Position on base		Groove	**No** need deaza analog	Biocompatible	Synthetically favorable
Pyrimidine	Purine				
5		Major	✓	✓	✓
4		Major	✓		
	8	Major	✓		✓
	2	Minor	✓		✓
	7	Major		✓	
	6	Major	✓		
	3	Minor			

1.3.2.2. Synthesis

Modifications at the 5 position of pyrimidine bases are accessible through a number of simple and selective methods. The most common route is to start with 5-halide derivatives of pyrimidine bases, which are usually commercially available. For example, 5-halo uridines can be coupled with aryl boronic acids,[105] organostannanes,[106] alkynes,[107] and alkenes (Figure 19 route A).[108] The less common approaches are to start with natural pyrimidine bases. For instant, uridine can be selectively halogenated at the 5 position,[109] or subjected to a direct C–H activated functionalization (Figure 19).[110]

Similarly, halide derivatives of purine bases can undergo reactions in route A (Figure 19). The 8 position of purine bases can be selectively halogenated to generate corresponding halide derivatives[111,112] or directly functionalized by C–H activation methods (Figure 20).[110] The 2-halogenated analogs of purine bases can be obtained from guanine base.[113] Modifications at the 7 position of purine bases often require the use of 7-deaza analogs (Figure 21). Halogenation at the 7 position of these deaza derivatives are synthetically accessible.[114-116]

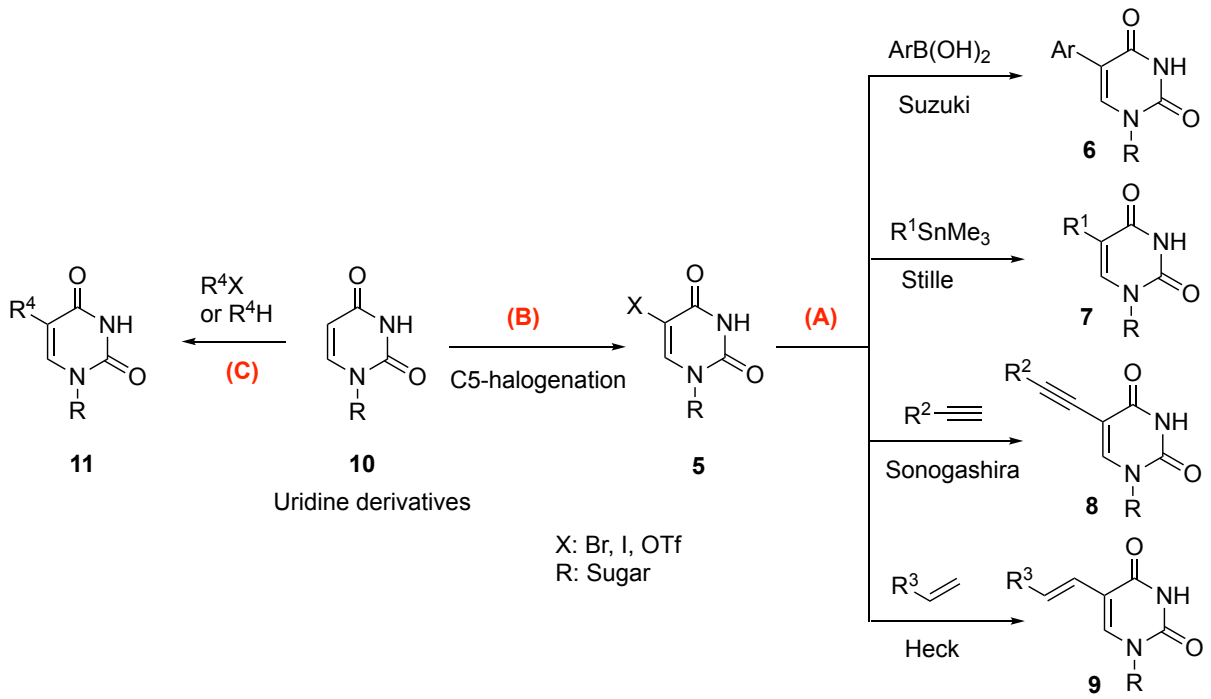

Figure 19. Common approaches for functionalization of uridine derivatives. (From: ref[110] and ref[117])

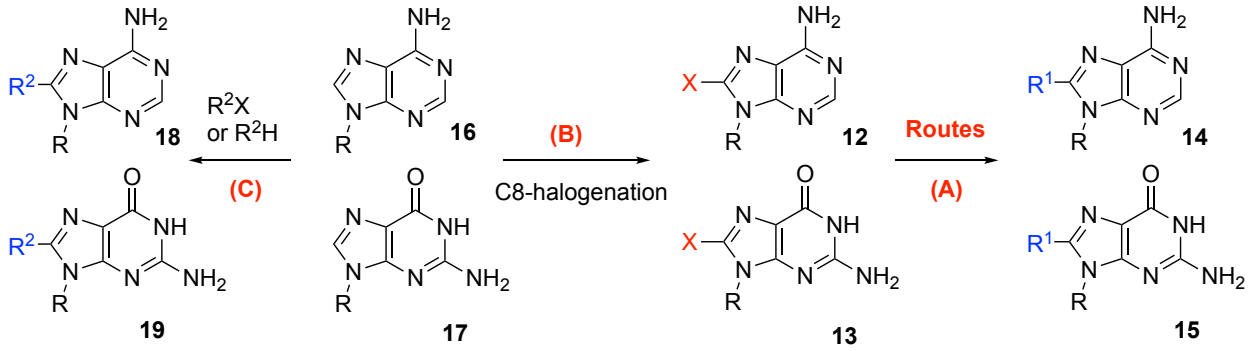

Figure 20. Common approaches for C-8 functionalization of purine bases.

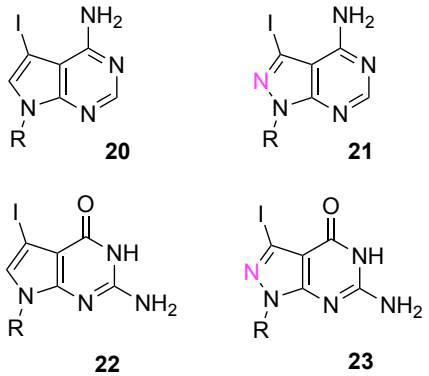

Figure 21. Structure of 7-deaza analogs of purine bases.

1.3.3. Substituent modification and isomorphic nucleobase

Substituent modifications focus either on replacing the original substituents with new functional groups or appending substituents on the nucleobase core structure.[104] The concept includes *isomorphic* nucleobase, where it was introduced to identify a class of nucleobase analogs that closely resemble their natural counterparts in terms of overall dimension (isosterism) and ability to form Watson–Crick base pairs.[118] The two concepts can sometimes be used interchangeably since the formation of an isomorphic nucleobase needs modifications on the nucleobase's substituents, and small modifications on the substituents can lead to an isomorphic nucleobase.

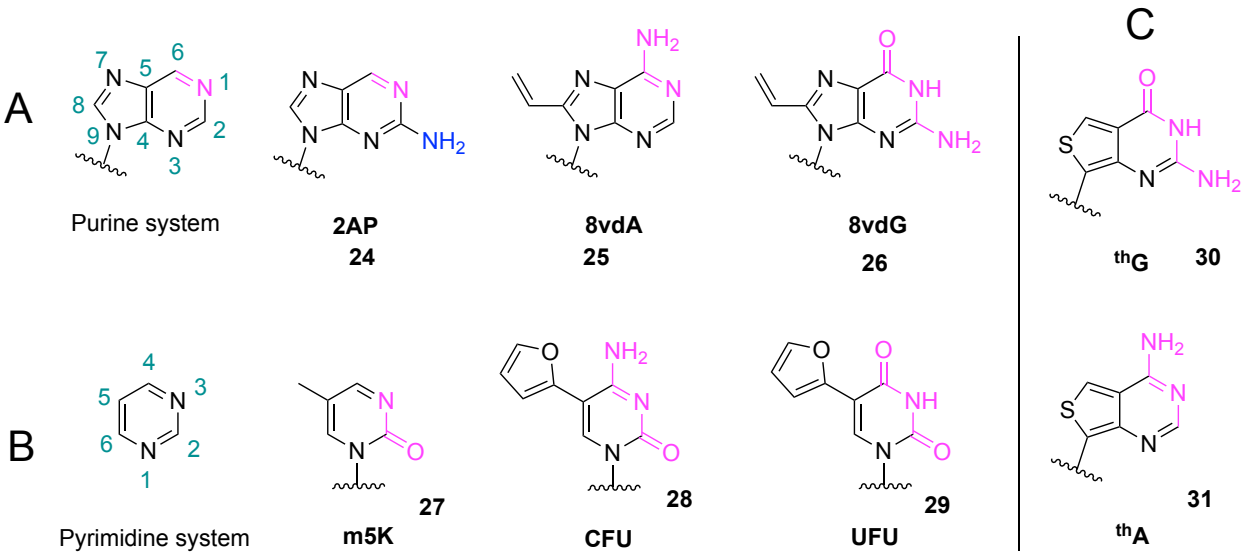

Figure 22. Examples of substituent modifications on purine and pyrimidine systems.

An early and very useful fluorescent nucleobase is 2-aminopurine (**2AP**, Figure 22).[103] By moving the 6-amino of adenine to the 2 position, **2AP** absorption maximum is centered ~305 nm while exhibits emission at 370 nm, about 50 nm red-shifted relative to adenine. It is highly fluorescent in free solution (QY 0.68) but strongly quenched when incorporated into nucleic acids with the amplitude of quenching highly sequence-dependent. This sensitivity to microenvironment has been used to investigate in several applications including nucleic acid structure and dynamics,[119-121] study DNA–protein interactions,[122] and study of photo-induced electron transfer.[123] However, **2AP** has less specificity in base-pairing relative to adenine. It can form stable base pairs with thymine (Figure 23(left)) and uracil but also moderately stable base pair with cytosine (Figure 23(right)).[8,124,125] This can cause some perturbation to the labeled DNA sequence.[83]

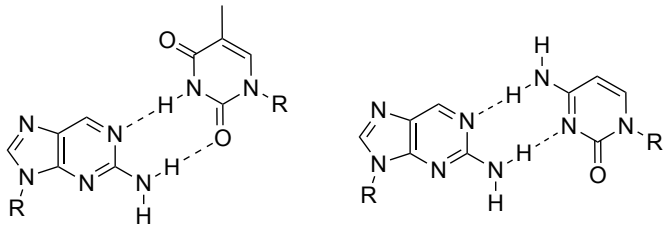

Figure 23. Base pairing between **2AP** and thymine (left); **2AP** and cytosine (right).

As an alternative to **2AP**, 8-vinyldeoxyadenosine (**8vdA,** Figure 22), adding a vinyl group to the 8 position of **dA**, was reported by our group with improved photophysical properties.[126] **8vdA** has absorption and emission maxima centered around 290 nm and 382 nm, respectively. Its emission is sensitive to solvent polarity and temperature; meanwhile, its QY is similar to that of **2AP**. Interestingly, **8vdA** not only shows less destabilization effect to its labeled ODN sequences but also maintains higher QYs in both ss and ds comparing to that of **2AP**. Eventually, **8vdA** is used as a non-perturbing alternative of **2AP** for similar purposes.[118] The same modification on guanine results in **8vdG** with emission at 400 nm and QY of 0.72.[104,126,127]

Tor et al. reported highly emissive isomorphic purine analogs: **thG** and **thA** (Figure 22).[128] These thieno analogs, constructed from thieno[3,4-d]pyrimidine, exhibit favorable features such as significant redshifts in both absorption (321, 341 nm) and emission (453, 420 nm), along with high QYs (0.46, 0.21). When incorporating into nucleic acids, **thG** containing sequences show good quantum yields; unlike **2AP**, quenching with flanking G residues was not observed. **thG** has been used in a variety of applications such as studying DNA conformational changes from B-DNA to Z-DNA, detection of DNA–protein interaction, etc.[118]

Modification of pyrimidine's substituents often concentrates at the 4 and 5 positions. One of the earliest examples was **m5K** (Figure 22), where removal of the amino group at the 4 position and adding a methyl group to the 5 position of cytosine were made. The absorption and emission of **m5K** are centered around 280 and 400 nm, respectively.[129] Appending a 5-membered aromatic ring to the position 5 on pyrimidine ring was another strategy to obtained isomorphic structures. For example, **CFU** and **UFU** (Figure 22) have absorption (310, 316 nm) and emission maxima (443, 431), respectively. Free rotation around the single bond between the furyl ring and pyrimidine base likely dissipates the excited-state energy, results in low QY (0.01 and 0.04) of nucleosides based on this approach.[118,130]

The main drawbacks of this type of modification come from their relatively small size. In fact, these fluorescent probes usually have small extinction coefficients as well as their absorption and emission are often in the ultra-violet region.

1.3.4. Ring-fused nucleobases

Looking back at the above approach of modifying the nucleobases, one can clearly see the number of π electrons in these conjugated systems, especially in pyrimidine-base, are still relatively small. Hence, these systems exhibit small extinction coefficients and having

absorption and/or emission maxima in the ultraviolet region. Dyes exhibiting larger extinction coefficients as well as absorption and emission at longer wavelengths are desirable for further applications. To this extent, ring fusion is one of the approaches to redshift absorption and emission as well as to increase extinction coefficient of the modified nucleobases.

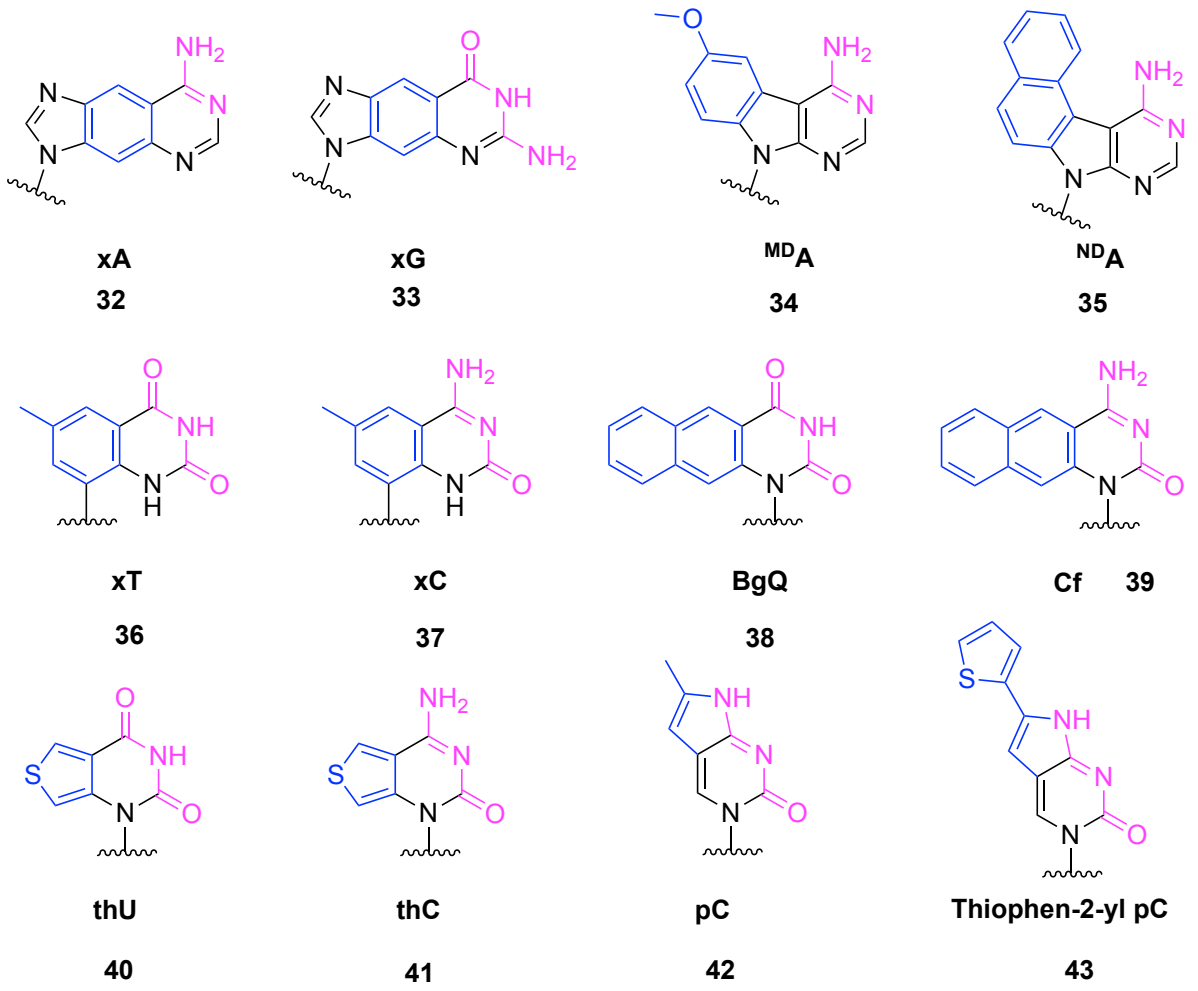

Figure 24. Examples of ring-fused nucleobases analogs.

To limit base-pairing perturbation, fusion at the 7 and 8 positions of the purine ring system is often a good choice for ring expansion. Examples are found with different ring sizes or substituents such as benzene or naphthalene rings. The introduction of tricyclic or tetracyclic structures significantly expands the π conjugated systems, leading to dramatic redshifts in absorption and emission maxima. For example, ^{MD}**A** (abs 327 nm in buffer) and ND**A** (abs 350 nm) emit around 380–420 nm (Figure 24) with QYs being 0.12 or lower.[131,132] The latter was probably due to the dissipation of excited energy by rotation of the methoxy group (^{MD}**A**) or structural distortion of the tetracyclic system (ND**A**). ^{MD}**A** has been used for base discriminating application, while ND**A** has been used in FRET in combination with fluorescein to distinguish C from all other bases.[83] Another important approach is inserting a phenyl ring in between the two rings of purine bases, reported by Leonard et al..[133] **xA** (abs ~332, em ~ 393) and **xG** (abs ~320, em ~413 nm), Figure 24, are both strongly fluorescent with high QYs (> 0.4).[104,133,134]

Ring fusion on pyrimidine rings can greatly influence or improve fluorescent properties of the natural bases and can be carried out on either the 5 and 6 positions or the 4 and 5 positions. The most important examples include **thU** and **thC**, where thiophene is fused to the 5 and 6 positions of uracil and cytosine, respectively. **thU** absorbs at 304 nm and emits at 409 nm, while the values for **thC** are 320 and 429 nm; they both exhibit robust QYs ~ 0.41.[128] In the same series with **xA** and **xG**, the fusion of a benzene ring to pyrimidine bases at the 5 and 6 positions results in **xC** and **xT**. **xC** absorbs at ~330 nm and emits at 388 nm with QY of 0.52. The values for **xT** are (320, 337 nm, and 0.3).[135] Importantly, the xDNA series (**xA**, **xG**, **xC**, and **xT**) have good biocompatibility since their corresponding nucleosides triphosphate can be incorporated into ODN using DNA polymerases with nearly the same efficiency to the natural nucleotides.[136] Unlike ND**A**, the fusion of naphthalene ring to pyrimidine (position 5 and 6) results in **BgQ** and **Cf** with remarkable fluorescent properties with QY 0.82 and 0.62; and emission maxima at 434 nm and 456 nm, respectively. The strong fluorescence of **BgQ** and **Cf** are likely due to the planarity and rigidity of the tricyclic systems.[104] Fusion of a pyrrole ring at the 4 and 5 positions is another approach. For example, **pC** exhibits a moderate QY (0.2) with absorption and emission at 350 and 460 nm.[137] Extension of the pyrrole in **pC** by replacing the methyl group with a thiophen-2-yl, named **thiophen-2-yl pC**, exhibits even greater redshifts (abs 370 nm, em 471 nm) as well as QY (0.42).[104]

1.3.5. Connecting the nucleobase with a fluorophore via a flexible linker (extended non-conjugated analogs)

One of the most common approaches is to connect the nucleobase with a fluorophore via a flexible linker. The approach often yields nucleobase analogs characterized by the photophysical properties of the parent dye. Pyrimidine bases have found the most success using this approach. In most cases, the dye is linked at position 5 of the base and is exposing to the major groove of labeled sequences. Such modification has found many examples with different linkers and fluorophores; some of them are presented in Figure 25.

Nucleosides **44** and **45** are analogs of uridine (and also thymine) with the former bearing a perylene fluorophore and the latter an anthraquinone-based. They were designed to function as a molecular beacon (MB), where **44** was the emitter and **45** was the quencher. The fluorescent signal of **44** showed a significant drop (98%) in ssODN where MB's stem-loop was formed, placing emitter and quencher in close proximal. The fluorescent signal was greatly enhanced upon hybridization with the complementary strand (49-fold increase with fully matched sequence) in dsODN as the result of separating the emitter and quencher.[118,138]

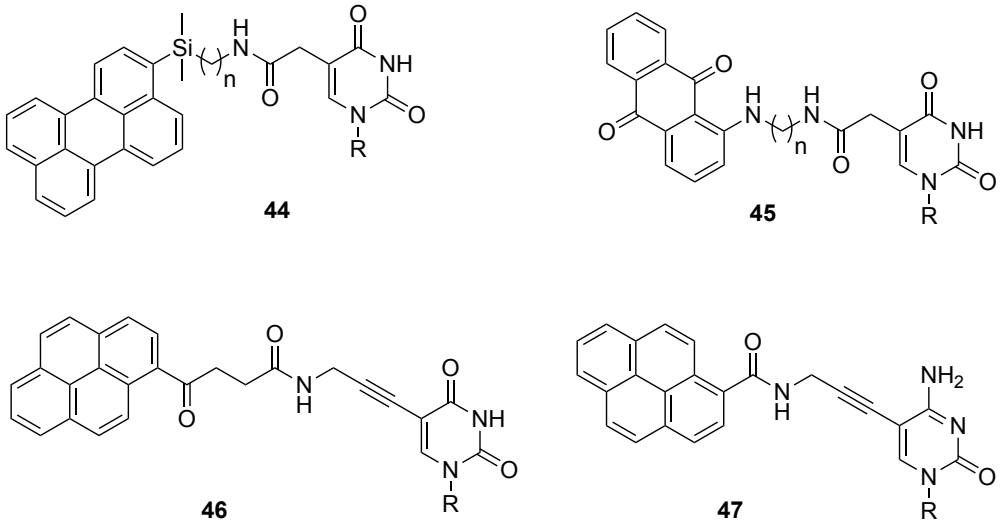

Figure 25. Examples of fluorescent analogs of pyrimidine nucleosides with different linkers and chromophores: R is deoxyribose.

Nucleoside **46** is an analog of uridine (also analog of thymine). It showed environmental sensitivity for both absorption and emission spectra vary from 345–355 nm and 396–467 nm, respectively. The emission of labeled sequences bearing **46** was sequence-dependent. It was quenched by neighboring guanosine while enhanced by a matched with adenosine. ssODN with two labeled sites showed unique emissive patterns depending on the number of adenosines on the complementary strand. This property is useful for the detection of adenosine-rich sequences.[118,139]

Nucleoside **47** is an emissive analog of deoxycytosine bearing a pyrene-1-carboxyaldehyde dye. The dye was known to have its fluorescent properties depending on solvent polarity. For example, the fluorescent quantum yield of pyrene-1-carboxaldehyde in the polar solvent is relatively high (0.15 in ethanol) while it is quite low in nonpolar solvent (0.001 in *n*-hexane). The probe **47** exhibits its emission depending on the base type of the complementary strand and can clearly identify the fully matched with guanine by a drastic change in its fluorescence intensity. Hence, the probe can be used to discriminate matched and mismatched at the labeling site on the target ODN. In the matched case, the chromophore is extruded outside of the duplex placing it in a highly polar environment, resulting in a strong emission. In contrast, the mismatched cases can locate the chromophore inside of the duplex, highly hydrophobic, causing fluorescent quenching.[118,140]

On the other hand, there are more positions on purine bases where a dye can be linked to (Figure 18). However, fewer successful examples using this approach were reported relative to that of pyrimidine ones. It is probably due to low oxidation potentials of the purine-based nucleosides, which can lead to fluorescent quenching of several chromophores. Some examples are given in Figure 26.

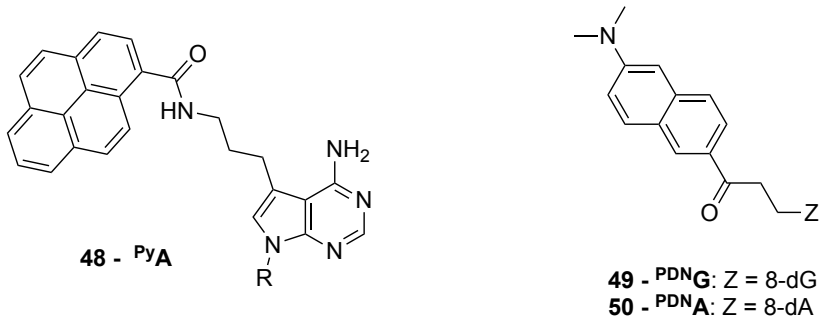

Figure 26. Examples of fluorescent analogs of purine nucleosides.

Nucleoside **48** (^{Py}**A**) is an analog of adenosine bearing a pyrene-1-carboxaldehyde fluorophore connecting with 7-deazadeoxyadenosine via a flexible linker at the 7 position of the base. The probe can distinguish fully matched from ss and mismatched sequences with a significant decrease of fluorescent intensity in the former case compared to the latter. For example, labeled sequence 5′-d(CGCAAT^{Py}**A**TAACGC)-3′ and the duplexes with a single mismatch at the base opposite to the probe in the complementary strand (A, G, or C instead of T) were moderately emissive (QY = 0.054–0.098); meanwhile, the fully matched was almost non-emissive (QY = 0.006). The author explained that the fluorescent quenching in the matched case was due to the intercalation of the pyrene chromophore into the duplex. Whereas, in the mismatched case, the intercalation was less favorable. The probe was used to detect single nucleotide polymorphism (SNP) of T/C (wildtype/mutant) present in the breast cancer type 1 susceptibility (BRCA1) gene based on the same quenching mechanism (Figure 27).[118,141]

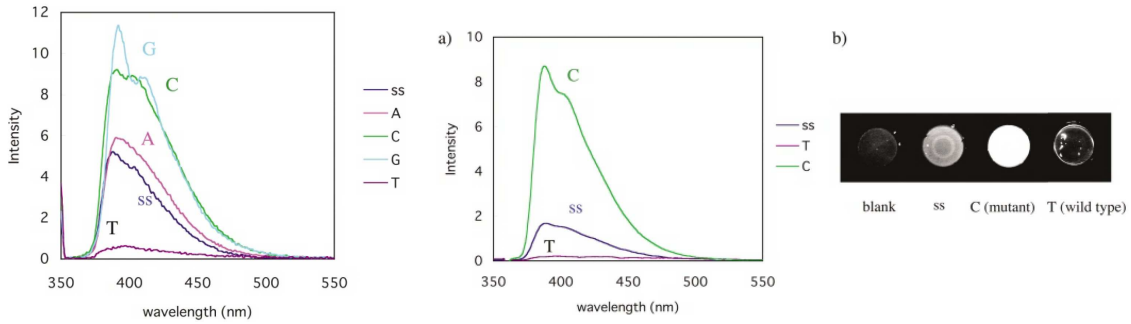

Figure 27. Detection of the T/C allele type of BRCA1 using fluorescence change of BDF probe. (a) Fluorescence spectra. (b) Detection of fluorescence image. (From: ref[141])

Nucleosides **49** and **50** were prepared by connecting Prodan to position 8 of deoxyguanosine and deoxyadenosine, respectively. The probes have excitation wavelength and QY sensitive to the local environment changes (hydration and polarity). For example, labeled ODNs bearing probe **49** have absorption maxima ranging from 373–406 nm, emission maxima ranging from 515–524 nm, and QY from 0.07 to 0.13. Similar values were obtained with labeled sequences bearing probe **50**: 382–405 nm, 517–526 nm, and 0.07–0.20, respectively. These properties are useful to probe DNA hybridization and single-based mismatched.[142,143]

Pros and cons:

Using this approach, the fluorophore can be linked to different positions of the nucleobase. Eventually, there are many probes using this approach because of the diversity of fluorophores could be used, positions at which the dye could be linked, and the type of linkers. The flexibility of the linker can find room for the dye in the labeled sequence. Hence, this approach often has a minor effect on DNA stability and structure. Moreover, the similarity between photophysics of the nucleosides to the parent dyes can help to understand the former more straightforward.

Meanwhile, there are also some drawbacks to this method. While a flexible linker can give flexibility for the chromophore, it is often hard to know the relative position of the chromophore to the DNA helix under study. For example, the same modified nucleoside put in different ODNs context can have a very different position and hence very different emission. This issue could give rise to some artifacts to the study.

1.3.6. Extension of the nucleobase with conjugated linker

This is an important category of base modification with great potential to redshift the absorption and emission spectra. The approach preserves a conjugation between an extended moiety, often is a chromophore and the base's electronic system. It allows the construction of new fluorophores with interesting photophysical properties such as red-shifted absorption and emission, sensitivity to base pairing, and/or environmental change. Also, it allows estimating the location of the fluorophores in the labeled sequence.

As mentioned above, connecting a dye to a purine base seems to have more problems than that of a pyrimidine base. One of the main problems arises from the electron-rich property of the purine base, especially guanine. This can cause a serious quenching effect on the fluorophore's emission. However, the connection of suitable chromophores through a conjugated linker at the 8 position of purine bases has given rise to several examples of highly emissive dyes. Modification at the 8 position is the most easily accessible in terms of chemical synthesis and has become the most common position to connect with the chromophore. For example, connection of pyrene chromophore to the 8 position on adenine and guanine via an acetylene linker results in probes, $\mathbf{A^P}$ and $\mathbf{G^P}$, which absorb long ultraviolet to short blue ranges (350 to 420 nm) while emitting blue light (~440 to 480 nm).[104,144,145] However, extension at this position can cause some disturbance to the structure and/or destabilizing effect to the labeled duplex. In terms of bio-compatibility, extension at the 7 position is the most suitable.[146,147] For example, a pyrene chromophore attached to the 7 position of 7-deazaadenine through an alkyne linker ($\mathbf{A^{Pyr}}$) results in a probe which absorbs at 364 nm while emits at 474 nm with QY 0.01 in water.[148] However, this approach is often more challenging and required the used of 7-deazapurine bases. These deazapurine bases are often more electron-rich compared to the natural ones and can cause significant fluorescent quenching due to photoinduced electron transfer (PET) (this is probably the reason for such a low QY of $\mathbf{A^{Pyr}}$). Eventually, this type of modification has found less common than that of the 8 position. Both positions can direct the chromophore in the major groove of labeled sequences (Table 2). Additionally, modifications at position 2 are also easily accessible in terms of chemical synthesis. Linked to this position,

the chromophore is often located in the minor groove of the labeled sequence. For example, $\mathbf{A^{Py}}$ has absorption maxima around 380–405 nm while emitting around 450–480 nm with QY 0.11–0.88.[142,149]

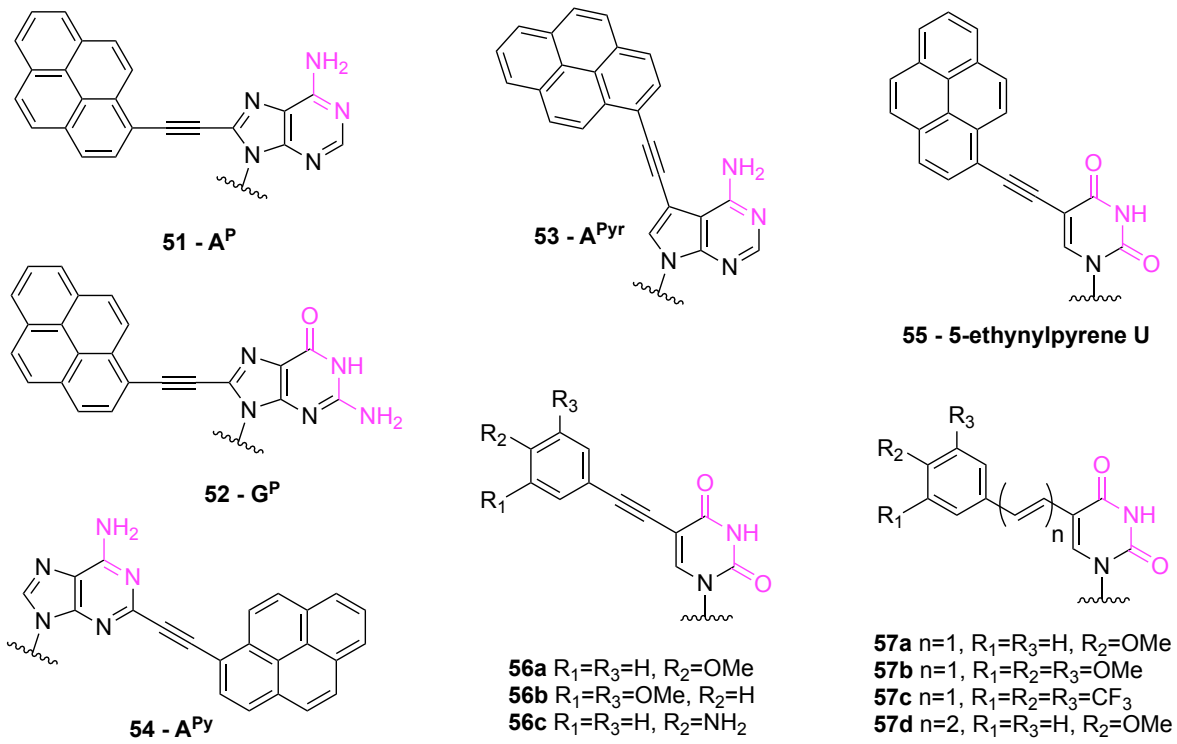

Figure 28. Representation the structures of nucleobase-fluorophore conjugations.

Extension of pyrimidine base's electronic system via conjugated linker is an important approach to construct advanced fluorescent pyrimidine analogs. The position 5 on the base is the best place for such modification since it benefits both the synthesis and bio-compatibility of the designed probes. The use of ethynyl or other conjugated linker allows the attachments of a diversity of fluorophores to the nucleobases. For example, **5-ethynylpyrene U** (Figure 28) is a highly emissive analog of dU, which has absorption and emission maxima at ~392 nm and 424 nm, respectively. Interestingly, the approach helps to increase the conjugated system of pyrene by N3 and the C4–C5 double bond, thus redshifts the absorption by 57 nm compared to pyrene (abs 335 nm in MeOH).[150] A library of uracil-based analogs was introduced by Fischer and coworkers, where the chromophore was connected to the base at the 5 position via a conjugated linker such as ethynyl (**56a–c**) or a mono or divinylene moiety (**57a–d**), Figure 28. In these examples, when the substituents on the extended chromophore are changed, electronic effects can be studied. The latter group (**57a–d**) exhibit longer absorption and emission wavelengths together with the higher emission quantum yields.[105] Among them, **57a** is the most promising with absorption and emission maxima at 335 and 478 nm, respectively, together with a quantum yield of 0.12 in water.[105] The probe was used for the detection of cyclin D1 mRNA in total RNA cell extract from cancerous human cells by following emission intensity change.[118,151] Noticeably, modification of cytidine using this approach is not common. It is

probably due to 5-endo cyclization reaction with the 4-amino group on the base which can cause some synthetic issues.

1.3.7. Synthesis of fluorescently labeled ODN via phosphoramidite chemistry

Oligonucleotide (ODN) plays a central role in applications in molecular biology and biotechnology. ODN sequences are used as primers for DNA sequencing and PCR reactions, as probes for hybridization assays in gene detection, as antisense molecules for the control of gene expression, etc. Eventually, with such useful applications, a number of methods have been described for the synthesis of ODN. The two most common are enzymatic and phosphoramidite approaches. The former approach often requires the use of nucleotide triphosphates building blocks and DNA polymerase to "connect" these building blocks into ODN sequences. This approach is suitable to synthesize long ODN sequences; however, it often has several constraints for incorporating fluorescent-labeled nucleotide into the sequence. On the other hand, the phosphoramidite approach is suitable for synthesizing relatively short ODN sequences, maximum ~200 nucleotides, but the incorporation of fluorescent-labeled nucleotide is often much more straightforward. Today, almost all the DNA synthesizers are designed to support the phosphoramidite approach.[152] Here, we present some basics of phosphoramidite chemistry, including the cycle of solid-phase synthesis and common protecting groups for the building blocks of this chemistry.

1.3.7.1. The cycle solid phase synthesis

In this chemistry, a phosphoramidite is coupled through its reactive 3′ phosphorous group to the 5′ hydroxyl group of a nucleoside immobilized on a solid support – a column. The phosphoramidite building block is often a nucleoside with protecting groups on its base and sugar to avoid unexpected reactions during the chain growing steps. The steps of oligonucleotide synthesis (Figure 29) include:

(1) Detritylation, in which the dimethoxytrityl (DMT or "trityl") group on the 5′ hydroxyl of the supported 5′-end nucleoside is removed by treatment with trichloroacetic acid (TCA). The step results in a reactive 5′-OH at the 5′-end of the growing chain (Figure 30).

(2) Coupling, a phosphoramidite, activated by tetrazole (a weak acid), is chemically coupled to the 5′-OH at the 5′-end of the growing chain (last base added to the column support material). Activation with tetrazole is to remove *i*Pr$_2$N group and transform the phosphoramidite into a powerful phosphitylating agent that readily reacts with the 5′-OH (Figure 31).

(3) In the capping step, any free 5′-OH groups from the previous step are shielded by treatment with acetic anhydride and *N*-methylimidazole (or phenoxyacetic anhydride – Pac$_2$O and Pyr). The step is to avoid further growth of this unexpected chain (Figure 32).

(4) Oxidation, the unstable phosphite linkage formed at the most recent coupling step is oxidized by treatment with iodine in the presence of water and pyridine to a more stable phosphotriester linkage protected with a 2-cyanoethyl group. The cyanoethyl group prevents undesirable reactions at the phosphorus center during subsequent synthesis cycles (Figure 33).

Noticeably, fluorescent analog(s) of natural nucleosides can be incorporated into the synthesis sequence at one or many expected positions. Thus, using this approach, fluorescently labeled sequences can be obtained.

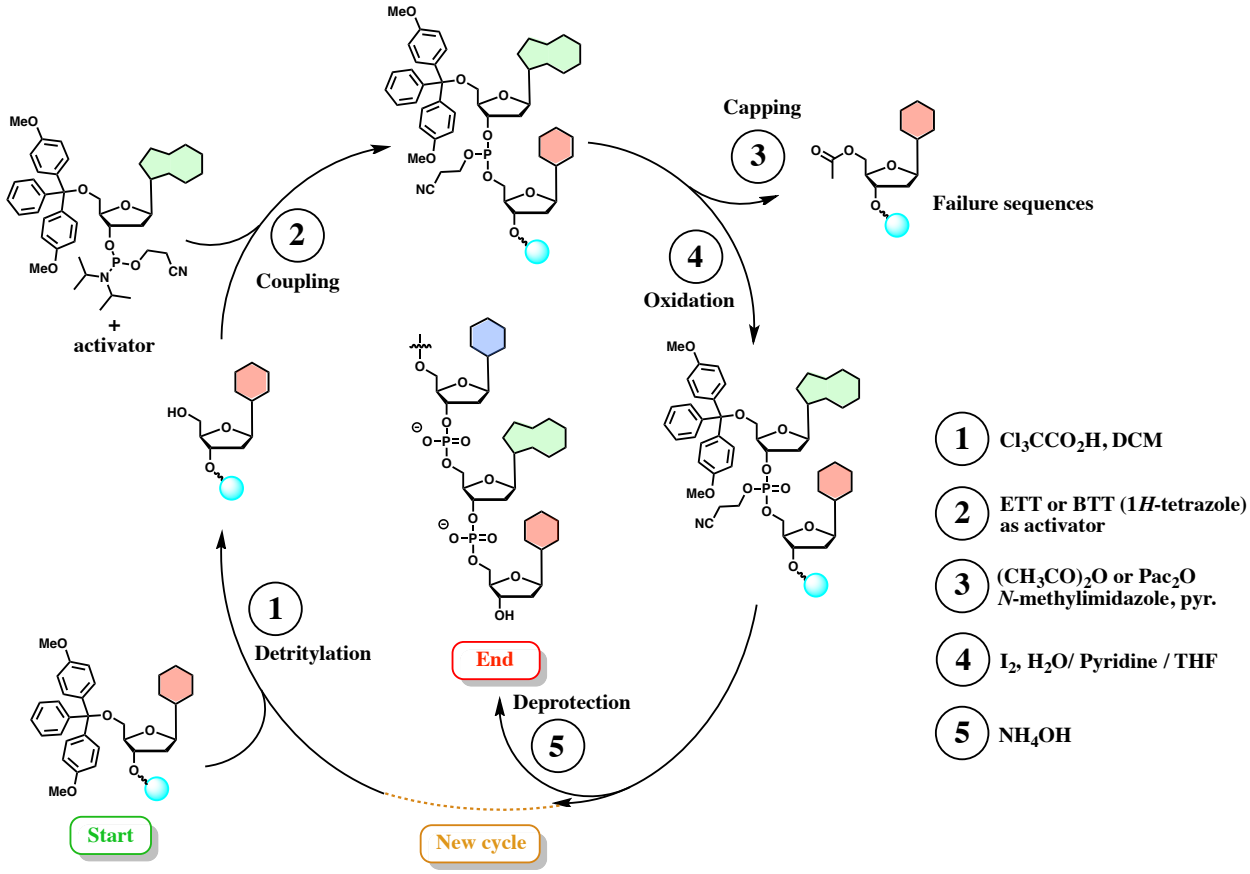

Figure 29. Representation of solid-phase synthesis of oligonucleotides via phosphoramidite building blocks. (Adapted from ref[153])

After the coupling of all building blocks into the ODN sequence, the completed nucleic acid chain is cleaved from the column by treatment with ammonium hydroxide; meanwhile, the base-protecting groups are removed in the same condition or by heating in the ammonium hydroxide solution (Figure 34 and 35). The latter depends on the choice of bases' protecting groups, especially for the purine building blocks. Importantly, it often depends on the purification strategy to decide whether the 5′-end DMT group is kept or removed before the cleavage of the synthesized ODN sequence from the solid support. The cycle of phosphoramidite chemistry is depicted in Figure 29.[152]

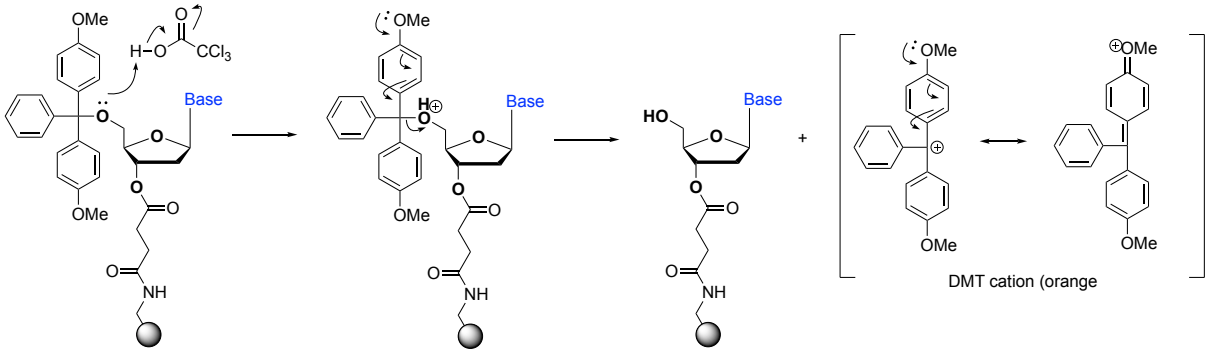

Figure 30. Mechanism of detritylation under acidic treatment. (From: https://www.atdbio.com/content/17/Solid-phase-oligonucleotide-synthesis#Synthesis-of-nucleoside-phosphoramidite-monomers)

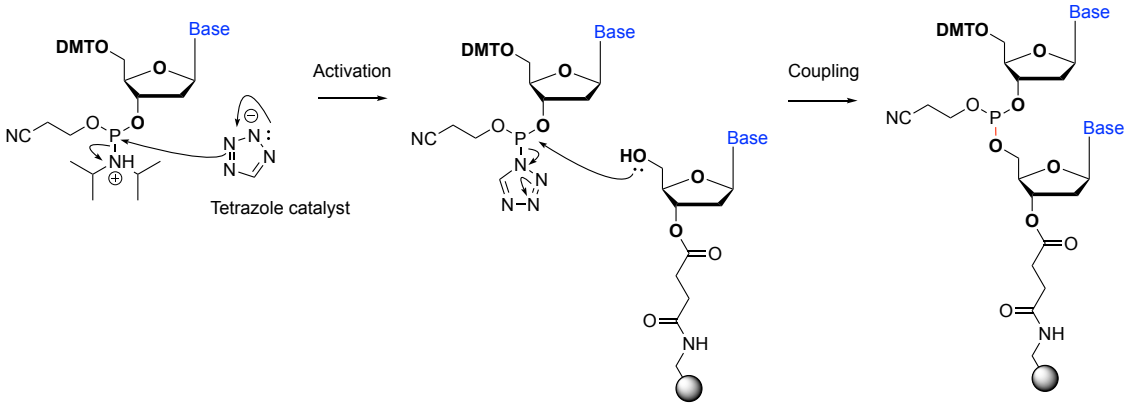

Figure 31. Mechanism of activation and phosphoramidite coupling reaction.

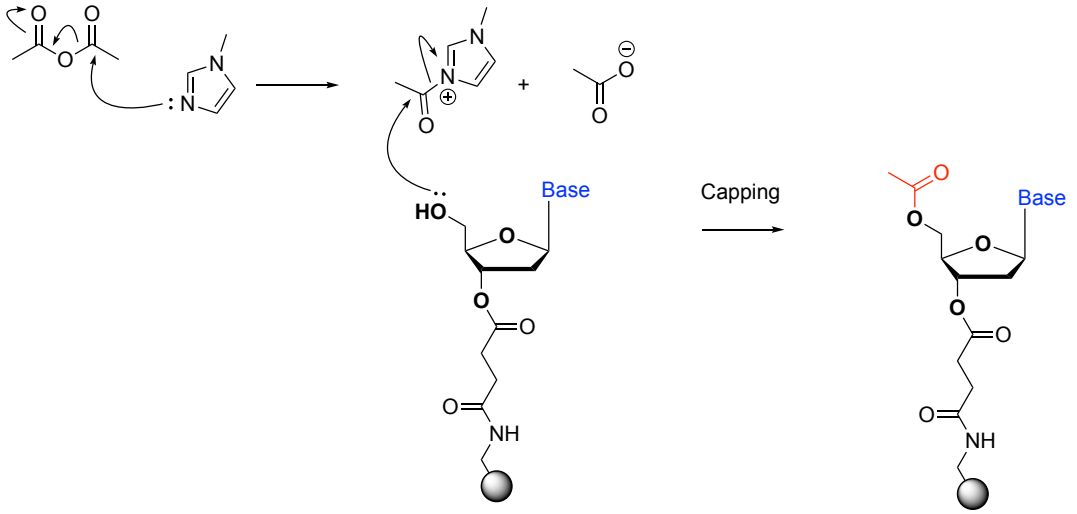

Figure 32. Mechanism of the capping step.

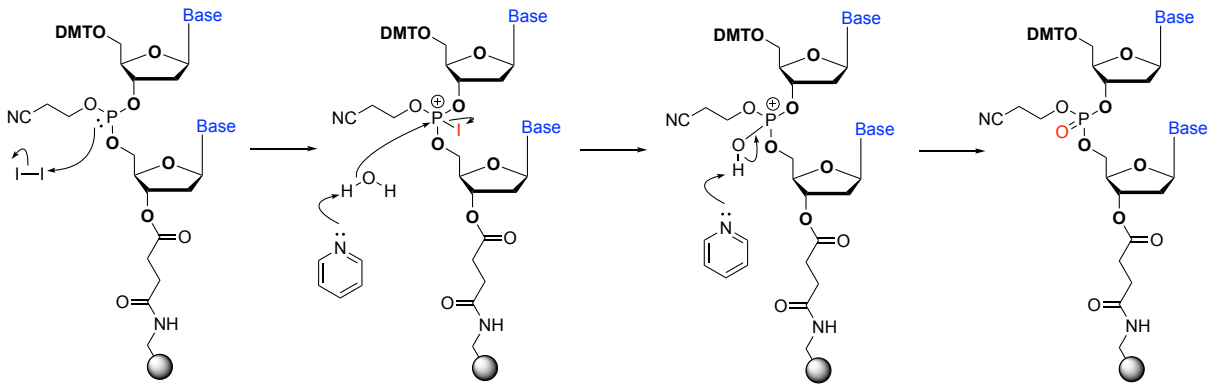

Figure 33. Mechanism of the oxidation step.

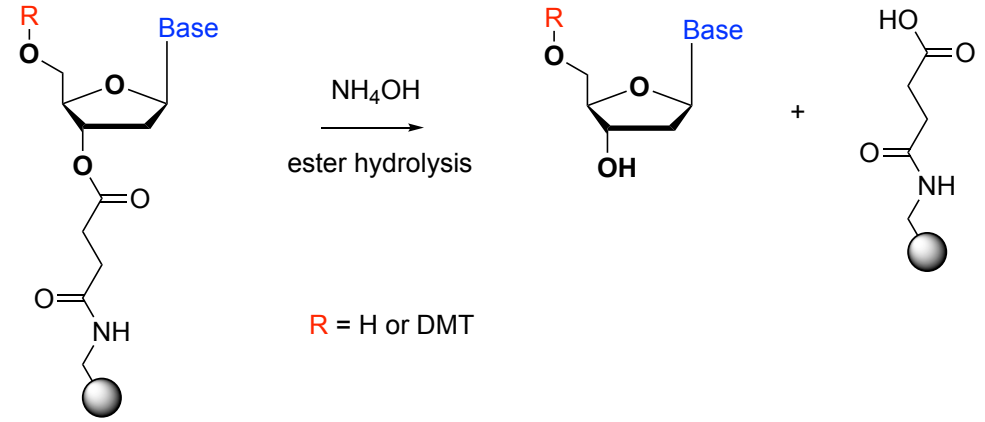

Figure 34. Cleavage of ODN from its support using NH_4OH.

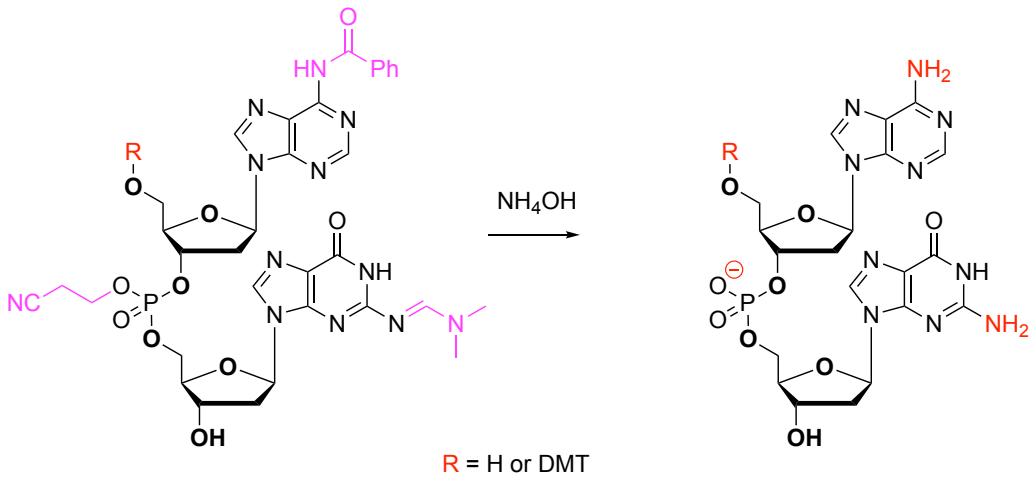

Figure 35. Deprotection of the ODN using concentrated NH_4OH.

1.3.7.2. Columns for phosphoramidite chemistry and synthesis yields

Columns have several scales, which are a function of the amount of the 3′ nucleoside coupled to the support material. One can readily start the synthesis with any of the four natural bases

(A, T, C, and G) by choosing appropriate columns, which are all commercially available at different sizes ranging from 40 nmol to 10 mmol. Common solid supports are controlled-pore glass (CPG, having pore sizes of either 500 or 1000 Å) and polystyrene. The choice of column scale depends on both the quantity and the length of the desired ODN. The larger the column scale, the greater the yield of ODN. Polystyrene or large-pore CPG columns are often recommended for synthesizing sequences at greater than 50 bases in length.[152]

Overall yield is the yield of the synthesized full-length product, while stepwise yield is coupling yield at each base addition. In an optimal condition, 98%-100% of stepwise yields can be expected. However, a small number of uncoupling molecules (~2%) will be capped and will be unavailable for any of the following cycles. Eventually, the longer the sequence, the lower the overall yield. At the detritylation step, the DMT group, which is removed under acidic conditions, has a characteristic bright orange color. As it is washed from the synthesis column, the fraction can be collected, diluted with *p*-toluenesulfonic acid monohydrate in acetonitrile, and essayed for absorbance at 498 nm. This essay will give us the value of each stepwise yield.[152]

1.3.7.3. Bases' protecting groups

Meanwhile, sugar's protecting groups are quite optimal, (2-cyanoethyl)-*N*,*N*-diisopropyl phosphoramidite group at 3′-OH and DMT group at 5′-OH, the bases' protecting groups can have a significant effect on the overall yields of expected sequences. More specifically, the protecting group on purine bases, especially adenine, can have a significant effect on the depurination process as well as the condition of the deprotection step. Standard phosphoramidite building blocks are given in Figure 36. Accordingly, thymine does not require any protecting group since all of its functional groups are not reactive during the solid phase synthesis. The exocyclic amino group (NH_2 at the position 4) of cytidine is often protected in the form of acetamide. Nowadays, the exocyclic amino group of guanine is often protected with dimethyl formamidine (dmf). This protecting group is labile under the cleavage step (NH_4OH) and can, therefore, be deprotected in the same spot.

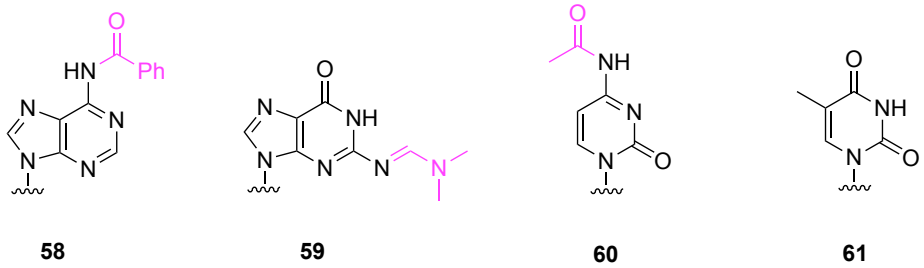

Figure 36. Standard phosphoramidite building blocks for ODN synthesis.

The standard protecting group for adenine is benzoyl (Bz). This protecting group is relatively stable and often requires the deprotection at ~55 °C in NH_4OH. Moreover, it can cause serious depurination under acidic treatment during the detritylation steps (Figure 29). Later, phenoxyacetyl (Pac) was introduced to have a more labile deprotection condition (at RT in

NH_4OH) while decrease the unexpected depurination by ~20%.[154] However, the protection step using Pac was not in good yield ~60%.[154] Since the report of dmf protecting group,[155] it is becoming a good replacement for the two formers.[141,156-158] This protecting group has better yield for the protecting step as well as decreasing the depurination by ~60% and ~40% comparing to Bz and Pac, respectively (see Figure 37). The dmf protecting group can also be deprotected under a mild condition similar to Pac.

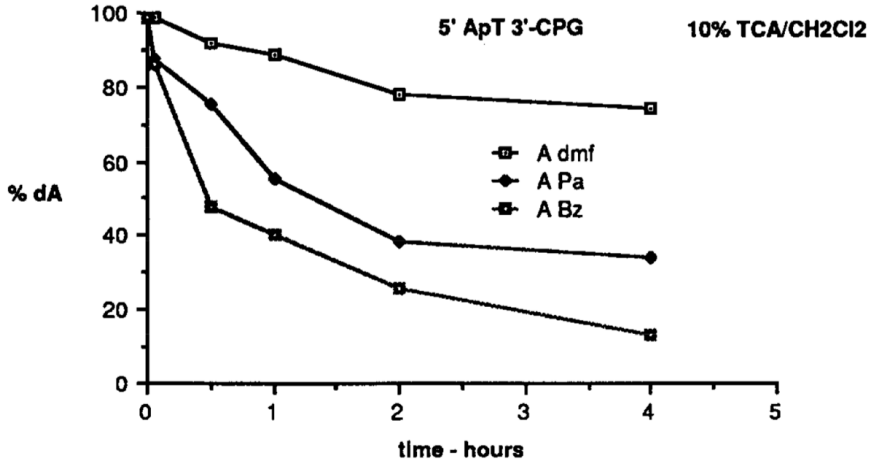

Figure 37. Depurination rates of N6-protected 2′-deoxyadenosines with 10% TCA/DCM; benzoyl (Bz), phenoxyacetyl (Pa), and dimethylformamide (dmf). (From: ref[155])

1.4. ESIPT reaction

1.4.1. Introduction to ESIPT

In the 1950s, Weller reported the process called excited-state intramolecular proton transfer (ESIPT) for salicylic acid.[159] Since then, the reaction has been studied extensively and applied to a variety of fields.[160-163] The most common fluorophores which demonstrate an ESIPT reaction are analogs of 2-(2′-hydroxyphenyl)benzimidazole (HBI), 2-(2′-hydroxyphenyl)benzoxazole (HBO), and 2-(2′-hydroxyphenyl)benzothiazole (HBT) (Figure 38). Fluorophores such as quinolines,[164] benzophenones,[165], 3-hydroxyflavones,[166,167] anthraquinones,[168] benzotriazoles,[169] *N*-salicylideneaniline,[170] and quinoxalines[171] were also reported to present an ESIPT. In general, these molecules possess an intramolecular hydrogen bonding interaction between an H-bond donor (such as –OH and –NH–) and an H-bond acceptor (=N– and C=O).[172]

ESIPT is a photochemical process displaying typically four-level molecular orbitals (MO). The ground state of these fluorophores is the normal (N) form. Upon photoexcitation, electronic redistribution from the Franck–Codon (FC) state results in more acidic hydrogen (from H-bond donor) and more basic center at the H-bond acceptor. Eventually, a phototautomerization process can take place in which the excited normal form (N*) is converted into its excited tautomeric form (T*).[173] This process can be either reversible or irreversible depending on the energetic levels the excited forms (N* and T*) and can be extremely fast at the rate ~ $4x10^{12}$ s^{-1}. Then, both excited forms (N* and T*) can follow radiative decays to return to their corresponding ground states (N and T, respectively). The T form can reproduce the N form through a reverse proton transfer (RPT) or back proton transfer (BPT) process.[172]

ESIPT fluorophores exhibit several attractive features that make them useful for different purposes. First of all, ESIPT dyes often have unusual Stokes shifts (~200 nm) compared to common dyes such as fluorescein and rhodamine. This feature helps to avoid fluorescence reabsorption and Homo-FRET. Moreover, ESIPT dye's emission is generally highly sensitive to its environment due to the transient nature of the four-level process. For example, emission intensity corresponding to each form is greatly affected by the polarity and acidity (H-bond donating ability) of the environment in which the dye is exposed. In extreme cases, emission of one form can be mostly inhibited while emission of the other one is greatly enhanced. Last but not least, most ESIPT dyes can be used for ratiometric sensing based on their two-band fluorescence spectra arising from emissions of N* and T*. The ratiometric response is a self-calibrated approach with a ratio intensity between the two emission wavelengths unaffected by the dye's concentration and several other instrumental parameters.[174] This is particularly useful for sensing selective species inside interest samples or probing biological events.[172]

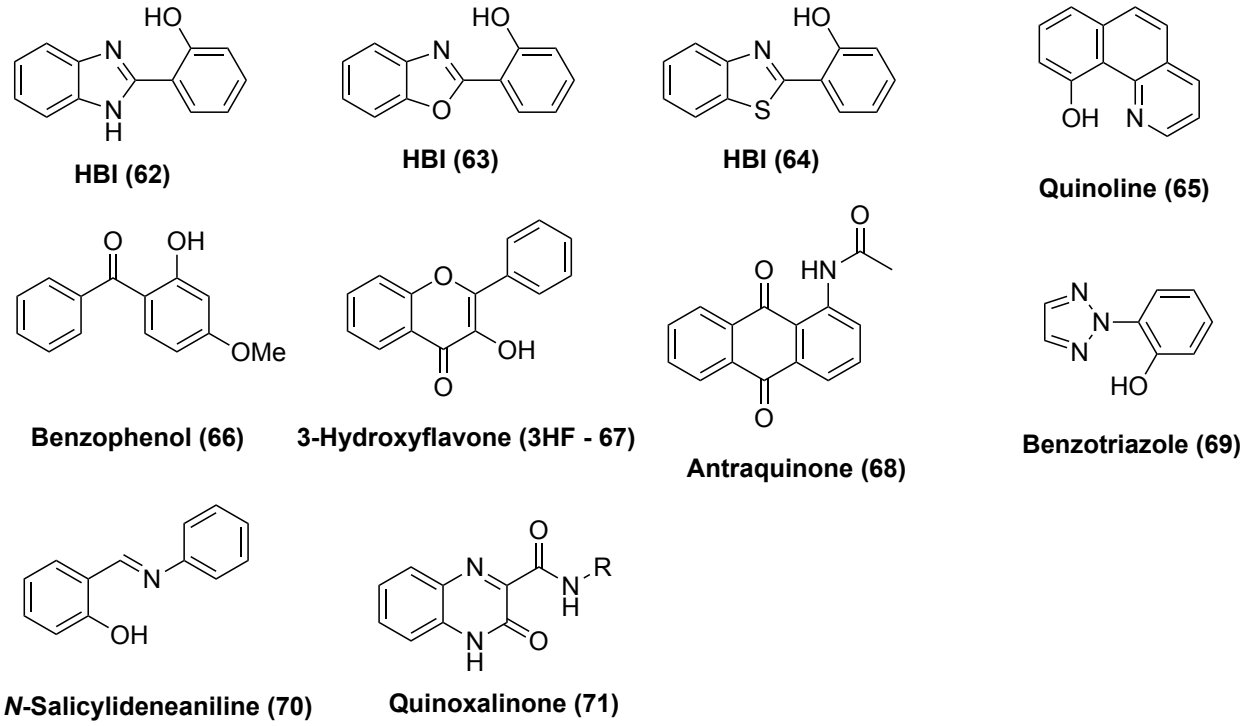

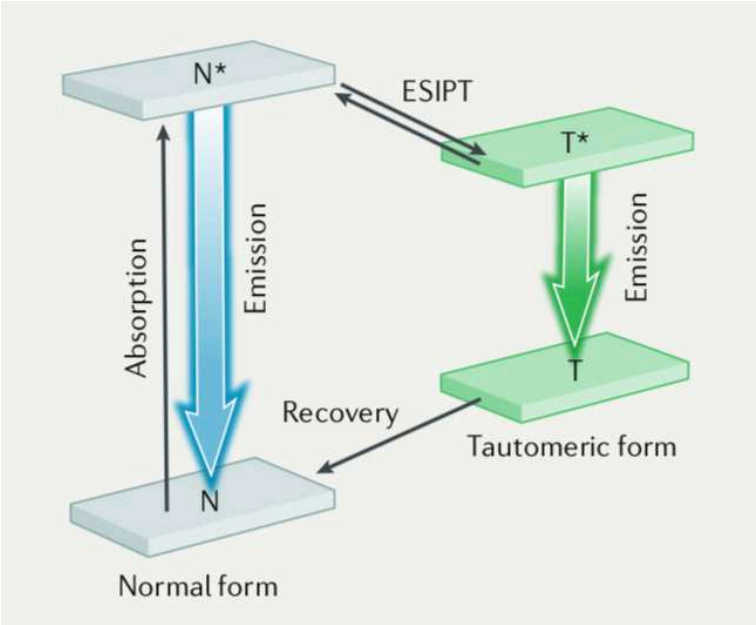

Figure 38. Structures of typical families of ESIPT fluorophores (top). The four-level ESIPT reaction (bottom). (Adapted from ref[172])

1.4.2. 3-Hydroxychromone (3HC)

3-Hydroxychromones, including 3-hydroxyflavones, are ESIPT fluorophores with remarkable fluorescence properties. Firstly, the two excited forms (N* and T*) emit photons with a substantial difference in energies. This gives rise to two well resolvable and often highly intense fluorescence bands. Moreover, the ESIPT reaction in these compounds proceeds between the H-bond donor and acceptor within a 5-membered cycle. The reaction in such a 5-membered cycle is slower than that same reaction in a 6-membered cycle because the intramolecular H-bond of the former is longer than that of the latter.[175,176] As the result, emission maxima and the ratio of intensities between the two bands exhibit a strong dependence on the environment, such as solvent polarity and acidity. These unique properties suggest a great potential for applications in different fields of research.[177]

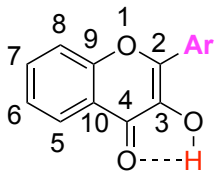

3HC

Figure 39. General structure and numbering of **3HC** dyes.

Common examples of **3HC** dyes present as 2-aryl group: a phenyl **3HF**, a 2-furyl **FC**, and a *p*-diethylaminophenyl **DEAF** rings (Figure 40). The non-substituted **3HF**[166] shows only single-band emission from its tautomeric form (T*) in aprotic solvents such as toluene, while it shows two emissive bands (N* and T*) in protic solvents. The ratio of intensities between the two bands depends on the polarity of protic solvents used, making it possible to sense environmental polarity by the ratiometric response. As for **FC,** it demonstrates improved photophysical properties compared to **3HF**. The replacement of the phenyl ring by furyl, a 5-membered – relatively electron-rich ring, provided not only a bathochromic effect in the absorption maxima and better absorptivity, but also a redshift in the emission maxima and better QY. Moreover, **FC** exhibits a dual emission in both protic and polar aprotic solvents (such as ACN and DMSO) with a greater range of ratiometric response, making it superior to **3HF**.[178] With its *p*-NEt_2Ph substituent showing strongly enhanced positive mesomerism, **DEAF** displayed several spectral improvements. First, its absorptivity is greatly increased as compared to **3HF**. Centered around ~410 nm, the absorption maximum became sensitive to solvent polarity by demonstrating a certain solvatochromism. The dye exhibits a dual emission in apolar to polar solvents such as AcOEt, $CHCl_3$, and ACN. In protic solvents (e.g., MeOH), T* emission revealed weak and overlapped with the N* signal resulting a single-band emission.[179,180]

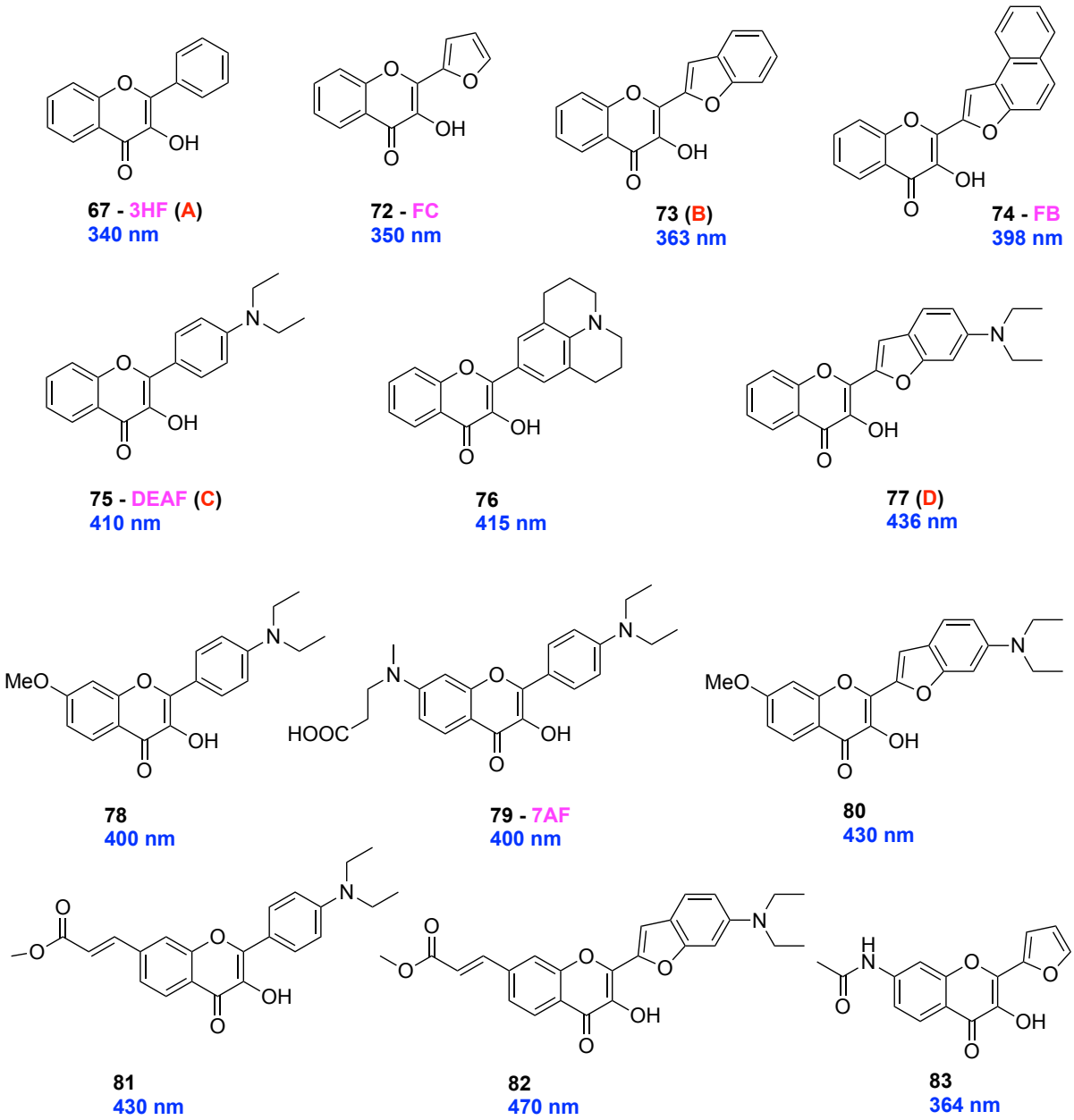

Figure 40. Examples of **3HC** dyes: Absorption maxima are given in blue, common names are given in magenta.

1.4.2.1. ESIPT reaction in 3HC

According to the four-level diagram (Figure 41), the proton to transfer (ESIPT proton) for **3HC** dye locates in the hydroxyl group on position 3 (see N form in the ground state). Upon photoexcitation, the relaxation from FC region generates the N* form, where the proton still locates on the OH group. After charge transfer from the endocyclic enol, the carbonyl function was converted into phenoxide and became definitely more basic. From this N* state, ESIPT reaction can take place either reversible or irreversible, depending on the electronic structure of the dye (mainly the 2-aryl substituent) as well as interactions with solvent molecules. The transient product of this ESIPT process is the T* form, in which, the proton was transferred to

the adjacent oxygen at C4 position making a significant redistribution of charges between the two excited states. Both N* and T* forms can relax to their corresponding ground states (N and T) via non-radiative and radiative relaxations. From the tautomeric (T) form, the proton is transferred back to its original position via a back proton transfer (BPT) process.

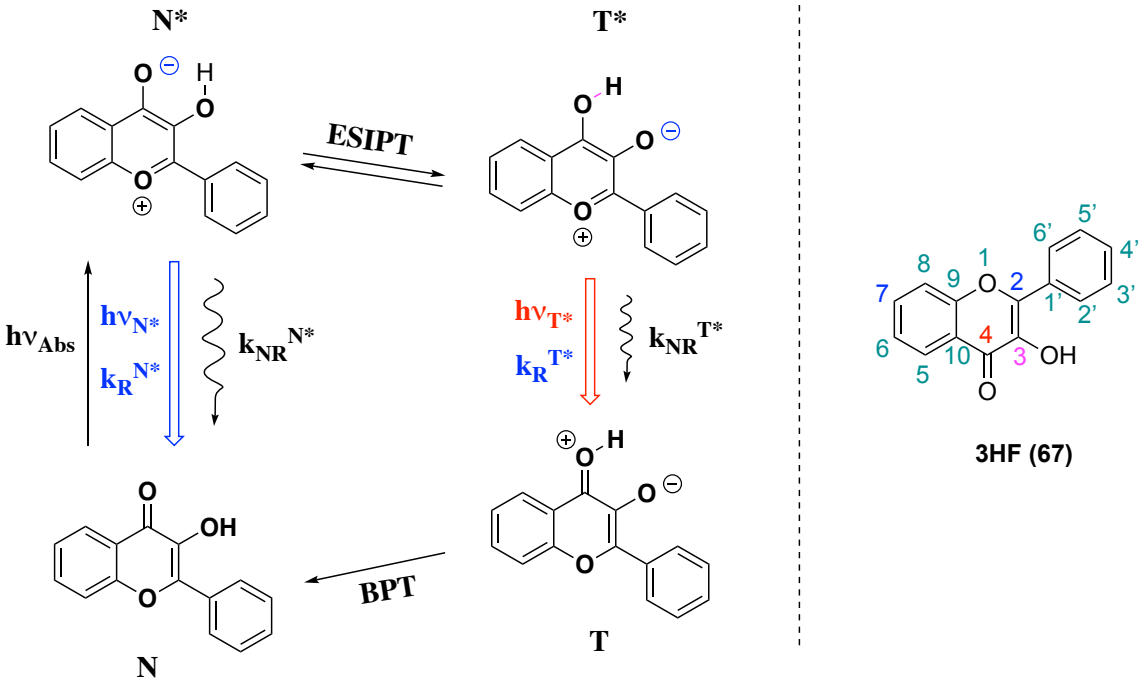

Figure 41. The four-level diagram ESIPT reaction with the corresponding rate constants for **3HF,** a typical **3HC** dye with a poor positive mesomerism at position 2 (left); numbering of **3HF** dye (right). (Adapted from ref[181])

1.4.2.2. Solvent effect

Solvent polarity

As mentioned above, wavelengths and intensities ratio of the two emissive bands depend on the scaffold of the dye and its microenvironment (such as solvents). In general, with increasing solvent polarity, the N* emission maximum undergoes a bathochromic shift. This could be explained by the fact that N* form has a greater dipole moment than that of the N form, and thus increasing the solvent polarity should favor the stabilization of the excited form. As a consequence, the energy gap between N* and N will decrease leading to the observed redshifts in the corresponding emission spectra. Moreover, polar environment also favors the N* emission from its tautomer form's emission making the ratio of intensities (I_{N*}/I_{T*}) increases. This is due in some examples to a greater stabilization effect of polar solvent on the N* form as compared to the T* level which can lead to a higher activation energy barrier resulting in a slower ESIPT reaction rate.

Hydrogen bonding

H-bond donating ability is an important solvent's parameter that could have a significant effect on the ESIPT reaction of **3HC** dyes. **3HC** has its site of ESIPT reaction localized on a low-stable five-membered ring cycle between the 3-hydroxyl and 4-carbonyl groups. This reaction is often slower than the ESIPT reaction on a more stable six-membered ring cycle and can present a strong dependence on the perturbation from the environment. For instance, **3HF** demonstrates a dual emission in alcohols while it exhibits mainly the T* band in aprotic solvents. In fact, the N* form has an electron-rich center located on the oxygen at C4 position. In protic solvents, H-bonding between the solvent molecules and the carbonyl can have a significant stabilization effect on the normal excited form of **3HC** dyes. This stabilizing H-bonds can greatly slow down or even inhibit the ESIPT reaction due to increasing activation barrier of the reaction. The effect of protic solvents is more easily observable on the ESIPT reaction of **DEAF**.[182] The ratio of intensities N*/T* was 10 times higher in protic than in aprotic solvents of the same polarity. This high sensitivity has the same origin to that of **3HF**.

Effect of H-bonding on the ESIPT reaction of 4′-dimethylamino-3-hydroxyflavone (**DMAF**) was investigated by steady-state and time-resolved fluorescence studies in protic and aprotic solvents as well as their mixtures. The authors observed the appearance of a new emitting species (at 500 nm) and the distortion on the excitation spectrum causing by this new species. These studies suggested a formation of a ground-state complex between **DMAF** and protic solvent molecules (the H-bonded form) in equilibrium with its free form, the non-H-bonded form (Figure 42). The two ground-state forms, N and N–H, were confirmed by their ability to be excited separately into their non-interconverted excited forms, N* and N–H*, as was shown by time-resolved fluorescence.[183]

The influence of H-bonding on the ESIPT reaction of **3HF** was also studied.[184] It was evidenced that H-bond donor concentration only affects the N*/T* ratio, while H-bond donating ability of the solvent influences both the intensity ratio and the position of emission maxima. The former effect is probably related to the increase of activation energy barrier, whereas the strength of the H-bond between solvent molecules and the dye is responsible for the latter effect. This solvent stabilization effect can be different for each of the four forms of the ESIPT process.

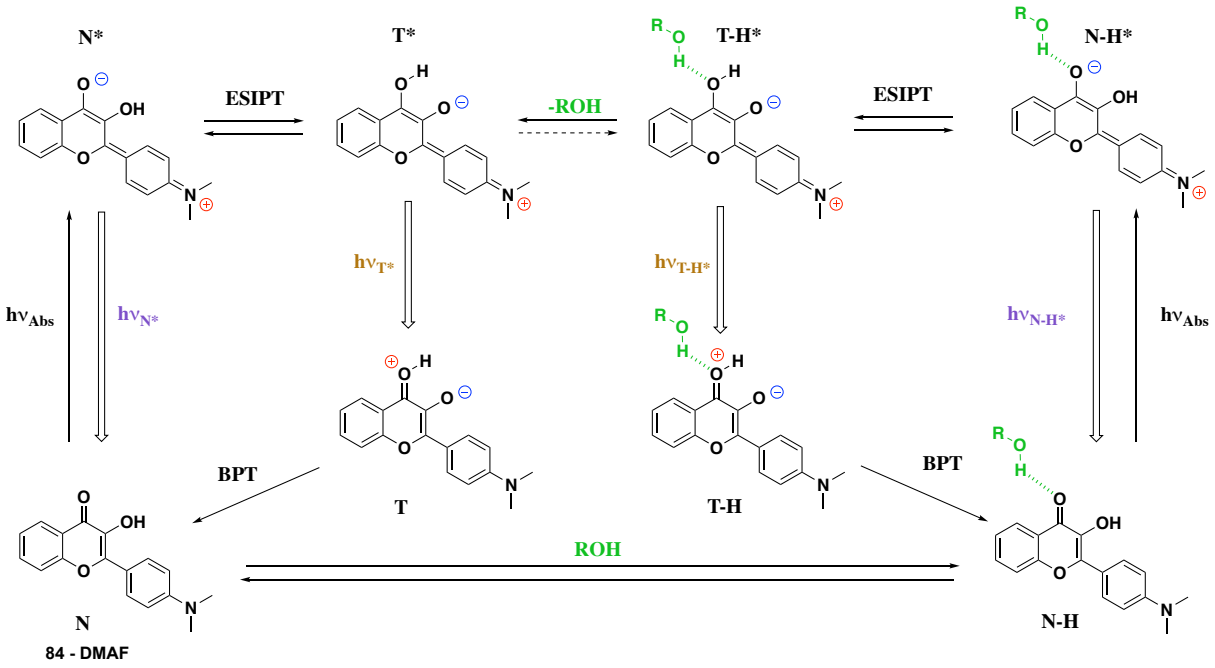

Figure 42. Ground and excited state transformations of DMAF in protic solvents. (Adapted from ref[183])

Ultimately, the simultaneous monitoring of four parameters, ν_{abs}, ν^{N*}, ν^{T*}, and N*/T*, makes these **3HC** dyes prospective tools for getting access to different properties of the microenvironment (such as polarity, polarizability, and H-bond donating ability).[181,184]

*1.4.2.3. Kinetics of the ESIPT reaction in **3HC***

Kinetics of ESIPT reaction in **3HF** was the subject of intensive studies. Brown et al. found that ESIPT reaction for **3HF** in aprotic solvents such as methylcyclohexane and acetonitrile is extremely fast with an estimated time constant of 35 fs.[185] In EtOH, a time constant of ca. 60 fs was found. In other studies, slow ESIPT kinetics (in the picosecond time range) occurring only in protic solvents, in which H-bonding between the solvent and dye could lead to an increased activation barrier of the proton transfer. In this case, the reaction is irreversible.[186,187] ESIPT kinetics on *p*-dialkylamino 3HF derivatives was also investigated (Figure 41). The authors suggested a fast reversible two-state ESIPT reaction in these derivatives.[188] In fact, in aprotic solvents, these derivatives have an ESIPT reaction occurring on the scale of tens of picoseconds, which are 1–2 orders of magnitudes slower than that of solvent relaxation (at sub-picosecond timescales).[188] The slower (picosecond) proton-transfer time constant of these derivatives compared to **3HF** (femtosecond) is due to the involvement of an intramolecular charge transfer (CT) induced by the dialkylamino group, which leading to an energy barrier for the ESIPT reaction as depicted in Figure 43.[177,189,190]

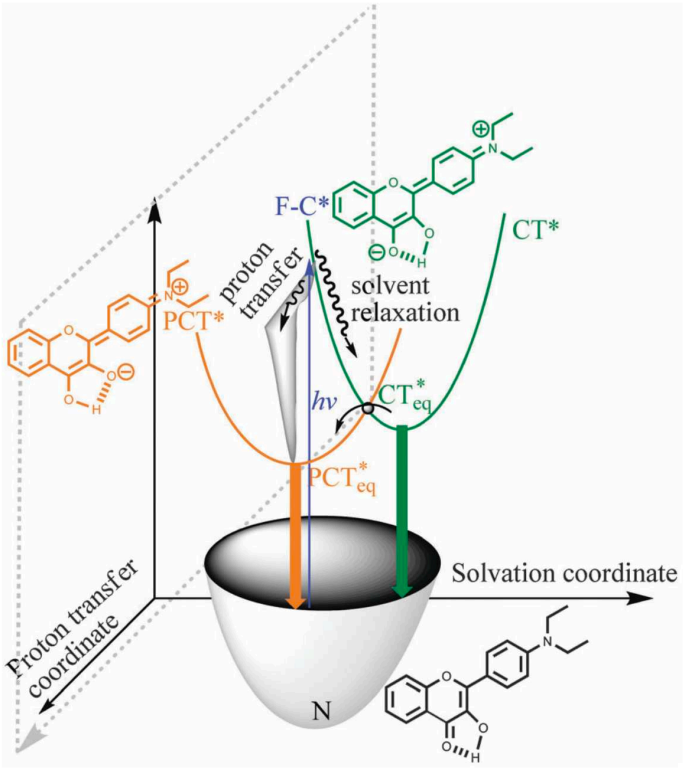

Figure 43. Proposed relaxation processes for dialkylamino 3HF dyes. F-C*, CT*, and PCT* denote the Franck–Condon region, potential diagram of N*, and potential diagram of T*, respectively. CT^*_{eq} and PCT^*_{eq} denote the potential equilibrium of CT* and PCT*, respectively. Due to intramolecular charge transfer and solvent relaxation, the relaxation process from F-C* to CT^*_{eq} can greatly increase the energy barrier for the ESIPT reaction. (Adapted from ref[191])

1.4.2.4. Tuning sensitivity and some applications

Tuning approaches and effect on the four-level ESIPT reaction

One of the greatest advantages of **3HC** dyes is in their highly tunable spectroscopic properties. Comparing to **3HF**, further improvements of **3HC** dyes require the increase of their brightness, the shift of their absorption and emission spectra to longer wavelengths, and the appropriate sensitivity for specific applications. The main approaches include extension of the electronic π-system, connection of a suitable electron-donating aryl group at position 2 of the chromone scaffold, and/or substitution at position 7 (Figure 39).

Extension of the electronic π-system is a common approach for redshifting the absorption maxima of **3HC** dyes. For example, replacing the furyl of **FC** successively by a benzofuryl (**73**) and then by a naphthofuryl group (**74)**, redshift finally the **FC** absorption of ca. 40 nm, making it in the visible range.[192] These substitutions provide additional π-electrons to the electronic systems of the dyes and increase the conjugation between the endocyclic oxygen of the furyl moiety and the carbonyl group, and thus the electron transfer in the excited state, and thereby the dipole moment of the molecule.

Conjugation of a strong electron-donating group with the carbonyl is an alternative strategy. Thus, the introduction of a dialkylamino group at position 4′ of **3HF** is known to increase the delocalization of electrons in the ground state and the charge-transfer nature of the N* form in the excited state. These effects can lead to a significant redshift in both absorption and emission as well as making the ESIPT reaction more sensitive to medium polarity.[179,180,193] For example, the introduction of diethylamino group at position 4′ of **3HF** formed **DEAF** with ca. a 60-nm redshift in absorption.[194,195] The dual emission of **DEAF** is also more sensitive in aprotic solvents compared to its parent chromone (**3HF**). Further increase of the donor strength leads to two-color dyes with even better delocalization of electron. For instance, with its two extra rings to lock the amino group, dye **76** displays a bathochromic shift in absorption (415 nm) and an increase of the intensity ratio N*/T*.[195]

This effect can be additionally modulated by an electron-donating substituent, for instance, a dialkylamino group at position 6 of the benzofuryl ring (compound **D**). This further shifts the absorption (~450 nm) and emission bands to longer wavelengths making the dye more attractive for applications in biological systems.[196]

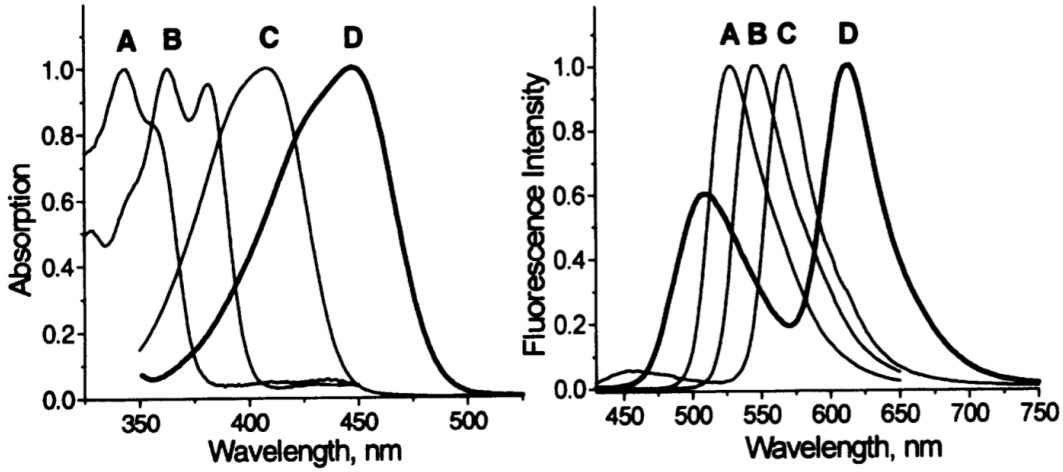

Figure 44. Absorption (left) and emission spectra (right) of **3HC** dyes (**A–D**). (Adapted from ref[197])

Substituents at position 7 also demonstrate significant effects on the spectroscopic properties of **3HC** dyes. Indeed, significant bathochromic shifts in absorption and emission could be obtained by connecting an electron-withdrawing group (EWG) at position 7 of dyes **C** and **D**.

For example, **81** and **82** exhibit redshifts of ca. 25 nm in their absorption and more than 50 nm in their emission compared to their parent analogs.[198] It turns out that the acceptor at position 7 leads to a better delocalization of electron in the ground state and an increase in the excited state's ICT character, thus explaining the mentioned spectral shifts. Conversely, opposite effects can be achieved by the introduction of an EDG at position 7. Incorporation of a methoxy group at position 7 of **75** and **77** results in a blueshift of about 6–10 nm in absorption and a significant decrease in their ratio intensity N*/T*.[195] The effect is even more substantial for 7-substituted **3HC**s with a dialkylamino group where a strong decline of ratio intensities N*/T* was observed.[199]

Tuning Sensitivity

The ratio of intensities at two emission maxima (N* and T*) is an important parameter that can be used to probe solvent polarity, H-bonding ability, and the local structure of molecules surrounding the fluorescent sensor. Fine-tuning of this parameter by rationally varying substituents on both sides of the **3HC** scaffold can help to construct the appropriate dye for specific applications. The most common way to fine-tuning the intensity ratio between the two emission bands (N* and T*) is by changing the aryl group at position 2 of **3HC**. In general, one can shift the sensitivity range of a **3HC** dye by changing its push–pull character (established from the aromatic system to the carbonyl group at positions 2 and 4, respectively), Figure 45. For example, probe **D** has its amplification of sensitivity within the range of low-polar solvents (solvents that are more hydrophobic than ethyl acetate). Due to this amplification, significant intensity ratio changes, half of its full scale, were recorded between hexane and toluene. This amplification brings great potential for analytical applications in the lipids field. On the other hand, probe **B** has its sensitivity range within solvents that are more polar than EtOH. This property can allow its applications for sensing environmental changes in an aqueous environment. Probe **C** (**DEAF**) has its amplification of sensitivity in the range of aprotic solvents of medium and high polarity. Therefore, the probe can be used for applications such as studies of membrane structures and dynamics.

Increasing of the electron-donating ability of the aromatic system at position 2 can result in the redshifts of absorption and emission spectra as well as to modulate the ESIPT reaction inducing a dramatic increase of the N*/T* ratio. Noticeably, many probes with strong donating groups at position 2 present low QYs in water due to larger dipole moments, classically observed for push–pull dyes. Hence, to construct an effective **3HC** dye for polar media, introducing a too strong donor at position 2 is not recommended. In this context, **FC** (2-furyl-3-hydroxychromone) is one of the most prospective aromatics to probe protic media.[178] Its N*/T* ratio has a sensitivity range varying from ~0.05 to ~2.5 from ACN to H_2O. This sensor has shown many applications for probing protein structures, dynamics, and interactions where polar environments were involved.[200-202]

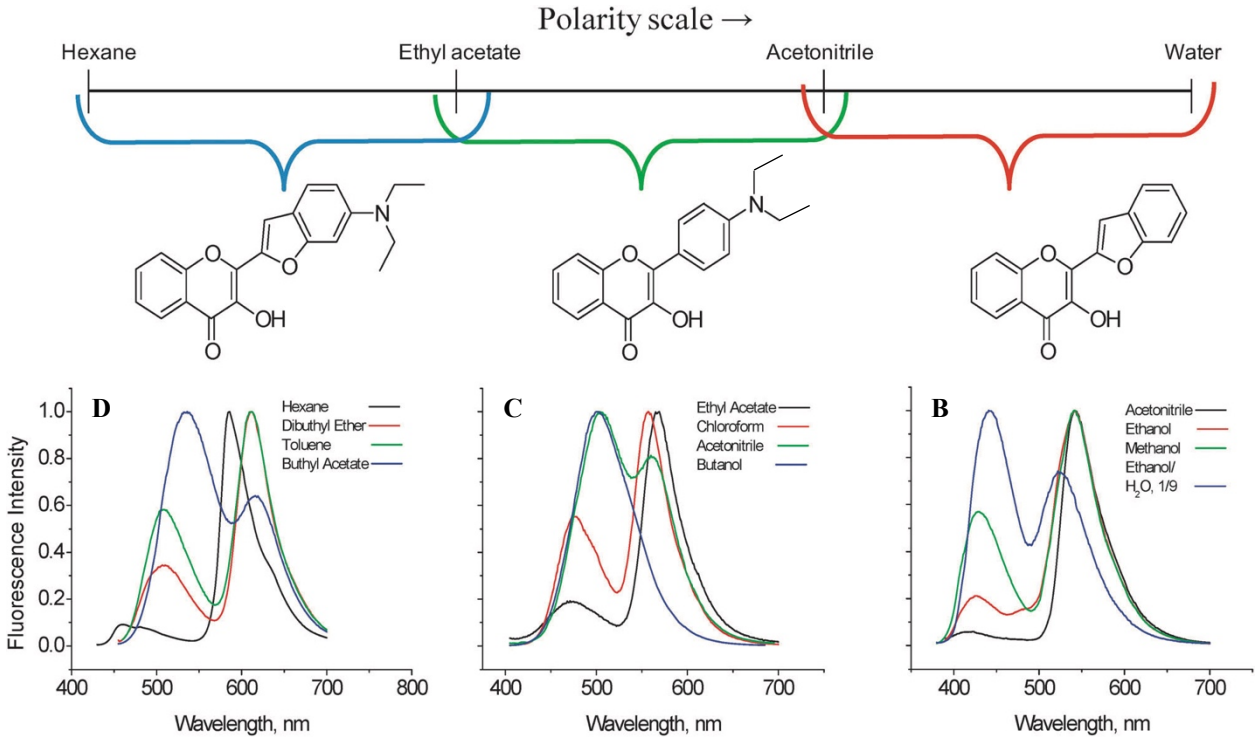

Figure 45. Dual-emissive response of **3HC** dyes with different solvent polarity ranges: respectively low-polar, medium-polar, and polar. (Adapted from ref[191])

Substituents at position 7 also have significant effects on the N*/T* ratio. Most of the time, an EDG connected at position 7 leads to the enhancement of ESIPT reaction, causing N*/T* decreases and vice versa. This is probably due to the cancelation of dipole moment in the excited state with increasing donating ability of the substituent. This, in turn, can lead to favoring the production of the T* form within the ESIPT equilibrium. For example, 7-acetamido-3-hydroxychromone (**83**), constructed by introducing an acetamido group at position 7 of **FC**, maintains the N*/T* sensitivity range in protic media. However, the smoothly donating acetamido group in **83** interestingly provokes a significant decrease of the N*/T* ratio by enhancing the T* emission (Figure 46) as compared to **FC**.[203]

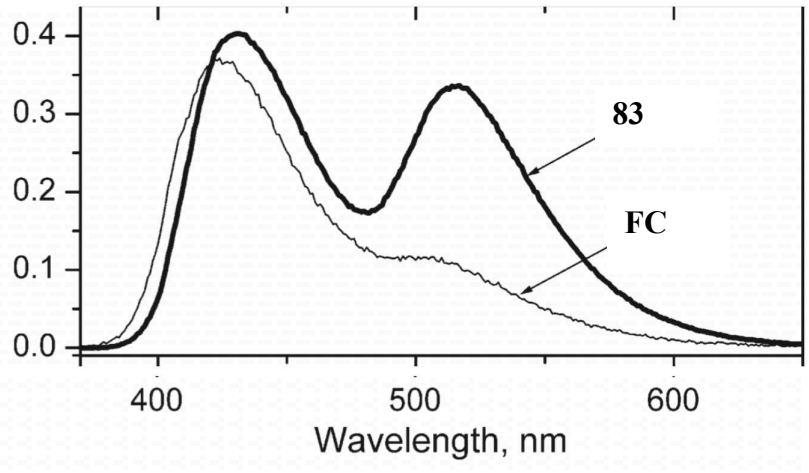

Figure 46. Emission spectra of **FC** and its 7-acetamido derivative, **83**, in water. (Adapted from ref[203])

1.5. Recent developments on dual-emissive nucleosides

At the time of writing this thesis, there is only a very limited number of nucleosides with dual emission in the literature. Among these few examples, Saito et al. developed dual-emissive purine nucleosides.[204-206] The origin of dual emission, in these studies, is originated from the coplanar and non-coplanar conformers of the nucleobase and naphthalene moiety. The former conformer with an ICT character exhibits red-shifted emission to the latter. Emission of the latter conformer can be observed as a blue-shifted locally excited (LE) band when the naphthalene ring was located in a sterically restricted environment. The introduction of an electron-withdrawing group (such as cyano group) could increase the ICT character, making the dyes more environmentally sensitive. In effect, these dyes could be used as thymine-discriminating probes. For example, when the base was matched with thymine in the duplex 5′-d(CGCAAT^{cna}ATAACGC)-3′/5′-d(GCGTTATATTGCG)-3′, the emission spectrum shows distinctive feature compared to other mismatched cases, such as blueshift of emission maxima (at 362 and 381 nm), and an enhanced of fluorescent intensity of both emissive bands (Figure 47). However, these dyes only show dual-band emission in some special cases, and the dual-emissive bands are not well-resolved from each other, limiting its applications as ratiometric probes.[204-206]

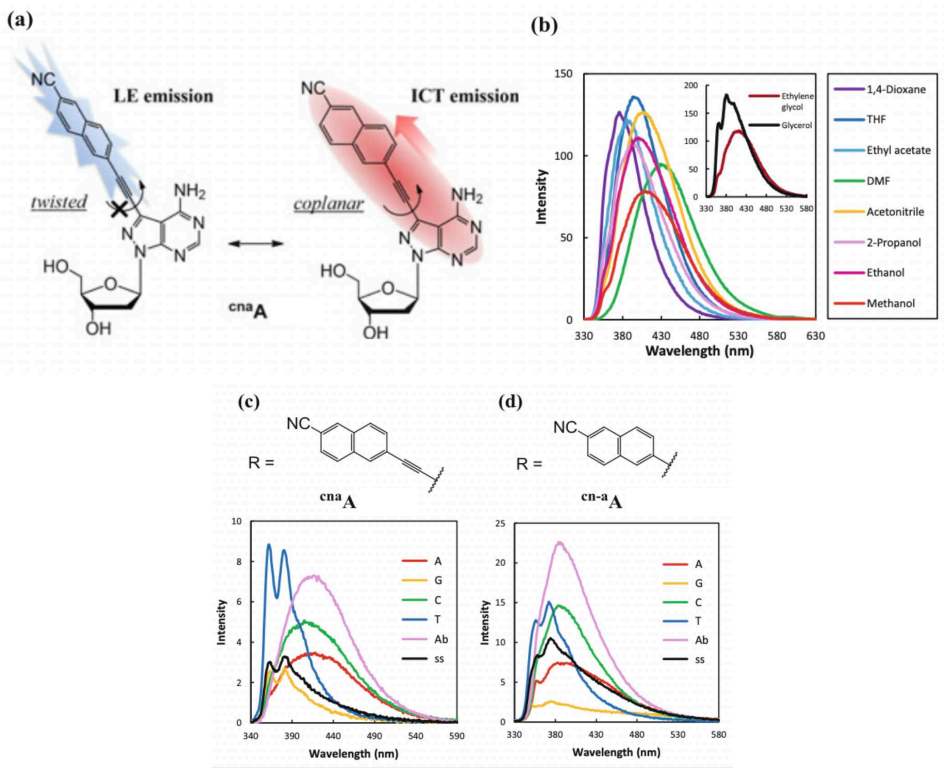

Figure 47. (a) Structures of the two ^{cna}**A** conformers. (b) Emission spectra of the fluorophore in different solvents. (c) Emission spectra of ^{cna}**A**-containing ODNs: ss denotes single-stranded ODN labeled with ^{cna}**A**; A, G, C, T, and Ab denote the base at the opposite position of ^{cna}**A** in its complementary strand. (d) Similar to (c) apply for $^{cn\text{-}a}$**A**. (From ref[118])

In this context, our research group reported the synthesis and photophysics of dual-emissive C-nucleosides bearing a two-color **3HC** dye as a base mimic (Figure 48).[207] Among the two targeted nucleosides, 2-thienyl-3HC (**3HCnt**) showed greater sensitivity to both the polarity and H-bonding ability of the solvent (Figure 48), as the parent chromone **TC** from which it originates.[208] **3HCnt** presents an absorption maximum around 360 nm with an extinction coefficient close to 21,000 $M^{-1}.cm^{-1}$. The dye exhibits two well-resolved emissive bands, due to the ESIPT reaction, in the blue and yellow regions (ca. 440 and 550 nm, respectively) for all the solvents studied with appreciable QYs (~10%). The ratio intensity between the two bands (N*/T*) exhibits high sensitivity in between ACN and water (Figure 48). Moreover, the intensity ratio N*/T* shows a correlation with water concentration present in the investigated solvent mixtures, attesting its high sensitivity to hydration. Ultimately, the dye has a great potential to probe DNA-related processes.

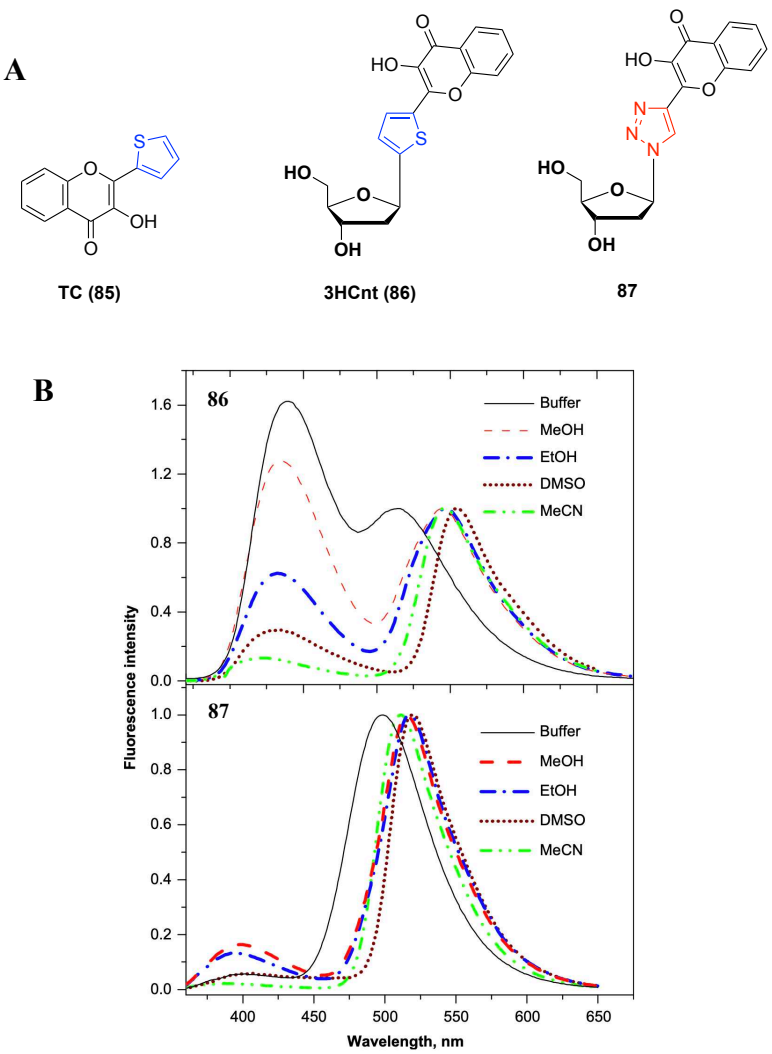

Figure 48. (A) Structures of the parent **3HC** (**TC**) and its derived C-nucleoside (**3HCnt**), as well as the 2-(1,2,3-triazol-4-yl)-3HC derivative (**87**). (B) Emission spectra in polar solvents of **3HCnt** and **87**. (From ref[207])

The dye was later used to label different ODN sequences via phosphoramidite chemistry and was proven to have many applications. For example, it can clearly distinguish between ssODN, dsODN, and ssODN binding to a peptide with its ratiometric response. In ss sequence, the probe is exposing to an average hydrated environment making it emits green light. The observed color is due to the sum of a low N* blue contribution and a high T* yellow contribution. When hybridized with the complementary strand, the probe is located "inside" of the duplex, thus referred as internal labeling. Due to the staking effect, the dye is shielded from the hydrated environment, and therefore emits a yellower fluorescence (because of the lower N* blue contribution). Binding of HIV-1 nucleocapsid protein (NC) to the ss labeled sequence, on the other hand, extrudes the probe outside of the interaction side, making it exposed to a more hydrated environment, hence emitting blue light (Figure 49).[209] Another important application is for studying the dynamics of methylated cytosine flipping by ubiquitin-like containing PHD and RING finger domains 1 (UHRF1) protein (Figure 50).[210] In this study, we have shown that the probe could be used to report the flipping of 5-methylcytosine (**5mC**) by its ratiometric response as well as fluorescent intensity. The study provided a potential platform for developing screening assays aimed at targeting UHRF1.[210]

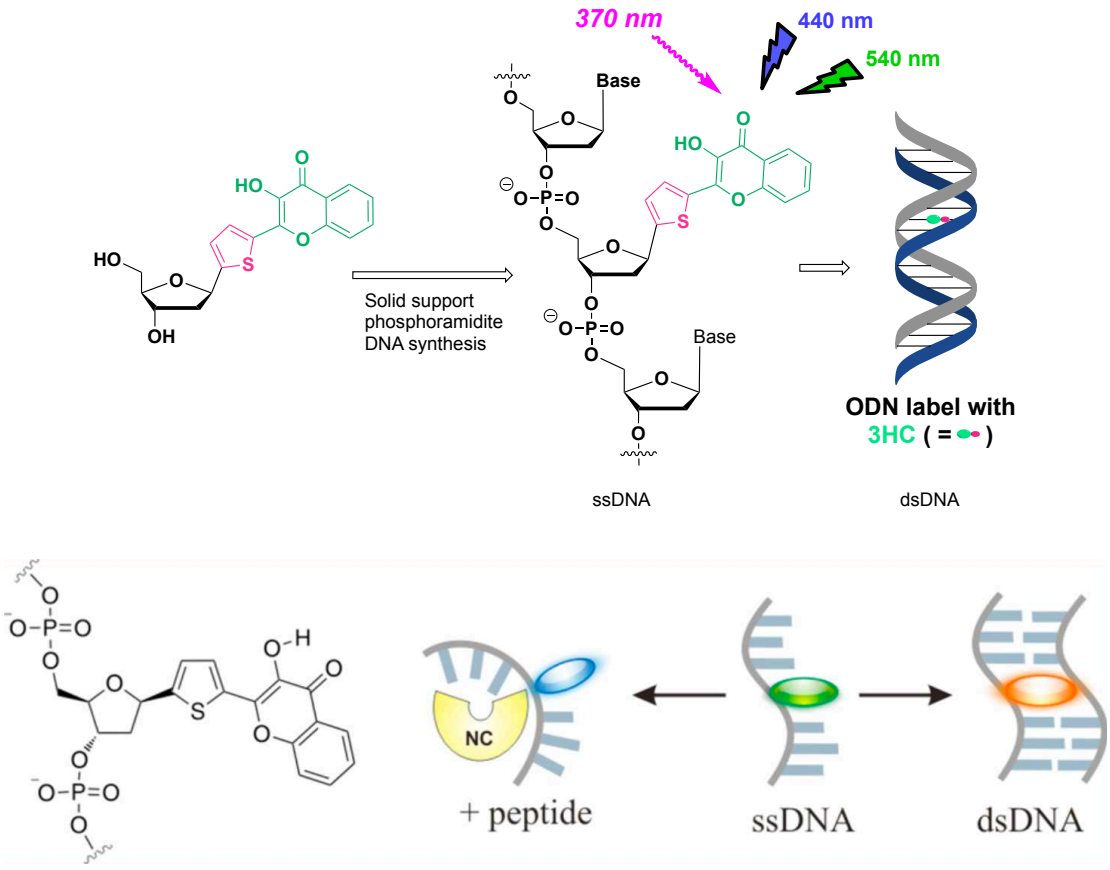

Figure 49. Incorporation strategy of **3HCnt** into an ODN leading to an internal duplex labeling (top). Schematic representation illustrating the developed sensing mechanism (bottom). (From ref[209])

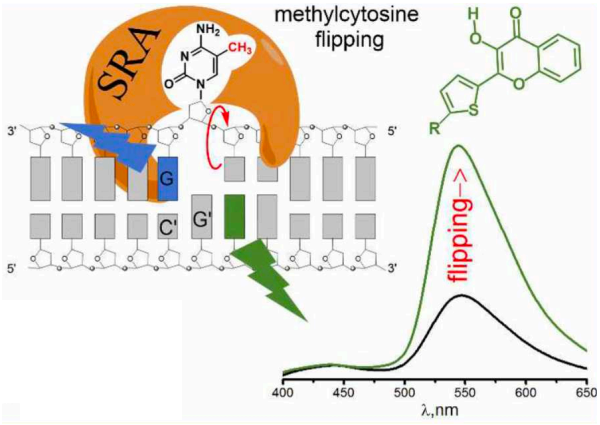

Figure 50. Two-color detection of **5mC** flipping upon binding with Set and Ring Associated (SRA) domain of UHRF1. (Adapted from ref[210])

However, this artificial nucleobase even has an Achilles heel. Indeed, because of favorable π-stacking interactions and its size is comparable to an A•T or C•G base pair, the dye fits nicely inside the duplex while tilting the opposite base, as it was evidenced by NMR spectroscopy (Figure 51).[211] Since this intercalation screens the two-color base from the outer shell of DNA, this reduces the sensitivity of the probe to environmental changes surrounding the duplex, and thus limits its scope of application.

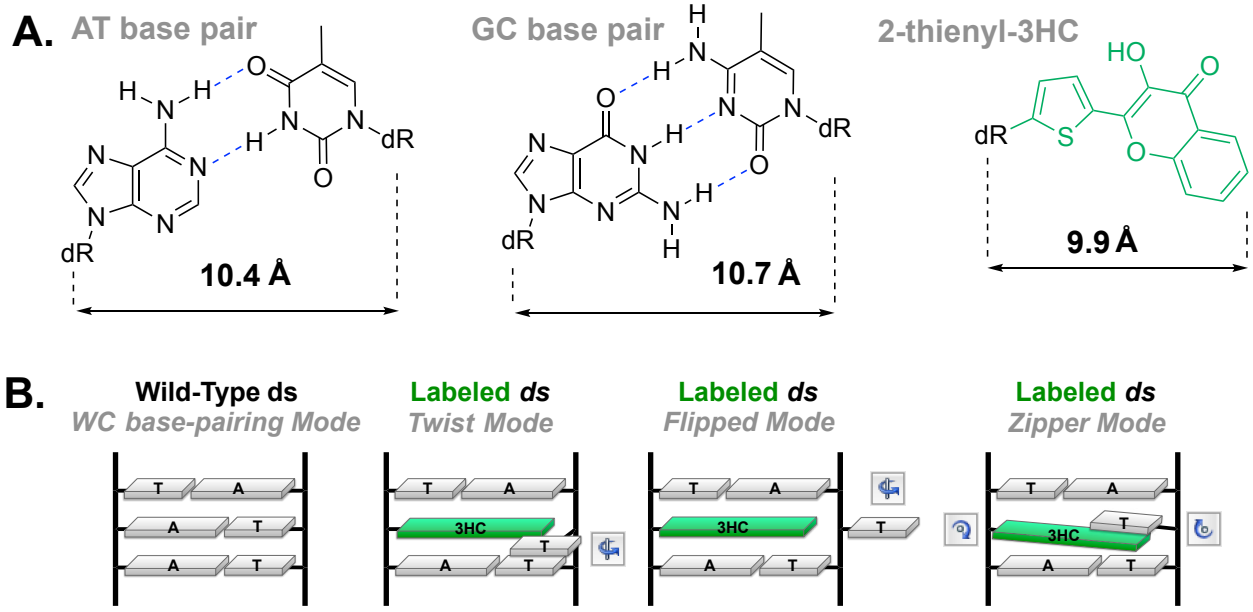

Figure 51. (A) Size comparison of the fluorescent reporter **3HCnt** with those of conventional Watson–Crick DNA base pairs; (B) Possible modes of **3HCnt** intercalation that have been investigated. (From ref[211])

To overcome this issue, a second generation of dual-emissive nucleosides was developed with significant improvements in their photophysics. These modified **dU** analogs were engineered by extending the electronic π-system of the nucleobase while maintaining its base-pairing properties. To this end, the uracil base was conjugated with a **3HC** moiety through a rigid acetylene linker connected to its C5-position.[212] Several **3HC-dU** conjugates (**PCU**, **FCU**, and **TCU**) were prepared, differing from each other by the 2-aryl group of the parent chromone, thus including **3HF**, **FC**, and **TC** (Figure 52). These two-color nucleosides are characterized by a red-shifted absorption into the visible range and a bathochromic shift of both emission bands in the cyan and orange regions, respectively, for the N* and T* forms. Compared to their parent chromone, the extension of conjugation almost doubled the absorptivity. For instance, **TCU** absorbs the violet light (ca. 400 nm) with an extinction coefficient of around 40,000 and fluoresce at 460 and 570 mn while displaying attractive QYs in protic media.[212]

Regarding the hydration probing, it clearly appears that **FCU** and **TCU** are the most promising reporters in terms of resolution of the dual emission. Both dyes have complementary sensitivity. **FCU** revealed to be highly sensitive in moderately hydrated environments (Figure 52, see the N* increment between 0–50 %), whereas **TCU** turned out still dual-emissive in media with strong water content. As previously mentioned, grafting a dye at position 5 of a pyrimidine ring will locate it into the hydrated major groove of the labeled sequence. Hence, this localization guarantees at the seat of the ESIPT reaction (i.e., the keto and OH groups), adequate exposure to the water coating surrounding the DNA.

TCU and **FCU** were later used to label different ODNs sequences using phosphoramidite chemistry and have proven to be extremely useful for several applications. In general, the probes have good brightness in ODN environment with QY around 10–15% and good sensitivity to hydration surrounding the duplex. For example, **TCU** could clearly discriminate between ssODN, B-DNA matched, B-DNA mismatched and A-DNA due to difference of hydration between these contexts (Figure 53). **FCU**, on the other hand, was used to discriminate between matched and mismatched sequences with an ON/OFF of the ESIPT reaction (ON/OFF of the T* band) (Figure 54).

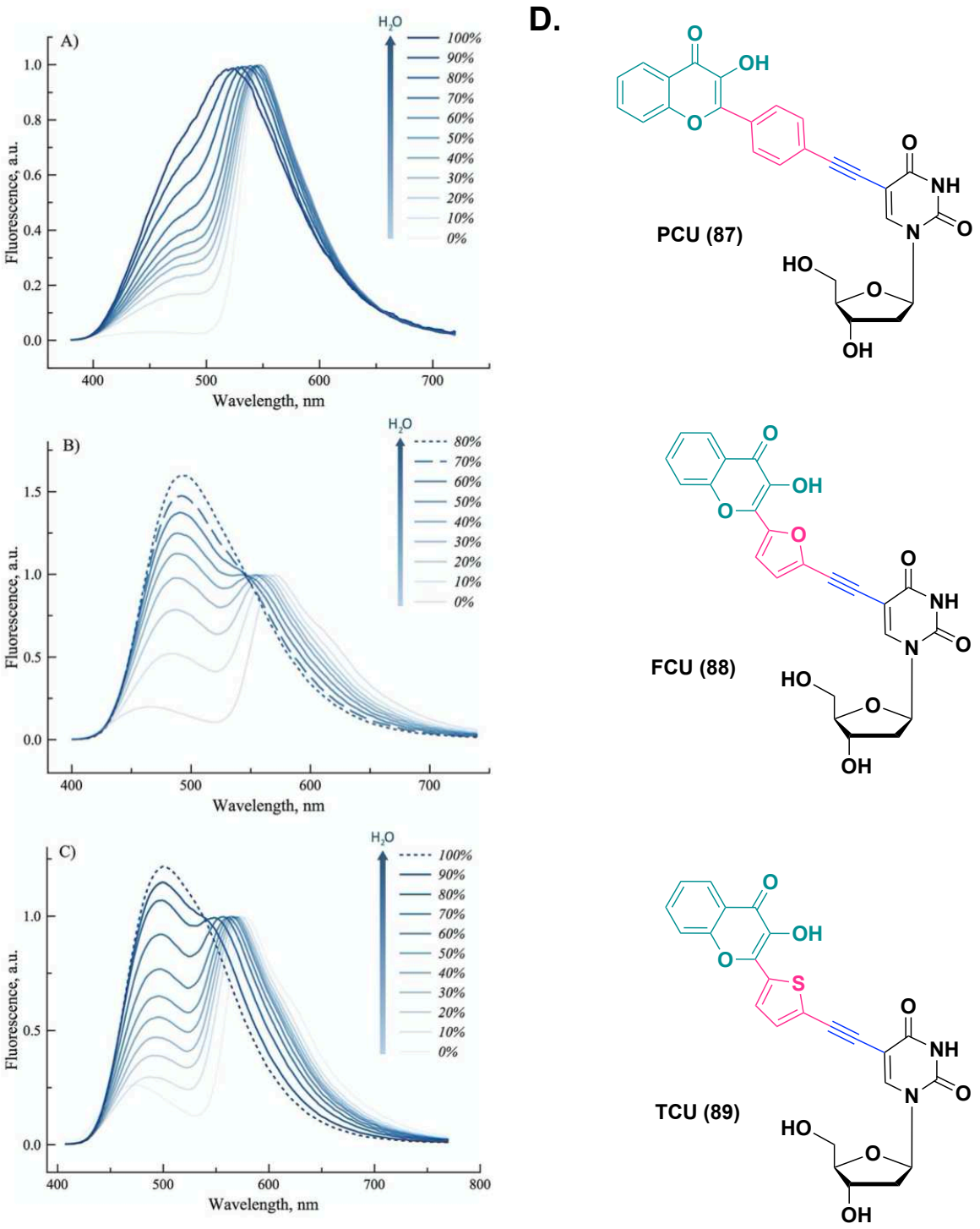

Figure 52. Dual-emissive response to variations in hydration for (A) **PCU**, (B) **FCU**, and (C) **TCU**. (D) Structures of the corresponding two-color nucleosides. (Adapted from ref[212])

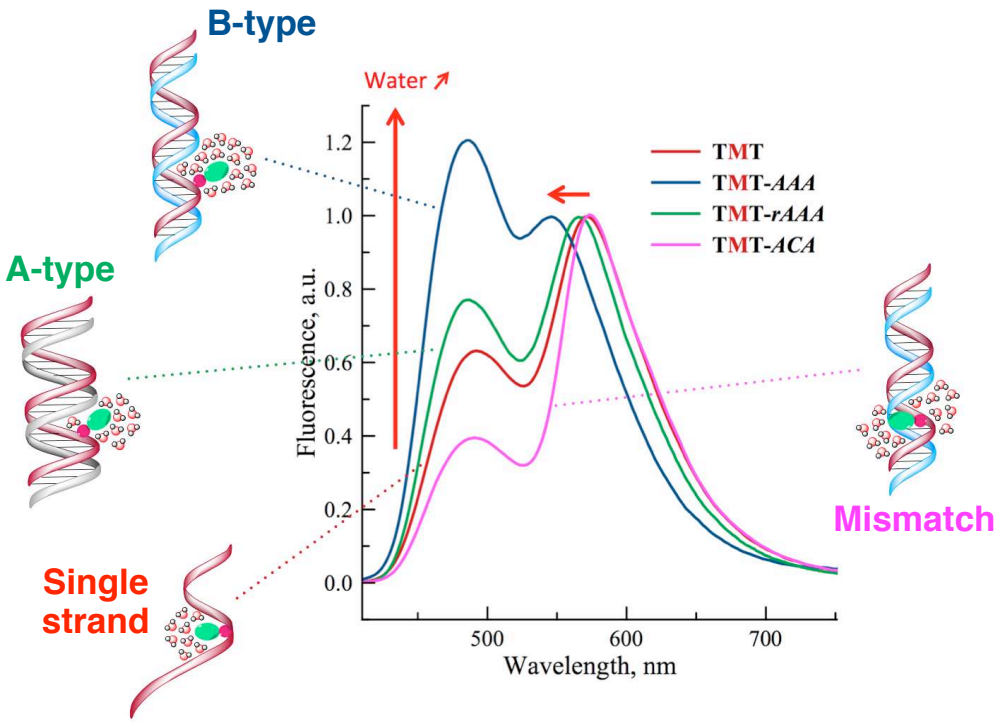

Figure 53. Ratiometric discrimination of different DNA structures based on hydration surrounding the **TCU** probe. (Adapted from ref[28])

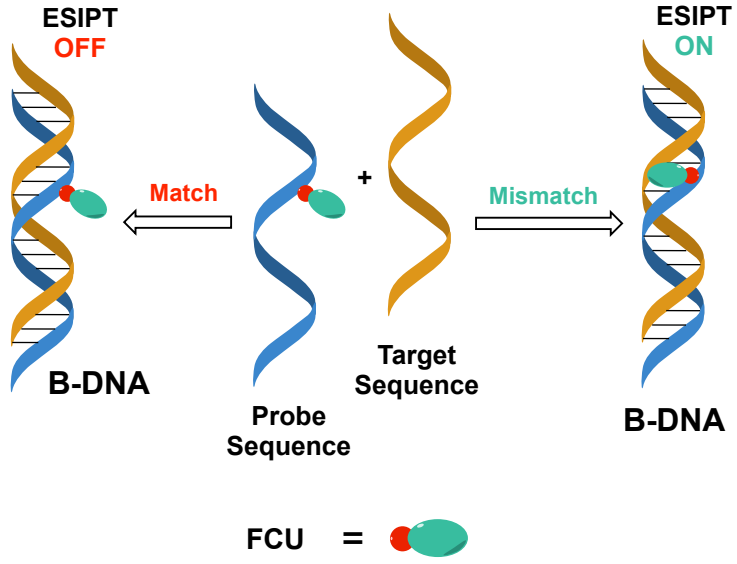

Figure 54. Discrimination of matched from any type of mismatched sequences by switching ON/OFF the ESIPT reaction. (Adapted from ref[213])

1.6. Introduction to the thesis subject

The 21st century has emerged an explosive development in the field of chemical biology. The discoveries of X-ray crystallography, electron microscopes, NMR, mass spectrometry, and fluorescence spectroscopy have accelerated the entire field of science. Among them, fluorescent-based techniques have contributed a great proportion due to several advantages. They provide ultra-high temporal and spectral resolutions; meanwhile, maintaining noninvasive, easy-to-use, and extremely sensitive techniques. Thus, fluorescent dyes become commonly used in chemical biology as cellular stains, environmental reporters, biomolecular labels, and enzyme substrates. The development of technology has reached such a threshold that a dye can be observed in a living cell at the single-molecule level; thereby providing an incredible sensitivity. Nowadays, we can look at a living cell and observe its processes with a fluorescent microscope.

Further advancement in the field of science requires an understanding of the biological processes at the molecular levels. These insights are essential for the design of medicine for disease treatment. Nucleic acid-related events such as transcription and translation are often central to most critical processes, as involved in the growth, development, and healthy maintenance of any living organism. However, the particularly weak intrinsic fluorescence of the nucleobases constituting the nucleic acids makes the study of these processes by this channel extremely difficult. Fortunately, the development of **2AP**, an emissive analog of adenine, has made it possible. The modified nucleoside (**2AP**) has found many applications both in the study of nucleic acid structures and their interactions with proteins.

In recent decades, the engineering of modified nucleic acids as emissive tools for the study of nucleic acids related processes has become an attractive area of research. There are fluorescent analogs for each nucleobase with improved properties compared to those of the ancestral **2AP**. Additionally, FRET pairs, including those with an acceptor or quencher, cover the entire visible range to offer users a wide choice of color emission depending on the specifications of the targeted application. All these fluorescent reporters can be site-selectively incorporated into ODN sequences in order to carry out studies as close as possible to the site of interest. Despite all these advances, there are still real needs for even more sensitive and refined tools, exhibiting original response mechanisms that overcome recurrent problems of concentration, signal-to-noise ratio (S/N), and laser compatibility for imaging.

In our research team, we are developing dual-emissive probes to study DNA, its conformations and biological processes directly involving them. As mentioned previously, these two-color probes draw their originality from their ratiometric response. This self-calibrated fluorescent signal offers a prospective alternative to conventional dyes with single-band emission since it could avoid false results. Our first generation of dual-emissive dyes – used as a nucleobase surrogate – turned out to be a very informative tool for a variety of applications (e.g., DNA methylation and repair). Meanwhile, our second-generation toolbox is currently under development. Our first candidates, dU analogs, revealed to be really instructive for monitoring structural changes in nucleic acids (hybridization and transition from B- to A- conformation).

In this thesis, namely *"Development of dual-emissive adenosine analogs for nucleic acid labeling and life sciences"*, we concentrated our efforts on the development of two-color **dA**-based sensors to broaden the scope of applications of our ratiometric toolbox. *Chapter 1* presents state of the art on DNA structures and functions, light-related processes, and fluorescent nucleobases with a focus on ESIPT-based fluorophores. *Chapter 2* consists of the "results and discussions", which is divided into three main parts. *Part A* describes the rational design, synthesis, and photophysics of dual-emissive nucleosides bearing **d7A** as a nucleobase mimic. Interestingly, a significant quenching of these fluorescent dyes in protic environment was observed. *Part B* presents our study on the PET processes causing the fluorescence quenching of our **dA** conjugates comprising a **3HC** moiety in 3-methoxy series. These investigations could be enlightening for further designs of efficient probes using a similar approach. Following up on this, *Part C* reports the engineering of dual-emissive transducers based on an **8d7A** base surrogate and their ability to probe hydration surrounding DNA and to sense the electron transfer occurring along the double helix. *Chapter 3* corresponds to the experimental part. Eventually, a general conclusion and future prospects are given.

Chapter 2. Results and Discussions

2.1. Dual-emissive analogs of 7-deazadeoxyadenosine

Using the same assembling approach as the designed dU analogs,[212] our work initially focused on the **d7A** scaffold. This base analog allows us to modify its 7-position in order to engineer push–pull conjugates with **3HC** moieties. The retrosynthetic analysis of these modified nucleosides is depicted in Figure 55. Noticeably, these modifications are expected to have minor effects on the stability and structure of ODN sequences containing this fluorescent label. This comes from the fact that both the A•T base-pairing is maintained and **3HC** is located into the "broad" major groove of the helix (Figure 56). Our synthesis of **d7A-3HC** conjugates were adapted from the reported Seela's approach[214] (see Figure 57) with some improvements.

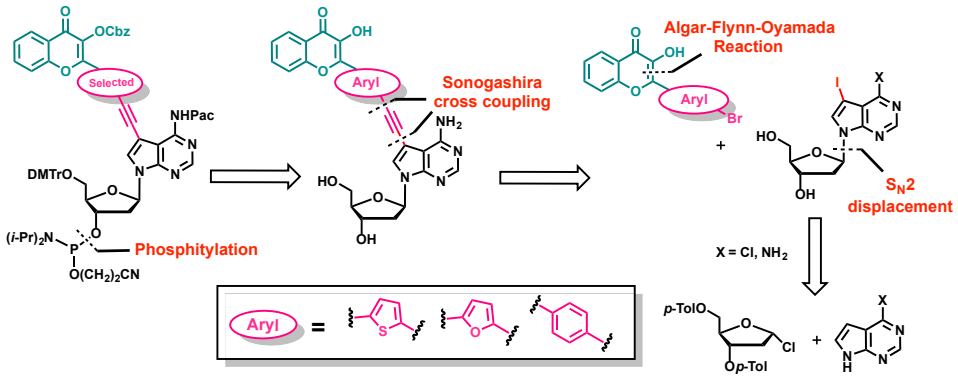

Figure 55. Retrosynthesis of dual-emissive **d7A** analogs targeted in this study.

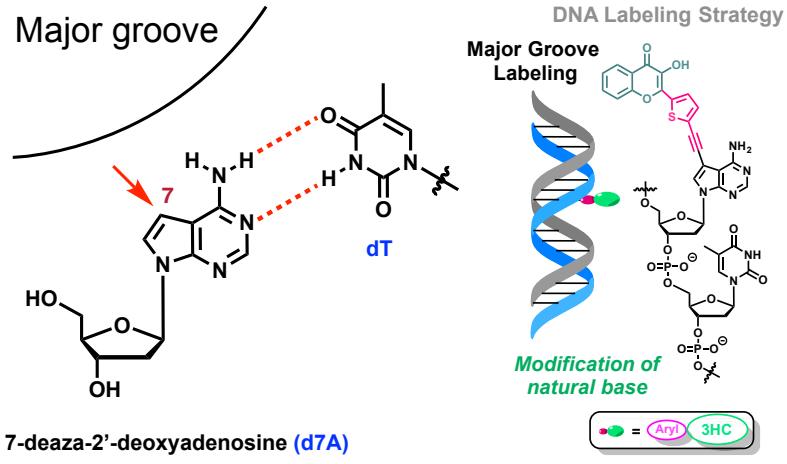

Figure 56. Base pairing between **d7A** and **dT** (left). Depicted structure of a dsODN-containing a **d7A-3HC** label (right).

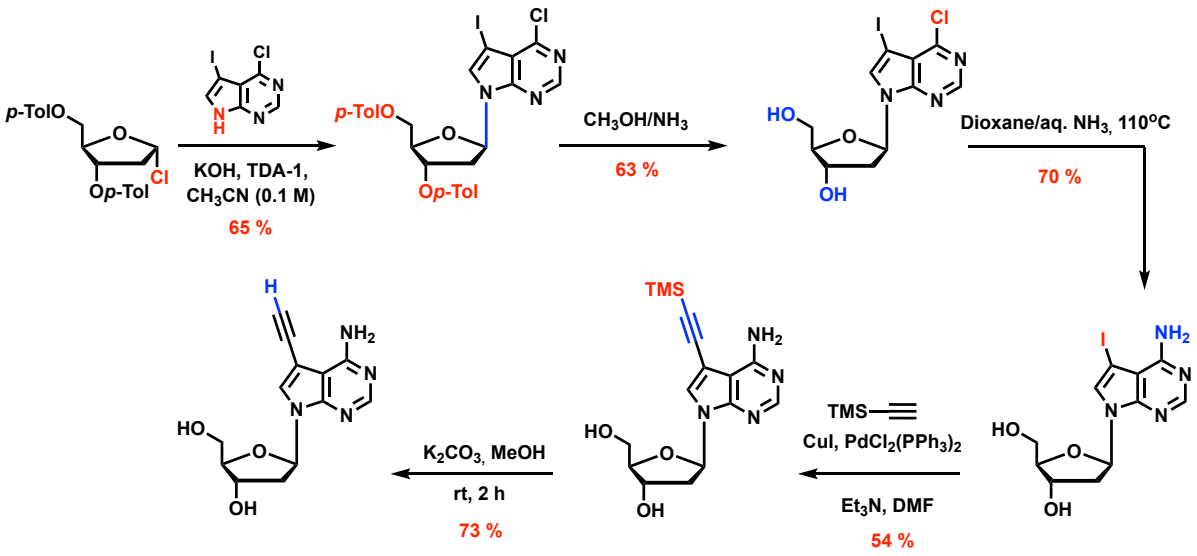

Figure 57. Synthesis of the ethynyl-d7A intermediate reported by Seela et al. (Adapted from ref[214])

PUBLICATION 1

Dyes and Pigments 170 (2019) 107553

Contents lists available at ScienceDirect

Dyes and Pigments

journal homepage: www.elsevier.com/locate/dyepig

Rational design, synthesis, and photophysics of dual-emissive deoxyadenosine analogs

Hoang-Ngoan Le[a,1], Caterina Zilio[a], Guillaume Barnoin[a], Nicolas P.F. Barthes[a], Jean-Marie Guigonis[b], Nadine Martinet[a], Benoît Y. Michel[a,**], Alain Burger[a,*]

[a] Université Côte d'Azur, CNRS, Institut de Chimie de Nice, UMR 7272 – Parc Valrose, 06108, Nice cedex 2, France
[b] Université Côte d'Azur, Faculté de Médecine, Plateforme "Bernard Rossi", Nice, France

A B S T R A C T

Dual-emissive deoxyadenosine analogs were engineered by compiling 7-deaza-7-ethynyl-2′-deoxyadenosine with two-color dyes, 3-HydroxyChromones (3HC), while electronically conjugating the *N*9-donor of the nucleobase with the 3HC carbonyl. Their spectroscopic properties were investigated in a set of solvents of different polarities. Several improvements in the 3HC photophysical features were obtained. A significant bathochromic shift moved absorption to the visible range, the extinction coefficient was almost doubled and the fluorescence emission displayed a mega-Stokes shift of the tautomer emission band (> 175 nm). The ratio intensity of the dual emission demonstrated high sensitivity to polarity changes, offering a well-resolved green-yellow emission. Considering the strong donating ability of the *N*9, angular and reversed assemblies were also considered in order to tune the photophysics by weakening the excited-state dipole moment.

1. Introduction

Nucleosides constitute the critical building blocks of nucleic acids [1]. Redesigning their structure and incorporating the resulting nucleoside analog into oligonucleotides is a conventional approach to produce modified DNA sequences for chemical biology purposes [2]. Changes that make DNA fluorescent is a dominant technique, thanks to the non-invasive character and high sensitivity of response of fluorescence spectroscopy [3,4]. Due to their low intrinsic fluorescence, the four DNA nucleobases cannot be used to report biological events, as can be achieved in proteins with the help of Trp residues [5–9]. Thus, modification of the nucleobase structure is one attractive option, to improve analyses of nucleic acids. This requires changing of the π-system or connecting of a fluorescent moiety [10]. Whichever strategy is chosen, the development of fluorophores that perfectly satisfy the demanding specification (such as the sensitivity to environment variations and interactions, the brightness, the compatibility with available laser lines for excitation to name a few) turns out to be an extremely complex task [11,12]. In this context, we have investigated the synthesis of advanced emissive nucleosides as responsive new sensors for the local hydrated environment of DNA, since structural changes and interactions with proteins and other ligands impact the proximal water distribution and polarity around the DNA [13]. These fluorophores are based on a 3-HydroxyChromone (3HC) scaffold and present dual emission, i.e. emission with two distinct colors. Indeed, through an excited-state intramolecular proton transfer (ESIPT reaction), these dyes have the unique ability to display two tautomer forms, emitting separately to each other at two well-defined wavelengths (green and yellow, N* and T* bands respectively, Scheme 1) [14–17].

3HCs proved to be extremely sensitive to proximal disturbances, as reflected by a considerable change in the intensity ratio of the two emission bands, and hence by a readily quantifiable change in color [18–21]. We first investigated internal DNA labeling by nucleobase replacement with 3HC fluorophores [22,23]. DNA sequences site-specifically tagged according to this strategy were applied to the mechanistic studies of DNA repair and methylation [24,25] as well as for HIV-1 replication [26]. These examples of a fluorescence-based approach attested the outstanding sensitivity of this nucleobase surrogate to structural changes accompanying protein binding and base flipping, while the structure of the duplex and its protein affinity were only marginally affected. Minimal DNA perturbation by the dye incorporation was further supported by NMR investigations [27].

Although these prospective probes helped overcome several bottlenecks encountered in nucleic acids labeled with commonly used fluorophores such as 2-aminopurine, their sensitivity to hydration changes was not optimal. Recently, we engineered efficient synthetic access to the DNA major groove labeling by electronically compiling 3HC fluorophores to a uracil moiety (Fig. 1, *left*) [13,28,29]. These

* Corresponding author.
** Corresponding author.
E-mail address: burger@unice.fr (A. Burger).
[1] Main contributor to these research works.

https://doi.org/10.1016/j.dyepig.2019.107553
Received 18 March 2019; Received in revised form 7 May 2019; Accepted 10 May 2019
Available online 13 May 2019
0143-7208/

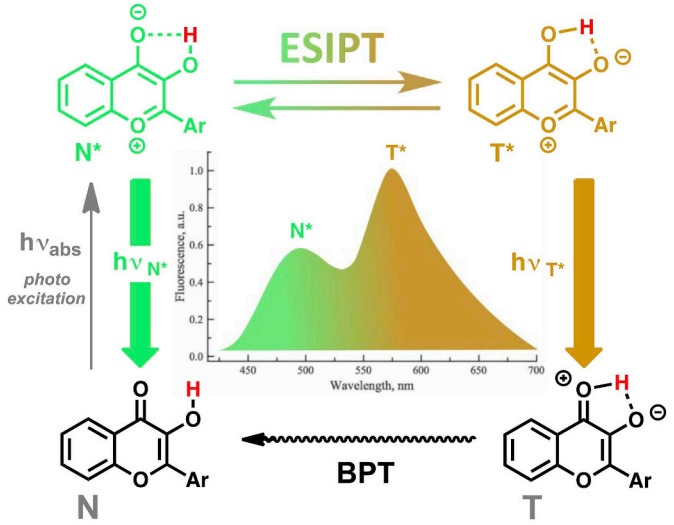

Scheme 1. ESIPT reaction: origin of the dual emission for 3HC fluorophores leading to a two-color response for sensing polarity changes. *BPT denotes Back Proton Transfer*.

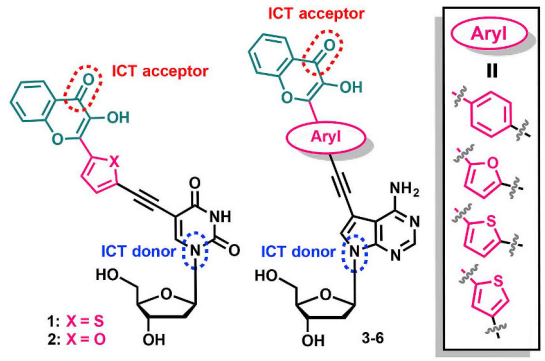

Fig. 1. Nucleoside labeling strategy – *Modification of a natural base:* structures of the 3HC-engineered dU (*left*, reported) [13,28,29] and dA analogs (*right*, present work). *ICT denotes Intramolecular Charge Transfer*.

fluorescent deoxyuridine analogs demonstrated exquisite sensitivity to hydration via two distinct sources: the wide variation of the intensity ratio of the two emission bands (Fig. S1, arrow A) and the hypsochromic shift of the T* form (*arrow B*) [13]. This multiparametric sensing mechanism appears to be completely unique since it presents the decisive advantage to precisely monitor subtle local changes of hydration – independently of the probe concentration or the fluctuations of the fluorometer being used – by simultaneously exploiting the two channels of fluorescence (Fig. S1) [29].

In the continuation of this work, we sought to complete our ratiometric toolbox of fluorescent nucleoside analogs to the purine series by preparing dA analogs presenting 2-aryl substituents with different donating abilities. Final targets **3–5**, namely **PCA**, **FCA**, **TCA** (P = phenyl, F = furyl, T = thienyl, C = 3HC, Figs. 1 and 2), were rationally designed in such a way that the *N*9 position is electronically conjugated to the ketone of the flavonoid C ring to establish an extended D-π-A push–pull system (D = donor, A = acceptor) and to favor intramolecular charge transfer (ICT; Fig. 1, right).

Hence, these two-color nucleoside analogs were expected to have a strong push–pull character in the excited state [30,31]. To modulate the latter, two different molecular architectures were also explored. One involves a 2,4-disubstituted thienyl isomer while the other presents a dipole moment attenuated due to a reversed connectivity orientation (**angTCA 6** and **revTCA 7**, ang = angular, and rev = reversed, Figs. 1 and 2). Herein, we report the synthesis of the five 3HC-based dA analogs by a convergent approach. To this end, the final assembly between 7-deaza-7-ethynyl-dA and 3HC parent dyes with various electronic features is performed by a Sonogashira coupling under mild conditions. A photophysical characterization of each dual-emissive dA analog is described for a set of 10 solvents with increasing polarity. Correlations between spectroscopic properties, polarity parameters and the strength of the push–pull character are discussed to discriminate and select the most promising analogs for a further oligodeoxynucleotide (ODN) incorporation.

2. Experimental section

2.1. General procedures – materials and methods

All reactions involving air- and water-sensitive conditions were performed in oven-dried glassware under argon by using Schlenk techniques employing a dual vacuum/argon manifold system and dry solvents. The synthetic intermediates were initially co-evaporated twice with toluene and dried *in vacuo* before use. All chemical reagents were purchased from commercial sources (Sigma-Aldrich, Acros, Alfa Aesar) and were used as supplied. Anhydrous solvents were obtained according to standard procedures [32]. The reactions were monitored simultaneously by liquid chromatography–mass spectrometry (LC-MS) and thin-layer chromatography (TLC, silica gel 60 F254 plates). Compounds were visualized on TLC plates by both UV radiation (254 and 365 nm) and spraying with a staining agent (Vanillin, PMA, $KMnO_4$ or ninhydrin) [33] followed by subsequent warming with a heat gun.

Column chromatography was performed with flash silica gel (40–63 μm) with the indicated solvent system using gradients of increasing polarity in most cases [34]. All NMR spectra (^{1}H, ^{13}C, 2D) were recorded on 200, 400 or 500 MHz Bruker Advance Spectrometers. ^{1}H NMR (200, 400 and 500 MHz) and ^{13}C{^{1}H}NMR (50, 101 and 126 MHz, recorded with complete proton decoupling) spectra were obtained with samples dissolved in $CDCl_3$, CD_2Cl_2, CD_3OD, DMSO-d_6, acetone-d^6, CD_3CN or C_5D_5N with the residual solvent signals used as internal references: 7.26 ppm for C*H*Cl_3, 5.32 ppm for CD*H*Cl_2, 3.31 ppm for CD_2*H*OD, 2.50 ppm for $(CD_3)(CD_2H)S(O)$, 2.05 ppm for $(CD_3)(CD_2H)C(O)$, 1.94 ppm for CD_2*H*CN, 8.74 ppm for C_5D_4*H*N regarding ^{1}H NMR experiments, and 77.2 ppm for $CDCl_3$, 53.8 ppm for CD_2Cl_2, 49.0 ppm for CD_3OD, 39.4 ppm for $(CD_3)_2S(O)$, 30.8 ppm for $(CD_3)_2C(O)$, 118.7 ppm for CD_3CN, 150.3 ppm for C_5D_5N concerning ^{13}C NMR experiments [35,36]. Chemical shifts (δ) are given in ppm to the nearest 0.01 (^{1}H) or 0.1 ppm (^{13}C). The coupling constants (J) are given in Hertz (Hz). The signals are reported as follows: (s = singlet, d = doublet, t = triplet, m = multiplet, br = broad). Assignments of ^{1}H and ^{13}C NMR signals were achieved with the help of D/H exchange, COSY, DEPT, APT, HMQC, HSQC, TOCSY, NOESY, and HMBC experiments. LC-MS spectra were recorded using an ion trap Esquire 3000 Plus mass spectrometer equipped with an electrospray ionization (ESI) source in both positive and negative modes. High-resolution mass spectrometry (HRMS) was conducted with a hybrid ion trap – Orbitrap mass spectrometer (combining quadrupole precursor selection with high-resolution and accurate-mass Orbitrap detection) using ESI techniques. Systematic flavone and nucleobase nomenclatures are used below for the assignment of each spectrum. All solvents for absorption and fluorescence experiments were of spectroscopic grade. Absorption spectra were recorded on a Cary 100 Bio UV–Vis spectrophotometer (Varian/Agilent) using Suprasil® quartz cuvettes with 1 cm path length. Stock solutions of dyes **3–7** were prepared using dimethylformamide. The samples used for spectroscopic measurements contained ≈0.2% v/v of solvents of the stock solution. Fluorescence spectra were recorded on a FluoroMax 4.0 spectrofluorometer (Jobin Yvon, Horiba) with a thermostated cell compartment at 20 ± 0.5 °C with slits open to 2 nm and were corrected for Raman scattering, lamp fluctuations and instrumental wavelength-dependent bias. Excitation wavelength was used as described in the corresponding experiments.

2.2. Synthesis

2.2.1. 6-Chloro-7-deaza-2′-deoxy-7-iodo-3′,5′-di-O-p-toluoyladenosine [37] (9)

To a stirred suspension of KOH (250 mg, 2.5 eq.) in dry CH_3CN (36 mL; previously sonicated over 1 min), were successively added TDA-1 (47 μL, 0.07 eq.) and 6-chloro-7-deaza-7-iodopurine (500 mg, 1.79 mmol). The resulting solution was stirred at room temperature (rt) for 10 min, until the suspension became clearer. Hoffer's sugar **8** (850 mg, 1.2 eq.) was added half at a time over 2 min and stirring was maintained for 10 min. The reaction mixture was diluted with CH_2Cl_2 (10 mL) and then the insoluble material was filtered and washed with CH_2Cl_2 (2 × 20 mL). The volatiles were removed under reduced pressure and the residue was purified by flash chromatography on silica gel eluted with toluene/EtOAc (1:0 → 4:1, v/v) to provide the desired product **9** as a white foam (860 mg, 76%). $C_{27}H_{23}ClIN_3O_5$ (631.85). R_f = 0.6 (toluene/EtOAc = 85:15); R_f = 0.5 (PE/EtOAc = 7:3). ^{1}H NMR (200 MHz, $CDCl_3$): δ 8.61 (s, 1H), 8.20–7.79 (m, 4H), 7.57 (s, 1H), 7.40–7.15 (m, 4H), 6.79 (t, *J* = 7.1 Hz, 1H), 5.75 (qd, *J* = 4.1, 2.1 Hz, 1H), 4.89–4.48 (m, 3H), 2.78 (dd, *J* = 7.1, 4.2 Hz, 2H), 2.45 (s, 3H), 2.43 (s, 3H). ^{13}C NMR (50 MHz, $CDCl_3$): δ 166.3, 166.1, 153.0, 151.1, 150.7, 144.7, 144.4, 131.6, 130.0, 129.8, 129.6, 129.4, 126.7, 126.5, 117.7, 84.6, 83.0, 75.2, 64.1, 53.0, 38.6, 21.9. HRMS (ESI$^+$): *m/z* calcd for $C_{27}H_{24}ClIN_3O_5$: 632.0444 $[M+H]^+$; found 632.0434.

2.2.2. 7-Deaza-2′-deoxy-7-iodo-3′,5′-di-O-p-toluoyladenosine (10)

To a saturated solution of NH_3 in BuOH (3.5 M, 4 mL), **9** (500 mg, 0.79 mmol) was added. The reaction mixture was stirred under microwave irradiation at 150 °C (100 W, 100 psi) for 15 min. The volatiles were removed *in vacuo* and the resulting residue was purified by flash chromatography on silica gel eluted with toluene/EtOAc (1:9 → 55:45, v/v) to provide the desired compound **10** as a white solid (402 mg, 83%). $C_{27}H_{25}IN_4O_5$ (612.42). R_f = 0.2 (PE/EtOAc = 1:1). ^{1}H NMR (200 MHz, $CDCl_3$): δ 8.29 (s, 1H), 8.15–7.82 (m, 4H), 7.58–7.14 (m, 4H), 6.80 (t, *J* = 7.1 Hz, 1H), 6.04 (s, 2H), 5.75 (td, *J* = 4.2, 2.3 Hz, 1H), 4.88–4.51 (m, 3H), 2.75 (dd, *J* = 7.2, 4.2 Hz, 2H), 2.46 (s, 6H). ^{13}C NMR (50 MHz, $CDCl_3$): δ 166.3, 166.1, 156.8, 151.9, 150.3, 144.6, 144.3, 129.9, 129.8, 129.5, 129.4, 126.9, 126.5, 125.9, 104.4, 84.0, 82.6, 75.3, 64.3, 51.6, 38.5, 21.9. MS (ESI$^+$, MeOH) *m/z*: 613.0 $[M+H]^+$. HRMS (ESI$^+$): *m/z* calcd for $C_{27}H_{26}IN_4O_5$: 613.0942 $[M+H]^+$; found 613.0947.

2.2.3. 7-Deaza-2′-deoxy-3′,5′-di-O-(p-toluoyl)-7-((trimethylsilyl)ethynyl) adenosine [37] (11)

To a stirred solution of **10** (940 mg, 1.5 mmol) in THF (31 mL) under argon, were sequentially added Et_3N (1.10 mL, 5 eq.), TMS-acetylene (330 μL, 1.5 eq.), and a mixture of CuI (8 mol%, 24 mg)/$PdCl_2(PPh_3)_2$ (8 mol%, 87 mg). The reaction mixture was stirred at 60 °C under argon for 2 h. Then, the resulting solution was diluted with CH_2Cl_2 (30 mL) and evaporated under reduced pressure. The residue was purified by flash chromatography on silica gel eluted with PE/EtOAc (9:1 → 4:6, v/v) to provide the desired compound **11** as a yellow foam (659 mg, 74%). $C_{32}H_{34}N_4O_5Si$ (582.73). R_f = 0.5 (PE/EtOAc = 2:3). ^{1}H NMR (500 MHz, CD_2Cl_2): δ 8.24 (s, 1H), 8.07–7.88 (m, 4H), 7.35 (s, 1H), 7.33–7.25 (m, 4H), 6.71 (dd, *J* = 8.2, 5.9 Hz, 1H), 5.93–5.52 (m, 3H), 4.66 (dd, *J* = 11.9, 4.1 Hz, 1H), 4.61 (dd, *J* = 11.9, 4.0 Hz, 1H), 4.56 (td, *J* = 4.1, 2.6 Hz, 1H), 2.80 (ddd, *J* = 14.5, 8.3, 6.4 Hz, 1H), 2.71 (ddd, *J* = 14.2, 5.9, 2.6 Hz, 1H), 2.43 (s, 3H), 2.42 (s, 3H), 0.26 (s, 9H). ^{13}C NMR (126 MHz, CD_2Cl_2): δ 166.7, 166.5, 158.1, 153.8, 150.5, 145.1, 144.7, 130.3, 130.1, 129.8, 129.8, 127.5, 127.3, 126.0, 104.1, 98.7, 97.9, 97.1, 84.5, 82.9, 75.6, 64.8, 38.6, 22.0, 0.1. HRMS (ESI$^+$): *m/z* calcd for $C_{32}H_{35}N_4O_5Si$: 583.2371 $[M+H]^+$; found 583.2374.

2.2.4. 7-Deaza-2′-deoxy-7-ethynyladenosine [37] (12)

To a stirred solution of **11** (620 mg, 1.1 mmol) in CH_2Cl_2 (5 mL), a saturated solution of K_2CO_3 in MeOH (20 mL) was added. The reaction mixture was stirred for 2 h at rt. The volatiles were evaporated under reduced pressure and the resulting residue was purified by flash chromatography on silica gel eluted with CH_2Cl_2/MeOH (98:2 → 85:15, v/v) to provide the desired compound **12** as a white solid (260 mg, 89%). $C_{13}H_{14}N_4O_3$ (274.28). R_f = 0.2 (CH_2Cl_2/MeOH = 9:1). ^{1}H NMR (400 MHz, CD_2Cl_2 with drops of CD_3OD): δ 8.04 (s, 1H), 7.50 (s, 1H), 6.34 (dd, *J* = 8.3, 5.9 Hz, 1H), 4.45 (td, *J* = 5.4, 2.5 Hz, 1H), 3.96 (q, *J* = 3.0 Hz, 1H), 3.74 (dd, *J* = 12.2, 3.0 Hz, 1H), 3.65 (dd, *J* = 12.2, 3.2 Hz, 1H), 3.51 (s, 1H), 2.58 (ddd, *J* = 13.8, 8.3, 5.9 Hz, 1H), 2.24 (ddd, *J* = 13.6, 6.1, 2.6 Hz, 1H). ^{13}C NMR (101 MHz, CD_2Cl_2 with drops of CD_3OD): δ 158.7, 152.8, 149.2, 128.8, 104.7, 95.7, 88.9, 87.1, 81.4, 77.3, 72.6, 63.3, 41.3. MS (ESI$^+$, MeOH) *m/z*: 275.0 $[M+H]^+$.

2.2.5. 7-Deaza-2′-deoxy-7-((4-(3-hydroxy-4-oxochromen-2-yl)phen-1-yl) ethynyl)adenosine (3 – PCA)

To a stirred solution of **12** (35 mg, 0.128 mmol) and **13** (81 mg, 1.3 eq.) in DMF (11 mL) that was previously degassed by sonication under argon, were sequentially added Et_3N (65 μL, 5 eq.), and a mixture of CuI (7 mol%, 2 mg)/$PdCl_2(PPh_3)_2$ (7 mol%, 6 mg). The reaction mixture was warmed to 60 °C under argon for 1 h. The resulting solution was diluted with CH_2Cl_2 (10 mL) and the volatiles were removed *in vacuo*. The residue was purified by flash chromatography on silica gel eluted with CH_2Cl_2/MeOH (98:2 → 85:15, v/v) to provide the coupled product as a yellow solid (50 mg, 61%). R_f = 0.4 (CH_2Cl_2/MeOH = 9:1). MS (ESI$^+$, MeOH) *m/z*: 645.2 $[M+H]^+$. The latter was sufficiently pure to be engaged in the next step without further purification. To a stirred solution of this Cbz-protected intermediate (40 mg, 0.062 mmol) in DMF (2 mL), a saturated methanolic solution of NH_3 (ca. 9 M, 5 mL) was added. The reaction was stirred for 5 min at rt. The volatiles were removed *in vacuo* and the residue was purified by flash chromatography on silica gel eluted with $CHCl_3$/(mixture MeOH/H_2O 5:1, v/v) (100:0 → 90:10, v/v) to provide the desired product **3** as a yellow-orange solid (19 mg, 60%). $C_{28}H_{22}N_4O_6$ (510.51). R_f = 0.3 (CH_2Cl_2/MeOH = 9:1); R_f = 0.6 ($CHCl_3$/MeOH/H_2O = 10:1:0.2). ^{1}H NMR (500 MHz, DMF-d^7): δ 9.99 (s, 1H), 8.47–8.37 (m, 2H), 8.22 (s, 1H), 8.17 (dd, *J* = 8.0, 1.5 Hz, 1H), 8.06 (s, 1H), 7.88 (ddd, *J* = 8.3, 6.6, 1.6 Hz, 1H), 7.87–7.82 (m, 3H), 7.53 (ddd, *J* = 8.0, 6.6, 1.4 Hz, 1H), 6.87 (s, 2H), 6.68 (dd, *J* = 8.2, 5.9 Hz, 1H), 5.43 (d, *J* = 3.9 Hz, 1H), 5.36 (t, *J* = 5.7 Hz, 1H), 4.66–4.49 (m, 1H), 4.02 (td, *J* = 3.9, 2.3 Hz, 1H), 3.79 (dt, *J* = 11.8, 4.5 Hz, 1H), 3.73 (ddd, *J* = 11.8, 6.2, 3.8 Hz, 1H), 2.69 (ddd, *J* = 13.5, 8.2, 5.7 Hz, 1H), 2.38 (ddd, *J* = 13.1, 6.0, 2.6 Hz, 1H). ^{13}C NMR (126 MHz, DMF-d^7): δ 174.4, 159.2, 156.2, 154.2, 151.0, 145.3, 134.9, 132.5, 132.3, 128.8, 128.6, 125.9, 125.7, 125.4, 122.6, 119.6, 103.7, 101.0, 96.1, 92.2, 89.5, 86.2, 85.4, 72.8, 63.7, 41.7. MS (ESI$^+$, MeOH) *m/z*: 510.9 $[M+H]^+$. HRMS (ESI$^+$): *m/z* calcd for $C_{28}H_{23}N_4O_6$: 511.1612 $[M+H]^+$; found 511.1623.

2.2.6. 7-Deaza-2′-deoxy-7-((5-(3-hydroxy-4-oxochromen-2-yl)furan-2-yl) ethynyl)adenosine (4 – FCA)

To a stirred solution of **12** (60 mg, 0.22 mmol) and **14** (122 mg, 1.2 eq.) in DMF (11 mL), previously degassed by sonication under argon, were sequentially added Et_3N (152 μL, 5 eq.), and a mixture of CuI (7 mol%, 3 mg)/$PdCl_2(PPh_3)_2$ (7 mol%, 11 mg). The reaction mixture was warmed to 60 °C under argon for 1 h. The resulting solution was diluted with CH_2Cl_2 (20 mL) and the volatiles were removed *in vacuo*. The residue was purified by flash chromatography on silica gel eluted with CH_2Cl_2/MeOH (98:2 → 85:15, v/v) to provide the coupled product as a yellow-orange solid (120 mg, 86%). R_f = 0.45 (CH_2Cl_2/MeOH = 9:1). MS (ESI$^+$, MeOH) *m/z*: 635.2 $[M+H]^+$. The latter was sufficiently pure to be used in the next step without further purification. To a stirred solution of this Cbz-protected intermediate (110 mg, 0.17 mmol) in DMF (1.5 mL), a saturated methanolic solution of NH_3 (ca. 9 M, 10 mL) was added. The reaction was stirred for 5 min at rt. The volatiles were removed *in vacuo* and the residue was purified by flash chromatography on silica gel eluted with CH_2Cl_2/MeOH (98:2 → 85:15, v/v) to provide the desired product **4** as an orange solid (30 mg, 35%).

$C_{26}H_{20}N_4O_7$ (500.47). R_f = 0.27 (CH_2Cl_2/MeOH = 9:1). ^{1}H NMR (400 MHz, DMF-d^7): δ 10.50 (s, 1H), 8.24 (s, 1H), 8.17 (dd, J = 7.9, 1.6 Hz, 1H), 8.14 (s, 1H), 7.86 (ddd, J = 8.6, 7.0, 1.7 Hz, 1H), 7.77 (dd, J = 8.6, 1.0 Hz, 1H), 7.53 (ddd, J = 8.0, 7.0, 1.1 Hz, 1H), 7.47 (d, J = 3.7 Hz, 1H), 7.24 (d, J = 3.7 Hz, 1H), 6.92 (s, 2H), 6.69 (dd, J = 8.1, 5.9 Hz, 1H), 5.44 (d, J = 3.9 Hz, 1H), 5.36 (dd, J = 6.2, 5.1 Hz, 1H), 4.58 (qd, J = 5.8, 2.7 Hz, 1H), 4.03 (td, J = 3.9, 2.4 Hz, 1H), 3.80 (ddd, J = 11.8, 5.1, 4.0 Hz, 1H), 3.74 (ddd, J = 11.8, 6.2, 3.9 Hz, 1H), 2.69 (ddd, J = 13.5, 8.1, 5.7 Hz, 1H), 2.40 (ddd, J = 13.1, 6.0, 2.7 Hz, 1H). ^{13}C NMR (101 MHz, DMF-d^7): δ 173.2, 159.1, 155.7, 154.3, 151.1, 146.5, 139.6, 139.5, 139.4, 134.9, 129.6, 126.0, 125.8, 123.3, 119.4, 119.4, 117.5, 103.6, 94.8, 90.7, 89.6, 85.5, 82.0, 72.8, 63.6, 41.8. HRMS (ESI$^+$): m/z calcd for $C_{26}H_{21}N_4O_7$: 501.1405 [M + H]$^+$; found 501.1408.

2.2.7. 7-Deaza-2′-deoxy-7-((5-(3-hydroxy-4-oxochromen-2-yl)thiophen-2-yl)ethynyl)adenosine (5 – TCA)

To a stirred solution of **12** (49 mg, 0.18 mmol) and chromone **15** (103 mg, 1.2 eq.) in DMF (4 mL), previously degassed by sonication under argon, were sequentially added Et_3N (125 μL, 5 eq.), and a mixture of CuI (7 mol%, 2 mg)/$PdCl_2(PPh_3)_2$ (7 mol%, 9 mg). The reaction mixture was warmed to 60 °C under argon for 1 h. The resulting solution was diluted with CH_2Cl_2 (10 mL) and the volatiles were removed *in vacuo*. The residue was purified by flash chromatography on silica gel eluted with CH_2Cl_2/MeOH (98:2 → 85:15, v/v) to provide the coupled product as a yellow-orange solid (78 mg, 67%). R_f = 0.5 ($CHCl_3$/MeOH = 85:15). MS (ESI$^+$, MeOH) m/z: 651.2 [M + H]$^+$. The latter was sufficiently pure to be used in the next step without further purification. To a stirred solution of this Cbz-protected intermediate (78 mg, 0.17 mmol) in pyridine (1 mL) a 10% aq. NH_4OH solution in MeOH (10 mL) was added. The reaction mixture was stirred for 5 min at rt and quenched with acetic acid until pH = 4. Additional H_2O (20 mL) was introduced to initiate the precipitation. The resulting mixture was stored overnight at 0–5 °C. The heterogeneous mixture was centrifuged to settle solid particles and the supernatant was carefully removed by a syringe with a fine needle. The solid was washed with a solution of MeOH/H_2O (7:3), and after centrifugation, the supernatant was removed by suction. This washing procedure was repeated twice more to provide the desired product **5** as an orange solid (15 mg, 24%). $C_{26}H_{20}N_4O_6S$ (516.53). R_f = 0.55 (acetone). ^{1}H NMR (500 MHz, DMF-d^7): δ 10.94 (s, 1H), 8.23 (s, 1H), 8.15 (dd, J = 8.0, 1.6 Hz, 1H), 8.08 (s, 1H), 7.98 (d, J = 4.0 Hz, 1H), 7.86 (ddd, J = 8.6, 7.0, 1.7 Hz, 1H), 7.79 (d, J = 8.2 Hz, 1H), 7.65 (d, J = 4.0 Hz, 1H), 7.52 (ddd, J = 8.0, 6.9, 1.1 Hz, 1H), 6.90 (s, 2H), 6.68 (dd, J = 8.1, 5.9 Hz, 1H), 4.61–4.54 (m, 1H), 4.02 (td, J = 3.9, 2.3 Hz, 1H), 3.79 (dt, J = 11.8, 4.3 Hz, 1H), 3.73 (ddd, J = 11.8, 5.8, 3.8 Hz, 1H), 2.68 (ddd, J = 13.5, 8.2, 5.7 Hz, 1H), 2.38 (ddd, J = 13.1, 6.0, 2.6 Hz, 1H). ^{13}C NMR (101 MHz, DMF-d^7): δ 172.6, 158.4, 155.1, 153.4, 150.4, 142.6, 134.1, 132.9, 128.4, 128.2, 127.0, 125.2, 124.9, 122.5, 118.5, 102.9, 95.0, 90.0, 88.8, 84.7, 84.4, 72.1, 62.9, 41.0. HRMS (ESI$^+$): m/z calcd for $C_{26}H_{21}N_4O_6S$: 517.1176 [M + H]$^+$; found 517.1178.

2.2.8. 7-Deaza-2′-deoxy-7-((5-(3-hydroxy-4-oxochromen-2-yl)thiophen-3-yl)ethynyl)adenosine (6 – angTCA)

To a stirred solution of **12** (59 mg, 0.215 mmol) and **16** (124 mg, 1.2 eq.) in DMF (11 mL), previously degassed by sonication under argon, were sequentially added Et_3N (150 μL, 5 eq.), and a mixture of CuI (7 mol%, 3 mg)/$PdCl_2(PPh_3)_2$ (7 mol%, 11 mg). The reaction mixture was warmed to 60 °C under argon for 1 h. The resulting solution was diluted with CH_2Cl_2 (10 mL) and the volatiles were removed *in vacuo*. The residue was purified by flash chromatography on silica gel eluted with CH_2Cl_2/MeOH (98:2 → 85:15, v/v) to provide the coupled product as a yellow solid (120 mg, 86%). R_f = 0.4 (CH_2Cl_2/MeOH = 9:1). MS (ESI$^+$, MeOH) m/z: 651.2 [M + H]$^+$. The latter was considered pure enough, and batched for the next step. To a stirred solution of this Cbz-protected intermediate (60 mg, 0.092 mmol) in CH_2Cl_2/MeOH (5:5 mL), a NH_3 saturated methanolic solution (ca. 9 M, 10 mL) was added. After 5 min, cold water (10 mL) and then aq. NaOH (20% w/w, 1 mL) were added to the reaction mixture. The mixture was reduced *in vacuo* by 2/3 of its volume and acidified with aq HCl 2 M to pH = 5. The resulting mixture was stored overnight in the fridge at 0–4 °C and filtered. The solid was sequentially washed with H_2O (3 × 10 mL), petroleum ether (3 × 10 mL), and MeOH (1 × 10 mL) to provide the desired product **6** as a brown-yellow solid (30 mg, 63%). $C_{26}H_{20}N_4O_6S$ (516.53). R_f = 0.28 (CH_2Cl_2/MeOH = 9:1). ^{1}H NMR (400 MHz, DMF-d^7): δ 10.82 (s, 1H), 8.52 (s, 1H), 8.38 (s, 1H), 8.32 (d, J = 1.4 Hz, 1H), 8.23 (s, 1H), 8.19–8.13 (m, 2H), 7.87 (ddd, J = 8.6, 6.9, 1.7 Hz, 1H), 7.84–7.79 (m, 1H), 7.53 (ddd, J = 8.1, 6.8, 1.3 Hz, 1H), 6.71 (dd, J = 7.6, 6.0 Hz, 1H), 4.61 (td, J = 5.8, 2.9 Hz, 1H), 4.05 (q, J = 3.6 Hz, 1H), 3.81 (dd, J = 11.8, 4.0 Hz, 1H), 3.76 (dd, J = 11.9, 3.9 Hz, 1H), 2.67 (ddd, J = 13.3, 7.7, 5.7 Hz, 1H), 2.46 (ddd, J = 13.2, 6.1, 3.0 Hz, 1H). ^{13}C NMR (101 MHz, DMF-d^7): δ 172.7, 155.1, 154.7, 148.4, 142.5, 138.2, 134.3, 134.1, 133.4, 130.5, 129.1, 125.2, 125.0, 122.5, 122.5, 118.6, 102.2, 97.2, 88.9, 87.5, 84.6, 81.4, 79.5, 71.8, 62.6, 41.2. MS (ESI$^+$, MeOH) m/z: 516.9 [M + H]$^+$. HRMS (ESI$^+$): m/z calcd for $C_{26}H_{21}N_4O_6S$: 517.1176 [M + H]$^+$; found 517.1190.

2.2.9. 2-(4-Bromothiophen-2-yl)-3-hydroxychromen-4-one (19)

To a stirred solution of **17** (883 μL, 7.345 mmol) and **18** (1.403 g, 7.345 mmol) in ethanol (15 mL), a 5 M NaOH solution (4.9 mL) was added dropwise. The reaction mixture was stirred 48 h at rt, before a dropwise addition of 30% aq. hydrogen peroxide solution (2.1 mL). The resulting mixture was stirred for 30 min at rt, poured into cold water (75 mL) and then acidified with 2 M HCl to pH = 5. The resulting precipitate was filtered and thoroughly washed with water and cyclohexane to provide the desired product **19** as a yellow solid (500 mg, 21%). $C_{13}H_7BrO_3S$ (323.16). R_f = 0.45 (toluene/EtOAc = 4:1). ^{1}H NMR (400 MHz, DMSO-d_6): δ 10.63 (s, 1H), 8.10 (dd, J = 8.0, 1.6 Hz, 1H), 8.00 (d, J = 1.6 Hz, 1H), 7.90 (d, J = 1.5 Hz, 1H), 7.81 (ddd, J = 8.5, 6.8, 1.7 Hz, 1H), 7.78–7.73 (m, 1H), 7.47 (ddd, J = 8.1, 6.8, 1.3 Hz, 1H). ^{13}C NMR (101 MHz, DMSO-d_6): δ 172.2, 154.2, 141.6, 137.5, 133.9, 133.9, 129.4, 128.2, 124.8, 124.7, 121.8, 118.2, 109.8. HRMS (ESI$^+$): m/z calcd for $C_{13}H_8BrO_3S$: 322.9372, 324.9352 [M + H]+; found 322.9375, 324.9351.

2.2.10. 2-(4-Bromothiophen-2-yl)-3-(((benzyloxy)carbonyl)oxy)chromen-4-one (16)

To a stirred suspension of **19** (483 mg, 1.495 mmol) in CH_2Cl_2 (25 mL), 25% aq. KOH solution (5 mL), 18-crown-6 (7 mol%, 28 mg) and benzyl chloroformate (674 μL, 4.484 mmol, 3 eq.) were added. The reaction mixture became homogenous after 2 h and was stirred overnight at rt. After quenching by addition of H_2O (40 mL), the organic layer was extracted with CH_2Cl_2 (3 × 30 mL), dried over $MgSO_4$, filtered and the volatiles were removed *in vacuo*. The residue was purified by flash chromatography on silica gel eluted with petroleum ether/EtOAc mixture (100:0 → 60:40, v/v) to provide the desired compound **16** as a light yellow solid (580 mg, 85%). $C_{21}H_{13}BrO_5S$ (457.29). R_f = 0.4 (PE/AcOEt = 4:1). ^{1}H NMR (400 MHz, CD_2Cl_2): δ 8.19 (dd, J = 8.0, 1.7 Hz, 1H), 7.84 (d, J = 1.5 Hz, 1H), 7.75 (ddd, J = 8.7, 7.1, 1.7 Hz, 1H), 7.63–7.53 (m, 2H), 7.51–7.34 (m, 6H), 5.35 (s, 2H). ^{13}C NMR (101 MHz, CD_2Cl_2): δ 171.7, 155.6, 152.2, 150.5, 135.2, 134.9, 133.3, 132.6, 129.7, 129.3, 129.2, 128.8, 126.2, 126.0, 124.1, 118.6, 111.9, 71.9. MS (ESI$^+$, MeOH) m/z: 457.0, 459.0 [M + H]$^+$. HRMS (ESI$^+$): m/z calcd for $C_{21}H_{14}BrO_5S$: 456.9740, 458.9719 [M + H]$^+$; found 456.9759, 458.9712.

3. Results and discussion

3.1. Preparation of the 3HC-based dA analogs

Like C5 of uracil, modifications at position 7 of adenine accommodate well into the hydrated major groove and minimally disturb base pairing and DNA structure. For that purpose, 7-deazaadenine is commonly used to attach of various reporting groups into DNA, including fluorescent ones [30,31,38,39]. Therefore, this scaffold was chosen to couple the 3HC fluorophore via an acetylenic moiety. A rigid and short linker was preferred in order to locate the dye in a precise position within the DNA major groove and to allow electronic communication between the nucleobase and the fluorophore. The targeted dA analogs, **3–6**, were synthesized according a convergent approach, involving a Sonogashira coupling between the 3HC fluorescent dye and 7-deaza-7-ethynyl-dA **12** as a key step (Scheme 2). The synthesis of intermediate **12** was directly inspired by Seela's previous work [37].

Nevertheless, we faced two critical challenges. First, for a reliable and scalable implementation, glycosylation of Hoffer's sugar **8** with 6-chloro-7-deaza-7-iodopurine must be conducted in diluted medium ([C] ≈ 0.05 M). The poor solubility of the nucleobase in acetonitrile makes the preparation of the anionic deazaadenyl moiety a limiting step. By taking this factor into account, the S_N2 type reaction provided the glycosylated product **9** in satisfying yields, and this key step was found to be scalable with reproducibility to the 1 g scale.

A second step for which we propose another solution concerns the amination of **9**. This S_NAr was performed initially under high-pressure in a stainless steel bomb. This approach also produced the unprotected nucleosides, which requires back protection of the free alcohols or working along the entire synthetic sequence with poorly soluble and polar compounds making the flash chromatography purifications more complex and low-yielding (*vide infra*). Microwave-assisted S_NAr amination has been used as an alternative to S_NAr amination [40]. The difficulty was to find suitable conditions, that offered the benefit of keeping *p*-toluoyl groups on the 3′ and 5′-positions. We tried different conditions using microwave irradiation to meet this goal. To our delight, by screening the reaction time and temperature, but mostly by

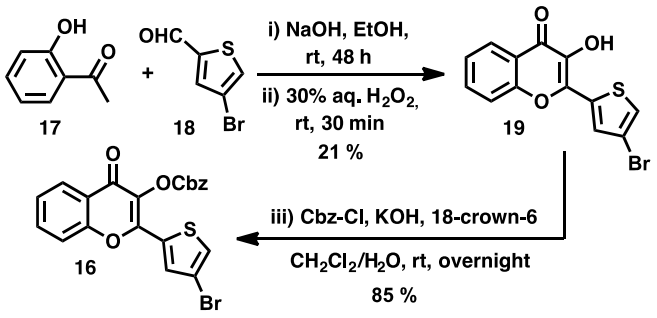

Scheme 3. Representative synthetic preparation of the Cbz-protected 3HC coupling partner **16**.

Table 1
Spectroscopic comparison in MeOH of parent 2-aryl-3HCs (**PC**, **FC** and **TC**) and their corresponding dA conjugates (**PCA**, **FCA**, **TCA**, **angTCA**, and **revTCA**).[a]

	ε_{max}[b]	λ_{Abs}[c]	λ_{N^*}[d]	$\Delta\lambda_{N^*}$[f]	λ_{T^*}[e]	I_{N^*}/I_{T^*}[g]
PC	18	343	401	–	532	0.24
PCA	30	364	464	63	551	0.31
FC	22	356	418	–	532	0.86
FCA	33	383	484	66	561	0.69
TC	21	359	423	–	542	0.41
TCA	31	392	492	69	569	0.48
angTCA	18	361	425	2	543	0.05
revTCA	21	356	429	6	551	0.16

[a] Reported values are the average of two or more independent and reproducible measurements, ± 1 nm for wavelengths. Excitation wavelength was at the corresponding absorption maximum.
[b] Molar absorptivity in $10^3\ M^{-1}\ cm^{-1}$.
[c] Position of the absorption maximum in nm.
[d,e] Positions of the normal N* and T* band maxima in nm, respectively.
[f] Difference of emission N* maxima between the conjugate and the parent 3HC in nm.
[g] Ratio intensity of the two emission maxima.

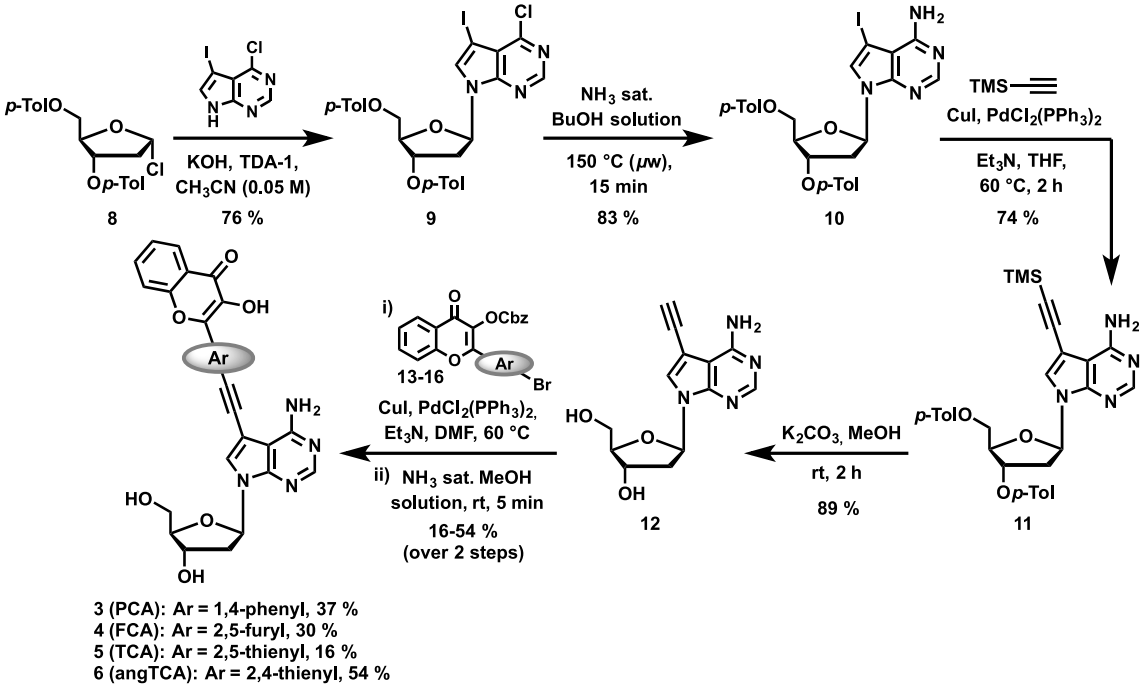

Scheme 2. Synthesis of the rationally designed dA analogs **3–6**, bearing a 3HC moiety as a fluorescent surrogate.

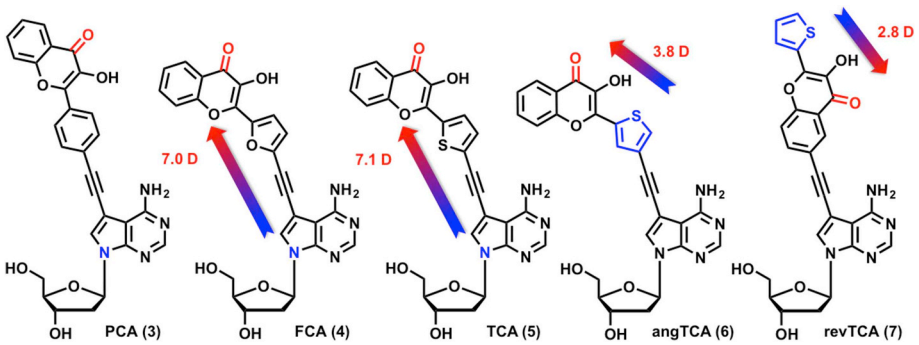

Fig. 2. Dual-emissive dA analogs investigated in this study. *Donor and acceptor groups are depicted in blue and red, respectively. Gradient colored arrows represent the D-π-A push–pull system. The differences in the dipole moments of excited and ground states – given in Debye (D) – were obtained according to the Lippert–Mataga model (Part S2). The length of the arrow reflects the magnitude of the difference.* (For interpretation of the references to color in this figure legend, the reader is referred to the Web version of this article.)

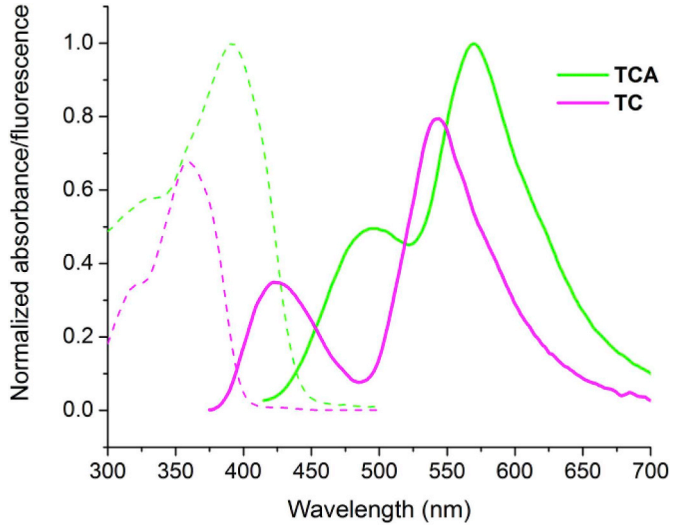

Fig. 3. Absorption (*dashed lines*) and fluorescence (*solid*) emission spectra of **TC** (magenta), and **TCA** (green) in MeOH. *Excitation wavelength corresponds to the absorbance maximum of each compound. Absorptions and emissions are proportional to their absorptivity and quantum yield, respectively.* (For interpretation of the references to color in this figure legend, the reader is referred to the Web version of this article.)

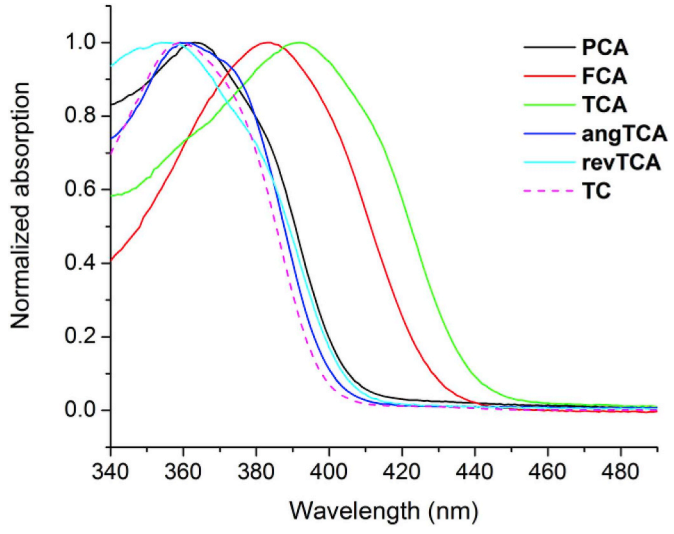

Fig. 4. Normalized absorption spectra in MeOH of the five 3HC-based dA analogs (*solid lines*) and the parent chromone **TC** (*dashed*).

making use of *n*-BuOH as a solvent, we achieved complete chemoselectivity of S_NAr over the concomitant ester aminolysis affording **10** with good yields (83%)[‡]. Introduction of the short and rigid alkynyl linker was achieved in two steps through a conventional Sonogashira coupling in the presence of TMS-acetylene followed by a methanolysis leading to **12** with satisfactory yields. This ethynyl derivative **12** constitutes the essential building block for the final assembly of the targeted two-colors dA analogs **3–6**.

In parallel, the protected 3HC-coupling partner was prepared by a one-pot, two-step procedure, involving a Claisen-Schmidt condensation of *o*-hydroxyacetophenone on a (hetero)aromatic aldehyde through an alkaline treatment followed by an Algar-Flynn-Oyamada reaction. This oxidative cyclization concomitantly occurs by addition of hydrogen peroxide to the basic media [41]. The reactive 3-OH was then masked by the Cbz group following a known procedure [42]. Compounds **13–15** were synthesized as previously reported [13,28]. Representative synthetic access was depicted in Scheme 3 for the 2-(4-bromothienyl)-3HC derivative **16** required to obtain **angTCA 6**. With the 2 coupling partners in hand, their electronic conjugation was efficiently carried out using classical Sonogashira reaction conditions. Carbonate aminolysis was conducted under methanolic ammonia treatment to provide **PCA**, **FCA**, **TCA**, and **angTCA 3–6**. Although removal of the protecting group proceeded cleanly, the poor solubility of final naked nucleosides made their purification difficult.

As for **revTCA 7**, the reversed orientation of the dipole moment necessitates an adaptation of the retrosynthetic access. In this approach, the ethynyl connector was first introduced to the 3HC before the assembly with the 7-deaza-7-iodo adenylate derivative **10**. The corresponding synthesis is described in SI (Scheme S1&S2). Methanolysis yielded **revTCA 7**, the last dA analog of this study with an inverted D-π-A design (D = thienyl, A = carbonyl group).

3.2. Photophysical characterization

3.2.1. Comparison with parent 3HCs

Absorption and emission properties of **TCA**, **FCA**, **PCA**, **angTCA** and **revTCA**, were first characterized in MeOH. To evaluate the impact on the photophysics of the aromatic linker conjugating 7-ethynyl-dA with 3HC, these data were compared to those of the parent 2-phenyl-, 2-furyl-, and 2-thienyl-3HCs, respectively **PC**, **FC,** and **TC** from which they originate (Table 1).

All conjugates exhibited a dual emission in MeOH, with the short and long wavelength bands that can be assigned to the N* and T* states, but with different features. Compared to their parent compounds, **PCA**, **FCA** and **TCA**, but not **angTCA** and **revTCA**, displayed significant red-shifted absorption and emission maxima that resulted in substantial improvements of their spectroscopic properties. Thus, the five compounds can be classified into two sets of dyes.

[‡] The only limitation to the scale-up of this reaction is the reception capacity of the heating area in the microwave apparatus with a fixed concentration.

Table 2
Photophysical properties of **FCA**, **TCA**, **angTCA** and **revTCA** in different solvents.[a]

Solvent		ε_{max} (10^3 M^{-1} cm^{-1})[b]		33	31	18	21	21
	$E_T^N(30)$[c]	$\Sigma\beta_2^H$[d]	λ (nm),[e] Φ (%)[f]	**FCA**	**TCA**	**angTCA**	**revTCA**	**TC**
MeOH	0.76	0.47	λ_{Abs}	383	392	361	356	359
			λ_{N^*}	484	492	425	429	423
			λ_{T^*}	561	569	543	551	542
			I_{N^*}/I_{T^*}	0.69	0.48	0.05	0.16	0.41
			Φ	4	5	0.5	2	4
EtOH	0.65	0.48	λ_{Abs}	384	393	360	356	360
			λ_{N^*}	479	487	421	425	420
			λ_{T^*}	566	574	547	555	545
			I_{N^*}/I_{T^*}	0.31	0.22	0.04	0.09	0.18
			Φ	12	11	1	3	6
i-PrOH	0.57	0.48	λ_{Abs}	387	394	362	358	361
			λ_{N^*}	478	483	418	422	417
			λ_{T^*}	566	575	547	554	544
			I_{N^*}/I_{T^*}	0.20	0.15	0.03	0.07	0.11
			Φ	23	22	4	4	7
CH_3CN	0.46	0.32	λ_{Abs}	381	389	355	353	354
			λ_{N^*}	459	465	421	419	409
			λ_{T^*}	570	576	544	549	543
			I_{N^*}/I_{T^*}	0.13	0.18	0.01	0.04	0.03
			Φ	18	16	1	1	7
DMSO	0.44	0.88	λ_{Abs}	391	400	364	359	361
			λ_{N^*}	478	482	428	432	422
			λ_{T^*}	579	587	552	557	549
			I_{N^*}/I_{T^*}	0.65	0.55	0.09	0.06	0.05
			Φ	21	19	0.5	2	8
Acetone	0.35	0.49	λ_{Abs}	382	390	356	354	354
			λ_{N^*}	456	463	418	416	408
			λ_{T^*}	572	582	548	555	547
			I_{N^*}/I_{T^*}	0.11	0.19	0.02	0.08	0.04
			Φ	18	24	3	2	7
EtOAc	0.23	0.45	λ_{Abs}	382	392	356	354	354
			λ_{N^*}	447	460	412	413	406
			λ_{T^*}	571	582	547	553	545
			I_{N^*}/I_{T^*}	0.07	0.14	0.02	0.03	0.02
			Φ	22	25	20	10	13
THF	0.21	0.48	λ_{Abs}	385	394	359	356	356
			λ_{N^*}	447	459	411	411	406
			λ_{T^*}	575	586	550	556	549
			I_{N^*}/I_{T^*}	0.10	0.21	0.03	0.07	0.06
			Φ	28	32	24	14	18
Dioxane	0.16	0.64	λ_{Abs}	385	394	359	356	356
			λ_{N^*}	443	455	409	410	405
			λ_{T^*}	572	583	548	556	547
			I_{N^*}/I_{T^*}	0.15	0.37	0.04	0.06	0.04
			Φ	25	26	25	19	18
Toluene	0.10	0.14	λ_{Abs}	387	396	362	358	357
			λ_{N^*}	443	455	408	410	406
			λ_{T^*}	577	589	551	558	548
			I_{N^*}/I_{T^*}	0.04	0.1	0.02	0.02	0.01
			Φ	33	27	39	31	33

[a] *Similar* to Table 1.
[b] *Molar* extinction coefficient was determined in methanol; relative standard deviations are lower or equal to 5%.
[c] *Reichardt's* empirical solvent polarity index [44].
[d] H-bond basicity [45].
[e] *Position* of the absorption maximum in nm; maximum of the normal N* emission band in nm; maximum of the tautomer T* emission in nm; ratio of the intensities at the two emission maxima.
[f] Fluorescence quantum yields Φ were determined using an excitation at the corresponding absorption maximum of each compound in the considered solvent. Quinine sulfate in 0.5 M H_2SO_4 solution (λ_{Ex} = 350 nm, Φ = 55%) [51] and *p*-DiMethylAminoFlavone (DMAF) in EtOH (λ_{Ex} = 404 nm, Φ = 27%) [52] were used as standard references, ± 10% mean standard deviation.

Upon conjugation of 7-ethynyl-dA with **PC**, **FC**, and **TC**, the resulting two-color nucleosides **PCA**, **FCA**, and **TCA** displayed: *i)* a 1.5-fold increase of their molar absorptivity, *ii)* a 20–35 nm bathochromic shift of their absorption and tautomer T* maxima, as well as *iii)* a significant redshift of their N* maxima (60–70 nm). Fig. 3 shows **TCA** *vs.* **TC** as a representative example. The shift of absorption and emission maxima to longer wavelengths follows the same sequence as for the parent dyes: **PCA** < **FCA** < **TCA** (Fig. 4). These observations are in line with previous studies and can be attributed to the fact that the 2-furyl- and 2-thienyl rings allow a more planar conformation for conjugation in comparison to the 2-phenyl ring [43]. Thus, the conjugation of furyl- and thienyl-3HC with 7-deazaadenine resulted in the strongest improvement of their spectroscopic properties. By contrast, **angTCA** and **revTCA** exhibited absorption and emission properties comparable to that of the parent **TC** dye (Fig. 4). The increased absorptivity and the bathochromic shifts of absorption and emission are observed when dA

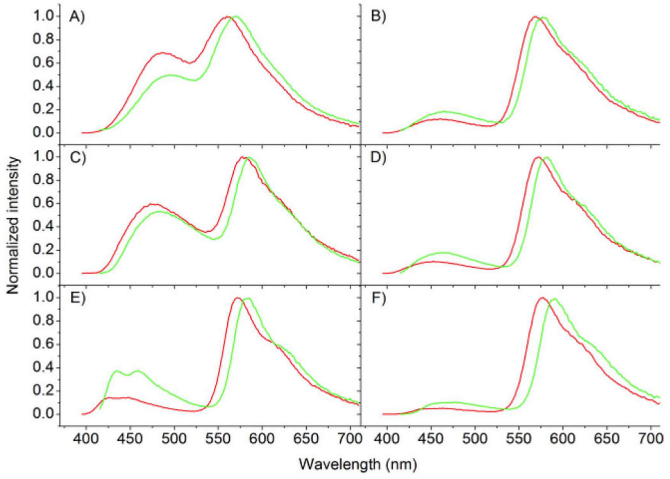

Fig. 5. Fluorescence spectra of **FCA** (red) and **TCA** (green) in different organic solvents: A) MeOH, B) acetonitrile, C) DMSO, D) acetone, E) dioxane, and F) toluene. (For interpretation of the references to color in this figure legend, the reader is referred to the Web version of this article.)

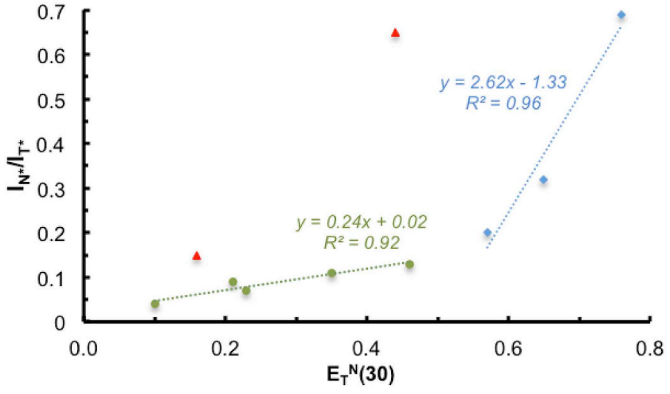

Fig. 6. Intensity ratio I_{N^*}/I_{T^*} of **FCA** as a function of the normalized Reichardt's parameter $E_T^N(30)$. *The green circles and blue diamonds represent aprotic (toluene, dioxane, THF, EtOAc, acetone, CH_3CN) and protic (MeOH, EtOH, i-PrOH) solvents, respectively. The green and blue dashed lines represent the corresponding linear fitting curves. The red triangles represent the results of DMSO and dioxane.* (For interpretation of the references to color in this figure legend, the reader is referred to the Web version of this article.)

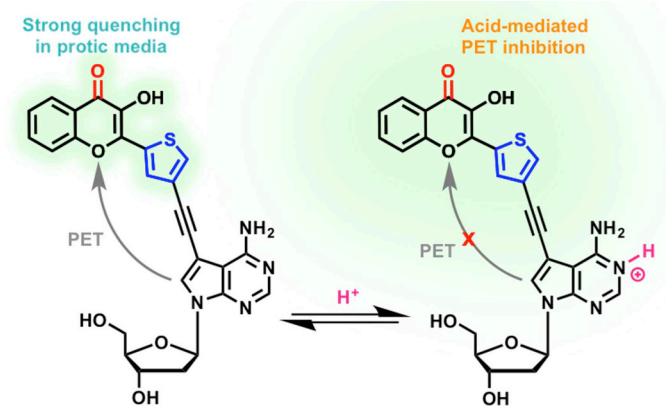

Fig. 7. Schematic representation of the proposed acid-mediated PET inhibition.

and chromone are coupled using the 1,4-phenyl (**PCA**), 2,5-furyl (**FCA**) and 2,5-thienyl (**TCA**) central connectors. These aromatic linkers, but not the 2,4- and reverse thienyl-3HC, allow mesomeric coupling between the electron-donating enamino nitrogen *N9* of 7-deazaadenine and the electron-withdrawing carbonyl of 3HC. The photophysics observed for these connectors support the hypothesis of an established push–pull relationship between the nucleobase and the original fluorophore. All these observations are consistent with those reported previously for the uracil series [13].

3.3. Comparison between *FCA* and *TCA*

The most prospective **FCA** and **TCA** dyes were subsequently studied in a set of solvents with a wide range of polarities to provide further insight into their photophysical properties. Three protic (MeOH, EtOH and *i*-PrOH) and seven aprotic solvents (CH_3CN, DMSO, Acetone, EtOAc, THF, Dioxane and Toluene) were investigated. The solvent polarity was ranked using the Dimroth-Reichardt $E_T^N(30)$ scale [44]. This empirical scale takes into account the dielectric constant and H-bond donating ability of the solvent. It is normalized from TMS (0) to water (1). The empirical Abraham $\Sigma\beta_2^H$ parameter was selected to rank the H-bonding basicity of the solvent (Table 2) [45].

FCA and **TCA** showed a single band absorption centered at 381–391 and 389–400 nm, respectively (Fig. S2). The absorption spectra of these dyes are almost independent of solvent polarity demonstrating little solvatochromism. By contrast, the dyes showed dual emissions in all tested solvents with strong sensitivity to the polarity changes (Figs. 5 and S3). Superimposition of the absorption curves with the excitation spectra from N* and T* bands confirmed that dual-emissive signature originates from an ESIPT process (Fig. S4).

From toluene to methanol, the N* bands of **FCA** and **TCA** shifted to the red by 41 and 37 nm, respectively (Fig. S5); while for the parent **TC**, the shift was halved (18 nm, Fig. S6). The positive solvatochromism of the N* is typical of dyes with ICT character [46]. To estimate their ICT ability, the polarity scale of Lippert-Mataga was used (Table S1, Figs. S9 and S10) [47]. Plotting the Stokes shifts for aprotic solvents as a function of the orientation polarizability showed linear fits with positive slopes for the compounds (Fig. S10). Extracting the slopes allowed us to calculate the difference in dipole moments between the excited and ground states for **FCA** and **TCA** (7.0 and 7.1 D, respectively). A 3-fold increase of the dipole moment difference was observed when **TCA** was compared with **TC** (7 *vs.* 2.3 D, respectively). These results are consistent with a larger increase of dipole moments of the normal excited states for **FCA** and **TCA** after light absorption, further supporting a push–pull D-π-A connectivity between the nucleobase and the 3HC moiety (blue to red atoms, Fig. 2).

The positions of T* band maxima of **FCA** and **TCA** were shifted to the blue in protic solvents, as compared with aprotic ones, likely as a consequence of the formation of a H bond between the chromone phenoxide in the excited tautomer and the alcohols, as was proposed for **FC** [48]. The Stokes shifts for the first and second emission bands of **FCA** and **TCA** are comprised between 56–101 and 177–193 nm, respectively. The large Stokes shifts obtained for the lowest energy emission bands are typical of ESIPT dyes. As a general trend, the I_{N^*}/I_{T^*} ratio increased along with solvent polarity (Figs. 5 and S3). The highest I_{N^*}/I_{T^*} ratios were observed for both strongly polar methanol (protic) and DMSO (aprotic), whereas the lowest values were noted for the most apolar toluene (Table 2). It is noteworthy that H-bonding dominates the polarity effect as evidenced by analyzing the plots of I_{N^*}/I_{T^*} ratio *vs.* $E_T^N(30)$. For instance, Fig. 6 illustrates the linear fits obtained for **FCA** in aprotic and protic solvents (for **TCA**, Fig. S7). For protic solvents, the slopes were steeper, highlighting superior sensitivity of the dyes to the probe's protogenic medium. These results also indicate specific interactions between the solvent and the dye. These properties are classical features of 3HC probes [49,50].

Specific interactions were also noticed for **FCA** and **TCA** in DMSO, and to a lower extent in dioxane, as those solvents showed upward deviations from the linear fits of aprotic solvents (Figs. 6 and S7). These deviations were evidenced only for the two most basic aprotic solvents (Table 2, $\Sigma\beta_2^H$ = 0.88 and 0.68), with the most basic DMSO displaying

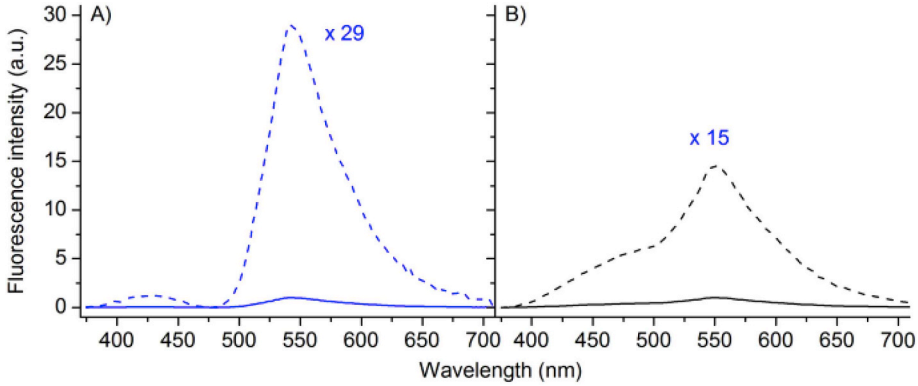

Fig. 8. Turn-on emission in MeOH upon TFA addition for A) **angTCA** (*blue*) B) **PCA** (*black*) as representative examples of the acid-mediated PET inhibition. (For interpretation of the references to color in this figure legend, the reader is referred to the Web version of this article.)

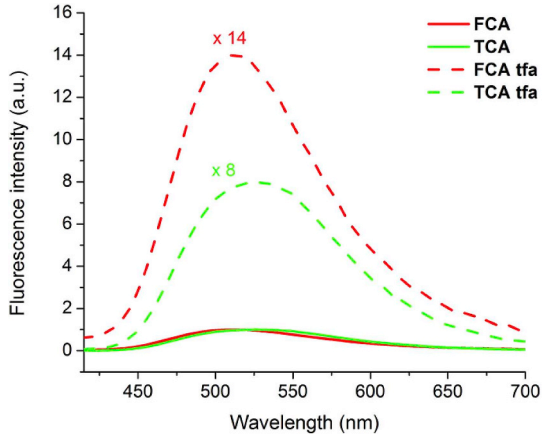

Fig. 9. Fluorescence turn-on in water upon TFA addition for **FCA** (red) and **TCA** (green). (For interpretation of the references to color in this figure legend, the reader is referred to the Web version of this article.)

the most pronounced effect. These deviations indicate that basic solvents frustrate the ESIPT reaction in **FCA** and **TCA**, likely by disrupting the intramolecular H-bonding. There are precedents in the literature of 3HCs, where the basicity of the solvent has an important influence on the variation of the intensity ratio [53,54]. Similar behavior was also observed for 3-hydroxyquinolones [55,56].

Thus, the superior absorptivity of **FCA** and **TCA** (1.5 fold, Table 1) together with their solvatochromic properties compares them favorably with the parent **FC** and **TC** dyes.

Since both **FCA** and **TCA** have similar molar absorptivity (~30,000, Table 1) comparing the quantum yields will directly give information on the brightness of the dual emitters. From a general point of view, QYs were rather good in all tested solvents except MeOH and EtOH, oscillating between 16 and 33%. In EtOH and MeOH, the quantum yields drop to 11–12 and 4–5%, respectively. This behavior is common in strong polar solvents like MeOH for dyes exhibiting a significant ICT character. Considering the strong donating ability of the *N*9 enamine, angular and reversed assemblies were thus considered (**angTCA** and **revTCA**), to reduce quenching in a polar protogenic medium by weakening the excited-state dipole moment (Fig. 2).

3.3.1. *Breaking the N9 conjugation:* ***angTCA*** *and* ***revTCA***

In all solvents, the absorption maxima of **angTCA** and **revTCA** were centered around 360 nm as for **TC** (Table 2 & Figs. 4 and S2). Both dyes also displayed similar absorptivity close to that of **TC** (Table 1). The absorption properties of **angTCA** and **revTCA** are consistent with an electronic disconnection between 7-ethynyl-dA and **TC**.

Concerning the fluorescence features, the two emission maxima appeared close to those of the parent chromone **TC**. Depending on the solvent polarity, N* and T* fluctuated between 408–432 and 543–558 nm, respectively (Fig. S6). The weak solvatochromism on the N* emission band demonstrated the attenuated push–pull relationship relating the thienyl and the carbonyl in line with the low dipole moment differences calculated for **angTCA** and **revTCA** as for **TC** (compare 3.8 and 2.8 D with 2.3 D, Table S1 & Fig. 2).

3.3.2. *Behavior in a protogenic environment and PET*

The main differences in photophysics that can be raised between both **angTCA** and **revTCA** conjugates and **TC** are the sensitivity for ratiometric sensing of the protic environment and the brightness in polar media. Indeed, **TC** is known to be one of the most sensitive 2-aryl-3HCs to probe H-bond donating solvents [13]. For instance, comparing the intensity ratios along the increasing proticity (*i*-PrOH, EtOH and MeOH) **angTCA** revealed to be almost insensitive (0.03 → 0.04 → 0.05), whereas **revTCA** showed a moderate increment of its N* emission band (0.07 → 0.09 → 0.16), in comparison to the parent **TC** (0.11 → 0.18 → 0.41). Moreover, both conjugates demonstrated more pronounced quenching than **TC** with the growing proticity of solvents. One plausible explanation to account for these observations in protic medium is a Photoinduced Electron Transfer (PET) from the 7-deazaadenine moiety to the 3HC [57].

PET is the photoquenching process by which an excited electron is transferred from a donor to an acceptor. This excited-state redox reaction is one form of photoquenching [47]. During our previous work on ODN labeling, fluorescence quenching of 3HC by flanking or opposite G was regularly observed. Among the 4 nucleobases, G is known to be the most reductive one because it has the lowest redox potential [58,59]. 7-deazaadenine possesses a similar feature [60]. Hence, in a polar protogenic solvent, the PET process is highly favored, likely through a proton-coupled process [61–64]. To prove this phenomenon, the idea was to protonate the nucleobase (Fig. 7), which should raise the redox potential of the 7-deazaadenine moiety and inhibit the coupled proton and electron transfer. To test this hypothesis, TFA (1‰, v/v) was added to a methanolic solution of each dye while monitoring the fluorescence emission.

As depicted on Fig. 8, addition of TFA supports this interpretation. The dual emission of each dye was turned on, reaching a 2- and 29-fold increase of the fluorescence intensity for **revTCA** and **angTCA**, respectively (Figs. 8 and S8). Similar treatment of **TC** showed no difference. Interestingly, when **PCA**, **FCA**, and **TCA** were treated in MeOH by adding TFA, the emission intensity was multiplied from 5 to 15 (Figs. 8 and S8). These results suggest that PET is a plausible quenching mechanism for all the new conjugates.

Since **TCA** and **FCA** aim to be incorporated in DNA, similar experiments were conducted in water. Addition of TFA resulted in an

impressive fluorescence turn-on leading to 8- and 14-fold enhancements of the signal respectively (Fig. 9).

These observations open up new prospects to utilize this acid-mediated PET inhibition for sensing the folding of adenine (A)-rich DNA sequences. The A-motif, also called poly(A) exhibits a unique secondary structure at acidic pH based on a right-handed helical duplex with parallel-mannered chains and tilted protonated A^+ bases [65].

4. Conclusion

To summarize, 5 dual-emissive dA nucleoside analogs incorporating 7-deazaadenine as a base and a 2-aryl-3HC as an initial fluorophore, were rationally designed and synthesized by a convergent and scalable approach. Their photophysics were investigated in solvents of various polarities to determine their ability to detect subtle environmental changes. During these spectroscopic investigations, a PET process appears to have occurred between the electron-rich nucleobase and the two-color dye, resulting in a strongly quenched fluorescence signal in a protogenic medium. Protonation of the nucleobase was found to resuscitate a well-resolved dual emission through a dramatic turn-on mechanism. The fully conjugated **FCA** and **TCA** were revealed to be the most promising emitters in terms of photophysical features including: *i)* a visible absorption allowing a violet excitation, *ii)* a two-channel fluorescence signature with strong N* positive solvatochromism and significant T* hypsochromic shift, *iii)* a ratiometric response that is highly sensitive to H-bonding and solvent basicity, and *iv)* a brightness exacerbated at lower pH. Hence, both multiparametric dyes present appealing characteristics for the sensing of acid-mediated A-motif folding. This is the current focus of our ongoing research and will be reported in due time.

Acknowledgments

We thank for the PhD grants of H.-N.L and G.B., the Agence Nationale de la Recherche (UCAJEDI project: ANR-15-IDEX-01) and the French Government, respectively; and for the postdoctoral fellowship of C.Z, the Région PACA (DNAfix-2014-07199). This research was financially supported by the Agence Nationale de la Recherche (ANR-12-BS08-0003-02) and the Région PACA (DNAfix-2014-02862).

Appendix A. Supplementary data

Supplementary data to this article can be found online at https://doi.org/10.1016/j.dyepig.2019.107553.

References

[1] Herdewijn P, editor. Modified nucleosides: in biochemistry, biotechnology and medicine. Weinheim, Germany: Wiley-VCH; 2008. p. 1–658.
[2] Nakatani K, Tor Y, editors. vol. 31. Cham, Switzerland: Springer International Publishing AG; 2016. p. 1–276. Modified nucleic acids, nucleic acids and molecular biology series.
[3] Wilhelmsson LM, Tor Y, editors. Fluorescent analogues of biomolecular building blocks: design and applications. Hoboken, NJ: John Wiley & Sons Inc.; 2016. p. 1–448.
[4] Xu W, Chan KM, Kool ET. Fluorescent nucleobases as tools for studying DNA and RNA. Nat Chem 2017;9:1043–55. https://doi.org/10.1038/NCHEM.2859.
[5] Daniels M, Hauswirth W. Fluorescence of the purine and pyrimidine bases of the nucleic acids in neutral aqueous solution at 300 degrees K. Science 1971;171:675–7. https://doi.org/10.1126/Science.171.3972.675.
[6] Pecourt JML, Peon J, Kohler B. Ultrafast internal conversion of electronically excited RNA and DNA nucleosides in water. J Am Chem Soc 2000;122:9348–9. https://doi.org/10.1021/ja0021520.
[7] Nir E, Kleinermanns K, Grace L, de Vries MS. On the photochemistry of purine nucleobases. J Phys Chem A 2001;105:5106–10. https://doi.org/10.1021/jp0030645.
[8] Onidas D, Markovitsi D, Marguet S, Sharonov A, Gustavsson T. Fluorescence properties of DNA nucleosides and nucleotides: a refined steady-state and femtosecond investigation. J Phys Chem B 2002;106:11367–74. https://doi.org/10.1021/jp026063g.
[9] Sinkeldam RW, Greco NJ, Tor Y. Fluorescent analogs of biomolecular building blocks: design, properties, and applications. Chem Rev 2010;110:2579–619. https://doi.org/10.1021/cr900301e.
[10] Wilhelmsson LM. Fluorescent nucleic acid base analogues. Q Rev Biophys 2010;43:159–83. https://doi.org/10.1017/S0033583510000090.
[11] Demchenko AP. Optimization of fluorescence response in the design of molecular biosensors. Anal Biochem 2005;343:1–22. https://doi.org/10.1016/j.ab.2004.11.041.
[12] Demchenko AP. Introduction to fluorescence sensing. second ed. Heidelberg, Germany: Springer Netherlands; 2015. p. 1–794.
[13] Barthes NPF, Karpenko IA, Dziuba D, Spadafora M, Auffret J, Demchenko AP, et al. Development of environmentally sensitive fluorescent and dual emissive deoxyuridine analogues. RSC Adv 2015;5:33536–45. https://doi.org/10.1039/C5RA02709H.
[14] Zhao J, Ji S, Chen Y, Guo H, Yang P. Excited state intramolecular proton transfer (ESIPT): from principal photophysics to the development of new chromophores and applications in fluorescent molecular probes and luminescent materials. Phys Chem Chem Phys 2012;14:8803–17. https://doi.org/10.1039/C2CP23144A.
[15] Sedgwick AC, Wu L, Han H-H, Bull SD, He X-P, James TD, et al. Excited-state intramolecular proton-transfer (ESIPT) based fluorescence sensors and imaging agents. Chem Soc Rev 2018;46:7105–39. https://doi.org/10.1039/C8CS00185E.
[16] Jacquemin D, Khelladi M, De Nicola A, Ulrich G. Turning ESIPT-Based triazine fluorophores into dual emitters_ from theory to experiment. Dyes Pigments 2019;163:475–82. https://doi.org/10.1016/j.dyepig.2018.12.023.
[17] Serdiuk IE, Roshal AD. Exploring double proton transfer: a review on photochemical features of compounds with two proton-transfer sites. Dyes Pigments 2017;138:223–44. https://doi.org/10.1016/j.dyepig.2016.11.028.
[18] Demchenko AP, Klymchenko AS, Pivovarenko VG, Ercelen S. Ratiometric probes: design and applications. Kraayenhof R, Visser AJWG, Gerritsen HC, editors. Fluorescence spectroscopy, imaging and probes: new tools in chemical physical and life sciences, Springer series on fluorescence, vol. 2. Springer-Verlag Berlin Heidelberg; 2002. p. 101–10.
[19] Demchenko AP. The concept of λ-ratiometry in fluorescence sensing and imaging. J Fluoresc 2010;20:1099–128. https://doi.org/10.1007/s10895-010-0644-y.
[20] Klymchenko AS, Mély Y. Fluorescent environment- sensitive dyes as reporters of biomolecular interactions. Morris MC, editor. Progress in molecular biology and translational science, vol. 113. Burlington, MA: Academic Press; 2013. p. 35–58.
[21] Demchenko AP. Practical aspects of wavelength ratiometry in the studies of intermolecular interactions. J Mol Struct 2014;1077:51–67. https://doi.org/10.1016/j.molstruc.2013.11.045.
[22] Spadafora M, Postupalenko VY, Shvadchak VV, Klymchenko AS, Mély Y, Burger A, et al. Efficient synthesis of ratiometric fluorescent nucleosides featuring 3-hydroxychromone nucleobases. Tetrahedron 2009;65:7809–16. https://doi.org/10.1016/j.tet.2009.07.021.
[23] Dziuba D, Postupalenko VY, Spadafora M, Klymchenko AS, Guérineau V, Mély Y, et al. A universal nucleoside with strong two-band switchable fluorescence and sensitivity to the environment for investigating DNA interactions. J Am Chem Soc 2012;134:10209–13. https://doi.org/10.1021/ja3030388.
[24] Kuznetsova AA, Kuznetsov NA, Vorobjev YN, Barthes NPF, Michel BY, Burger A, et al. New environment-sensitive multichannel DNA fluorescent label for investigation of the protein-DNA interactions. PLoS One 2014;9:e100007. https://doi.org/10.1371/journal.pone.0100007.
[25] Kilin V, Gavvala K, Barthes NPF, Michel BY, Shin D, Boudier C, et al. Dynamics of methylated cytosine flipping by UHRF1. J Am Chem Soc 2017;139:2520–8. https://doi.org/10.1021/jacs.7b00154.
[26] Sholokh M, Sharma R, Grytsyk N, Zaghzi L, Postupalenko VY, Dziuba D, et al. Environmentally sensitive fluorescent nucleoside analogues for surveying dynamic interconversions of nucleic acid structures. Chem Eur J 2018;5. https://doi.org/10.1002/chem.201802297. 388–13.
[27] Zargarian L, Ben Imeddourene A, Gavvala K, Barthes NPF, Michel BY, Kenfack CA, et al. Structural and dynamical impact of a universal fluorescent nucleoside analogue inserted into a DNA duplex. J Phys Chem B 2017;121:11249–61. https://doi.org/10.1021/acs.jpcb.7b08825.
[28] Dziuba D, Karpenko IA, Barthes NPF, Michel BY, Klymchenko AS, Benhida R, et al. Rational design of a solvatochromic fluorescent uracil analogue with a dual-band ratiometric response based on 3-hydroxychromone. Chem Eur J 2014;20:1998–2009. https://doi.org/10.1002/chem.201303399.
[29] Barthes NPF, Gavvala K, Dziuba D, Bonhomme D, Karpenko IA, Dabert-Gay AS, et al. Dual emissive analogue of deoxyuridine as a sensitive hydration-reporting probe for discriminating mismatched from matched DNA and DNA/DNA from DNA/RNA duplexes. J Mater Chem C 2016;4:3010–7. https://doi.org/10.1039/C5TC03427B.
[30] Saito Y, Suzuki A, Ishioroshi S, Saito I. Synthesis and photophysical properties of novel push–pull-type solvatochromic 7-deaza-2′-deoxypurine nucleosides. Tetrahedron Lett 2011;52:4726–9. https://doi.org/10.1016/j.tetlet.2011.06.089.
[31] Suzuki A, Kimura K, Ishioroshi S, Saito I, Nemoto N, Saito Y. Synthesis of solvatofluorochromic 7-arylethynylated 7-deaza-2′-deoxyadenosine derivatives: application to the design of environmentally sensitive fluorescent probes forming stable DNA duplexes. Tetrahedron Lett 2013;54:2348–52. https://doi.org/10.1016/j.tetlet.2013.02.063.
[32] Armarego WLF, editor. Purification of laboratory chemicals. eighth ed.Oxford: Elsevier Butterworth-Heinemann; 2017. p. 1–1198.
[33] Jork H, Funk W, Fischer WR, Wimmer H, editors. vol. 1a. Weinheim, Germany: Physical and Chemical Detection Methods: Fundamentals, Reagents I; VCH; 1990. p. 1–464. Thin-layer chromatography: reagents and detection methods.
[34] Still WC, Kahn M, Mitra A. Rapid chromatographic technique for preparative separations with moderate resolution. J Org Chem 1978;43:2923–5. https://doi.org/

10.1021/jo00408a041.
[35] Gottlieb HE, Kotlyar V, Nudelman A. NMR chemical shifts of common laboratory solvents as trace impurities. J Org Chem 1997;62:7512–5. https://doi.org/10.1021/jo971176v.
[36] Fulmer GR, Miller AJM, Sherden NH, Gottlieb HE, Nudelman A, Stoltz BM, et al. NMR chemical shifts of trace impurities: common laboratory solvents, organics, and gases in deuterated solvents relevant to the organometallic chemist. Organometallics 2010;29:2176–9. https://doi.org/10.1021/om100106e.
[37] Seela F, Zulauf M. Palladium-catalyzed cross coupling of 7-iodo-2'-deoxytubercidin with terminal alkynes. Synthesis 1996:726–30. https://doi.org/10.1055/s-1996-4282.
[38] Suzuki A, Nemoto N, Saito I, Saito Y. Design of an environmentally sensitive fluorescent 8-aza-7-deaza-2′-deoxyadenosine derivative with dual fluorescence for the specific detection of thymine. Org Biomol Chem 2014;12:660–6. https://doi.org/10.1039/C3OB41757C.
[39] Saito Y, Suzuki A, Yamauchi T, Saito I. Design and synthesis of 7-naphthyl-8-aza-7-deaza-2′-deoxyadenosines as environmentally sensitive fluorescent nucleosides. Tetrahedron Lett 2015;56:3034–8. https://doi.org/10.1016/j.tetlet.2014.10.116.
[40] Bazureau J-P, Paquin L, Carrié D, L'Helgoual'ch J-M, Guihéneuf S, Wacothon K, et al. Microwaves in heterocyclic chemistry. In: de la Hoz A, Loupy A, editors. Microwaves in organic synthesis, 3rd ed., Part II: applications of microwave irradiation. Weinheim, Germany: Wiley-VCH; 2013. p. 673–735.
[41] Dean FM, Podimuang V. 737. The course of the algar–flynn–oyamada (A.F.O.) reaction. J Chem Soc Perkin Trans 1965;0:3978–87. https://doi.org/10.1039/JR9650003978.
[42] Dziuba D, Benhida R, Burger A. A mild and efficient protocol for the protection of 3-hydroxychromones under phase-transfer catalysis. Synthesis 2011:2159–64. https://doi.org/10.1055/s-0030-1260034.
[43] Klymchenko AS, Pivovarenko VG, Demchenko AP. Perturbation of planarity as the possible mechanism of solvent-dependent variations of fluorescence quantum yield in 2-aryl-3-hydroxychromones. Spectrochim Acta, Part A 2003;59:787–92. https://doi.org/10.1016/S1386-1425(02)00233-0.
[44] Reichardt C. Solvatochromic dyes as solvent polarity indicators. Chem Rev 1994;94:2319–58. https://doi.org/10.1021/cr00032a005.
[45] Abraham MH. Hydrogen bonding. 31. Construction of a scale of solute effective or summation hydrogen-bond basicity. J Phys Org Chem 1993;6:660–84. https://doi.org/10.1002/poc.610061204.
[46] Klymchenko AS. Solvatochromic and fluorogenic dyes as environment-sensitive probes: design and biological applications. Acc Chem Res 2017;50:366–75. https://doi.org/10.1021/acs.accounts.6b00517.
[47] Lakowicz JR. Principles of fluorescence spectroscopy. third ed. New York, NY: Springer; 2006. p. 1–954.
[48] Kenfack CA, Klymchenko AS, Duportail G, Burger A, Mély Y. Ab initio study of the solvent H-bonding effect on ESIPT reaction and electronic transitions of 3-hydroxychromone derivatives. Phys Chem Chem Phys 2012;14:8910. https://doi.org/10.1039/c2cp40869d.
[49] Demchenko AP, Tang K-C, Chou P-T. Excited-state proton coupled charge transfer modulated by molecular structure and media polarization. Chem Soc Rev 2013;42:1379–408. https://doi.org/10.1039/c2cs35195a.
[50] Skilitsi AI, Agathangelou D, Shulov I, Conyard J, Haacke S, Mély Y, et al. Ultrafast photophysics of the environment-sensitive 4′-methoxy-3-hydroxyflavone fluorescent dye. Phys Chem Chem Phys 2018;20:7885–95. https://doi.org/10.1039/c7cp08584b.
[51] Melhuish WH. Quantum efficiencies of fluorescence of organic substances: effect of solvent and concentration of the fluorescent solute. J Phys Chem 1961;65:229–35. https://doi.org/10.1021/j100820a009.
[52] Ormson SM, Brown RG, Vollmer F, Rettig W. Switching between charge-and proton-transfer emission in the excited state of a substituted 3-hydroxyflavone. J Photochem Photobiol, A 1994;81:65–72. https://doi.org/10.1016/1010-6030(94)03778-7.
[53] Klymchenko AS, Demchenko AP. Multiparametric probing of intermolecular interactions with fluorescent dye exhibiting excited state intramolecular proton transfer. Phys Chem Chem Phys 2003;5:461–8. https://doi.org/10.1039/b210352d.
[54] M'Baye G, Klymchenko AS, Yushchenko DA, Shvadchak VV, Ozturk T, Mély Y, et al. Fluorescent dyes undergoing intramolecular proton transfer with improved sensitivity to surface charge in lipid bilayers. Photochem Photobiol Sci 2007;6:71–6. https://doi.org/10.1039/b611699j.
[55] Yushchenko DA, Shvadchak VV, Klymchenko AS, Duportail G, Pivovarenko VG, Mély Y. Modulation of excited-state intramolecular proton transfer by viscosity in protic media. J Phys Chem A 2007;111:10435–8. https://doi.org/10.1021/jp074726u.
[56] Bilokin MD, Shvadchak VV, Yushchenko DA, Duportail G, Mély Y, Pivovarenko VG. Dual-fluorescence probe of environment basicity (hydrogen bond accepting ability) displaying no sensitivity to polarity. J Fluoresc 2009;19:545–53. https://doi.org/10.1007/s10895-008-0443-x.
[57] Aso T, Saito K, Suzuki A, Saito Y. Synthesis and photophysical properties of pyrene-labeled 3-deaza-2′-deoxyadenosines comprising a non-π-conjugated linker: fluorescence quenching-based oligodeoxynucleotide probes for thymine identification. Org Biomol Chem 2015;13:10540–7. https://doi.org/10.1039/C5OB01605C.
[58] Seidel CAM, Schulz A, Sauer MHM. Nucleobase-specific quenching of fluorescent dyes. 1. Nucleobase one-electron redox potentials and their Correlation with static and dynamic quenching efficiencies. J Phys Chem 1996;100:5541–53. https://doi.org/10.1021/jp951507c.
[59] Weatherly SC, Yang IV, Armistead PA, Thorp HH. Proton-coupled electron transfer in guanine oxidation: effects of isotope, solvent, and chemical modification. J Phys Chem B 2003;107:372–8. https://doi.org/10.1021/jp022085r.
[60] Seela F, Pujari SS. Azide − Alkyne "click" conjugation of 8-Aza-7-deazaadenine-DNA: synthesis, duplex stability, and fluorogenic dye labeling. Bioconjug Chem 2010;21:1629–41. https://doi.org/10.1021/bc100090y.
[61] Huynh MHV, Meyer TJ. Proton-coupled electron transfer. Chem Rev 2007;107:5004–64. https://doi.org/10.1021/cr0500030.
[62] Weinberg DR, Gagliardi CJ, Hull JF, Murphy CF, Kent CA, Westlake BC, et al. Proton-coupled electron transfer. Chem Rev 2012;112:4016–93. https://doi.org/10.1021/cr200177j.
[63] Luber S, Adamczyk K, Nibbering ETJ, Batista VS. Photoinduced proton coupled electron transfer in 2-(2′-hydroxyphenyl)-benzothiazole. J Phys Chem A 2013;117:5269–79. https://doi.org/10.1021/jp403342w.
[64] Pannwitz A, Wenger OS. Photoinduced electron transfer coupled to donor deprotonation and acceptor protonation in a molecular triad mimicking photosystem II. J Am Chem Soc 2017;139:13308–11. https://doi.org/10.1021/jacs.7b08761.
[65] Choi J, Majima T. Conformational changes of non-B DNA. Chem Soc Rev 2011;40:5893–909. https://doi.org/10.1039/c1cs15153c.

To sum up, **FCA** and **TCA** turn out to be the most promising dyes. They exhibit some photophysical advances compared to their parent **3HC** dyes such as their red-shifted absorption and emission maxima as well as their doubled extinction coefficient. Despite these notable improvements, there is a major problem to overcome, namely the quenching effect. These dyes have poor QYs in protic media such as MeOH, limiting their applications in nucleic acid sensing. We hypothesized a PET reaction to explain this detrimental quenching. However, due to the lack of experimental data and the underlying complexity of the ESIPT reaction, the PET process was not well evidenced.

2.2. PET reaction between dA analogs and chromones

Generally speaking, the design of emissive nucleosides needs to take into account the PET process between the fluorophore and the nucleobases. In this context, a detailed study of fluorescence quenching of coumarin dyes by different nucleobases was reported by Seidel's group.[215] The study finds out that **dG** could quench several coumarin dyes by the PET process. Quenching of several commercial dyes by **dG** due to PET was also reported.[216] 7-deaza-2′-deoxyadenosine (**d7A**), an analog of **dA**, was reported by Seela's group as a quencher to anthracene dye when the fluorophore is connected to the **d7A** nucleobase through an alkyl chain linker.[156]

In general, purine nucleosides (**dG** and **dA**) are more electron-rich than pyrimidine ones (**dT** and **dC**), realized in the formers' lower oxidation potentials compared to the laters. The order of oxidation potentials is as follow **dG** (+1.47 V) ≈ **d7A** < **dA** < **dT** ≈ **dC** (+2.14V).[156,215] **dG** and **d7A** are common quenchers to several fluorophores due to their unique low oxidation potentials, which act as electron donors in several PET processes.[118] For this reason, one should concern about the PET process when designing emissive purine nucleosides.

As a continuation of the work previously initiated, a series of experiments was conducted to better understand the origin of the PET reaction between **dA** analogs and chromones in order to orient our future research in the most appropriate direction. Herein, we describe the synthesis of emissive deoxyadenosine (**dA**) nucleosides and our investigations on the PET process occurring among these fluorophores. The model nucleosides were constructed as π-π conjugated systems between **dA** analogs (**d7A** and **8d7A**) and 3-MethoxyChromone (**3MC**) at the 7 position of the nucleobase. Our studies reveal that PET reaction from **d7A**, an electron-rich analog of **dA**, to **3MC** is much more favorable than that from **8d7A**. Although intramolecular PET is often held responsible for fluorescence quenching, our studies suggest that the PET reaction in **d7A-3MC** conjugates are likely due to an intermolecular process. To be more precise, we found out that these conjugates form ground-state complexes, in a head-to-tail manner, even at very low concentrations (nM range), favoring an intermolecular PET reaction. Interestingly, the formation of ground-state complexes as well as the inherent PET process can be switched off under acidic conditions or using the **8d7A** base analog. These results are not only important for reconsidering the too quickly ignored PET-quenching dyes, but also for designing advanced fluorescent probes based on deoxyadenosine.

Structures of all the compounds are given in publication 2.

PUBLICATION 2

Full Paper
doi.org/10.1002/chem.202003456

Electron Transfer | *Hot Paper*

Control of Intermolecular Photoinduced Electron Transfer in Deoxyadenosine-Based Fluorescent Probes

Hoang-Ngoan Le,[a] Johanna Brazard,[b, c] Guillaume Barnoin,[a] Steve Vincent,[a] Benoît Y. Michel,*[a] Jérémie Leonard,[b] and Alain Burger*[a]

Abstract: In this work, we report on the Photoinduced Electron Transfer (PET) reaction between a donor (adenine analogue) and an acceptor (3-methoxychromone dye, **3MC**) in the context of designing efficient fluorescent probes as DNA sensors. Firstly, Gibbs energy was investigated in disconnected donor–acceptor systems by Rehm-Weller equation. The oxidation potential of the adenine derivative was responsible for exergonicity of the PET reaction in separated combinations. Then, the PET reaction in donor-π-acceptor conjugates was investigated using steady-state fluorescence spectroscopy, acid-mediated PET inhibition and transient absorption techniques. In conjugated systems, PET is a favorable pathway of fluorescent quenching when an electron-rich adenine analogue (**d7A**) was connected to the fluorophore (**3MC**). We found that formation of ground-state complexes even at nM concentration range dominated the dye photophysics and generated poorly emissive species likely through intermolecular PET from **d7A** to **3MC**. On the other hand, solution acidification disrupts complexation and turns on the dye emission. Bridging an electron-poor adenine analogue with high oxidation potential (**8d7A**) to **3MC** presenting low reduction potential is another alternative to prevent complex formation and produce highly emissive monomer conjugates.

Introduction

Redesigning the structure of nucleosides to generate environment-sensitive fluorescent analogues and incorporating them into nucleic acids (NA) is a leading approach for the development of NA-related advanced sensors for sequencing and probing NA conformations, dynamics and interactions.[1–3] A common strategy is grafting a chromophore to the nucleobase preferentially on a position not affecting Watson–Crick base pairing. In term of biocompatibility, extension at positions 5 and 7 of pyrimidine and purine rings, respectively, is the most favorable.[1,4,5] Connecting a fluorophore is attractive as it opens the route to the development of emissive probes based on sensing parameters of the original dye.[6,7] Extension of electronic nucleobase π-scaffolds to construct push–pull systems is particularly interesting since it could generate probes with unique photophysical properties including sensitivity to polarity and red-shifted absorption and emission.[8] The responsiveness of the fluorescence reporter can be greatly increased if the emissive signal is based on the change between two spectrally resolved forms.[9,10] In order to achieve this, we have selected fluorophores of the 3-hydroxychromone (**3HC**) family that can exist in two excited-state forms—the normal and tautomer ones—due to an excited-state intramolecular proton transfer (ESIPT). Both forms fluoresce at different wavelengths and thus generate a dual emission proving sensitive to H-bonding and electric field of the environment for which the intensity ratio of the two bands can be used as the reporting unit. In this context, we first reported push-pull probes with advanced features, elaborate from **dU** and **3HC**. These probes were characterized by a two-color emission (cyan and yellow), good quantum yields in different solvents including water and especially high sensitivity to hydration and NA conformations.[11,12] The possibility to connect the **3HC** moiety to adenine nucleobases for NA labeling was next explored by electronically coupling 7-deazadeoxyadenosine (**d7A**) with **3HC** dyes (Figure 1. **FCA** and **TCA**).[13] The new conjugates showed several improvements in the photophysical properties of **3HC** as evidenced by red-shifted absorptions from UV to the violet range, up to 1.5-fold increase in absorptivity and strong sensitivity to environmental changes. However, they revealed to be strongly quenched in polar protic solvents and almost non-emissive in water. Thus, the access of fluorescent purine-based nucleosides for NA labeling turned out to be more problematic

[a] *H.-N. Le, G. Barnoin, S. Vincent, Dr. B. Y. Michel, Prof. Dr. A. Burger*
Université Côte d'Azur, Institut de Chimie de Nice
UMR 7272, CNRS
Parc Valrose, 06108 Nice cedex 2 (France)
E-mail: benoit.michel@univ-cotedazur.fr
alain.burger@univ-cotedazur.fr

[b] *Dr. J. Brazard, Dr. J. Leonard*
Université de Strasbourg, Institut de Physique et Chimie des Matériaux de Strasbourg and Labex NIE
UMR 7504, CNRS
67200 Strasbourg (France)

[c] *Dr. J. Brazard*
Present address: Université de Genève
Département de Chimie Physique
1211 Genève (France)

Supporting information and the ORCID identification number(s) for the author(s) of this article can be found under: https://doi.org/10.1002/chem.202003456.

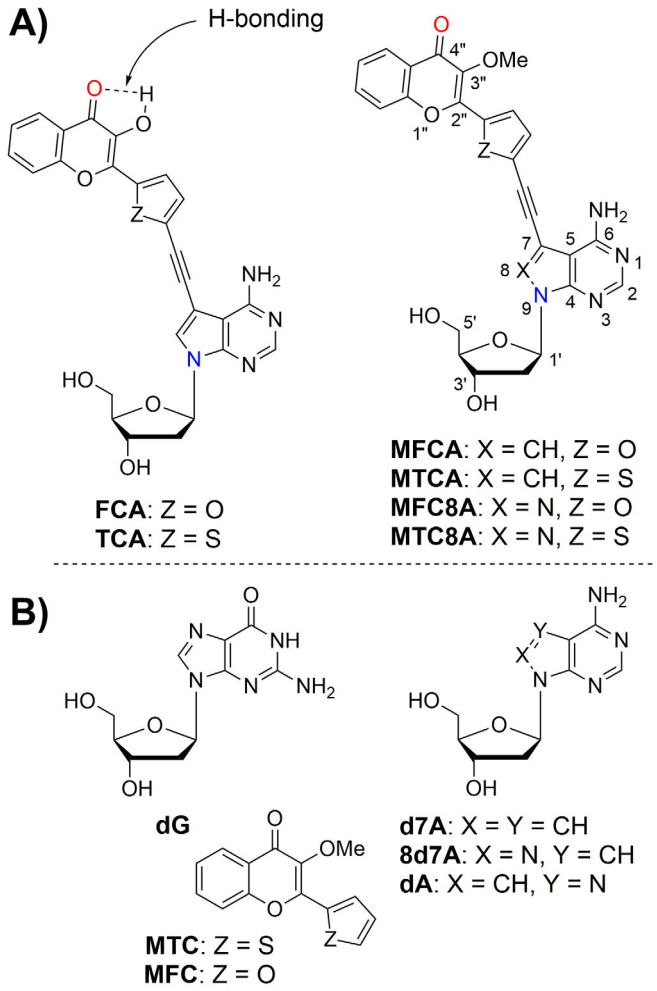

Figure 1. A) Synthesized push-pull conjugated systems investigated here: electron donors and acceptors are depicted in blue and red, respectively. B) Structures of separated donors (**dG**, **dA** and analogues) and acceptors (**3MC** derivatives).

than for the pyrimidine nucleobase. Since **7 dA** is a potent donor for photoinduced electron transfer (PET), we hypothesized that a proton-coupled PET[14] from the **7 dA** fragment to the **3HC** could be a plausible mechanism to account for fluorescence quenching of **FCA** and **TCA**. Proposing such a process also raises the question of whether the electron transfer is intramolecular or intermolecular?

It is often difficult to prove the mechanism of quenching. The mechanism may not be exclusive and can be a combination of different processes (e.g. internal conversions, Dexter energy transfer, or twisted intramolecular charge transfer (TICT) conformation) making the task even more difficult.[15] To have more convincing evidences, we carried out several experiments with 3-methoxychromones (**3MCs**) to avoid spectroscopic and kinetic complications due to the ESIPT reaction (H-bond, Figure 1 A). Herein, we report on our investigation of push-pull systems between **dA** analogues and **3MCs**. First, the energetic aspect of the PET reaction was studied between the separated **d7A** electron donor and **3MC** electron acceptor using cyclic voltammetry to demonstrate whether **d7A** can be oxidized and **3MC** reduced. Given that **dG** has the lowest oxidation potential (E) and that incorporation of an *N* atom at position 8 of the purine increases this value (E(**dG**) ~ E(**7 dA**) < E(**8 d7A**) ~ E(**dA**)),[16–18] comparison experiments were implemented with positive (**dG**) and negative controls (**dA** and **8 d7A** (8-aza-7-deaza-2′-deoxyadenosine)). Secondly, the photophysical investigations of the single-band emissive conjugates (**MFCA** and **MTCA**) and their corresponding negative controls (**MFC8A**, **MTC8A** and acidification) were performed to verify quenching of **MFCA** and **MTCA** in polar protic solvents. Lastly, UV/Vis transient absorption (TA) spectroscopy was performed on the conjugates to establish direct evidence of PET for **MFCA** and **MTCA** in methanol. This study not only provides a better understanding of the PET quenching reaction in separated as well as conjugated systems of **dA** analogues and chromones but also brings useful information for the design of fluorescent DNA sensors. Noticeably, fluorescence could be switched ON/OFF by using the suitable **dA** analogue or simply by fine tuning the medium pH.

Results and Discussion

Separated donors and acceptors, and conjugated deoxyadenosine analogues

The compounds required for the photophysics were synthesized **(MTCA, MFCA, MTC8A, and MFC8A**) or obtained from commercial sources **(MFC, dG, d7A, 8 d7A, and dA**). The synthesis of **MTC** was recently reported by our group.[19] Synthesis of conjugates were adapted from Seela's previous works.[17,20] The full details of their preparation and characterization are given in the Supporting Information.

Standard free energy changes of PET reaction between separated donors and acceptors

PET is the most common mechanism proposed to account for quenching of fluorophores by nucleobases.[9] Upon PET, the **3MC** fluorophore can be reduced by the nucleobase to form a radical ion pair, which can further undergo radiationless relaxation to the ground state. Comparison of the redox potentials of the fluorophore and nucleobase allows us to examine the possibility for PET.[16] Among the canonical nucleobases, guanine is the most potent electron donor with the lowest oxidation potential.[16,21] The redox potential of **7 dA**, a prospective nucleobase moiety to engineer adenosine-based probes, is close to that of guanosine.[16] One strategy to raise the oxidation potential of **7 dA** is to incorporate an endocyclic nitrogen in position 8 of the purine framework. Seela et al. exploited this approach and demonstrated its efficiency to affect the oxidation potential, placing **8 d7A** in the range comparable to **dA**.[17]

To determine if PET is energetically favorable, we have correlated fluorescence quenching of the bridged donor-acceptor systems with the redox potentials of the separated donors and acceptors and their corresponding Gibbs energies calculated from the Rehm–Weller equation [Eq. (1)].[15,22] Based on the

latter, one could predict whether the electron transfer process is exergonic or endergonic.

$$\Delta G^{\circ}_{et} = E^{ox}(D) - E^{red}(A) - E_{00}(A) + \Delta G^{\circ}(\varepsilon) \quad (1)$$

Where E^{ox}(D) is the oxidation potential of the donor (purine base); E^{red}(A) is the reduction potential of acceptor (**3MC** derivative); E_{00}(A) is the zero-zero transition energy (1240/λ (nm) in eV), where λ is the intersection of the normalized absorption and emission spectra of the acceptor.[15] $\Delta G^{\circ}(\varepsilon)$ is the solvent term contribution and depends on the dielectric constant of the solvent. It was estimated to be 0.1 eV in H_2O.[16]

In this study, we assumed that **dA** analogues (**d7A** and **8d7A**) being the electron donors, and **3MCs**, the electron acceptors (Figure 1B). In order to compare with **dA** analogues, natural **dG** and **dA** were investigated as positive and negative controls, respectively.[21] Oxidation and reduction potentials (Figure S1), as well as calculated Gibbs energies are reported in Table 1.

Analysis of these data allows several conclusions to be drawn. First, the oxidation potentials obtained for the known purine compounds were comparable to the reported values highlighting the consistency of our data (e.g. compare +1.46 V with +1.48 V for **d7A**, for the other compounds see Table S2).[17] The oxidation potential of **d7A** (+1.46 V) is close to that of **dG** (+1.42 V); similarly, **8d7A** (+1.81 V) is comparable to **dA** (+1.85 V).

According to the Rehm–Weller equation, ΔG°_{et} depends on three main parameters. Firstly, it depends on the oxidation and reduction potentials of the donor and acceptor, respectively. Table 1 shows that the reduction potentials of the two chromones are identical; by contrast, the oxidation potentials of the purine bases are discriminant (compare **d7A** vs. **dG** with **8d7A** vs. **dA**). Hence, ΔG°_{et} of any pair between donor (**d7A** or **dG**) and acceptor (**MTC** or **MFC**) will be about 0.35–0.43 eV smaller than that of **8d7A** or **dA** as the donor. Basically, oxidation of the donor and reduction of the acceptor in a PET process requires energy. Therefore, this energy contributes a positive value to the ΔG°_{et} of the PET reaction. Secondly, ΔG°_{et} depends on the zero-zero transition energy (E_{00}) of the fluorophore (**3MC**). E_{00} is the energy gain of the photoexcited **3MC**, it contributes a negative value to the free energy. The zero–zero transition energy of the furyl chromone (**MFC**, +3.18 eV) is just slightly higher than that of thiophene-containing chromone (**MTC**, +3.16 V). This result is consistent with the fact that the larger sulfur atom probably decreases of the HOMO–LUMO energy gap compared to the smaller oxygen atom due to resonance effects.[23,24] Lastly, the solvent term contribution $\Delta G^{\circ}(\varepsilon)$ depends on the dielectric constant of the solvent. Generally, it decreases with increasing permittivity; however, its contribution to the total energy is small. According to ΔG°_{et}, electron transfer from **d7A** to **MFC** and **MTC** is exergonic with −0.30 eV; while, it is slightly endergonic from **8d7A** to the chromones **MTC** and **MFC** with +0.05 eV. Assuming that $\Delta G^{\circ}_{et} = -0.30$ eV is in the normal region according to the Marcus theory,[25–27] our results suggest that the electron transfer from **d7A** to the chromone should be faster and more favorable than that from **8d7A**.

Table 1. Oxidation potentials of donors, reduction potentials of acceptors and Gibbs energies.

Donor	Acceptor	E^{ox}(D)[a] vs. NHE [V]	E^{red}(A)[a] vs. NHE [V]	E_{00}(A)[b] [eV]	ΔG°_{et} [eV]
dG	**MTC**	+1.42	−1.50	+3.16	−0.33
d7A	**MTC**	+1.46	−1.50	+3.16	−0.30
8d7A	**MTC**	+1.81	−1.50	+3.16	+0.05
dA	**MTC**	+1.85	−1.50	+3.16	+0.10
dG	**MFC**	+1.42	−1.50	+3.18	−0.33
d7A	**MFC**	+1.46	−1.50	+3.18	−0.30
8d7A	**MFC**	+1.81	−1.50	+3.18	+0.05
dA	**MFC**	+1.85	−1.50	+3.18	+0.10

[a] Cyclic voltammetry was conducted against Ag/AgCl (KCl saturated) in acetonitrile containing 1 M tetra-*n*-butylammonium hexafluorophosphate ($TBAPF_6$) as the electrolyte, and saturated solution of the purine base or 1 mM **3MC**. Data were converted into normal hydrogen electrode (NHE) for comparison. Scan speed was 100 mV s^{-1}. [b] E_{00}(A) values were obtained from absorption and emission spectra of the corresponding fluorophore in water (see Figure S2).

General photophysical characterization

The photophysics of the newly synthesized push-pull nucleosides were characterized in a set of four protic solvents (water, methanol, ethanol, and *i*-propanol) of different polarities, and the results are summarized in Table 2 (Figures S3–S6). The Dimroth–Reichardt polarity index parameter[28] is used to rank the solvents. This empirical scale takes into account the dielectric constant and H-bonding ability of the medium. The solvent acidity (SA) according to the Catalán scale is also given for comparison and discussion.[29]

The **MFCA** and **MTCA** exhibit similar absorptivity and little variation of absorption maxima whatever the solvent studied. The maxima are centered near the visible range (377–379 and 388–391 nm, respectively). Both conjugates displayed a 35–41 nm bathochromic shift of their absorption by comparison to the parent **MFC** and **MTC** chromones (Figure S2 and ref. [19]) as expected for dyes with extended conjugation. The same conclusion can be deduced from the UV/Vis spectra of **MFC8A** and **MTC8A**, albeit with slightly blue-shifted absorption maxima (362–383 nm). Unsurprisingly, substitution of the 3-hydroxyl proton by the methyl group in the chromone inhibits its ESIPT and thus, the dual emission. **MFCA** and **MTCA** displayed bathochromic shifts of their emission maxima with the increase in solvent polarity (e.g., from 534 nm in *i*PrOH to 571 nm in MeOH for **MFCA**, Table 2), as illustrated in Figure 2. Their quantum yields gradually drop as the polarity increases (Figure 3). For chromones, it is known that in the excited state, the electron-enriched 4′′-carbonyl oxygen (Figure 1) is particularly sensitive to H-bonding for which H-bond interactions are all the stronger as the acidity of the solvent increases.[31–33] There are many examples in chemistry and biology supporting that intermolecular site-specific interactions through H-bonding can increase PET.[14,16,34] As with **FCA** and **TCA** compared to

Table 2. Photophysical properties of nucleoside analogues in different solvents.

ε_{max} [10^3 M^{-1} cm^{-1}][a]	--	40	40	34	37
Solvent	$E_T^N(30)$[b]	λ [nm][d]	**MFCA**	**MTCA**	**MFC8A**	**MTC8A**
	SA[c]	Φ [%][e]	**(10)**	**(11)**	**(12)**	**(13)**
H_2O[f]	1.00	λ_{Abs}	378	388	372	366
	1.062	λ_{Em}	567	579	472	479
		Φ	0.2	0.7	30	NA[g]
H_2O–TFA 5‰[f]		λ_{Abs}	377	384		
		λ_{Em}	521	527		
		Φ	6.0	6.0		
MeOH[f]	0.76	λ_{Abs}	378	388	372	366
	0.605	λ_{Em}	571	580	464	469
		Φ	1.3	0.9	38	36
MeOH[h]		λ_{Em}	512	512	464	469
MeOH–TFA 5‰[f]		λ_{Abs}	371	382		
		λ_{Em}	501	508		
		Φ	41	35		
EtOH[f]	0.65	λ_{Abs}	378	390	368	379
	0.400	λ_{Em}	555	564	458	464
		Φ	6	4.2	33	30
*i*PrOH[f]	0.57	λ_{Abs}	379	391	368	379
	0.283	λ_{Em}	534	546	453	459
		Φ	19	18	29	26

[a] Molar extinction coefficient was determined in MeOH; relative standard deviations are $\leq$5%. [b] Reichardt's empirical solvent polarity index.[28] [c] Acidity scale.[29] [d] Wavelength of absorption (λ_{Abs}) and emission maxima (λ_{Em}) in nm. [e] Fluorescence quantum yields (Φ) were determined using an excitation at the corresponding absorption maximum of each compound in the considered solvent. *p*-Dimethylaminoflavone (DMAF) in EtOH (λ_{Abs} = 404 nm, Φ = 27%)[30] was used as the standard reference, ±10% mean standard deviation. [f] Absorption and emission spectra were recorded at concentrations of 11 and 1.1 μM, respectively. [g] Not investigated due to very low solubility. [h] Emission maximum obtained for solution at concentration < 10 nM.

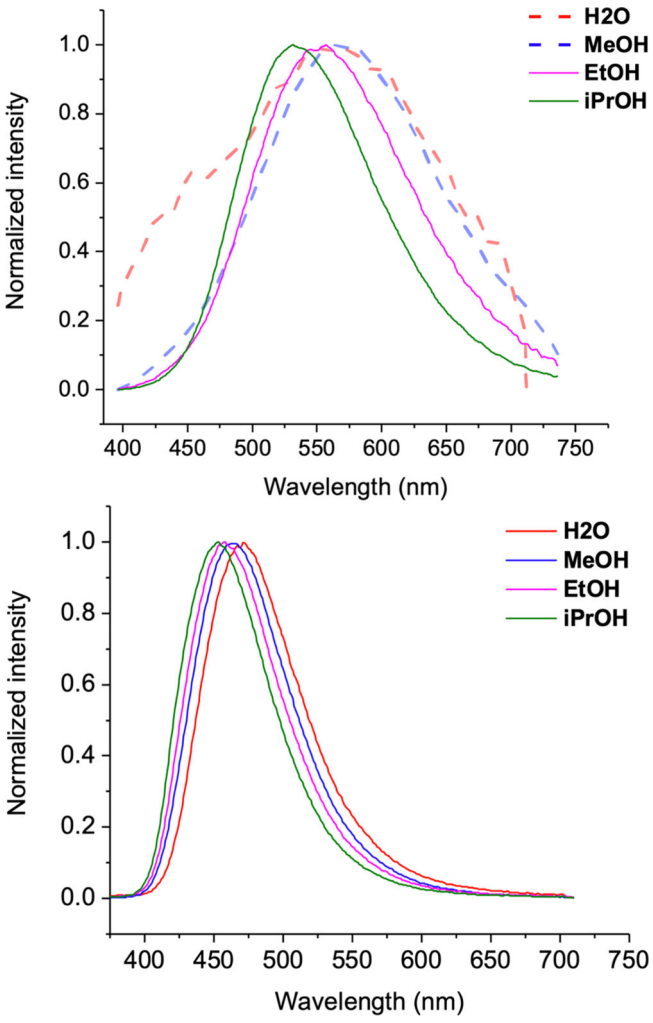

Figure 2. Normalized emission spectra of **MFCA** (*top*) and **MFC8A** (*bottom*) at 1.1 μM, in a set of protic solvents of increasing polarity. Excitation wavelength was set at the absorption maximum (Table 2).

TCU, the corresponding methylated derivatives behave differently. They turn almost non-emissive in MeOH and H_2O (e.g. compare Φ = 0.9% for **MTCA** in MeOH with Φ = 49% for **MTCU**) and show larger bathochromic shifts, which can be seen from the shifts in emission since the compounds have close absorption maxima (e.g. compare 501 nm for **MTCU** in MeOH with 580 nm for **MTCA**).[19]

Why do these compounds demonstrate such large spectral shifts and drop in quantum yields in protic solvents? Are these variations due to solvent specific effects, conformational changes generating a TICT conformer or probe-probe interactions? To address these questions, we examined the emission spectra recorded at different concentrations ranging from 60 μM to 1.25 nM as shown in Figure 4 (see also Figure S8) and observed concentration-dependent spectral shifts.

For example, the emission maximum of **MTCA** in MeOH was gradually blue-shifted from 580 nm (at concentrations larger than 0.5 μM) to 512 nm ([C] < 2 nM). At concentrations as low as 5 nM, we have already detected a contribution of the 580-nm emissive species (see Figure 4, top). The high-energy emission band was close to that of **MTCU**. We therefore attribute the 512-nm emission band to the monomer dye, and that at 580 nm to a complex. Excimers are typically observed as a broad emission band, red-shifted relative to that of the fluorophore monomer. Excimer is a complex formed between two monomers when at least one component is in the excited state. Noticeably, the changes in the emission spectra of **MTCA** and **MFCA** clearly showed that the complexes are formed at concentrations as low as few nM, which are far below the mM-concentration range for which excimers are typically observed.[15,35]

Indeed at 2 μM concentration, the average distance between solute molecules of d ≈0.1 μM corresponds to a typical diffusion time $\tau = d^2/D$ in the 20-μs range for two molecules to encounter (assuming D = 500 μm^2 s^{-1} for the diffusion coefficient),[36,37] which is 4 orders of magnitude longer than the excited-state lifetime. Thus, the emission spectra observed at concentrations of 0.5 μM or larger are attributed to a complex resulting from ground-state interactions. Analyzing the excitation spectra recorded at different concentrations further supports this interpretation as the existence of two absorbing spe-

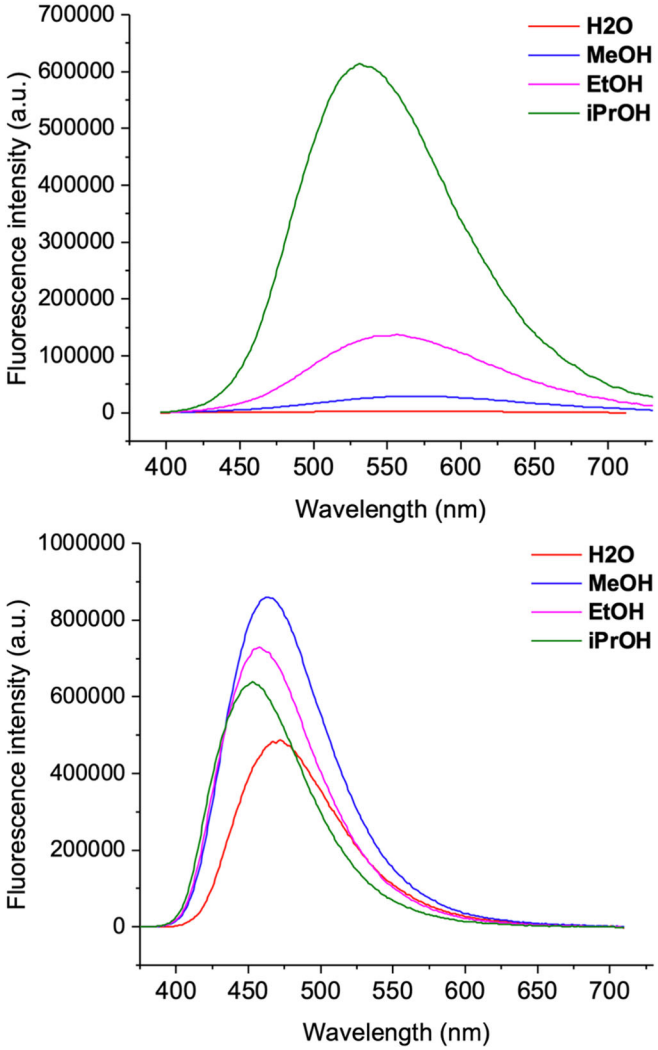

Figure 3. Fluorescence spectra of **MFCA** (*top*) and **MFC8A** (*bottom*) at 1.1 μM, in a set of protic solvents of increasing polarity. Excitation wavelength was set at the absorption maximum (Table 2).

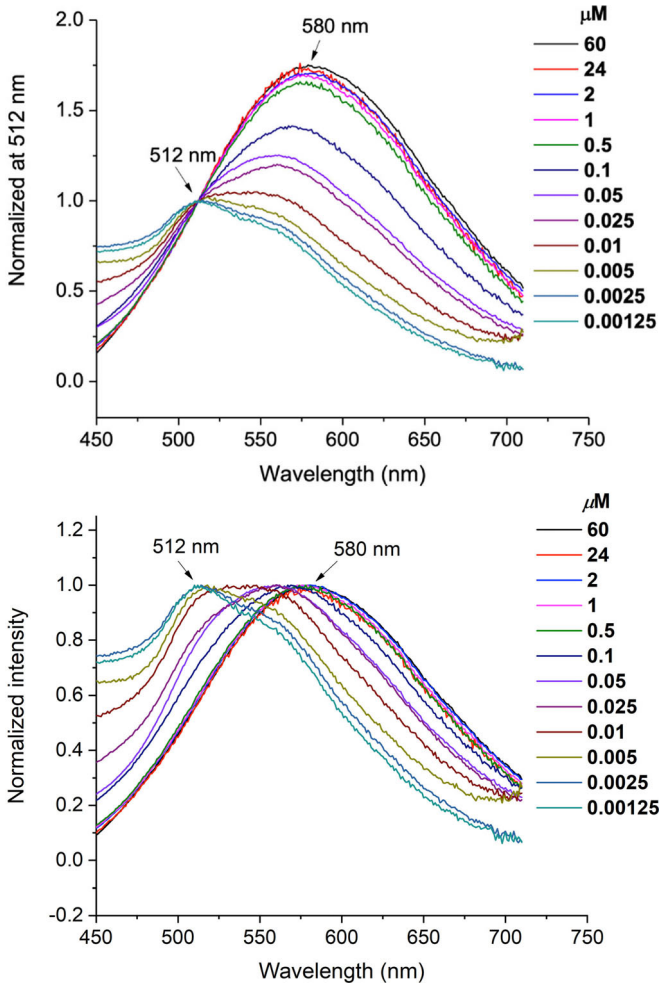

Figure 4. Emission spectra of **MTCA** for different concentrations in MeOH, normalized at 512 nm (top) and on their maximum (bottom). Excitation wavelength was set at 370 nm.

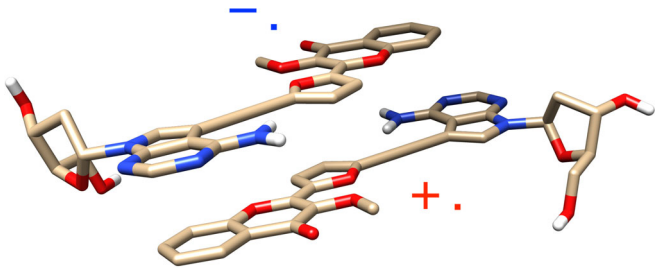

Figure 5. Proposed representation of the complexed, radical pair structure (generated from Chimera).

cies was evidenced at low concentration (Figures S7 and S8). Formation of ground-state complexes of acceptor–donor pairs is known.[38,39] The close association of both species favors PET affording radical ion pairs. The radical ion pair generated from the charge-transfer complex can be compared to the well-known poorly emissive geminate radical ion pairs for exciplexes, although the latter, as for the excimer, generally refer to bimolecular contacts of the excited dye and a quencher.[40–43] The peculiarity of our compounds is that they formed complexes even at very low concentrations. We are not aware of other examples of such intermolecular tight interactions reported in the literature. In the case of **MTCA** and **MFCA**, their complexation could be favored in polar solvents due to the hydrophobic nature of the extended flat fluorophore, favorable π-stacking and van der Waals interactions as well as a quadrupole arrangement allowing strong Coulombic coupling. A head-to-tail orientation of the two dyes should favor intermolecular PET, because the nucleobase donor in one specie would be in contact with the chromone acceptor of the other specie (Figure 5). Thus, the complexation of **MTCA** and **MFCA** and photoinduced formation of poorly emissive radical ion pairs likely dominate the photophysics of these dyes in polar protic solvents.

The 8-aza series (**MTC8A** and **MFC8A**) behave differently. They showed reduced redshifts of their emission maxima along with the increase in solvent polarity (e.g. from 453 nm in *i*PrOH to 474 nm in MeOH for **MFC8A**) and bright emissions in polar protic solvents (e.g. 30% in water for **MFC8A**). Importantly, the emission spectra remain unchanged even down to the 1–2 nM range for both dyes by contrast to **MTCA** and **MFCA** (Figures S11, S12). These results suggest that the **MTC8A** and

MFC8A were observed as monomers in MeOH solution at all studied concentrations from nM to μM. Since both types of dyes have the same size and area, the only difference between them is the introduction of an electron-withdrawing nitrogen at the 8 position on the nucleobase. This considerably reduces the electron-donating ability of **8d7A** as evidenced by the increased of the oxidation potential (Table 1, compare 1.81 and 1.46 V for **8d7A** and **d7A**, respectively). Therefore, the difference between the oxidation potential of the donor and the reduction potential of the acceptor increases. As a consequence, the propensity to form charge-transfer complexes between the **8d7A** donor and the **MTC** or **MFC** acceptor should be greatly affected by contrast to that formed with **d7A**. Previous reports have shown that the association constant of donor/acceptor complexes decreases as the difference in the redox potential increases,[38,39] albeit they form at concentrations several orders of magnitude higher than those required for **MFCA** and **MTCA.** Our data highlights that the difference in the redox potential is one important contributor to the complex association for our dyes.

Acid-mediated inhibition of the PET process

Protonation of amines linked to weakly emissive systems is a common way to switch on their fluorescence.[44] The purine bases have 2-electron-rich centers at N3 and N1 atoms with pK_a of around 4.3.[45] In acidic media, the most basic *nitrogen N1* will be protonated. Protonation of the purine base should therefore reduce its electron-donating ability and disrupt both the complex formation and electron transfer process (Figure 6). To check this hypothesis, the absorption and emission spectra of **MFCA** and **MTCA** in MeOH and H_2O, with and without adding TFA (0.5% *v/v*), were investigated. Upon addition of this strong Brønsted acid, turn-on emissions were recorded (Figures 6 and S13). For instance, the poor quantum yields (< 1%) of **MTCA** increased to 35% and 6% for acidified MeOH and H_2O solutions, respectively. Analysis of the excitation and emission spectra of **MFCA** and **MTCA** in acidified MeOH (TFA, 0.5% *v/v*) at different concentrations led to the same conclusion, as for **MTC8A** and **MFC8A** (Figures S9, S10), that only the monomer spectra are observed at all concentrations employed here.

Direct observation of PET on conjugated systems using UV/Vis TA spectroscopy

To further support the proposed PET reaction and observe the corresponding reaction kinetics, femtosecond UV/Vis transient absorption (TA) spectroscopy was used. Methanolic solutions of **MTCA**, **MTC8A** and **MTCA** with TFA (0.5% *v/v*)—as well as **MFCA**, **MFC8A** and **MFCA** with TFA (0.5% *v/v*)—were prepared at a concentration of 330 μM and investigated by TA, with a 60 to 70-fs time resolution, using a 370-nm pump pulse, and a white-light probe pulse offering an absorption detection window spanning from 330 to 700 nm. The experimental set-up is the same as previously described (see General methods, Experimental Section).[33] Quantitative analysis of the TA data is

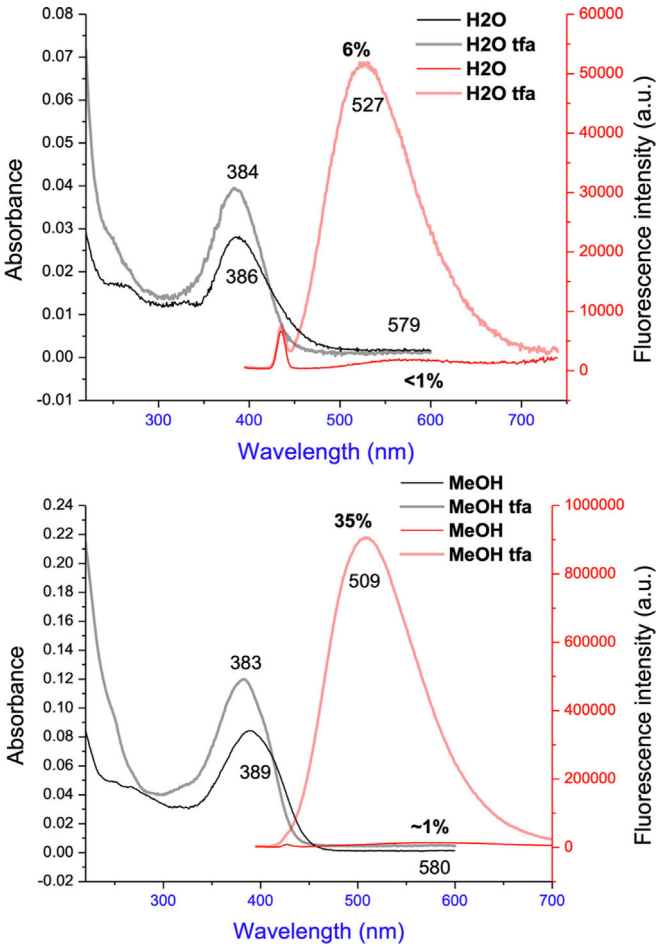

Figure 6. Substantial fluorescent turn-on signal of **MTCA** upon TFA addition recorded in H_2O (top) and MeOH (bottom). Absorption (grey and black) and emission (pink and red) spectra were measured at 2 μM. Maxima are given in nm and quantum yields mentioned above, in %. Their determination took into account the change in absorbance at the excitation wavelength of 370 nm.

performed by global analysis and illustrated by presenting the so-called decay-associated spectra (DAS, Figures 7 and S14–S18), which reveal the time scales and associated spectral modifications characterizing the TA decay kinetics recorded across the entire UV/Vis observation window.

Immediately after excitation, the early signature of the first excited state S_1 is similar in the three samples (0.2-ps spectra in Figure 7a, d, and g). We identify the ground-state bleach (GSB) as a negative signal around 380 nm, a stimulated emission (SE) band—also negative—around 450 nm, and a positive excited-state absorption at wavelengths > 500 nm. Early spectral relaxation occurs in all three samples already within the instrument response function, and with a 0.5 to 0.6-ps time scale (Figure S16), likely due to the fast solvent relaxation[46] and possibly to the early vibrational relaxation out of the Franck–Condon (FC) region. Then, in the case of **MTCA**, the early SE and an excited-state absorption (ESA) band decay on the 2.8-ps time scale, corresponding to the formation of a first transient state that we named **U**, which is still an excited state (possibly the **MTCA** complex in a different conformation), since the GSB does not recover on this time scale (Figure 7a and b). This

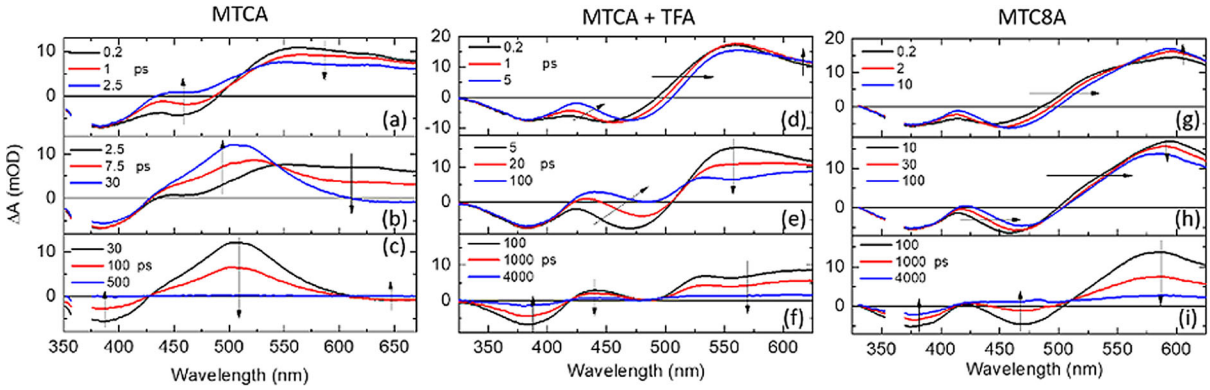

Figure 7. TA data *(ΔA)* measured upon 370-nm excitation of methanolic solutions of **MTCA** (left), **MTCA** + TFA (middle), and **MTC8A** (right). A selection of transient spectra at early (first line: panels a, d, and g), intermediate (second line: panels b, e, and h) and later (third line: panels c, f, and i) pump-probe time delays are displayed to illustrate the spectral evolutions observed on different times (highlighted by the black arrows).

state then decays on the 12-ps time scale to form a new state, that we name **V**, characterized by an intense absorption band around 510 nm and a new, weak (negative) SE band at $\lambda >$ 610 nm (see the 30-ps spectrum in panel b), while still hardly any recovery of the GSB signal occurs. The **V** state then decays with a 100-ps time scale, with the TA signal decaying completely to zero while keeping the same shape (see panel c), thus indicating the reformation of the original ground state on this time scale. The two successive SE bands observed here—at 450 nm with a 2.8-ps lifetime, and >610 nm with a 100-ps lifetime—must be closely related to the emission spectrum displayed for the same compound in Figure S4. In the observed spectroscopic signatures of the transient **V** state, the intense (positive) 510-nm ESA band overlaps and masks the (negative, less intense) SE band which is expected to be maximum at 580 nm, according to the steady-state spectrum (see Table 2). Due to this spectral overlap and larger intensity of the ESA signal, we actually only observe the red tail of the **V** emission in the TA data. The short-lived 450-nm SE band of the initially populated S_1 state is very short-lived and its contribution to the steady-state emission spectrum—expected in its high-energy tail—is strongly quenched.

In the case of **MTC8A**, following the early, sub-ps kinetics attributed to solvation and early relaxation away from the FC region, the SE and ESA bands both redshift with a 7-ps time constant (Figure S16). Further redshift of the SE band towards 470 nm occurs together with a slight decay of the ESA band on the 30-ps time scale (Figure S16). This overall multiexponential spectral relaxation is possibly due to structural reorganization of the **MTC8A** monomer excited state, resulting in the formation of the 469-nm emissive state detected by steady-state emission (Table 2), that we named **U′**. Here, the long-lived 470-nm SE band is not hidden by any ESA overlapping and therefore in perfect agreement with the observed steady-state emission. No strong ESA band at 510 nm corresponding to the **MTCA V** state is observed here.

The **U′** lifetime is measured to be 1.0 ns (Figure S*16*). Unlike for **MTCA**, the TA signal of **MTC8A** does not return to zero within the maximum 5-ns time scale achievable in our TA experimental set-up, meaning that the **U′** state does not decay back to the original ground state, but to a long-lived (⩾5 ns) photoproduct (PP) state. Specifying the nature of this PP would require complementary investigations and is beyond the scope of this work.

Upon acidification by addition of TFA, the TA signal of **MTCA + TFA** resembles that of **MTC8A**, with no intense ESA band at 510 nm, but a multiexponential spectral relaxation, resulting in the redshift of the initial SE band towards 490 nm. The slowest component of this multiexponential relaxation is found to be 23 ps (Figure S16) and characterizes a decay of the SE and ESA bands while the GSB remains constant. The time scale is similar to that of the formation of the **U′** intermediate in **MTC8A**, we therefore also name **U′** the transient state formed on the 23-ps time scale in **MTCA** in the presence of TFA. Importantly, **MTCA** is strongly fluorescent in the presence of TFA (with $\lambda_{Em} = 509$ nm and $\Phi = 35\,\%$, Table 2). Therefore, we must describe the apparent decay of SE on the 23-ps time scale as the rise of an underlying ESA, leading to a net decay of the TA signal to zero at 480 nm, as a result of two significant but cancelling positive (ESA) and negative (SE) contributions. This emissive **U′** state is then observed to decay on the 2.2-ns time scale, with no further spectral modification, to reform the original ground state, as indicated by the TA signal decaying fully to zero on this time scale. The same TA data, analysis and interpretation hold for the **MFCA**, **MFC8A** and **MFCA + TFA** methanol solutions (Figures S17, S18).

All together our data are consistent with the following plausible scenario (Figure 8). In polar protic solvents, **MTCA** or **MFCA** exist in their ground states most likely as face-to-face complexes in head-to-tail relative orientation (vide supra). Light absorption of these complexes generates a first transient **U** state within the first 3 ps (vibrational relaxation), which rapidly (12 ps) leads to the **V** state characterized by a strong absorption band at 510 nm (**MTCA**, Figure 7c) or 490 nm (**MFCA**, Figure S17) and weak emission band at 580 nm (**MTCA**, Table 2) or 571 nm (**MFCA**, Table 2). Based on the relative redox potentials and accompanying the discussion above, we interpret the **V** state as resulting from an intermolecular electron transfer from the **d7A** donor part of one molecule to the **MTC** or **MFC** acceptor part of the other molecule of a ground-

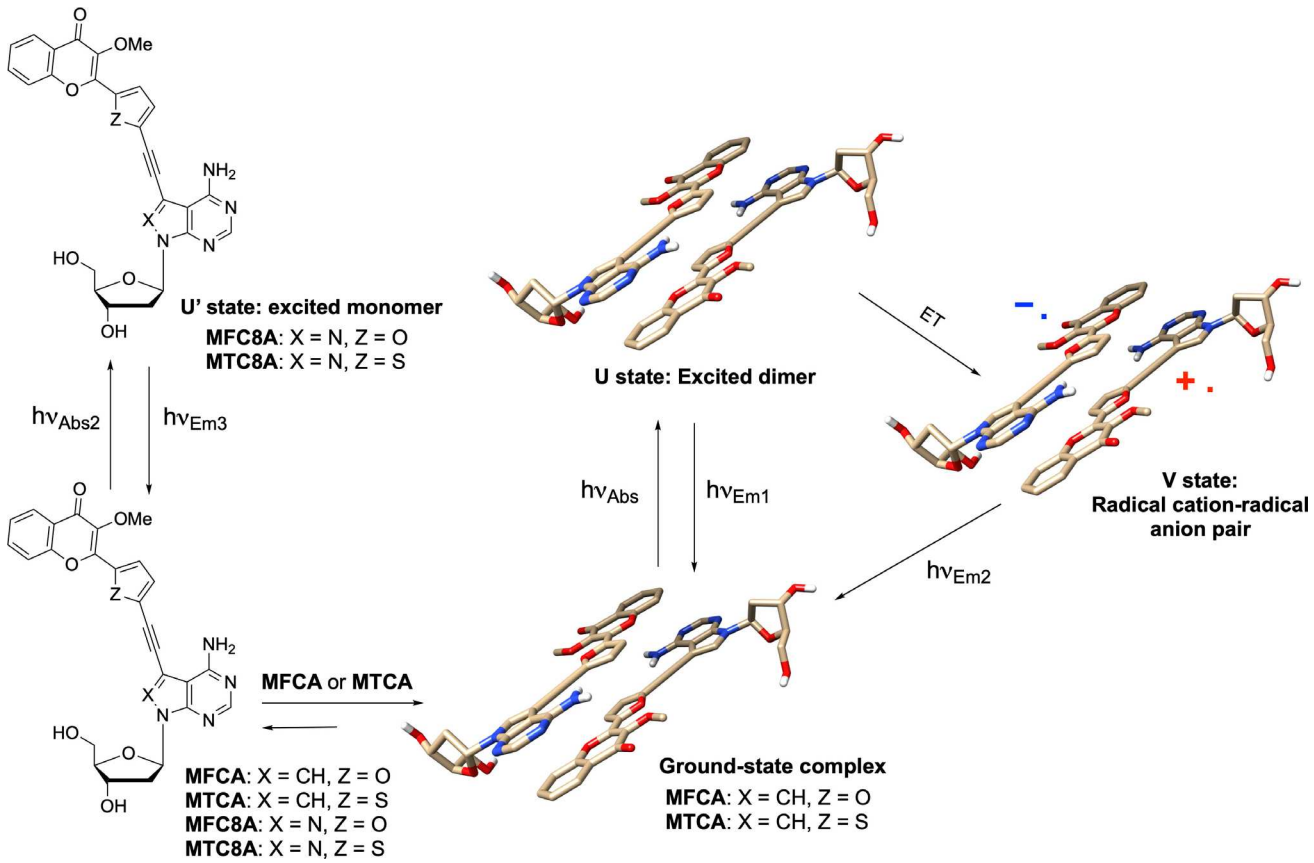

Figure 8. Schematic representation illustrating the formation of ground-state complexes favorable only for **MFCA** and **MTCA**, PET and radical ion pair products. For clarity, H-bonding with the protic solvent was not presented. The proposed representation of the dimer structure was generated from Chimera.[47]

state preformed complex. On the 100-ps time scale, this geminate radical ion pair would recombine so as to reform to the ground state, therefore quenching the already weak 580/571 emission and explaining the very low quantum yield (≈1%) of these species.

On the other hand, our data did not bring any evidence of the existence of ground-state complexes for **MTC8A** or **MFC8A**. After excitation of **MTC8A** or **MFC8A**, a multiexponential spectral relaxation is assigned to excited-state conformational relaxation producing the **U**′ excited state characterized by an emission spectrum centered at 469/464 nm and a 1-ns-long lifetime in good agreement with a high quantum yield of these nucleoside analogues in MeOH (36–38%). Interestingly, acidified solutions of **MTCA** or **MFCA** (0.5% *v/v* of TFA in MeOH) show results similar to those of **MTC8A** or **MFC8A**. A strong spectral relaxation on a comparable time scale yields to a 2-ns long-lived **U**′ state emitting fluorescence around 508/501 nm, with no sign of the 510 nm absorption characterizing the **V** state in the absence of TFA (Figures 7 and S17). As the introduction of an electron-withdrawing nitrogen at position 8, protonation of **d7A** reduces the electron-rich properties of the nucleobase, which should raise its oxidation potential. As a consequence, no ground-state complexation occurs, and the monomer keeps a long lifetime explaining the quantum yields (35–41%) of **MTCA** and **MFCA** upon acidification with TFA in MeOH (Figure 6).

Conclusions

In the field of fluorescent sensors based on donor-bridge-acceptor fluorophores, intramolecular PET is generally proposed to account for fluorescence quenching.[48–50] Our data are consistent with a different scenario. **MFCA** and **MTCA** likely form head-to-tail complexes in the ground state in polar protic solvents. Upon excitation, such configuration should be favorable for intermolecular proton-coupled PET from the electron-donor nucleobase to the electron-acceptor chromone. Photoexcitation of these complexes produces a weakly emissive and short-lived state that we assigned to a radical ion pair generated by PET, responsible for low-emission quantum yields. The question of whether the monomer itself is quenched by the intramolecular PET remains in abeyance as the photophysics of these compounds was dominated by the formation of ground-state complexes even at very low concentrations. Will through-bound electron transfer be competitive in this case?[49,50] Incorporation of **MFCA** and **MTCA** into double-stranded DNA may help to answer this question because adjacent natural nucleobases should shield the **7dA** base from complex formation while exposing the electronically coupled chromone to the major groove and water.[51] In the light of our results, it would be interesting to know if formation of poorly emissive charge-transfer complexes is particular to our compounds or more common to donor electronically coupled to acceptor.[52–54] Ad-

dressing this question could help reconsidering conjugates that may have been eliminated too quickly as fluorescent probes of biomolecular structures and interactions. On the other hand, protonation of the purine base or introduction of an electron-withdrawing nitrogen at position 8 of the nucleobase are expected to disfavor the putative electron transfer. Both approaches may certainly prevent the formation of such a complex and thus, make the monomers highly fluorescent. Introduction of the new conjugates into DNA and photophysical characterization of the labeled sequences are currently in progress.

Experimental Section

General methods

All reactions involving air- and water-sensitive conditions were performed in oven-dried glassware under argon by using Schlenk techniques employing a dual vacuum/argon manifold system and dry solvents. The synthetic intermediates were initially co-evaporated twice with toluene and dried in vacuo before use. All chemical reagents were purchased from commercial sources (Sigma–Aldrich, Acros, Alfa Aesar) and were used as supplied. Anhydrous solvents were obtained according to standard procedures.[55] The reactions were monitored simultaneously by liquid chromatography–mass spectrometry (LC-MS) and thin-layer chromatography (TLC, silica gel 60 F254 plates). Compounds were visualized on TLC plates by both UV radiation (254 and 365 nm) and spraying with a staining agent (vanillin, PMA, $KMnO_4$ or ninhydrin) followed by subsequent warming with a heat gun. Column chromatography was performed with flash silica gel (40–63 μm) with the indicated solvent system using gradients of increasing polarity in most cases.[56] All NMR spectra (^1H, ^{13}C, ^2D) were recorded on 200, 400 or 500 MHz Bruker Advance Spectrometers. ^1H NMR (200, 400 and 500 MHz) and $^{13}C\{^1H\}$NMR (50, 101 and 126 MHz, recorded with complete proton decoupling) spectra were obtained with samples dissolved in $CDCl_3$, CD_2Cl_2, CD_3OD, [D_6]DMSO, [D_6]acetone, CD_3CN or C_5D_5N with the residual solvent signals used as internal references: 7.26 ppm for $CHCl_3$, 5.32 ppm for $CDHCl_2$, 3.31 ppm for CD_2HOD, 2.50 ppm for $(CD_3)(CD_2H)S(O)$, 2.05 ppm for $(CD_3)(CD_2H)C(O)$, 1.94 ppm for CD_2HCN, 8.74 ppm for C_5D_4HN regarding ^1H NMR experiments, and 77.2 ppm for $CDCl_3$, 53.8 ppm for CD_2Cl_2, 49.0 ppm for CD_3OD, 39.4 ppm for $(CD_3)_2S(O)$, 30.8 ppm for $(CD_3)_2C(O)$, 118.7 ppm for CD_3CN, 150.3 ppm for C_5D_5N concerning ^{13}C NMR experiments.[57,58] Chemical shifts (δ) are given in ppm to the nearest 0.01 (^1H) or 0.1 ppm (^{13}C). The coupling constants (J) are given in Hertz (Hz). The signals are reported as follows: (s = singlet, d = doublet, t = triplet, m = multiplet, br = broad). Assignments of ^1H and ^{13}C NMR signals were achieved with the help of D/H exchange, COSY, DEPT, APT, HMQC, HSQC, TOCSY, NOESY, and HMBC experiments. LC-MS spectra were recorded using an ion trap Esquire 3000 Plus mass spectrometer equipped with an electrospray ionization (ESI) source in both positive and negative modes. High-resolution mass spectrometry (HRMS) was conducted with a hybrid ion trap-Orbitrap Thermo Scientific™ mass spectrometer (combining quadrupole precursor selection with high-resolution and accurate-mass Orbitrap detection) using ESI techniques. Systematic flavone and nucleoside nomenclatures are used in the Supporting Information for the assignment of each spectrum. All solvents for absorption and fluorescence experiments were of spectroscopic grade. Absorption spectra were recorded on a Cary 100 Bio UV/Vis spectrophotometer (Varian/Agilent) using Suprasil® quartz cuvettes with 1-cm path length. Stock solutions of dyes **MFCA, MTCA, MFC8A,** and **MTC8A** were prepared using DMSO. The samples used for spectroscopic measurements contained ≈0.2% *v/v* of solvents of the stock solution. Fluorescence spectra were recorded on a FluoroMax 4.0 spectrofluorometer (Jobin Yvon, Horiba) with a thermostatically controlled cell compartment at 20 ± 0.5 °C with slits open to 2 nm and were corrected for Raman scattering, lamp fluctuations and instrumental wavelength-dependent bias. Excitation wavelengths were set at the absorption maxima except when mentioned in the corresponding experiments. Redox potentials were recorded on EG&G Princeton Applied Research Model 273A. A three-electrode cell system was used for the measurements. The working, reference, and auxiliary electrodes were glassy carbon, Ag/AgCl, and platinum foil, respectively. Concerning the transient absorption (TA) experiments, the pump-probe setup for TA spectroscopy and data analysis methods have already been described elsewhere.[33,59–61] In brief, a 40-fs pulses of a Ti: sapphire regenerative amplifier (5 kHz) is used to pump a commercial optical parametric amplifier (TOPAS; Light Conversion) followed by 4th harmonic generation to produce pulses at 370 nm. The probe white-light continuum is generated in a 2-mm thick CaF_2 crystal. The polarization of the pump beam is set at the magic angle (54.7°) with respect to that of the probe. The samples were circulated through a 0.5-mm-path-length, fused silica, flow cell using a peristaltic pump. Data sets were acquired displaying the spectrally resolved (350 to 700 nm) pump-induced absorbance change ΔA as a function of pump-probe delay. All TA data presented here are post-processed in order to *(i)* subtract the "solvent" signal around time-zero resulting from the coherent interaction of pump and probe laser fields, and *(ii)* compensate for the group velocity dispersion in the probe beam—independently determined from the pure solvent signal—so as to define time-zero accurately (within ≈20 fs) at all wavelengths. Singular value decomposition (SVD) was used for data reduction and noise filtering. Global fitting of the 5 dominant singular traces was performed. The fitting function was a sum of exponential decaying functions convolved with a normalized Gaussian curve of standard deviation σ standing for the temporal instrument response function (IRF). The residuals of the fits of the 5 dominating singular transients were structureless, and of amplitude similar to or larger than that of the 6th and 7th singular transients, justifying that only the first five singular transients were considered as significant in this global analysis. The result of the global fitting was analyzed by computing and displaying the Decay-Associated Spectra (DAS). Each decay time constant is associated to a DAS representing the spectral dependence of the prefactor of this decay component in the original 2D data set. The DAS reveal the spectral evolution occurring within their associated time constant, along the course of the molecule photoreaction. Supplementary data associated with this article, including the experimental protocols of intermediates and target compounds, some ^1H, ^{13}C, ^1H–^1H COSY, ^1H–^1H NOESY, ^1H–^{13}C HSQC, and ^1H–^{13}C HMBC NMR spectra of derivatives previously mentioned as well as additional photophysical characterization, can be consulted in the Supporting Information.

Acknowledgements

We thank Dr. Sandra Olivero for her support to cyclic voltammetry. We are grateful for the ANR (UCAJEDI project: ANR-15-IDEX-01; ANR-12-BS08-0003-02) and the French Government concerning the PhD grants of H.-N.L., S.V. and G.B., respectively. This research program was financially supported by the ANR

(ANR-12-BS08-0003-02, ANR-15-CE11-0006 "PICO2", ANR-11-LABX-0058_NIE) and PACA region (DNAfix-2014-02862).

Conflict of interest

The authors declare no conflict of interest.

Keywords: deoxyadenosine probes · fluorescence · ground-state complexes · photoinduced electron transfer · push–pull dyes

[1] K. Nakatani, Y. Tor in *Modified nucleic acids, nucleic acids and molecular biology series, Vol. 31* (Eds.: K. Nakatani, Y. Tor), Springer International Publishing, Cham **2016**. p. 276.
[2] M. S. Gonçalves, *Angew. Chem. Int. Ed.* **2017**, *56*, 4655; *Angew. Chem.* **2017**, *129*, 4727.
[3] W. Xu, K. M. Chan, E. T. Kool, *Nat. Chem.* **2017**, *9*, 1043 – 1055.
[4] S. De Ornellas, J. M. Slattery, R. M. Edkins, A. Beeby, C. G. Baumann, I. J. S. Fairlamb, *Org. Biomol. Chem.* **2015**, *13*, 68 – 72.
[5] H. Cahová, R. Pohl, L. Bednárová, K. Nováková, J. Cvačka, M. Hocek, *Org. Biomol. Chem.* **2008**, *6*, 3657 – 4.
[6] L. M. Wilhelmsson, *Q. Rev. Biophys.* **2010**, *43*, 159 – 183.
[7] A. M. Agafontsev, A. Ravi, T. A. Shumilova, A. S. Oshchepkov, E. A. Kataev, *Chem. Eur. J.* **2019**, *25*, 2684 – 2694.
[8] A. Dumas, G. Mata, N. W. Luedtke in *Fluorescent Analogues of Biomolecular Building Blocks: Design and Applications.* Hoboken, Wiley, Hoboken, **2016**. pp. 242 – 275.
[9] B. Y. Michel, D. Dziuba, R. Benhida, A. P. Demchenko, A. Burger, *Front. Chem.* **2020**, *8*, 112.
[10] V. G. Pivovarenko, O. Bugera, N. Humbert, A. S. Klymchenko, Y. Mély, *Chem. Eur. J.* **2017**, *23*, 11927 – 11934.
[11] N. P. F. Barthes, I. A. Karpenko, D. Dziuba, M. Spadafora, J. Auffret, A. P. Demchenko, Y. Mely, R. Benhida, B. Y. Michel, A. Burger, *RSC Adv.* **2015**, *5*, 33536 – 33545.
[12] N. P. F. Barthes, K. Gavvala, D. Dziuba, D. Bonhomme, I. A. Karpenko, A. S. Dabert-Gay, D. Debayle, A. P. Demchenko, R. Benhida, B. Y. Michel, A. Burger, *J. Mater. Chem. C* **2016**, *4*, 3010 – 3017.
[13] H.-N. Le, C. Zilio, G. Barnoin, N. P. F. Barthes, J.-M. Guigonis, N. Martinet, B. Y. Michel, A. Burger, *Dyes Pigm.* **2019**, *170*, 107553.
[14] D. R. Weinberg, C. J. Gagliardi, J. F. Hull, C. F. Murphy, C. A. Kent, B. C. Westlake, A. Paul, D. H. Ess, D. G. McCafferty, T. J. Meyer, *Chem. Rev.* **2012**, *112*, 4016 – 4093.
[15] J. R. Lakowicz in *Principles of fluorescence spectroscopy*, 3rd ed, Springer, New York, **2006**. p. 954.
[16] C. A. M. Seidel, A. Schulz, M. H. M. Sauer, *J. Phys. Chem.* **1996**, *100*, 5541 – 5553.
[17] F. Seela, S. S. Pujari, *Bioconjugate Chem.* **2010**, *21*, 1629 – 1641.
[18] T. Aso, K. Saito, A. Suzuki, Y. Saito, *Org. Biomol. Chem.* **2015**, *13*, 10540 – 10547.
[19] D. Dziuba, I. A. Karpenko, N. P. F. Barthes, B. Y. Michel, A. S. Klymchenko, R. Benhida, A. P. Demchenko, Y. Mély, A. Burger, *Chem. Eur. J.* **2014**, *20*, 1998 – 2009.
[20] F. Seela, M. Zulauf, *Synthesis* **1996**, 726 – 730.
.
[21] M. Torimura, S. Kurata, K. Yamada, T. Yokomaku, Y. Kamagata, T. Kanagawa, R. Kurane, *Anal. Sci.* **2001**, *17*, 155 – 160.
[22] D. Rehm, A. Weller, *Isr. J. Chem.* **1970**, *8*, 259 – 271.
[23] B. Calitree, D. J. Donnelly, J. J. Holt, M. K. Gannon, C. L. Nygren, D. K. Sukumaran, J. Autschbach, M. R. Detty, *Organometallics* **2007**, *26*, 6248 – 6257.
[24] Y. Koide, Y. Urano, K. Hanaoka, T. Terai, T. Nagano, *ACS Chem. Biol.* **2011**, *6*, 600 – 608.
[25] R. A. Marcus, *J. Chem. Phys.* **1956**, *24*, 966 – 978.
[26] R. A. Marcus, *Can. J. Chem.* **1959**, *37*, 155 – 163.
[27] N. J. Turro, V. Ramamurthy, J. C. Scaiano, *Principles of Molecular Photochemistry: an Introduction*, University Science Books, Philadelphia, **2009**.
[28] C. Reichardt, *Chem. Rev.* **1994**, *94*, 2319 – 2358.
[29] J. Catalán, *J. Phys. Chem. B* **2009**, *113*, 5951 – 5960.
[30] S. M. Ormson, R. G. Brown, F. Vollmer, W. Rettig, *J. Photochem. Photobiol. A* **1994**, *81*, 65 – 72.
[31] V. V. Shynkar, A. S. Klymchenko, E. Piémont, A. P. Demchenko, Y. Mély, *J. Phys. Chem. A* **2004**, *108*, 8151 – 8159.
[32] A. Sougnabé, D. Lissouck, F. Fontaine-Vive, M. Nsangou, Y. Mély, A. Burger, C. A. Kenfack, *RSC Adv.* **2020**, *10*, 7349 – 7359.
[33] A. I. Skilitsi, D. Agathangelou, I. Shulov, J. Conyard, S. Haacke, Y. Mély, A. Klymchenko, J. Léonard, *Phys. Chem. Chem. Phys.* **2018**, *20*, 7885 – 7895.
[34] M. H. V. Huynh, T. J. Meyer, *Chem. Rev.* **2007**, *107*, 5004 – 5064.
[35] B. Ma, P. I. Djurovich, M. E. Thompson, *Coord. Chem. Rev.* **2005**, *249*, 1501 – 1510.
[36] P.-O. Gendron, F. Avaltroni, K. J. Wilkinson, *J. Fluoresc.* **2008**, *18*, 1093 – 1101.
[37] T. Dertinger, V. Pacheco, I. von der Hocht, R. Hartmann, I. Gregor, J. Enderlein, *ChemPhysChem* **2007**, *8*, 433 – 443.
[38] I. R. Gould, R. H. Young, R. E. Moody, S. Farid, *J. Phys. Chem.* **1991**, *95*, 2068 – 2080.
[39] I. R. Gould, R. H. Young, L. J. Mueller, S. Farid, *J. Am. Chem. Soc.* **1994**, *116*, 8176 – 8187.
[40] I. R. Gould, D. Noukakis, L. Gomez-Jahn, R. H. Young, J. L. Goodman, S. Farid, *Chem. Phys.* **1993**, *176*, 439 – 456.
[41] K. K. Mentel, R. M. D. Nunes, C. Serpa, L. G. Arnaut, *J. Phys. Chem. B* **2015**, *119*, 7571 – 7578.
[42] J. Eriksen, C. S. Foote, *J. Phys. Chem.* **1978**, *82*, 2659 – 2662.
[43] A. R. Melnikov, E. V. Kalneus, V. V. Korolev, I. G. Dranov, A. I. Kruppa, D. V. Stass, *Photochem. Photobiol. Sci.* **2014**, *13*, 1169 – 1179.
[44] J. Qi, D. Liu, X. Liu, S. Guan, F. Shi, H. Chang, H. He, G. Yang, *Anal. Chem.* **2015**, *87*, 5897 – 5904.
[45] S. Chatterjee, W. Pathmasiri, O. Plashkevych, D. Honcharenko, O. P. Varghese, M. Maiti, J. Chattopadhyaya, *Org. Biomol. Chem.* **2006**, *4*, 1675 – 1686.
[46] M. L. Horng, J. A. Gardecki, A. Papazyan, M. Maroncelli, *J. Phys. Chem.* **1995**, *99*, 17311 – 17337.
[47] E. F. Pettersen, T. D. Goddard, C. C. Huang, G. S. Couch, D. M. Greenblatt, E. C. Meng, T. E. Ferrin, *J. Comput. Chem.* **2004**, *25*, 1605 – 1612.
[48] D. Escudero, *Acc. Chem. Res.* **2016**, *49*, 1816 – 1824.
[49] A. C. Benniston, A. Harriman, *Chem. Soc. Rev.* **2006**, *35*, 169 – 179.
[50] G. L. Closs, J. R. Miller, *Science* **1988**, *240*, 440 – 447.
[51] F. Seela, H. Xiong, P. Leonard, S. Budow, *Org. Biomol. Chem.* **2009**, *7*, 1374 – 1387.
[52] P. Trojanowski, J. Plötner, C. Grünewald, F. F. Graupner, C. Slavov, A. J. Reuss, M. Braun, J. W. Engels, J. Wachtveitl, *Phys. Chem. Chem. Phys.* **2014**, *16*, 13875 – 13888.
[53] Y. Saito, R. H. E. Hudson, *J. Photochem. Photobiol. C* **2018**, *36*, 48 – 73.
[54] P. Leonard, D. Kondhare, X. Jentgens, C. Daniliuc, F. Seela, *J. Org. Chem.* **2019**, *84*, 13313 – 13328.
[55] W. L. F. Armarego, C. L. L. Chai in *Purification of Laboratory Chemicals*, 7th ed., Butterworth-Heinemann, Oxford, **2012**, p. 1024.
[56] W. C. Still, M. Kahn, A. Mitra, *J. Org. Chem.* **1978**, *43*, 2923 – 2925.
[57] H. E. Gottlieb, V. Kotlyar, A. Nudelman, *J. Org. Chem.* **1997**, *62*, 7512 – 7515.
[58] G. R. Fulmer, A. J. M. Miller, N. H. Sherden, H. E. Gottlieb, A. Nudelman, B. M. Stoltz, J. E. Bercaw, K. I. Goldberg, *Organometallics* **2010**, *29*, 2176 – 2179.
[59] J. Briand, O. Bräm, J. Réhault, J. Léonard, A. Cannizzo, M. Chergui, V. Zanirato, M. Olivucci, J. Helbing, S. Haacke, *Phys. Chem. Chem. Phys.* **2010**, *12*, 3178 – 3187.
[60] C. García-Iriepa, M. Gueye, J. Léonard, D. Martínez-López, P. J. Campos, L. M. Frutos, D. Sampedro, M. Marazzi, *Phys. Chem. Chem. Phys.* **2016**, *18*, 6742 – 6753.
[61] M. Paolino, M. Gueye, E. Pieri, M. Manathunga, S. Fusi, A. Cappelli, L. Latterini, D. Pannacci, M. Filatov, J. Léonard, M. Olivucci, *J. Am. Chem. Soc.* **2016**, *138*, 9807 – 9825.

Manuscript received: July 23, 2020
Accepted manuscript online: August 6, 2020
Version of record online: ■■ ▮▮, 0000

Full Paper
doi.org/10.1002/chem.202003456

FULL PAPER

Yin and yang PET: intramolecular photoinduced electron transfer (PET) is often responsible for fluorescence quenching of many dyes. Herein, a different scenario has emerged for our push-pull nucleosides. These fluorophores preform a ground-state complex with a head-to-tail arrangement evidencing an intermolecularly controllable process. Ultimately, these results could help reconsider several useful dyes as well as guide the development of advanced adenine-based probes.

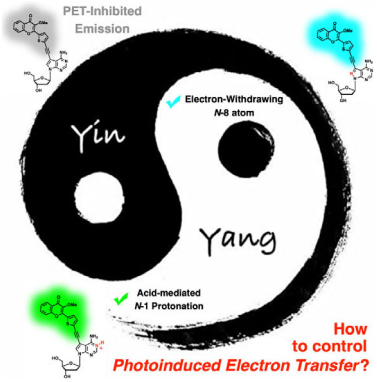

Electron Transfer

H.-N. Le, J. Brazard, G. Barnoin, S. Vincent, B. Y. Michel, J. Leonard, A. Burger**

■■ – ■■

Control of Intermolecular Photoinduced Electron Transfer in Deoxyadenosine-Based Fluorescent Probes

Overall, the PET reactions between **dA** analogs and the chromone dyes can be controlled by a couple of approaches. On one side, to avoid PET, **8d7A** is recommended rather than **d7A**. This is mainly due to the higher oxidation potential of the former to the latter. On the other hand, PET reaction between **d7A-3MC** conjugates could be inhibited under acidic conditions. The question is still arising of whether the incorporation of **d7A-3MC** conjugates into ODN could stop the ground-state complex formation and hence the intermolecular PET process.

2.3. Dual-emissive analogs of 8-aza-7-deazadeoxyadenosine with the capability to report hydration and electron transfer in DNA

Abstract

In this chapter, we report the development of dual-emissive analogs of deoxyadenosine (**dA**) with great potential for sensing DNA-related processes. The two modified nucleosides were synthesized through a scalable route with appreciable yields. Both of them have absorption maxima around 380–400 nm with good brightness even in aqueous media. Moreover, they have suitable pKa and hydration sensitivity to probe DNA, especially **FC8A**, which exhibits a remarkable linear response to hydration. For this reason, a phosphoramidite bearing **FC8A** was synthesized, and the dye was used to label different oligonucleotides (ODN) sequences. The fluorophore showed minor effects on the structure and stability of DNA, as confirmed by circular dichroism (CD) and melting temperature (Tm) experiments. In the double-stranded (ds) environment, the hydration reporter maintains its attractive features such as satisfying quantum yields and unique ratiometric response. Its dual emission not only responded to changes in environmental stimuli but also to the process of electron transfer along the duplex. This latter parameter made the probe unique in view of several applications, such as the discrimination of the mismatched contexts and the detection of DNA conformational changes. Considering all this, the two-color probe turns out to be prospective for bringing new insights in the study electron transport in DNA.

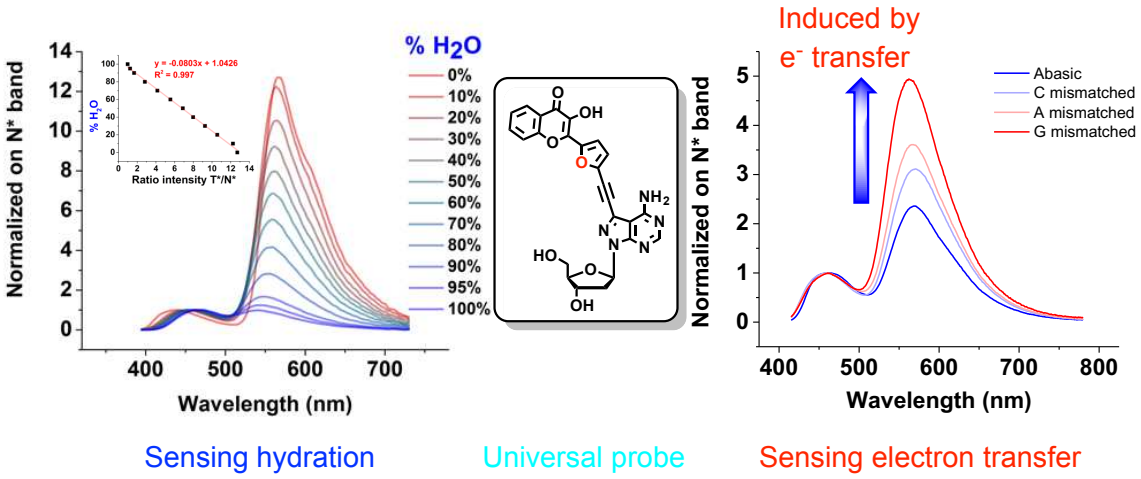

2.3.1. Introduction

As described previously, the push–pull conjugates **MTCA** and **MFCA** (Figure 3.1) showed low QYs in protic solvents such as MeOH. These dyes were constructed from **d7A** (an electron-rich analog of **dA**) and 3-methoxychromone (**3MC**), **MTC** or **MFC**. The conjugated nucleobase forms a ground-state complex, even in the nM range, which promotes an intermolecular PET reaction in protic solvents, leading to a strongly quenched fluorescence. On the one hand, the formation of the ground-state complex and the quenching due to PET could be inhibited under acidic conditions. On the other hand, conjugates between **8d7A**, an analog of **d7A** with a higher oxidation potential, and **3MC** dyes showed no evidence of ground-state complex formation and fluorescence quenching due to PET. Therefore, we selected the **8d7A** platform to connect the 3-hydroxychromone fluorophore (**TC** or **FC**) in order to engineer our dual-emissive analogs of **dA**, given that ESIPT originates from the dual-emissive feature of **3HC** dyes (Scheme 3.1).

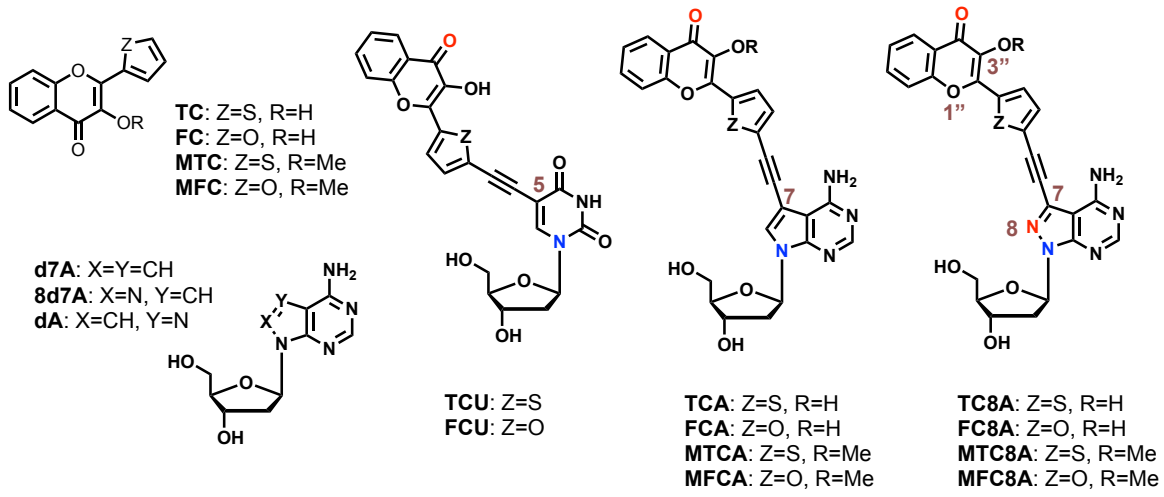

Figure 3.1. Structures of parent chromones and modified nucleosides referring to this study.

Herein, we report the development of dual-emissive **dA** analogs based on the **8d7A** skeleton. The design and retrosynthesis were depicted in Scheme 3.2. First of all, the nucleosides were synthesized, and their photophysical properties were characterized by absorption and steady-state fluorescence spectroscopy. Secondly, a phosphoramidite bearing **FC8A** was synthesized. Then, different oligonucleotides (ODN) sequences labeled with **FC8A** were synthesized via the phosphoramidite approach. Finally, the sequences were studied to demonstrate the potential of our probe for studying DNA-related processes.

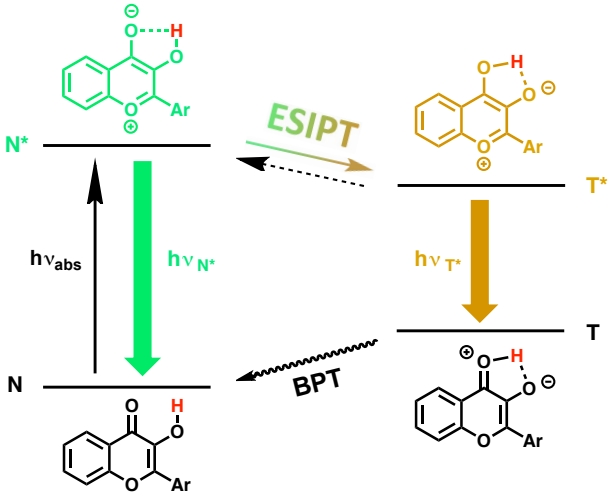

Scheme 3.1. The four-level diagram for a typical ESIPT reaction of **3HC**. *BPT denotes Back Proton Transfer.*

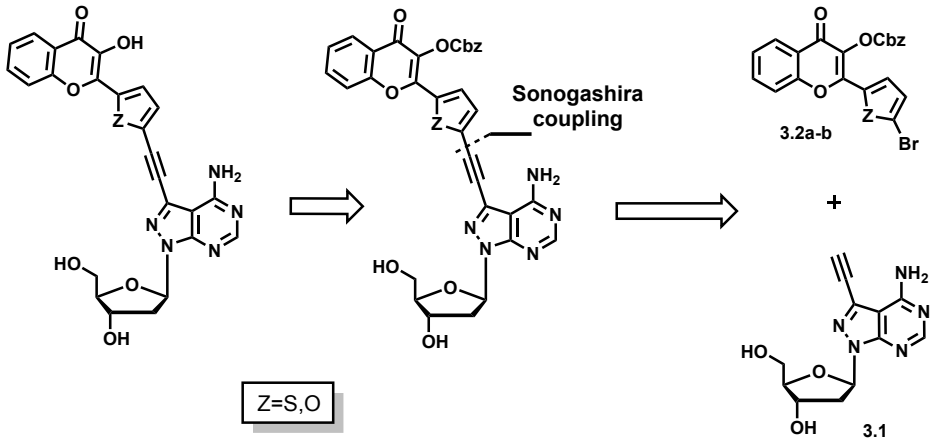

Scheme 3.2. Retrosynthesis of the two dual-emissive nucleosides used in this study.

2.3.2. Results and Discussion

2.3.2.1. Synthesis and characterization of the nucleosides

Synthesis

The two nucleosides (**TC8A** and **FC8A**) were synthesized via a two-step procedure starting from the key intermediate **3.1** (Schemes 3.2 and 3.3). This intermediate was synthesized according to our previous report.[1] The first step was a Sonogashira coupling in DMF, which gave the conjugated intermediates **3.3a–b** in good yields (70 and 73%). DMF was used as a solvent to ensure solubility of both starting material and product. Column chromatography was performed to obtain the products with good purity for the next step. The intermediates **3.3a–b** were then reacted in a saturated solution of NH_3 in MeOH to afford the final deprotected nucleosides in good yields (73 and 78%). The products were isolated and purified by

crystallization several times in different solvent mixtures (see SI) to ensure high purity for photophysical characterization.

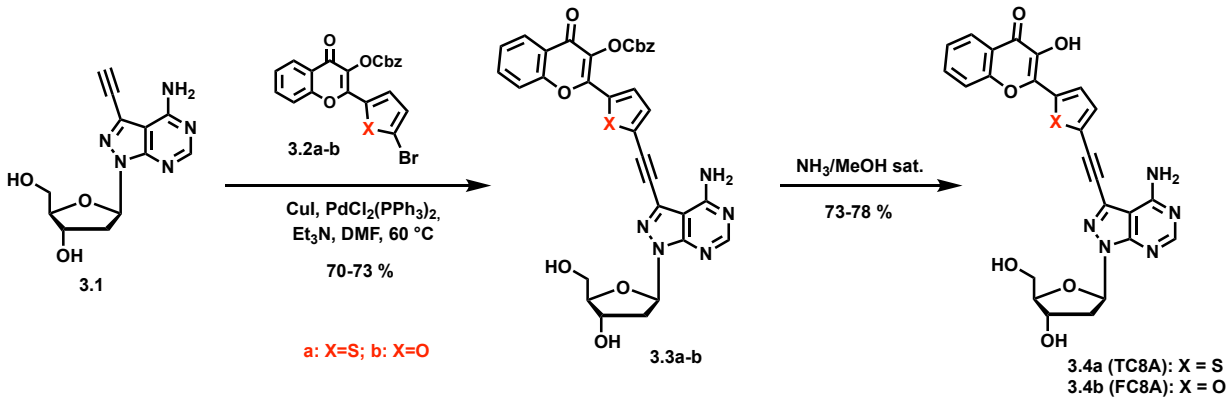

Scheme 3.3. Synthesis of the modified nucleosides.

General photophysics

Absorption and emission spectra of the two nucleosides (**TC8A** and **FC8A**) were measured in different solvents covering a wide range of polarity from toluene to water and HFIP. Solvents' polarity was reported according to the Dimroth–Reichardt polarity index.[2] This empirical scale takes into account the contributions of the dielectric constant and H-bond donor ability of the solvent. The main photophysical data were presented in Table 3.1.

Table 3.1. Photophysical properties of the two nucleosides in different solvents.

Solvent	$E_T(30)$[a]	λAbs[b]		λN^*[c]		λT^*[d]		I_{T^*}/I_{N^*}[e]		Φ[f]	
		TC8A	*FC8A*	*TC8A*	*FC8A*	*TC8A*	*FC8A*	*TC8A*	*FC8A*	*TC8A*	*FC8A*
HFIP	65.3	392	383	466	462	516	501	0.86	0.95	21	35
H_2O	63.1	384	387	471	468	554	542	2.20	0.96	1[g]	6
MeOH	55.4	388	381	462	453	572	568	4.73	3.99	20	20
EtOH	51.9	390	382	462	455	577	567	5.92	5.93	21	23
BuOH	50.2	394	386	456	448	576	569	8.06	6.50	32	26
iPrOH	49.2	391	383	462	443	577	568	8.87	8.65	25	25
ACN	45.6	387	377	451	440	575	566	6.39	12.71	23	23
DMSO	45.1	397	389	456	444	582	575	15.95	9.84	27	22
Acetone	42.2	388	378	451	439	578	569	4.64	9.18	17	29
DCM	40.7	390	383	427	441	575	564	9.56	22.61	12	31
EA	38.1	387	381	425	415	578	568	6.41	14.01	26	30
THF	37.4	390	383	429	419	580	571	3.31	6.28	31	36
Dioxane	36	391	382	427	417	582	572	1.95	5.37	26	30
Toluene	33.9	391	386	431	427	582	572	18.09	18.04	22	28

[a] Solvent polarity; [b] Absorption maximum; [c] Maximum of N* emission; [d] Maximum of T* emission; [e] I_{T^*}/I_{N^*} Ratio intensity of the two emission bands at their maxima; [f] Quantum yields

determined by using *p*-dimethylaminoflavone (dMAF, Φ=0.27) in EtOH as a standard reference. Excitation wavelengths were at 390 and 380 nm for **TC8A** and **FC8A**, respectively; [g] Low value was likely due to the poor solubility of **TC8A** in water.

The absorption spectra of the nucleosides showed favorable properties comparing to the parent **3HC** dyes. **TC8A** and **FC8A** absorbed light at the border of UV and visible region with absorption maxima around 377–394 nm (Figure 3.2), red-shifted ca. 30 nm. The two nucleosides have extinction coefficients of around 40,000 $cm^{-1}.M^{-1}$, two-fold of the value for **TC** or **FC**.[3] The extension of conjugation for the parent **3HC**'s electronic system via the C≡C triple bond, C7=N8 double bond, and N9 (see the structures in Figure 3.1) was responsible for such improvements. Noticeably, their absorption maxima showed little dependence on the solvents' polarity, indicating a weak dipole moment of the dyes in the ground-state (Figure 3.2).[4,5] These results parallel what we observed for the corresponding methoxy derivatives, **MTC8A** and **MFC8A** (structures are given in Figure 3.1).[1]

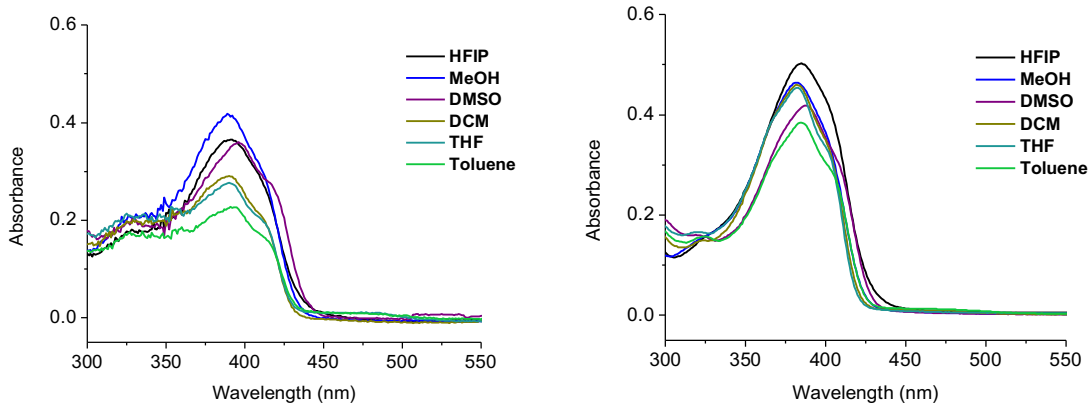

Figure 3.2. Absorption spectra of **TC8A** (left) and **FC8A** (right) in a set of solvents covering a wide range of polarity.

In terms of emission spectra, the removal of the methyl group restored the dual emission of **3HC**s. Indeed, the two dyes showed two well-resolved bands in all solvents studied with acceptable QYs (0.12–0.36), except in water likely due to poor solubility of the dyes in this solvent. At around 417–470 nm, the emissive band was assigned to the N* band, and around 500–570 nm to the T* band. Interestingly, the compounds showed good QYs in polar protic solvents such as MeOH (QY ca. 0.2, approximately 2.5 to 5-fold of the QYs reported for the parent **3HC**s in the same solvent)[3,6] indicating the lack of PET in these conjugated systems. These results are in line with the QYs observed for **MTC8A** and **MFC8A**, where the PET process was absent.

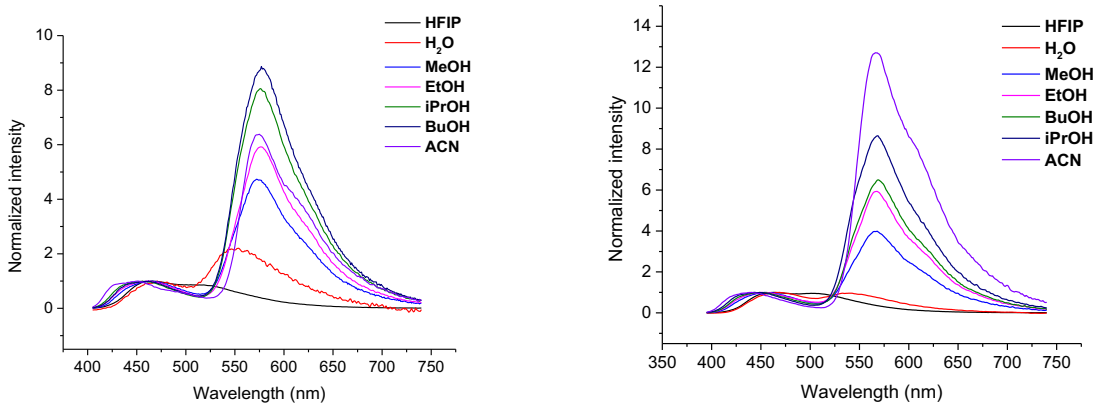

Figure 3.3. Normalized mission spectra on N* band of **TC8A** (left) and **FC8A** (right) in ACN and protic solvents.

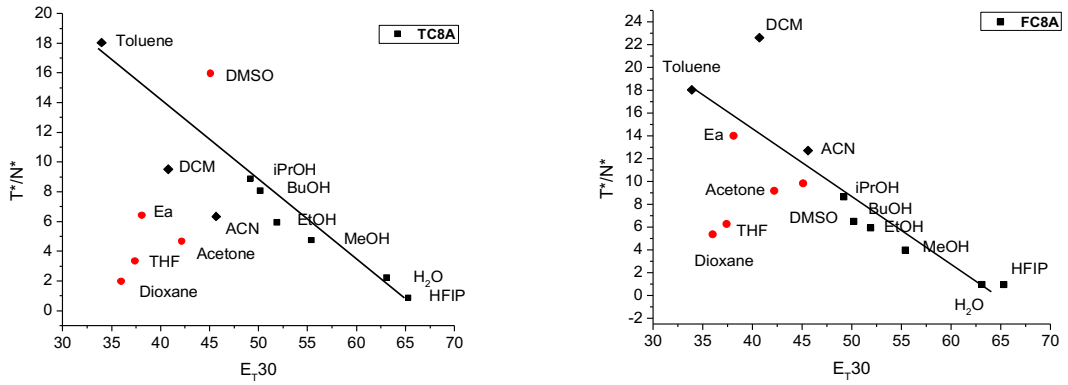

Figure 3.4. Effect of solvents' polarity on the ratios of intensity T*/N*: **TC8A** (left), **FC8A** (right). ■, ◆, and ● represent protic, neutral, and basic solvents, respectively.

The fluorescence spectra of these nucleosides showed a strong solvent dependence. The emission of the T* form is dominating in all solvents except in the highly acidic HFIP and water. Noticeably, in apolar solvents such as toluene and dioxane, the N* band shows some vibrational characters or local excited (LE) emission indicating a low dipole moment (or lack of intramolecular charge transfer (ICT)) in the excited state corresponding to the N* band in such apolar solvents (Figure S1).[7] The small redshift of the N* band accompanying the solvent change from the apolar toluene to the polar CH_3CN (13–20 nm) further confirmed the low dipole moment of the N* form. The above results indicated that the N* form is more stabilized than the N form, while the T form is more stabilized than the T* form during the interaction with polar solvents (demonstrated in Scheme 3.4).[8] In protic and neutral aprotic solvents, the intensity ratio I_{T^*}/I_{N^*} of both dyes decreased gradually with increasing $E_T(30)$ values from 18 in toluene to about 0.9 in HFIP. This observation suggests that ESIPT and, therefore, the formation of the T* form is slowed down in particular in polar protic solvents, as for its analogs 2-(2-furyl)-3-hydroxychromone and 2-(2-thienyl)-3-hydroxychromone.[9,10] The importance of

H-bonding on ESIPT could be seen with a sharp increase of the intensity ratio I_{T*}/I_{N*} of **FC8A** and **TC8A** in acetonitrile as compared to methanol (see also Figure 3.3), though both solvents possess similar dielectric constants. The inhibition of ESIPT reaction with increasing proticity of the solvent is a well-known character of **3HC**.[11,12] Interestingly, the ratio I_{T*}/I_{N*} displayed a linear relationship to the polarity of protic solvents, indicating an appropriate sensitivity range of the dyes for biological applications. The impact of H-bond donor solvents, especially water and HFIP, could also be seen from the blueshift of the T* band. Scheme 3.5 tentatively explains the importance of H-bond interactions on the ESIPT reaction, which is discussed in the hydration study chapter that follows.

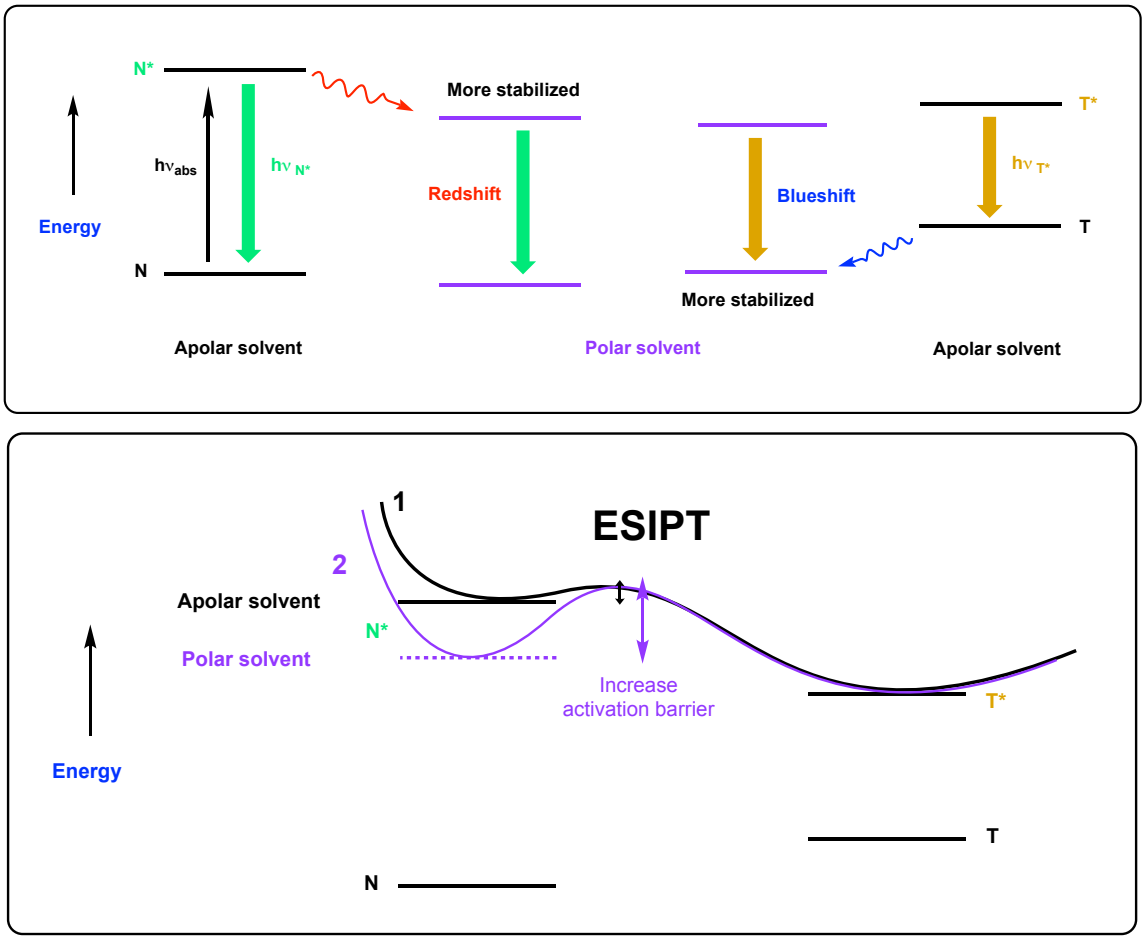

Scheme 3.4. Different stabilization effects on the four molecular orbitals (MO) of an ESIPT reaction due to polar solvent (top). Effect of polar solvent on the dynamic of the ESIPT reaction (bottom). The stabilization by polar solvent slows down the ESIPT by increasing the activation barrier of the reaction. The potential energy curve of the ESIPT reaction in polar solvent is depicted in purple.

Deviation from linearity of the intensity ratios versus $E_T(30)$ was noticed in aprotic solvents presenting strong H-bond acceptor ability (basicity) as DMSO, THF, EtOAc, acetone, and dioxane. This deviation indicates that basic aprotic solvents can hamper the ESIPT reaction in **FC8A** and **TC8A**, likely by disrupting the intramolecular H-bonding arrangement. To be more

precise, H-bonding between the basic solvent and the ESIPT proton of hydroxychromone should slow down the ESIPT reaction leading to a decrease of the I_{T*}/I_{N*} ratio, which is in good agreement with the results obtained in these solvents (Figure 3.4 and 3.5). We do not fully understand the exception observed for **TC8A** in DMSO (Figure 3.4). This exception suggests that other parameters may also affect the I_{T*}/I_{N*} ratio. Perturbation of ESIPT in aprotic-basic solvents is common for hydroxyquinolone derivatives[13] but was not usually observed for **3HC** dyes, except for the **dU** analog and some **thienyl-3HCs**.[3,14-16] In contrast to other **3HCs**, **FC8A** and **TC8A** possess relatively high quantum yields in these solvents likely indicating that the disrupted H-bonding solute-solvent complexes are emissive.

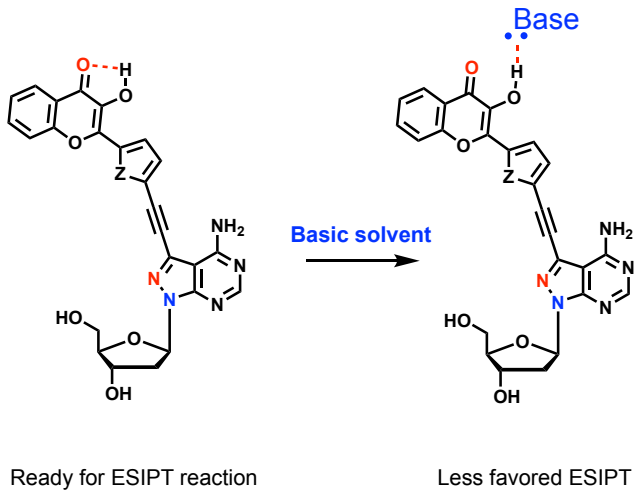

Figure 3.5. The attenuating effect of basic solvent on the ESIPT reaction. The outcome of this effect is the decrease of I_{T*}/I_{N*} compared to that in solvent of equal polarity. (Adapted from ref[16])

Hence, the dyes showed several improvements compared to the parent **3HC** dyes such as redshifts of absorption and emission, increased extinction coefficient, and improved QYs in polar protic solvents; while retaining the appropriate range of sensitivity, in protic solvents, of the parents **3HC** dyes.

Hydration study

Since the nucleoside analogs were designed for DNA labeling and sensing hydration, their photophysical properties were characterized in different mixtures of H_2O in MeCN from 100 to 0%. In all cases, dual emission was observed and the two emission bands were well-resolved from each other (Figure 3.6). This is a well-known character of the parent **TC** and **FC** dyes. These results are in sharp contrast from what we observed for the **dU** conjugates, as the two bands merged in a single band at high water concentration due to the redshift and blueshift of the N* and T* bands, respectively. Remarkably, **FC8A** demonstrated a linear relationship over the entire concentration range (Figure 3.6). The linear response is quite unique, as it was not observed in other studies related to other **3HC** dyes.[3,17,18] For example, a linear relationship was obtained only when $\log(I_{N*}/I_{T*})$ was plotted against water concentration for some **3HC**

dyes,[18] while we report a linear response directly of I_{T^*}/I_{N^*}, not the log scale of the ratio. Surprisingly, the linear response did not hold for **TC8A** at low concentration of water indicating preferential solvent-solute interactions (Figure 3.7). Such effect is known as the preferential solvation effect and was detected for other **3HC** dyes.[18] Moreover, the dyes show average quantum yields (0.11-0.14) up to 80% water.

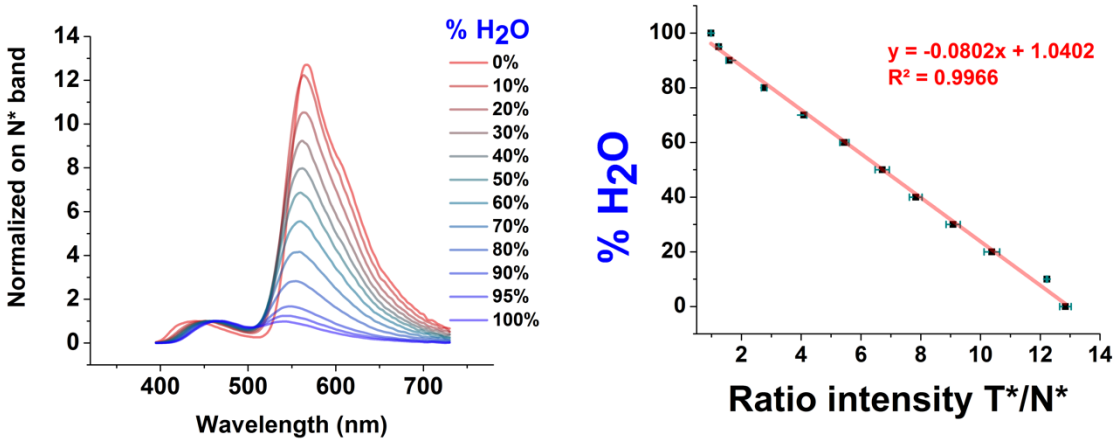

Figure 3.6. Hydration study of **FC8A**. Normalized emission spectra at N* maxima, 0% water corresponds to 100% MeCN, and so on (left). Plotting percentage of H_2O to ratio intensity T*/N* (right).

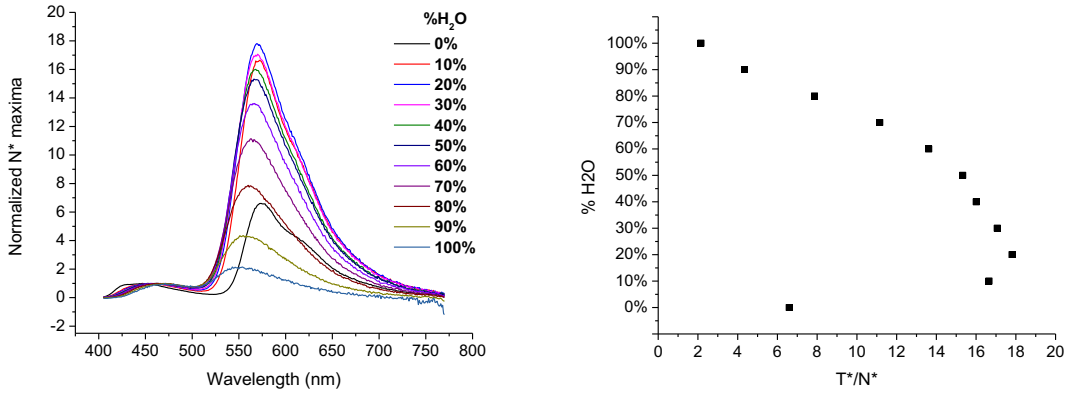

Figure 3.7. Hydration study of **TC8A**. Normalized emission spectra at N* maxima, 0% water corresponds to 100% MeCN, and so on (left). Plotting percentage of H_2O to ratio intensity T*/N* (right).

The high sensitivity to hydration of the two dyes correlates with studies realized on the parent **TC** and **FC** dyes, **dU** analogs and other derivatives of **3HCs** for which a model was proposed.[9,17-19] This model is represented in Scheme 3.5 and shows specific H-bonds of water molecules with the oxygens of the electron-rich carbonyl and phenoxide of the chromone. In water solution, hydrated and non-hydrated species are in equilibrium. The four species are emissive; however, dual emission is generally observed because the emissions of each hydrated

and non-hydrated form collapse in a single band. For the hydrated normal form, the energy barrier is considerably increased compared to that of the non-hydrated N* form leading to inhibition of proton transfer.[9] Thus the more hydrated the medium, the more abundant the hydrated N* form, the less proton transfer and the more intense the emission band of the normal form compared to that of the tautomer (I_{T*}/I_{N*} decreases). Growing water concentration also favors H-bonding of the T species leading to a blueshift of the low energy emission band.

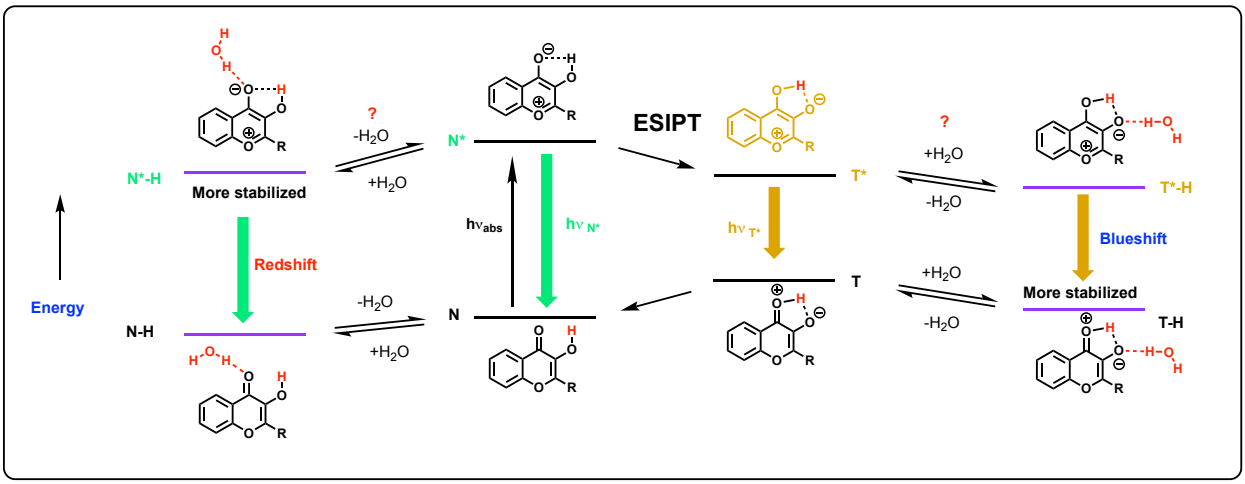

Scheme 3.5. Schematic explanation of the redshifts of N* bands and the blueshifts of T* bands causing by water.

pKa determination

3HC dyes can exist in either the neutral or anionic form as the consequence of deprotonation of the 3-OH group (Figure 3.1). The equilibrium between the two forms depends on the pH of the solution and the pKa of the dye. Since our objective was the incorporation of the **3HC** conjugate into ODNs for studies in buffered solutions, the pKa of the 3-OH group is an important value that needs to be considered.[20,21] The pKas of the dyes were determined using absorption spectra in aqueous solutions at different pH. The dye was first dissolved in a basic aqueous solution at pH around 14 to give the anionic form (λ_{max} around 450 nm). Then pH was adjusted by aqueous HCl with the total added volume kept smaller than 5% volume of the above solution to ensure a constant dye's concentration. The spectra of **TC8A** and **FC8A** showed isosbestic points at 335, 357, 409 nm (Figure 3.8 – top), and at 350, 401 nm (Figure 3.8 – bottom), respectively. These observations are in line with the fact that the neutral and anionic species are under equilibrium. The pKas were obtained by fitting the absorbance at 458 nm and 442 nm using the Boltzmann function to give 8.8 and 8.1 for **TC8A** and **FC8A**, respectively. Importantly, at pH 7.0–7.2, these dyes exist mostly in the corresponding normal forms, Figure 3.8, which favored their application for DNA sensing.

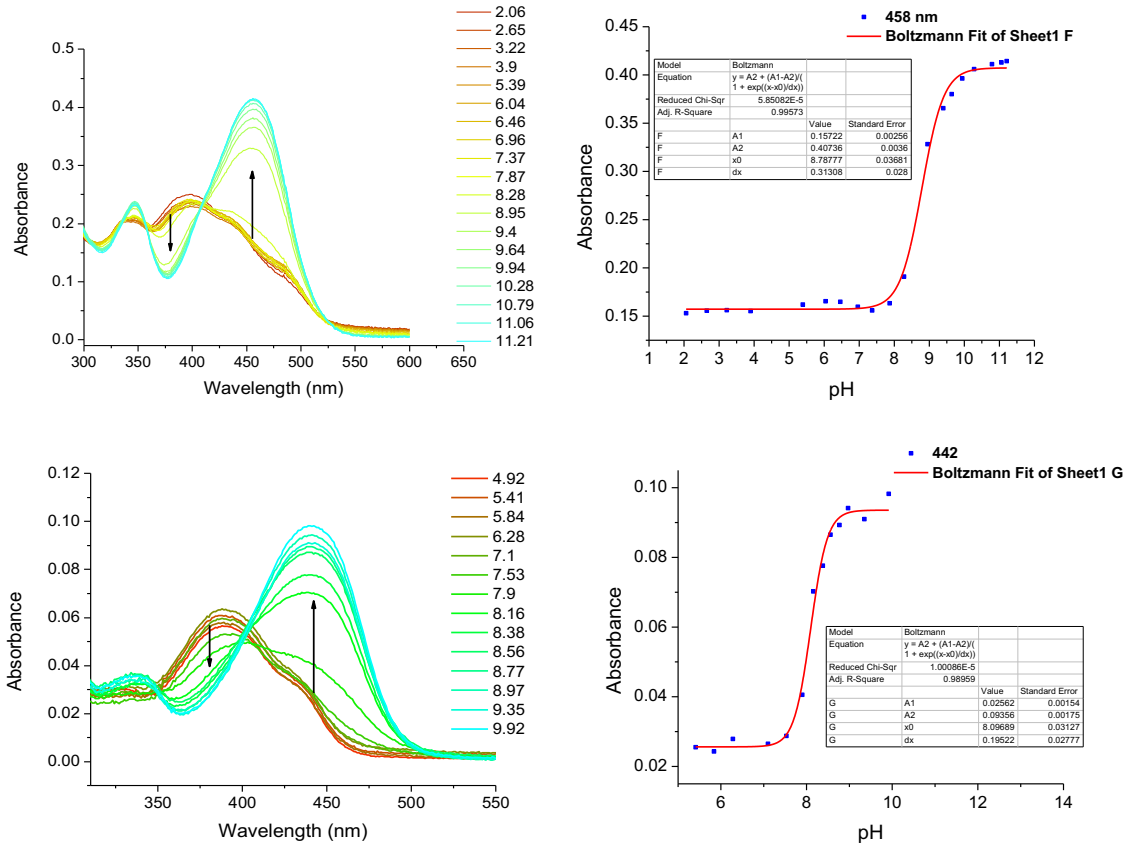

Figure 3.8. pKa determination of the two nucleosides: **TC8A** (top); and **FC8A** (bottom).

Both nucleosides are suitable for DNA labeling and sensing in terms of brightness, absorption and emission maxima, the resolution between the two emissive bands, the sensitivity to hydration, and the pKa. As **TCU**, **TC8A** and **FC8A** conjugates showed red-shifted absorption and emission compared to the parent chromones. Meanwhile, the new conjugates demonstrate high sensitivity to hydration and more extensive dynamic ranges for sensing. This property is likely the consequence of the poorer ICT character of the N* form, which results in weakly red-shifted emission maximum of the N* along with the increase of the media's polarity, as evidenced by the observation of two well-resolved emission bands in all tested solvents. In terms of sensitivity to hydration, **FC8A** is more favorable than **TCU**. The former provides a linear response of its I_{T^*}/I_{N^*} ratio channel to hydration as well as two well-resolved emission bands over the entire concentration range from 0% to 100% water.

2.3.2.2. Oligonucleotides synthesis and characterization

Synthesis of phosphoramidite

First attention was paid to **FC8A** due to its remarkable linear and dynamic response to hydration which could be promising for sensing DNA conformational changes, detection of abasic sites, or sensing DNA–protein interactions.[21] For this reason, a phosphoramidite corresponding to this nucleoside was synthesized (Scheme 3.4) and used to replace a natural **dA** on model sequences.[22-25] The phosphoramidite **3.8** was synthesized via a straightforward four-step procedure with acceptable to good yields. Firstly, the exocyclic amino (NH_2) group of the key intermediate **3.1** was selectively protected by reaction with dimethylformamide dimethylacetal (DMF-DMA) in MeOH with good yields (85%). Secondly, the DMTr protection at the 5′-OH was achieved with 70% yield using a standard procedure. Intermediates **3.5** and **3.6** were previously synthesized by Seela and coworkers with comparable yields.[26] The next intermediate **3.7** was obtained by Sonogashira coupling with the bromo derivative of the Cbz-protected **FC** (compound **3.2b**). Compound **3.2b** is synthesized routinely in our lab, as described elsewhere.[17] Finally using standard procedure, the 3′-OH of the deoxyribose sugar was reacted with the (2-cyanoethyl)-*N*,*N*-diisopropylchlorophosphoramidite to give with acceptable yield the phosphoramidite building block (**3.8**, 49%) required for DNA synthesis.

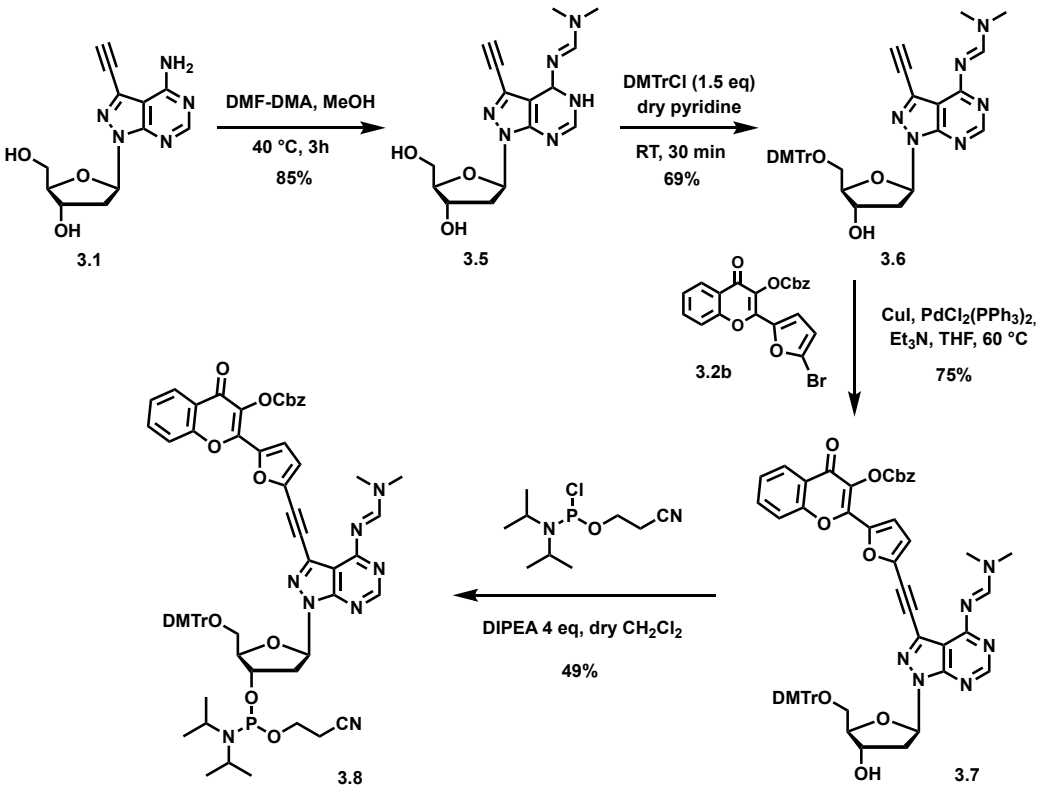

Scheme 3.6. Synthesis of the phosphoramidite building block.

Synthesis of ODN sequences and effects of the probe on DNA stability and structure

In this study, four symmetric ODN sequences (5′-CGT TTT **XOX** TTT TGC-3′) were synthesized and used to evaluate the probe's responsiveness for sensing DNA related events. The composition of the sequences was similar to that employed in our previous studies on the fluorescent **dU** probe.[27,28] In these ssODN sequences, named **ssAOA**, **ssTOT**, **ssCOC**, and **ssGOG**, **O** depicts the label **FC8A** and **X** substitutes **A, T, C**, or **G**. The 15-mer ODN ends with **GC** as "closing or capping" nucleotides at both 5′ and 3′ terminal positions to ensure sufficient stable duplexes at room temperature. The label **O** was incorporated in the middle of the sequence rather than in the end to reduce structural disorders. The sequences differed by the nucleobases flanking the modified **dA** to compare the properties of the label **O** in different ODN contexts.

Table 3.2. Results of the solid phase synthesis of the four ssODN.

Sequence	Full sequence 5′ to 3′	OD[a]	Exact mass	Found mass
ssAOA	CGT TTT **AOA** TTT TGC	4.6	4795.810	4795.813
ssTOT	CGT TTT **TOT** TTT TGC	5.5	4777.787	4777.797
ssCOC	CGT TTT **COC** TTT TGC	2.1	4747.787	4747.787
ssGOG	CGT TTT **GOG** TTT TGC	2.6	4827.800	4827.801

[a] The OD value is equal to the absorbance of the solution of purified ODN dissolved in 1mL of water.

The four ssODN sequences were synthesized via phosphoramidite chemistry using the DMTr OFF mode on 1 micromole columns. The synthesized sequence was cleaved from the solid phase and deprotected in a single step by treating the column with saturated aqueous NH_4OH. Each ssODN sequence was purified by semi-prep HPLC using a gradient of buffer A and B (Buffer A: 10 mM of Et_3N in H_2O adjusted by CO_2 gas until pH 7.0; Buffer B: 80% MeCN/20% buffer A, v/v). The purified sequence was further qualified by analytical HPLC and HRMS (Figure 3.9 and S3, Table 3.2). ODN sequence was quantified by absorption at 260 nm in water with the extinction coefficients of 143500, 135000, 132500, 139000 $M^{-1}.cm^{-1}$ for **ssAOA**, **ssTOT**, **ssCOC**, and **ssGOG**, respectively.

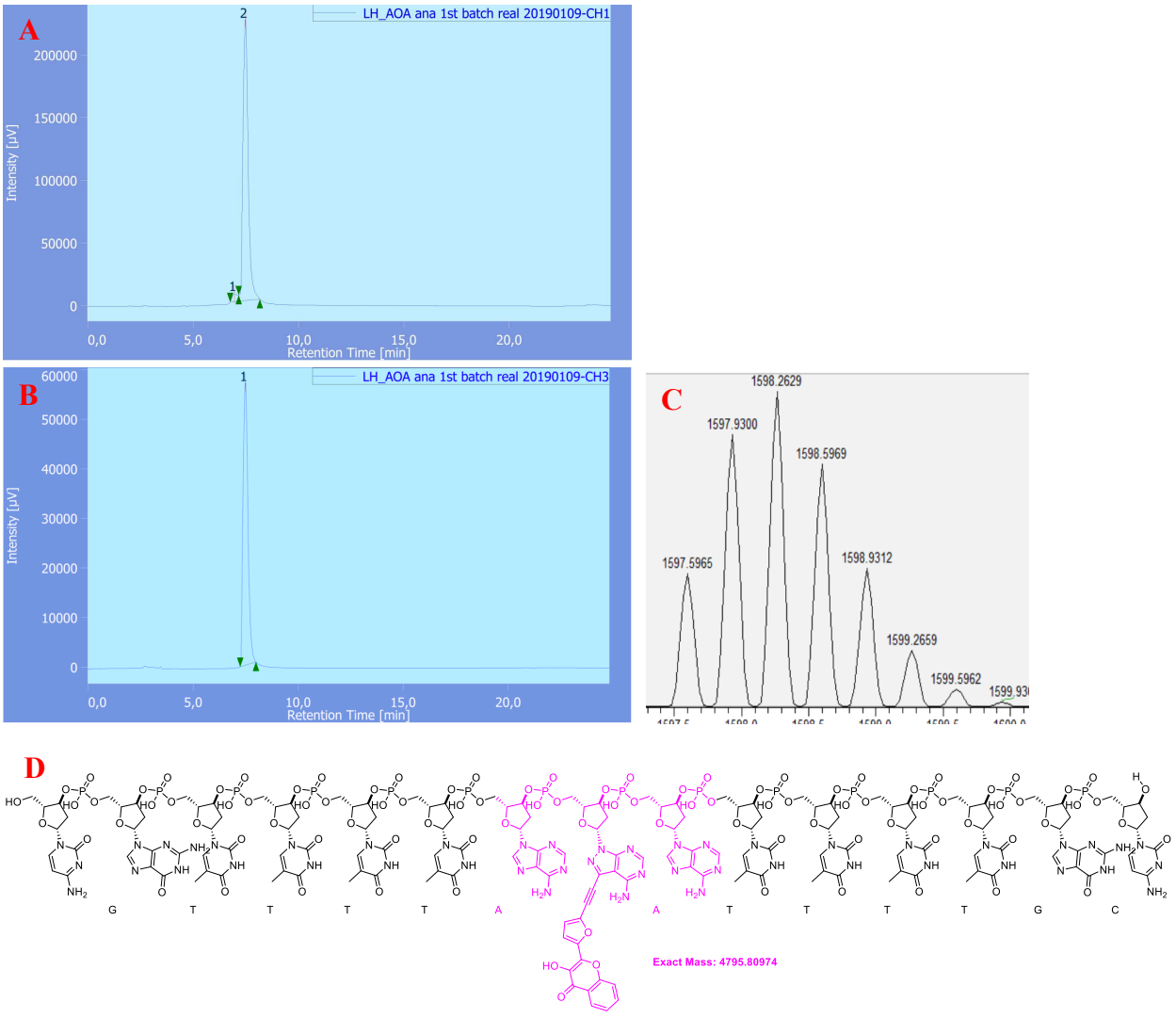

Figure 3.9. Analytical HPLC chromatogram of the purified **ssAOA** following by absorption at (A) 260 nm and (B) 400 nm. (C) The fragment corresponding to $(M-3H)^{3+}$ found for the **ssAOA** sequence on HRMS analysis. (D) The structure and exact mass of the **ssAOA** sequence.

Each ss sequence was hybridized with its complementary strand, *3′-GCA AAA **YMY** AAA ACG-5′*, from now depicted ***YMY***. ***X*** and ***Y*** are complementary bases, and **M** is one of the four canonical bases: **A**, **T**, **C**, and **G**; or the 1′,2′-dideoxyribose unit (**Ab**), a mimic of an abasic site. The accomplished double-stranded (ds) would then be written **XOX-*YMY*** and called labeled duplex. Therefore, each of the four synthesized ss sequences (context) could form five different labeled duplexes. For example, **ssAOA** would have **AOA-*TAT***, **AOA-*TTT*** (fully matched), **AOA-*TCT***, **AOA-*TGT***, and **AOA-*TAbT***; they are under **AOA** contexts.

The probe's effect on the stability and structure of the labeled duplex was studied by melting temperature (Tm) and circular dichroism (CD), using wild-type duplexes (WT – non-modified ODN) as the controls. Measurements were carried out at the duplex concentration of 2 μM. The Tm of labeled duplexes and corresponding WT duplexes were obtained from recording the temperature-induced absorbance changes at 260 nm. The ΔTm was obtained by subtracting the Tm of a labeled duplex with its corresponding WT (Table 3.3). In general, the fully matched

sequences gave the most stable duplexes. The labeled duplexes were slightly less stable than the corresponding WT (ΔTm = −4.9 to −1 °C); except mismatched with **C** (ΔTm = 0 to +1.2 °C) and **Ab** (ΔTm = +3.4 to +6.9 °C). The latter observations are similar to what were reported for our **dU** analog, where stacking and hydrophobic interactions between the extended probe and surrounding bases raised the duplex stability.[27] Noticeably, the matched duplexes where purine bases flanked the probe (**AOA-*TTT*** and **GOG-*CTC***) showed slightly less stable duplexes, about 1–2 °C, than with pyrimidine neighboring ones (**TOT-*ATA*** and **COC-*GTG***), see Table 3.3. CD spectra of selected labeled and WT duplexes were recorded from 320–200 nm. The CD spectra were plotted together to compare and elucidate the effect of the probe on the B-form structure of dsODNs. In all cases, including matched and mismatched, the CD spectra of labeled sequences show all the typical spectral characters of reference B-form structure (with typical positive and negative signals centered at 283 and 250 nm, respectively – Figure 3.10). Hence, the probe has minimal effect on the overall stability and structure of labeled ODN. As predicted, extension at the 7 position on the purine ring exposes the dye to the major groove of the DNA duplex with sufficient space resulting in minimal destabilization.[29,30]

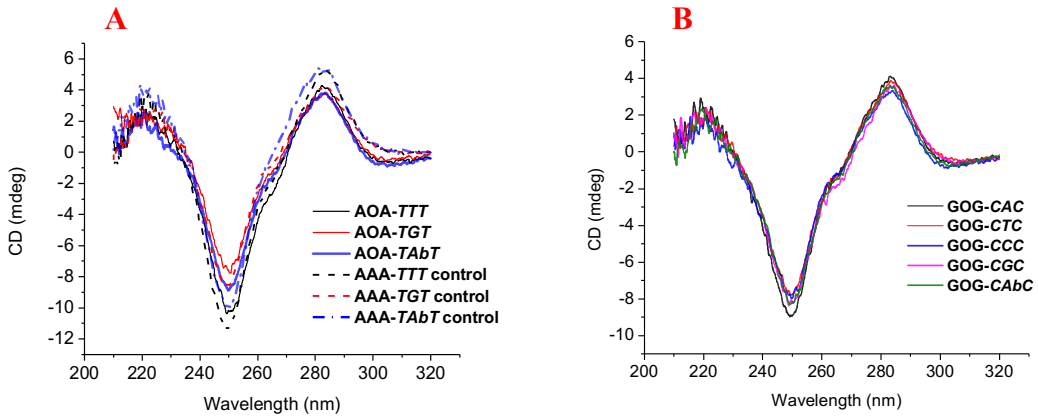

Figure 3.10. CD spectra of some selected duplexes with B-form signatures: (A) Comparison between labeled and corresponding WT duplexes; (B) CD spectra of all labeled duplexes with **GOG** contexts.

2.3.2.3. DNA hydration study – introduction of a new sensing parameter

Absorption and emission spectra of all ssODNs and dsODNs in buffer pH 7.17 were employed to study the responsiveness of the probe to report changes in DNA. The quantum yields of all entries were calculated using *p*-dimethylaminoflavone (DMAF) as the external standard. The essential values of these studies are reported in Table 3.3. Given that, in different contexts (ss or ds sequences), the hydration surrounding the dye could vary from slightly to significantly.

Table 3.3. Photophysical properties of the probe in different ODN contexts.

Sample	Tm[a] (°C)	ΔTm (°C)	% H_2O	λ_{Abs}[b]	λ_{N^*}[c]	λ_{T^*}[d]	I_{T^*}/I_{N^*}[e]	Φ[f]
Nucleoside			100	387	468	542	0.98	5.0
			90	385	460	549	1.67	7.9
			80	384	461	554	2.82	10.5
			70	384	458	559	4.16	12.1
			60	383	456	559	5.55	13.6
			50	382	454	559	6.88	15.3
ssTOT				393	466	562	3.01	10.4
TOT-*AAA*	36	−2.6		394	463	567	3.72	13.0
TOT-*ATA*	46.2	−2.2		386	463	556	3.36	9.0
TOT-*ACA*	37.5	0.0		392	461	571	2.05	14.0
TOT-*AGA*	38.7	−3.3		393	464	562	4.33	7.4
TOT-*AAbA*	39.2	+6.9		394	465	572	1.79	15.4
TOT-r_M*AUA*	36.6	--		389	463	558	4.00	10.0
ssAOA				396	463	568	3.36	6.1
AOA-*TAT*	35.4	−1.9		394	460	566	3.61	14.3
AOA-*TTT*	44.3	−4.1		390	463	555	1.79	8.7
AOA-*TCT*	37.1	+1.2		394	461	571	3.11	15.4
AOA-*TGT*	35.3	−3.2		395	461	562	4.94	7.2
AOA-*TAbT*	36.2	+3.4		395	463	569	2.36	16.9
AOA-r_M*UUU*		--		394	460	561	2.71	10.0
ssCOC				395	465	565	2.80	4.1
COC-*GAG*	42.8	−1.0		393	467	556	2.62	2.1
COC-*GTG*	49.7	−3.3		388	462	553	2.76	6.3
COC-*GCG*	44.7	+0.8		396	484	558	2.12	0.3
COC-*GGG*	45.6	−2.9		391	461	553	3.01	3.2
COC-*GAbG*	44	+4.7		395	480	562	1.91	0.2
ssGOG				397	461	570	4.98	0.8
GOG-*CAC*	44.9	−1.2		397	459	571	3.62	0.6
GOG-*CTC*	49.7	−4.9		389	459	560	2.46	0.6
GOG-*CCC*	45.5	+1.2		393	459	573	4.28	0.5
GOG-*CGC*	44.3	−4.7		392	461	564	3.14	0.5
GOG-*CAbC*	44.6	+4.4		398	463	568	3.90	0.4

[a] Melting temperature; [b] Absorption maximum; [c] Maximum of N* emission; [d] Maximum of T* emission; [e] I_{T^*}/I_{N^*} Ratio intensity of the two emission bands at their maxima; [f] Quantum yields determined by using *p*-dimethylaminoflavone (DMAF, Φ=0.27) in EtOH as a standard

reference. The excitation wavelength was 400 nm. All the measurements were performed at 2 μM concentration of ODN in phosphate buffer 10 mM, 150 mM NaCl, 1 mM EDTA at pH 7.17 at 20 °C.

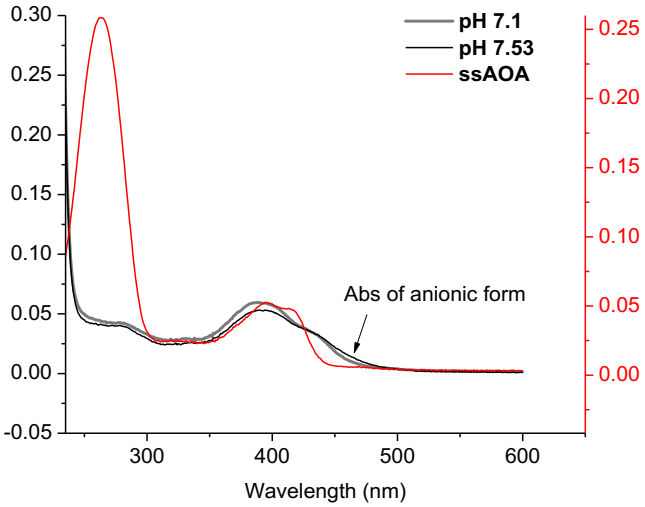

Figure 3.11. Absorption spectra of **FC8A** in water at pH 7.1 (black), pH 7.53 (grey), and **ssAOA** in buffer pH 7.17 (red). The spectra show that the probe exists mostly in the neutral form at pH 7.17.

Discrimination between ss and ds by absorption and emission spectra

First of all, in ss sequences, the probe exhibited absorption maxima at around 388–398 nm (about 10–20 nm red-shifted compared to **FC8A** in water). This is common for **3HC** dyes incorporated in DNA as well as many other fluorophores.[27,31] Noticeably, inspection of the absorption spectra of the labeled ODNs showed the disappearance of the contribution of the anionic form in buffer pH 7.17. For example, the absorption spectrum of **ssAOA** was plotted together with the absorption spectra of the free dye in buffer pH 7.1 and 7.53 to illustrate that point (Figure 3.11). Increase of the pKa was already observed for the **dU** analog after incorporation in DNA. This upward variation is consistent with the fact that the proton density around DNA is larger than that of the bulk solvent.[32-35] The emission spectra of the labeled ssODNs showed two well-resolved bands at around 461–466 nm (N* band) and 562–568 nm (T* band). The 6–13 nm redshifts of T* bands compared to that of **FC8A** in water were connected with the dye exposed to a less hydrated environment, which was assigned to the DNA strand's shielding effect. Interestingly, the intensity ratios I_{T*}/I_{N*} of ssODN sequences show a very strong sequence dependence (from 4.98 for **ssGOG** to 2.80 for **ssCOC**, ca. 78%, see also Table 3.3). By comparison to **TCU**, this is quite surprising as hydration surrounding ssODN sequences did not vary significantly.[27]

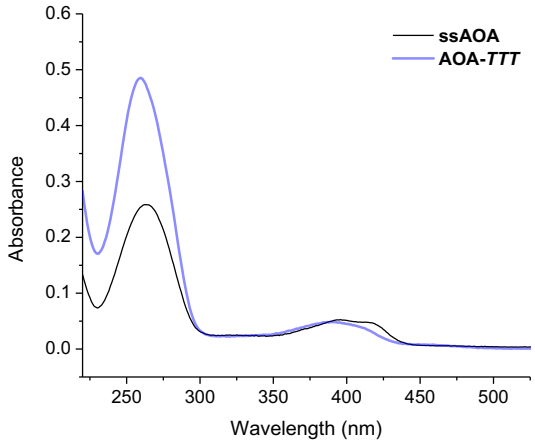

Figure 3.12. Absorption spectra discrimination between ssODN *vs.* matched dsODN.

In matched dsODN, the probe showed absorption maxima around 386–390 nm, ca. 5 nm blue-shifted when compared to the absorption maxima of the corresponding labeled ssODNs (Figure 3.12). The emission spectra showed two well-resolved bands with N* maxima at 459–463 nm and T* maxima at 553–560 nm. Noticeably, the emissions of the tautomeric (T*) bands were ca. 6–13 nm blue-shifted when compared to that of the corresponding labeled ssODNs (Figure 3.13), likely as a consequence of exposing the dye to the more hydrated major groove. Analyzing the I_{T*}/I_{N*} of the fully matched duplexes under the **AOA** and **GOG** contexts further support this statement. They were significantly lower than those obtained for the corresponding ssODNs (e.g., compare 1.79 *vs.* 3.36 for **AOA-*TTT*** and **ssAOA**, respectively). The I_{T*}/I_{N*} ratios measured for the probe in **AOA-*TTT*** and **GOG-*CTC*** were comparable to the values determined for **FC8A** in about 90% and 80% water, respectively. All these results are in good agreement with that reported for the **dU** probe.[27] In these sequences, the **O** label reports the environmental changes efficiently through hydration changes.

On the other hand, the I_{T*}/I_{N*} for the matched duplexes under the **COC** and **TOT** contexts were comparable or higher than the I_{T*}/I_{N*} for the corresponding ssODNs (2.76 *vs.* 2.80 and 3.36 *vs.* 3.01, respectively). These results are in sharp contrast with the results reported for the **dU** analog, where the I_{T*}/I_N ratios were the lowest for the matched labeled duplexes.[27] However, the blueshifts (6–13 nm) of T* emission bands were still observed after hybridization with the complementary strand (Figure 3.13C–D, compare **COC** and **TOT** with **COC-*GTG*** and **TOT-*ATA***). These variations are consistent with exposing the probe to a more hydrated environment in the matched duplexes. Therefore, the apparently contradictory results (blueshifts of the T* band and weak variations of the I_{T*}/I_{N*}) raise the question of knowing what other parameters than hydration changes could modulate the sensitivity of **FC8A** once incorporated into ODNs?

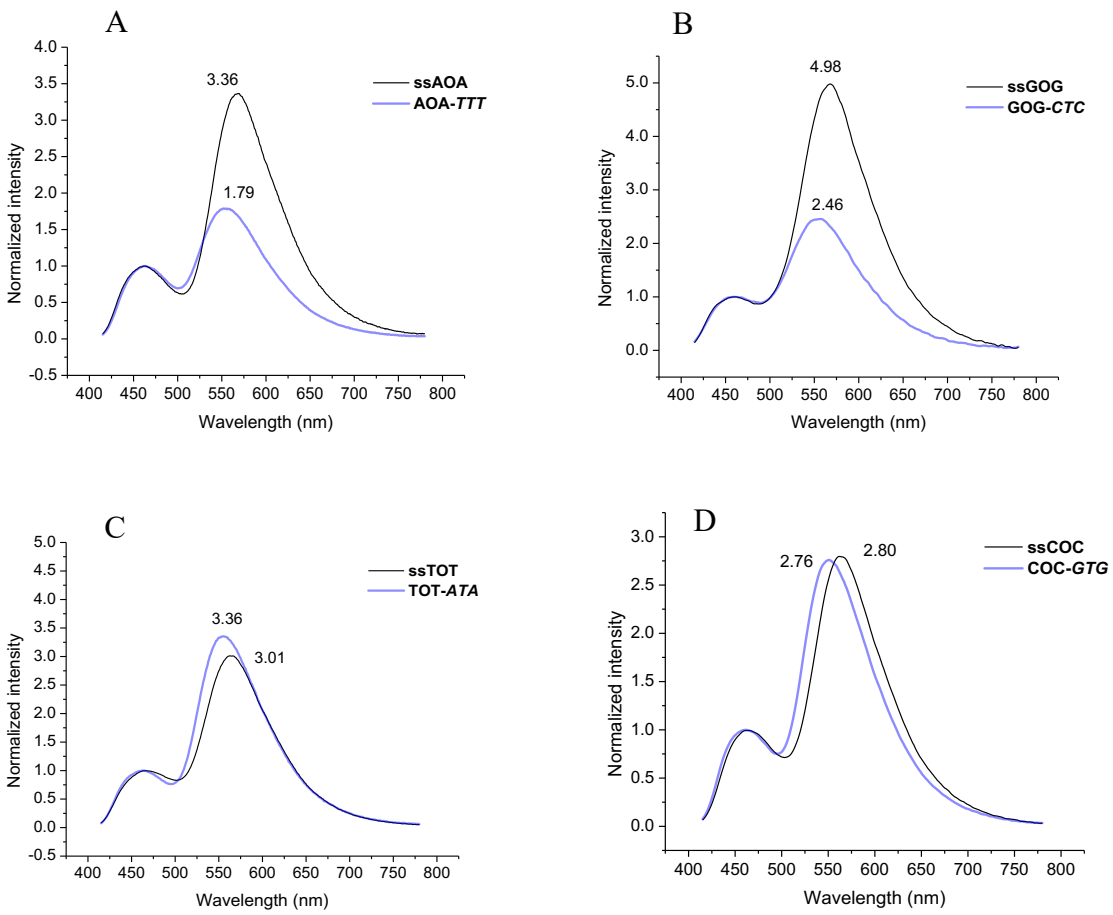

Figure 3.13. Ratio intensity for discriminating of ssODN *vs.* matched dsODN. All the spectra are normalized at the maximum of the N* band. The values of I_{T*}/I_{N*} are given next to the maximum of T* emission. In all cases, blueshifts of T* band are observed, which is consistent.

Intensity ratio affected by electron transfer process along DNA.

Why does **FC8A** produce seemingly contradictory results when incorporated into DNA depending on the sequence and context? Is a photoinduced electron transfer or/and another phenomenon at the origin of this particular behavior?

To address this question, we first analyzed the single-stranded sequences in more detail to better understand the influence of the flanking bases on the probe's photophysics.

For this and for each of the ss sequences, we have plotted:

a) the quantum yields as a function of the oxidation and reduction potentials of the probe-neighboring nucleosides (X), Figures 3.14. Typically, quenching by either **dG** or **dA** results in a reduction of the fluorophore while quenching with **dC** and **dT** results in oxidation;[36]

b) the intensity ratios I_{T*}/I_{N*} as a function of the oxidation potentials of the neighboring nucleosides (X), Figures 3.15.

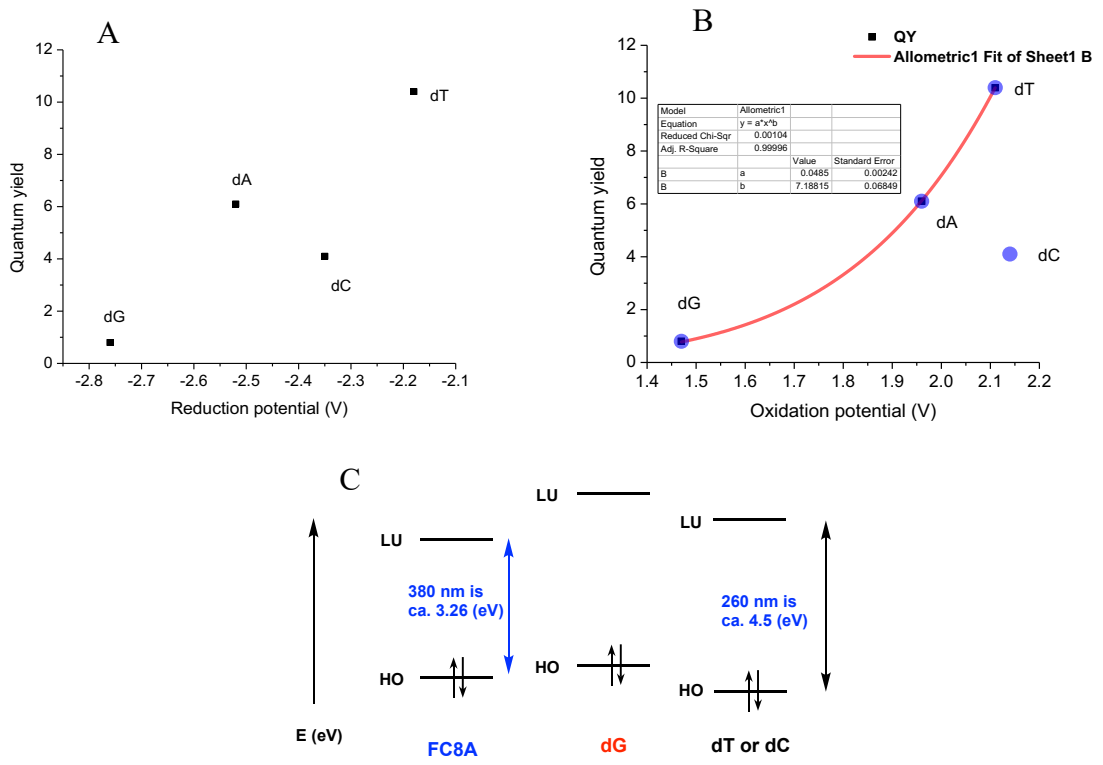

Figure 3.14. (A) QYs *vs.* reduction potentials of surrounding bases in ss sequences. (B) QYs *vs.* oxidation potentials of surrounding bases in ss sequences. (C) Relative HOMO and LUMO levels of **FC8A** compared to the natural nucleosides **dG**, **dC**, and **dT**.

Except for **C**, the Figures 3.14 A and B show that the quantum yields gradually decreases when the reduction and oxidation potentials decrease (**G** < **A** < **T**).[37] Lower oxidation potential means easier to give its electron in an electron transfer process. It suggests that the PET is a plausible mechanism to account for the lowest quantum yields. An approximately 8-fold drop in quantum efficiency of **ssGOG**, when compared to **ssAOA**, highlights **G** being by far the most efficient electron donor as expected if PET proceeds. Accordingly, the HOMO of **FC8A** should fall below that of **G** to explain the proposed PET reaction in the case of **ssGOG** (Figure 3.14C).

With a slightly lower reduction potential than **dC** (Figure 3.14A), **dT** is the most efficient electron acceptor among the canonical nucleosides, albeit the fact that only **C** proves to be an efficient quencher and not **T** disfavors the reverse PET mechanism (electron transfer from the fluorophore to the nucleobase). Hence, with the absorption maximum around 380–400 nm, the LUMO level of **FC8A** should therefore fall below that of all the nucleosides (Figure 3.14C). It is worth noting that the PET mechanism may not be exclusive. The quenching of organic fluorophores in DNA may be more complex and involve multiple non-radiative relaxation pathways. Alternatively, reduction of the quantum yield may result from the formation of dark non-emissive states via mixing and delocalization of molecular orbitals of the fluorophore among neighboring nucleobases. Such mechanism was proposed for the 2-aminopurine, 8-vinyladenosine, and parent **3TC** fluorophores to account for the quenching of these probes with neighboring **C** in DNA.[38,39]

Inspection of the intensity ratios I_{T*}/I_{N*} versus the oxidation potentials gives further information to the PET mechanism (Figure 3.15).

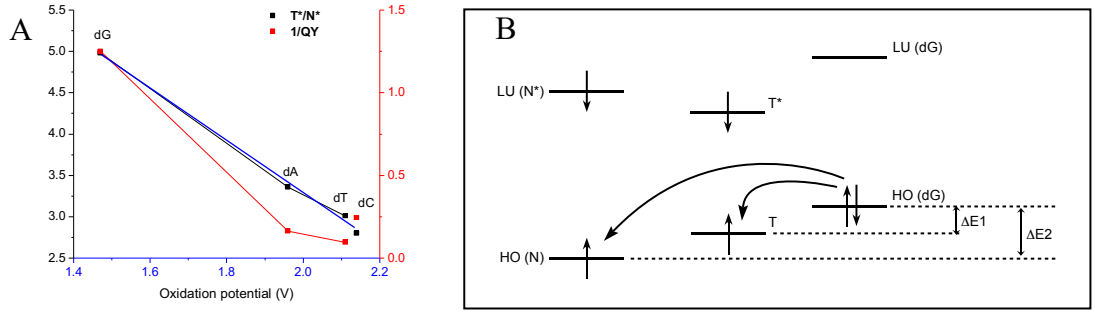

Figure 3.15. (A) Correlation between quenching efficiency (presented as 1/QY) and intensity ratio T*/N* to the oxidation potentials of neighboring nucleoside under different ss contexts. Linear relationship (blue line) between ratio intensity and oxidation potential of surrounding bases in ss sequences (equation: y = −3.1833x + 9.6494). (B) Representation of electron transfer process affects ratio intensity T*/N*. Quenching effects on two emissive forms happen with different driving forces. ΔE2 > ΔE2 should correlate with corresponding rate k2 > k1.

Figure 3.15 shows that I_{T*}/I_{N*} is decreasing (from 4.98 for **ssGOG** to 2.80 for **ssCOC**) with increasing oxidation potential of the neighboring base (**dG** +1.49 V to **dC** +2.14 V). The fact that **ssGOG** gave the largest I_{T*}/I_{N*} and lowest quantum yield suggests that the PET has an effect on the I_{T*}/I_{N*} where the neighboring **G** base likely transfers its HOMO electron to the photoexcited fluorescent probe (dynamic quenching). Does this conclusion hold for surrounding **A** base will be answered after? Except redshifts in absorption and emission due to extended conjugation, the photophysics of **FC8A** is quite similar to **TC** and **FC**. The ESIPT reaction in such systems of low push–pull character is known to be irreversible.[8,9,40] For that, the ESIPT reaction is a four-level process where the HOMO of T has higher energy than the HOMO of N (Figure 3.15). As a consequence, after photoexcitation of label **O**, electron transfer from **G** on the HOMO of N should be faster than on the HOMO of T in terms of standard free energy differences (ΔGet). For an irreversible ESIPT, this difference in rate transfer should result in an increase in the I_{T*}/I_{N*} ratio in line with experimental data.

At this stage, the following partial conclusion can be deduced.

- PET affects quantum efficiency and contributes to an increase in the I_{T*}/I_{N*} ratio. Important to note: hydration affects the intensity ratio in the opposite direction.
- In the case of **ssCOC**, the formation of dark fluorophore (static quenching) due to ground-state complex with **C** is expected to have no effect on the I_{T*}/I_{N*} ratio since the ESIPT reaction occurs in the excited-state.
- Likely the neighboring **G** base transfers its electron to the photo-activated label **O**.

Do the other flanking nucleobases contribute directly to PET?

According the decrease of oxidation potentials (**G< A < T < C**), **A** should be the most efficient electron donor after **G**. This proposal can be ruled out for two reasons. First, the Gibbs energy calculated on the methoxy derivative using the Rehm–Weller equation indicates that this

transfer is unlikely with **A**.[1] Second, as for the **G** flanking nucleobase, the contribution of **A** to PET should be reflected for the single and all double-stranded combinations in reduced quantum yields of comparable values; which is not the case. Indeed under **AOA** context, the ss, the matched, and the mismatched with **G** opposite **O** have moderate quantum yields, while those of all other mismatched combinations are nearly 2-fold brighter. For the **AOA-*TGT***, the direct contribution of **G** opposite **O** is likely involved in the observed reduced quantum yield. For the ss and matched dsODNs, the **Gs** positioned at the 5′ and/or 3′-end of the sequence may play this role. For the ss, the flexible strand can rearrange itself in such a way that the terminal **G** may be sufficiently close to transfer its electron. This hypothesis is supported by previous observations made by Giese and coworkers on single-stranded ODNs.[41] So why is electron transfer more efficient for **ssAOA** compared to **ssTOT**? This difference may be the consequence of the **A** flanking base and **AAA**-like nature of **AOA.** Indeed, the **AAA** triplet is known to be an effective relay for electron transfer from **dGs** in line with its lower oxidation potential.[36,42-44]

Sensing electron transfer in DNA by ratiometric response: matched and mismatched discrimination

It has been accepted worldwide that DNA duplex can mediate the long-distance electron transfer from **G**. DNA duplex can support the electron transfer mainly through its base pairings and base stackings. Electron transfer efficiency is a distance-dependent process, which can also be affected by the introduction of a mismatch or an abasic site in duplex.

Taken into account the effect of PET on the photophysics of the label **O**, we can clearly distinguish between **ssAOA** and **GOG** versus matched ds **AOA-*TTT*** and **GOG-*CTC***; the latter showed dramatic decreases of the I_{T*}/I_{N*} ratios along with blueshifts of the T* bands. For these sequences, the sensitivity to hydration is dominating the photophysics of the probe. For **TOT** and **COC**, the situation is different as the I_{T*}/I_{N*} ratio of **ssTOT** is higher than that of **TOT-*ATA*** and those of **ssCOC** and **COC-*GTG*** are comparable (Table 3.3 and Figure 3.13). These results suggest that PET canceled the ratiometric response to hydration.

Introduction of a mismatch or an abasic site into the duplex can significantly affect the electron transfer. For example, an **Ab** site can switch off PET. Depending on the nature of the mismatch, the electron transfer along the duplex can be attenuated to different degrees. For instance, electron transfer decreases in the order of **A**(mismatch) > **C**(mismatch) > **Ab**.[36]

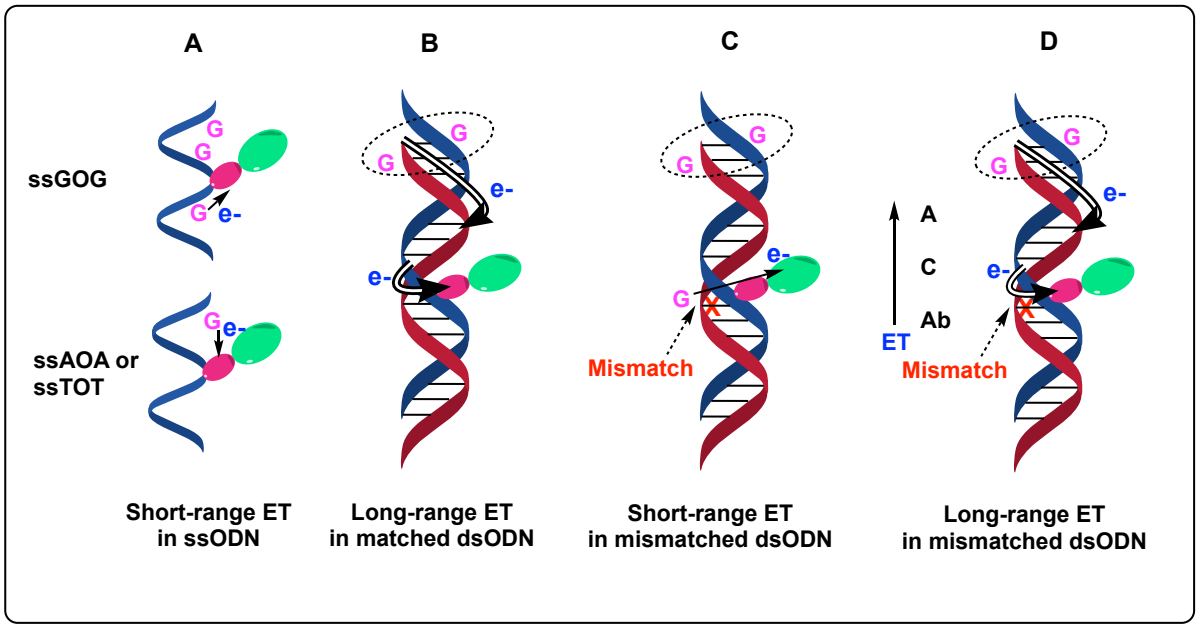

Scheme 3.7. Electron transport in DNA. (A) short-range electron transfer in ssODN sequences. (B) long-range electron transfer in fully matched dsODNs. (C, D) Attenuation of the electron transfer in dsODN sequence by a mismatched position.

The probe showed a remarkable ratiometric response to distinguish the different mismatched cases and abasic site for all the combinations obtained with the **ssAOA**, **ssTOT**, and **ssCOC**. They follow the same trend with I_{T*}/I_{N*} decreasing for pairs with **G** (mismatch) > **A** (mismatch) > **C** (mismatch) > **Ab** (Table 3.2, Figure 3.15). For example, the I_{T*}/I_{N*} ratios for the **AOA** duplexes are 4.49, 3.61, 3.11, and 2.36 with **G**, **A**, **C**, and **Ab** opposite **O**, respectively. Noticeably, the QYs are gradually increasing in the same order from 0.072 to 0.169 from **G** to **Ab** (See also Table 3.3). The largest increase of I_{T*}/I_{N*} and decrease of quantum yield for the **G** (mismatch) suggest more efficient PET likely due to the fact that **G** is directly in contact with the probe. Meanwhile, duplexes bearing mismatched with **A**, **C**, and **Ab** are known to attenuate with increasing magnitude the electron transfer from **G** located at a longer distance. Thus the probe **O** can clearly distinguish between the different mismatched and abasic cases by a remarkable ratiometric response, which is likely correlated to electron transfer from **G** at short and longer distances (Figure 3.15). On the other hand, the duplexes obtained from **GOG** responded differently. The I_{T*}/I_{N*} ratios were high for all the dsODNs, and the quantum yields were low and comparable. These results indicate that, for this sequence, the main contributors to PET and quenching are the flanking **G**s.

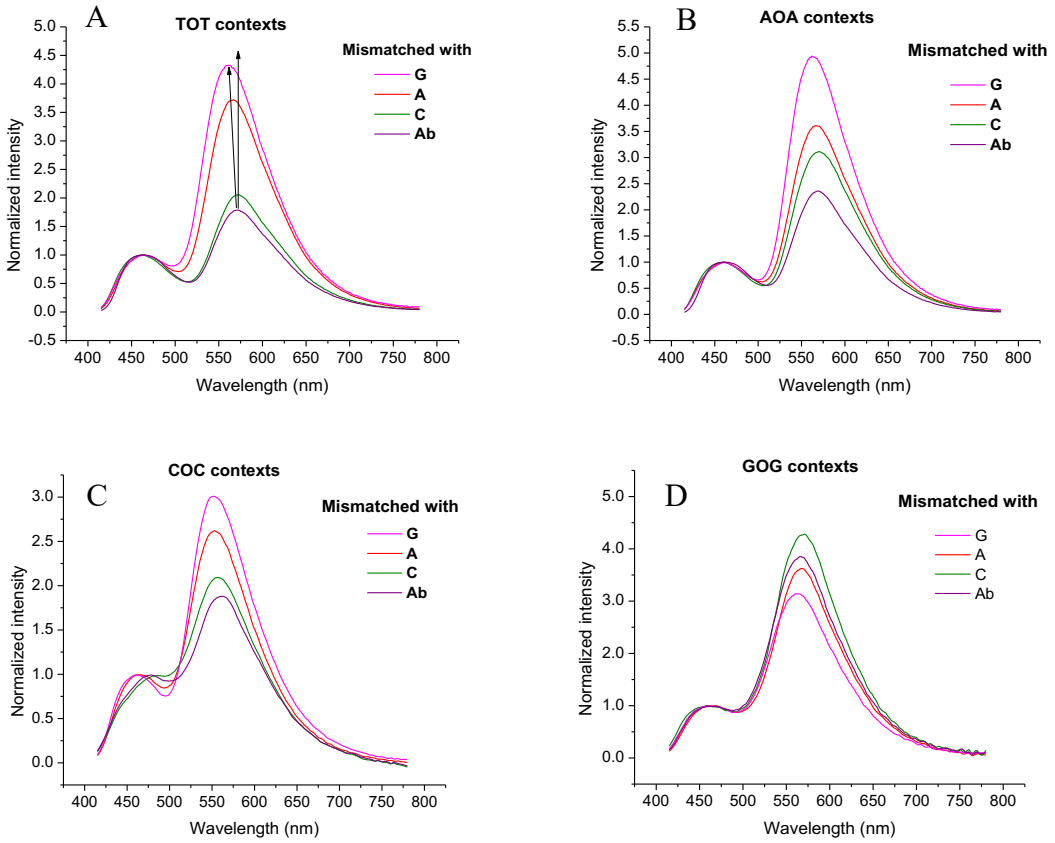

Figure 3.16. Discrimination of different mismatches by fluorescent ratiometric response: Normalized emission spectra of mismatched duplexes: (A) **TOT** context, (B) **AOA** context, (C) **COC** context, and (D) **GOG** context.

Discrimination of B-form from A-form DNA

In the previous section, we saw that PET was likely one of the main parameters controlling the photophysics of the probe in the ssODNs and dsODNS. Is this still the case in nucleic acids of different conformation? To get more insight into that question, we looked at A and B forms of nucleic acid helixes, which are the two most common and well-known forms. Nucleic acids can fold into helixes of A or B forms depending on the nucleotide composition, physical conditions, and upon protein binding. The RNA helix is exclusive of A form, while the Watson–Crick B-DNA can switch to A form under low water concentration (humidity) or upon protein binding. All the base pairing and base stacking are retained after the transition. The A form is quite similar to the B form, albeit the structure is more compact and shorter. Alternatively, the hybridization of a ssDNA with its complementary RNA sequence drives the helix to adopt an A-like form without the need to dehydrate.[27]

In this experiment, the **ssTOT** and **ssAOA** sequences were employed to study their ability to probe the conformational change from B to A form. These 2 sequences were selected as representative pyrimidine and purine flanking bases. They were chosen also because they are bright and respond differently to stimuli. For example, **AOA** is PET sensitive in its single form

and distinguish through the I_{T*}/I_{N*} channel the ssODN from the matched dsODNs, while the **TOT** gives opposite responses. Because the A conformation is kept unaffected by the 2′-OMe modification and gives more stable duplexes, the methoxy RNA was employed for annealing with DNA. Each ssODN was hybridized with its complementary methoxy RNA strand, depicted as ***r_MYUY*** (***r_M*** means methoxy RNA) to give two hybrids **TOT-*r_MAUA*** and **AOA-*r_MTUT***. The CD spectra of the hybrids show the typical characteristics of an A-form DNA/RNA with maxima and minima centered at 248 nm and 268 nm, respectively, which are distinct from that of B-form DNA (Figure 3.17). In terms of ratiometric response, the probe exhibits strong variations of I_{T*}/I_{N*} ratios between the two helix forms (Figure 3.17). For both combination the label in A-DNA/RNA shows I_{T*}/I_{N*} ratios higher than for the B-dsDNA. The T* bands are also red-shifted ca. 5 nm from that of the corresponding B-form DNA. These results indicate that for the former, the dye is exposed to a less hydrated environment. Our data are consistent with the fact that the deeper and narrower major groove of A-DNA/RNA hybrid is less hydrated in comparison to that of B-DNA. These results are in line with previous studies, including ours with the **TCU** probe.[27,45] They indicate that whatever the sequence, the discriminating factor is the sensitivity of the probe to its more or less hydrated environment and not PET. This is probably due to the fact that the efficiency of electron transfer is quite similar for the two forms, as reported by Barton and coworkers.[36,46] As a consequence, if PET there is its influence on the I_{T*}/I_{N*} ratios should not be detectable. Interestingly, for **AOA** the **O** label can clearly distinguish between ss, A-DNA/RNA, and B-dsDNA by either the shift of the T* band and variation of the I_{T*}/I_{N*} ratio (Figure 3.17). The variations of the two parameters indicate that the dye is exposed to a less hydrated environment in the order of B-DNA, A-DNA/RNA, and ssDNA. This result is fully consistent with our previous report using the **TCU** probe, for which the impact on PET on I_{T*}/I_{N*} ratios was negligible.[27] By contrast, for **TOT** the I_{T*}/I_{N*} ratio of the A-form was higher than that of **ssTOT**, even though the T* band was blue-shifted as expected for the dye exposed to a more hydrated environment. In this case, our results indicate that electron transfer likely affects the I_{T*}/I_{N*} ratio.

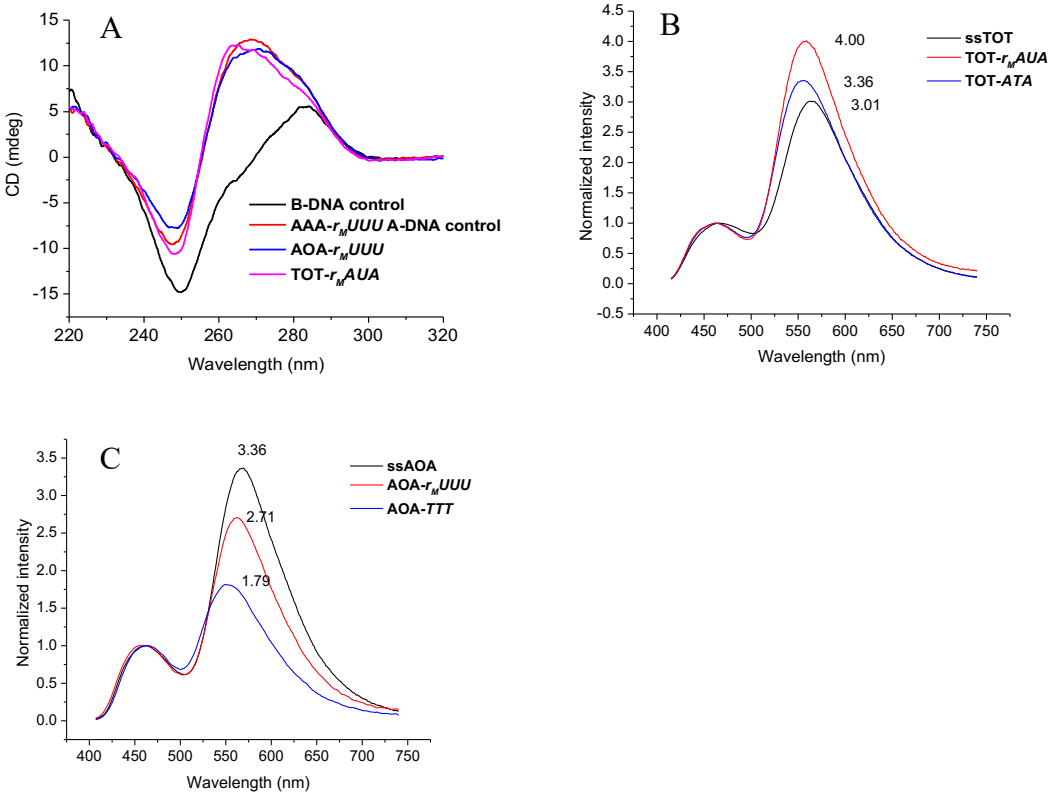

Figure 3.17. (A) Discrimination of A-DNA/RNA from B-DNA by CD spectra. Discrimination of ss, A-DNA/RNA, and B-DNA by the I_{T*}/I_{N*} ratio under: (B) **TOT** context and (C) **AOA** context. The emission spectra were normalized on N*.

2.3.3. Conclusion

The introduction of a nitrogen atom at the 8 position brought unique photophysical properties to the dual-emissive **dA** analog. First of all, as an EWG, N-8 has decreased the oxidation potential of **8d7A** comparing to that of **d7A**. As a consequence coupling the **TC** and **FC** fluorophores to **8d7A** gives rise to 2 conjugates with good brightness in polar protic media. Secondly, this EWG also decreases the dipole moment in the molecules' excited-state, which reduces the ICT character of the probes in the excited state. Consequently, the N* band exhibits reduced redshift with increasing solvent polarity given two well-resolved bands in all tested solvents, even in highly hydrated environments. This character is "natured" of the parent **3HC** dyes.

Both nucleosides were optimal for probing DNA for several reasons. They both have conjugation extended from position 7, which should have minimal effect in labeled DNAs. The probes have maxima of absorption at the regime of visual light with relatively high extinction coefficients. Moreover, the pKas of both nucleosides are suitable for using at biological pH. Especially, the probes show high sensitivity to hydration with a linear response of **FC8A** covering all the concentration range (e.g., from 0 to 100% water). For this reason, this probe was chosen to label different ODN sequences to evaluate its sensitivity and efficiency to bring new applications.

Under the ODN environment, the **FC8A** probe is not only sensitive to hydration stimuli but also to report the electron transfer process in DNA. This is an advanced property compare to that of our previous probes, **TCU** and **FCU**. This advantage is probably related to the larger aromaticity of **dA** analog comparing to **dU** analogs. With the combination of the two sensing parameters, the probe shows remarkable abilities to distinguish single strands from the matched duplexes when purines sandwiched the label, mismatched base pairs, and A *vs*. B helical forms.

This probe has likely high potential for other DNA-related applications, such as studying conformational changes and DNA-protein interactions. Conformational changes or binding of protein was known to change the hydration surrounding DNA as well as the electron transfer through the DNA helix.[36] Electron transfer in DNA is known to affect the luminescence of many fluorescent probes.[47] However, a probe with dual-emissive response sensitive to electron transfer in DNA is, to the best of our knowledge, without precedent in the literature. Hence, we report, for the first time, a dual-emissive probe being able to report hydration surrounding DNA and electron transfer in DNA. Of course, the two parameters can sometimes cancel each other out; however, the possibility to probe electron transfer processes in DNA or hydration surrounding DNA should bring more advantages than disadvantages. For instance, one can fix the hydration level by using a fixed sequence with the probe located at a distance from the protein binding site. Then the ratiometric response of the probe may be used to report the protein binding through a change in electron transfer. Again, this is a self-calibrated approach and hence should provide a good reproducibility of the measurement. This type of tracking is not possible with the **dU-3HC** conjugate, which is mainly sensitive to hydration. Moreover, probing DNA mismatched/ or modified base at distance-position relative to the labeling site should also be possible. These properties could be beneficial for detecting modified cytosine, which is highly demanded for early-stage cancerous detection. Thus the probe could be an attractive tool for sensing electron transfer in DNA, a topic with a massive effort from several scientists though a large part still remains uncovered. Moreover, the dynamic of two fluorescent states may be employed to get further insight into this interesting field of science.

References

[1] H.-N. Le, J. Brazard, G. Barnoin, S. Vincent, B. Michel, J. Léonard, A. Burger, *Chem. Eur. J.* **2020**, *n/a*, chem.202003456.

[2] C. Reichardt, *Chem. Rev.* **1994**, *94*, 2319–2358.

[3] H.-N. Le, C. Zilio, G. Barnoin, N. P. F. Barthes, J.-M. Guigonis, N. Martinet, B. Y. Michel, A. Burger, *Dyes Pigm.* **2019**, *170*, 107553.

[4] U. S. Raikar, C. G. Renuka, Y. F. Nadaf, B. G. Mulimani, A. M. Karguppikar, M. K. Soudagar, *Spectrochim. Acta, Part A* **2006**, *65*, 673–677.

[5] S. K. Patil, M. N. Wari, C. Y. Panicker, S. R. Inamdar, *Spectrochim. Acta, Part A* **2014**, *123*, 117–126.

[6] A. S. Klymchenko, A. P. Demchenko, *New J. Chem.* **2004**, *28*, 687–692.

[7] A. Suzuki, N. Nemoto, I. Saito, Y. Saito, *Org. Biomol. Chem.* **2014**, *12*, 660–666.

[8] C. A. Kenfack, A. S. Klymchenko, G. Duportail, A. Burger, Y. Mély, *Phys. Chem. Chem. Phys.* **2012**, *14*, 8910–8918.

[9] R. Das, A. S. Klymchenko, G. Duportail, Y. Mély, *Photochem. Photobiol. Sci.* **2009**, *8*, 1583–1589.
[10] M. Spadafora, V. Y. Postupalenko, V. V. Shvadchak, A. S. Klymchenko, Y. Mély, A. Burger, R. Benhida, *Tetrahedron* **2009**, *65*, 7809–7816.
[11] A. S. Klymchenko, D. A. Yushchenko, Y. Mély, *J. Photochem. Photobiol., A* **2007**, *192*, 93–97.
[12] D. McMorrow, M. Kasha, *J. Phys. Chem.* **1984**, *88*, 2235–2243.
[13] D. A. Yushchenko, V. V. Shvadchak, A. S. Klymchenko, G. Duportail, Y. Mély, V. G. Pivovarenko, *New J. Chem.* **2006**, *30*, 774–781.
[14] D. Dziuba, I. A. Karpenko, N. P. F. Barthes, B. Y. Michel, A. S. Klymchenko, R. Benhida, A. P. Demchenko, Y. Mély, A. Burger, *Chem. Eur. J.* **2014**, *20*, 1998–2009.
[15] L. Giordano, V. V. Shvadchak, J. A. Fauerbach, E. A. Jares-Erijman, T. M. Jovin, *J. Phys. Chem. Lett.* **2012**, *3*, 1011–1016.
[16] G. M'Baye, A. S. Klymchenko, D. A. Yushchenko, V. V. Shvadchak, T. Ozturk, Y. Mély, G. Duportail, *Photochem. Photobiol. Sci.* **2007**, *6*, 71–76.
[17] N. P. F. Barthes, I. A. Karpenko, D. Dziuba, M. Spadafora, J. Auffret, A. P. Demchenko, Y. Mély, R. Benhida, B. Y. Michel, A. Burger, *RSC Adv.* **2015**, *5*, 33536–33545.
[18] V. G. Pivovarenko, O. M. Zamotaiev, V. V. Shvadchak, V. Y. Postupalenko, A. S. Klymchenko, Y. Mély, *J. Phys. Chem. A* **2012**, *116*, 3103–3109.
[19] A. J. Strandjord, P. F. Barbara, *J. Phys. Chem.* **1985**, *89*, 2355–2361.
[20] L. D. Lavis, T. J. Rutkoski, R. T. Raines, *Anal. Chem.* **2007**, *79*, 6775–6782.
[21] O. M. Zamotaiev, V. Y. Postupalenko, V. V. Shvadchak, V. G. Pivovarenko, A. S. Klymchenko, Y. Mély, *Bioconjugate Chem.* **2011**, *22*, 101–107.
[22] H. Vu, C. McCollum, K. Jacobson, P. Theisen, R. Vinayak, E. Spiess, A. Andrus, *Tetrahedron Lett.* **1990**, *31*, 7269–7272.
[23] Y. Saito, Y. Miyauchi, A. Okamoto, I. Saito, *Chem. Commun.* **2004**, *0*, 1704–1705.
[24] M. K. Schlegel, E. Meggers, *J. Org. Chem.* **2009**, *74*, 4615–4618.
[25] F. Seela, S. S. Pujari, *Bioconjugate Chem.* **2010**, *21*, 1629–1641.
[26] S. S. Pujari, S. A. Ingale, F. Seela, *Bioconjugate Chem.* **2014**, *25*, 1855–1870.
[27] N. P. F. Barthes, K. Gavvala, D. Dziuba, D. Bonhomme, I. A. Karpenko, A. S. Dabert-Gay, D. Debayle, A. P. Demchenko, R. Benhida, B. Y. Michel, et al., *J. Mater. Chem. C* **2016**, *4*, 3010–3017.
[28] K. Gavvala, N. P. F. Barthes, D. Bonhomme, A. S. Dabert-Gay, D. Debayle, B. Y. Michel, A. Burger, Y. Mély, *RSC Adv.* **2016**, *6*, 87142–87146.
[29] S. Jäger, G. Rasched, H. Kornreich-Leshem, M. Engeser, O. Thum, M. Famulok, *J. Am. Chem. Soc.* **2005**, *127*, 15071–15082.
[30] F. Seela, M. Zulauf, *Helv. Chim. Acta* **1999**, *82*, 1878–1898.
[31] D. Dziuba, V. Y. Postupalenko, M. Spadafora, A. S. Klymchenko, V. Guérineau, Y. Mély, R. Benhida, A. Burger, *J. Am. Chem. Soc.* **2012**, *134*, 10209–10213.
[32] S. Hanlon, L. Wong, G. R. Pack, *Biophys. J.* **1997**, *72*, 291–300.
[33] G. Lamm, G. R. Pack, *PNAS* **1990**, *87*, 9033–9036.
[34] K. Friedrich, P. Woolley, *Eur. J. Biochem.* **1988**, *173*, 227–231.
[35] R. Sjöback, J. Nygren, M. Kubista, *Biopolymers* **1998**, *46*, 445–453.
[36] J. C. Genereux, J. K. Barton, *Chem. Rev.* **2009**, *110*, 1642–1662.
[37] C. A. M. Seidel, A. Schulz, M. H. M. Sauer, *J. Phys. Chem.* **1996**, *100*, 5541–5553.
[38] C. A. Kenfack, A. Burger, Y. Mély, *J. Phys. Chem. B* **2006**, *110*, 26327–26336.
[39] A. Sougnabé, D. Lissouck, F. Fontaine-Vive, M. Nsangou, Y. Mély, A. Burger, C. A. Kenfack, *RSC Advances* **2020**, *10*, 7349–7359.

[40] V. I. Tomin, A. P. Demchenko, P.-T. Chou, *J. Photochem. Photobiol., C* **2015**, *22*, 1–18.
[41] E. Meggers, A. Dussy, T. Schäfer, B. Giese, *Chem. Eur. J.* **2000**, *6*, 485–492.
[42] A. Peluso, T. Caruso, A. Landi, A. Capobianco, *Molecules* **2019**, *24*, 4044.
[43] M. Rooman, R. Wintjens, *J. Biomol. Struct. Dyn.* **2014**, *32*, 532–545.
[44] H. Sugiyama, I. Saito, *J. Am. Chem. Soc.* **1996**, *118*, 7063–7068.
[45] W. Fuller, M. H. Wilkins, H. R. Wilson, L. D. Hamilton, *J. Mol. Biol.* **1965**, *12*, 60–76.
[46] E. M. Boon, J. K. Barton, *Bioconjugate Chem.* **2003**, *14*, 1140–1147.
[47] M. A. O'Neil, J. K. Barton, *J. Am. Chem. Soc.* **2004**, *126*, 11471–11483.

Conclusions and Perspectives

Conclusions

This research aimed to develop dual-emissive analogs of deoxyadenosine for nucleic acid labeling and life sciences. We have successfully developed dual-emissive analogs of dA with advanced properties for such purposes. These dyes possess visible absorption and emission, good brightness, suitable pKa, and appropriate sensitivity range. One of the analogs has been used to labeled different ODN sequences via phosphoramidite chemistry for examining its capability in sensing DNA-related events. The probe has made labeled ODN sequences fluoresce with two distinctive colors at sufficient brightness. The ratios of intensities between those two bands of colors can be used as a self-calibrated approach for studying DNA-containing biological systems.

In order to achieve this unique tool, we need lessons from the two former studies. Firstly, a set of dual-emissive dyes bearing **d7A** moiety was synthesized, and their photophysical properties were investigated. These dyes show improvements compared to the corresponding parent **3HC**, especially **FCA** and **TCA**. Unfortunately, all the dyes exhibit low quantum yields in protic solvents such as MeOH, where PET was an explanation. Secondly, investigations on the PET reaction between **dA** analogs and chromones were performed. Push–pull conjugations between an analog of **dA** and **3MC** were synthesized. The PET reaction was studied by cyclic voltammetry, steady-state absorption and emission spectroscopy as well as fs-TA experiments. The study reveals that conjugates bearing **d7A** form a ground-state complex in a head-to-tail manner, which supports an intermolecular PET reaction. Meanwhile, the formation of the ground-state complex and the PET reaction were not observed with **8d7A** conjugate or under acidic conditions. This study raises questions about similar push–pull conjugations that were quenched by PET. These dyes may have applications provided that intramolecular PET reaction is absent. Importantly, this study suggests that **8d7A** would be attractive for constructing dual-emissive probes based on **3HC** dyes.

Eventually, dual-emissive nucleosides based on an **8d7A** scaffold were developed. Their photophysics demonstrates a unique sensitivity to hydration and undeniable improvements compared to parent chromones. The dyes present a high extinction coefficient (almost the double of their parent), good quantum yields, redshifts of their absorption and emission, and especially for **FC8A**, a ratio intensity with linear response to hydration. The corresponding phosphoramidite of **FC8A** was synthesized, and the two-color fluorescent nucleoside was used to label different ODN sequences. Interestingly, the probe's ratiometric response is not only sensitive to environmental factors surrounding DNA duplex such as hydration but also the electron transfer in DNA. Recently, the latter topic has attracted intensive studies as well as debates. We report, for the first time, a dual-emissive probe as a tool for studying the electron transfer process. Our self-calibrated probe could bring new insights and opportunities to elaborate informative applications into this interesting field of life sciences.

Perspectives

In continuation of this work, we are interested in carrying the following researches.

Firstly, as mentioned previously, the intermolecular PET reaction is responsible for fluorescence quenching of **d7A-3MC** dyes in polar protic media. It would be interesting to know whether the incorporation of **d7A-3MC** conjugate into ODN can inhibit the PET reaction. Given that the formation of the ground-state complex and hence the intermolecular PET reaction should be inhibited under the ODN context. For this purpose, it is essential to synthesize a phosphoramidite corresponding to the conjugate and then incorporate the extended nucleobase into ODN. The labeled sequences will be used to study in-depth PET reaction.

Secondly, advanced applications can be envisioned using the **FC8A** reporter. We would like to see the probe's capability to report the interaction between MITF (Microphthalmia-associated transcription factor) and its binding sequences. Given that continuous expression of MITF at a certain level is one of the necessary elements for the development of a type of skin cancer, called melanoma. The crystal structures of the complexes between MITF and its binding sequences, M-Box and E-Box, were reported (Figure 58).[217] The binding of MITF to the DNA showed very little variations on the latter's structure and conformation. Hence probing the event may be challenging. However, achieving that could lead to further development of high-throughput screening assay for MITF inhibitors. In parallel, by fixing the level of hydration surrounding the designed system, we would like to know if the dual emission could be helpful to transduce the electron transfer in DNA. Achieving this goal should open new routes for probing "long-distance" protein–DNA interactions, damaged nucleoside in the DNA duplex as well as studying base excision repair pathway.

Lastly, continuing the development of our dual-emissive toolbox, we would like to investigate on 3HC-conjugates engineered from **dG** and **dC** analogs. A similar retrosynthetic approach will be applied to **dC** analogs; whereas, special consideration in the design should be taken to avoid the PET reaction for **dG** analogs.

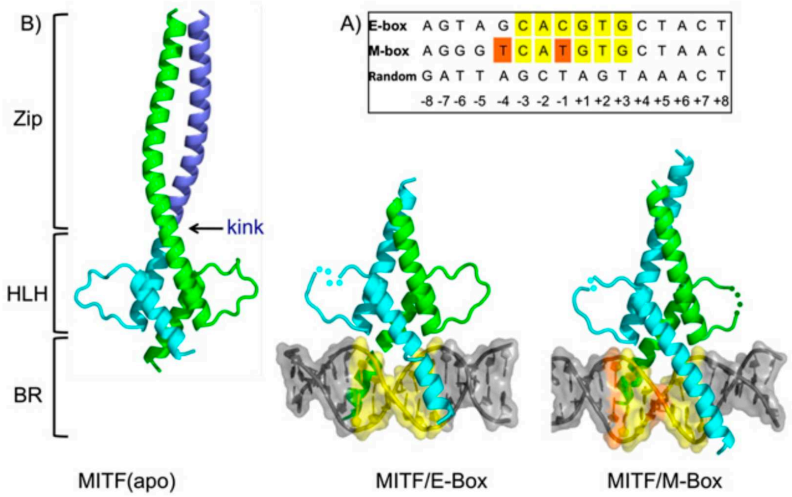

Figure 58. Crystal structures of MITF protein, the complex MITF/E-Box, and MITF/M-Box. (From ref[217])

Chapter 3. Experimental Part

3.1. SI of publication 1

Supporting Information To:

Rational design, synthesis, and photophysics of dual-emissive deoxyadenosine analogs

Hoang-Ngoan Le [a,†], Caterina Zilio [a], Guillaume Barnoin [a], Nicolas P.F. Barthes [a], Jean-Marie Guigonis,[b] Nadine Martinet [a], Benoît Y. Michel*[a], Alain Burger*[a]

a) Université Côte d'Azur, CNRS, Institut de Chimie de Nice, UMR 7272 – Parc Valrose, 06108 Nice cedex 2, France
b) Université de Nice Sophia Antipolis, Faculté de Médecine, Plateforme "Bernard Rossi", Nice, France

Corresponding authors: benoit.michel@unice.fr, burger@unice.fr

Graphical Abstract: **dA**: **d**ual-emissive **A**denosine

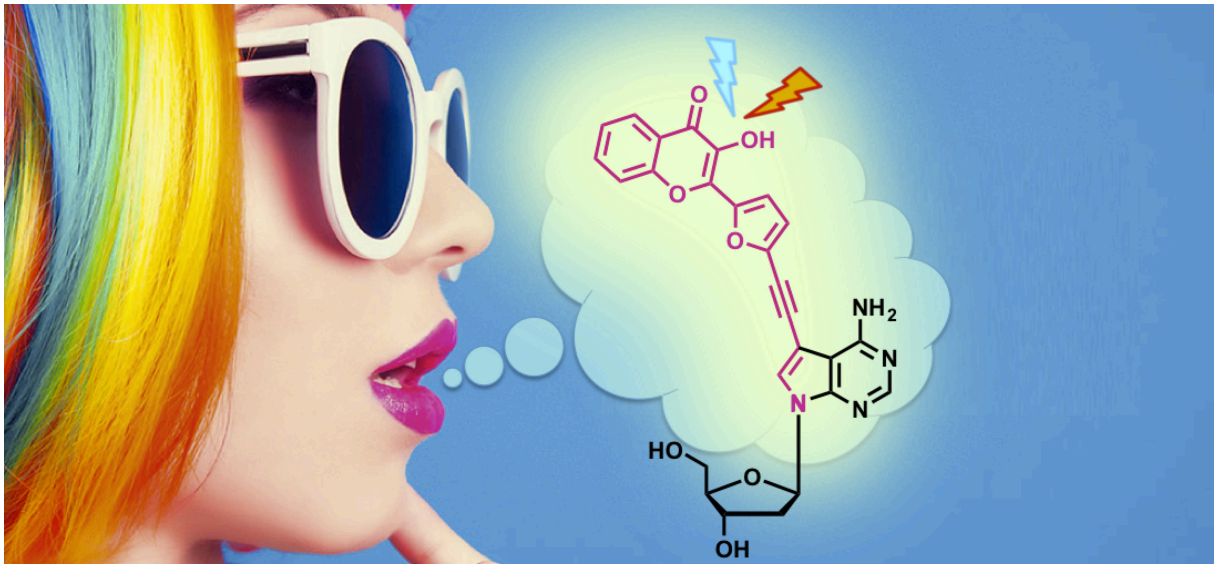

Table of contents

Supporting Information *Pages*

1. Additional Figures & Schemes

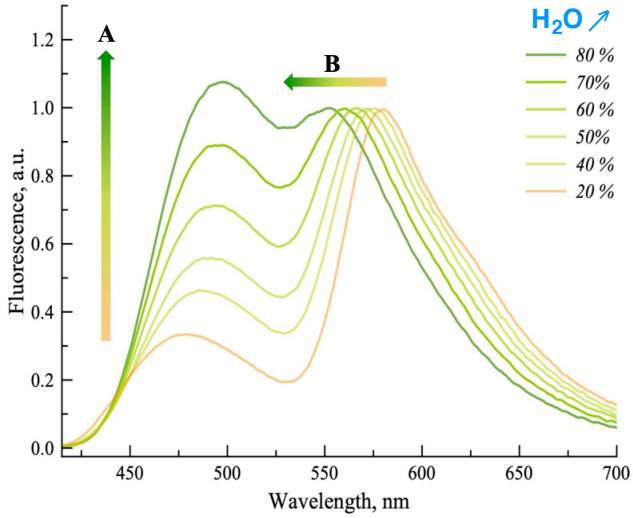

Figure S1. Representative fluorescence spectra for the 3HC-dU analog **1** over a H_2O titration highlighting the 2 original channels of information (ratiometry and λ-shift, respectively A & B arrows).

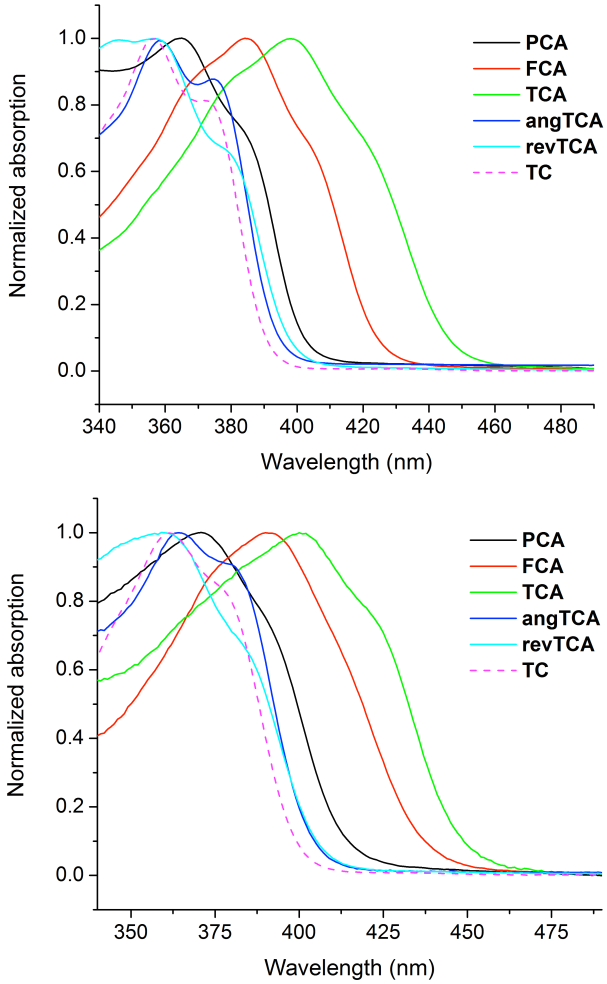

Figure S2. Absorption spectra in dioxane. (*top*) and in DMSO (*bottom*) of the 5 synthesized dual-emissive dA analogs and the parent **TC**.

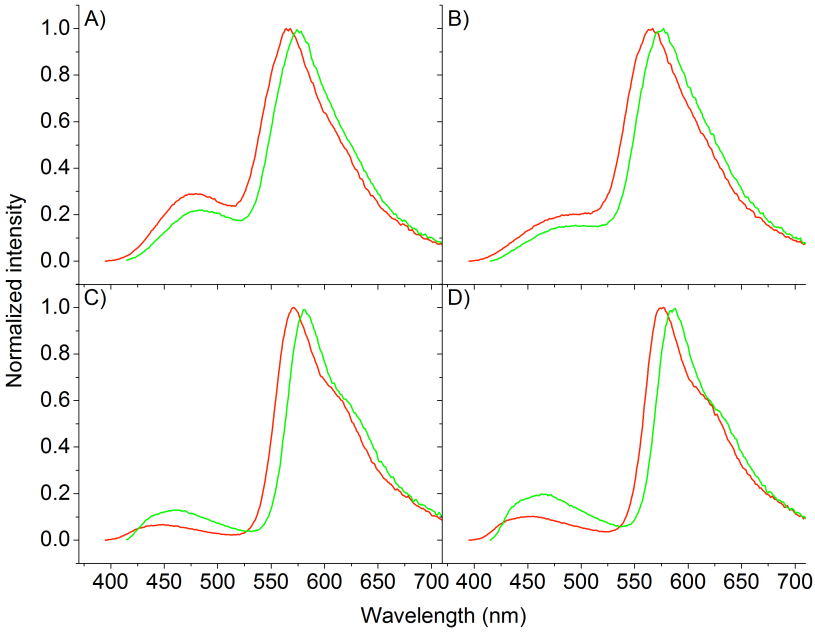

Figure S3. Emission spectra of **FCA** (red) and **TCA** (green) in additional organic solvents: A) EtOH, B) *i*-PrOH, C) EtOAc, and D) THF.

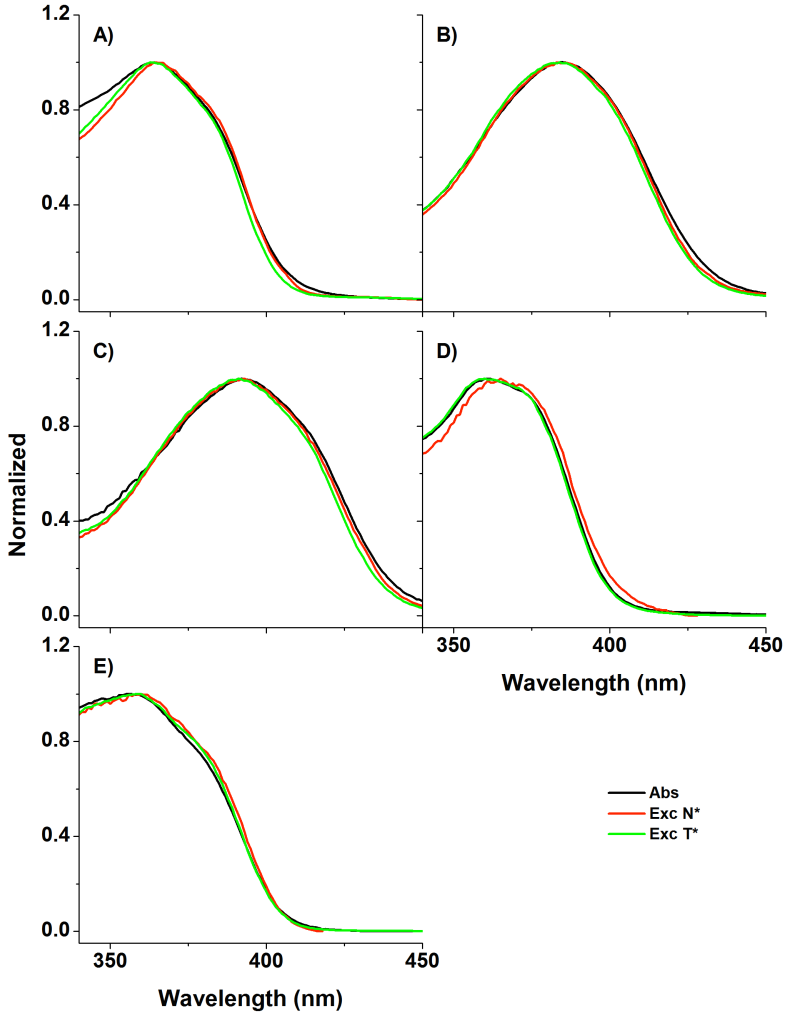

Figure S4. Absorption curves (*black*) and excitation spectra originated from N* and T* emission bands (*red* and *green*, respectively) in MeOH for A) **PCA**, B) **FCA**, C) **TCA**, D) **angTCA**, and E) **revTCA**.

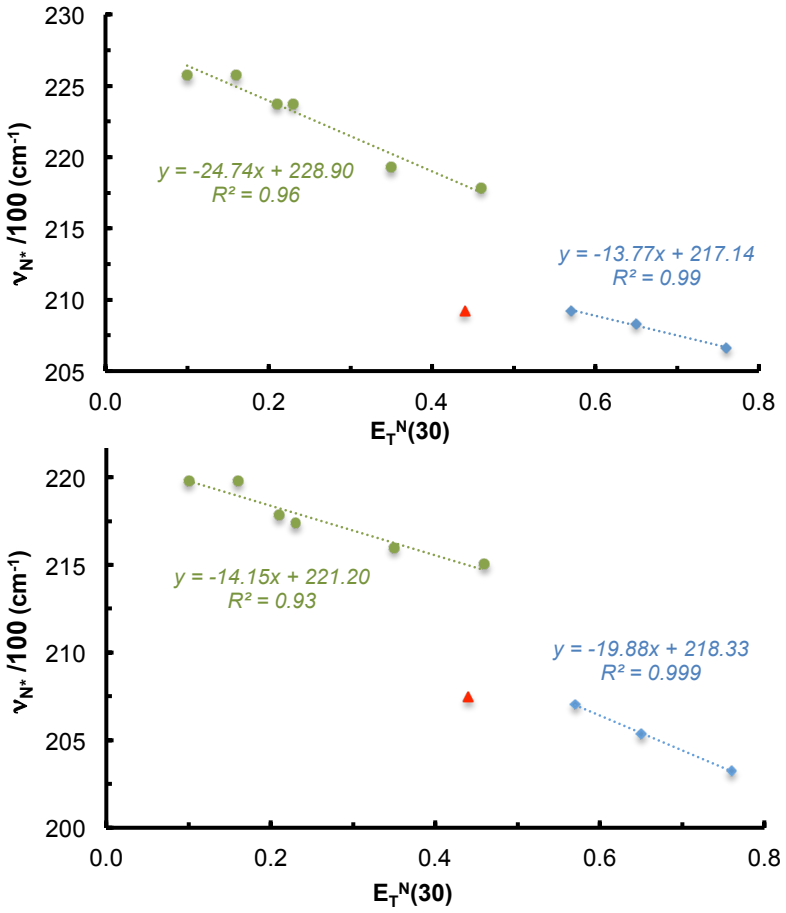

Figure S5. Dependence of the normal N* emission band of **FCA** (top) and **TCA** (bottom) on the normalized solvent polarity index $E_T^N(30)$. The green circles and blue diamonds represent aprotic (toluene, dioxane, THF, EtOAc, acetone, CH_3CN) and protic (MeOH, EtOH, i-PrOH) solvents, respectively. The green and blue dashed lines reflect the corresponding fitting curves. The red triangle displays the result of DMSO.

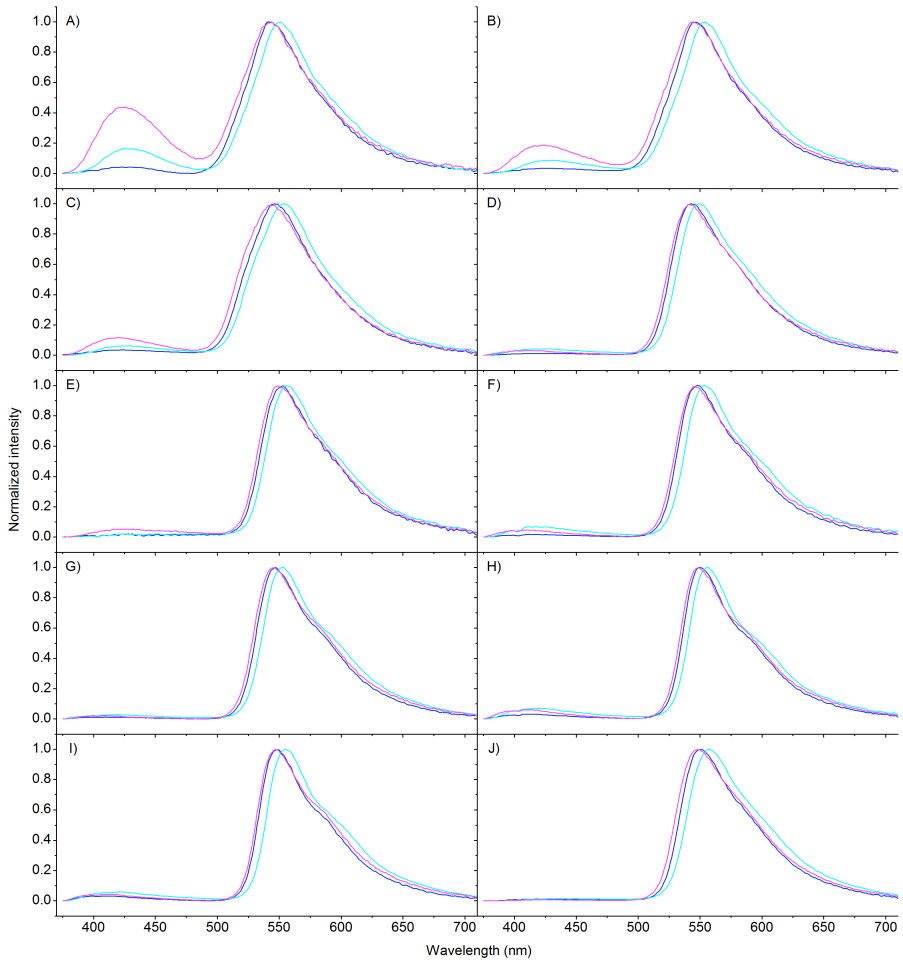

Figure S6. Emission spectra of **angTCA** (blue), **revTCA** (cyan), and **TC** (magenta) in different organic solvents: A) MeOH, B) EtOH, C) i-PrOH, D) acetonitrile, E) DMSO, F) Acetone, G) EtOAc, H) THF, I) Dioxane and J) Toluene.

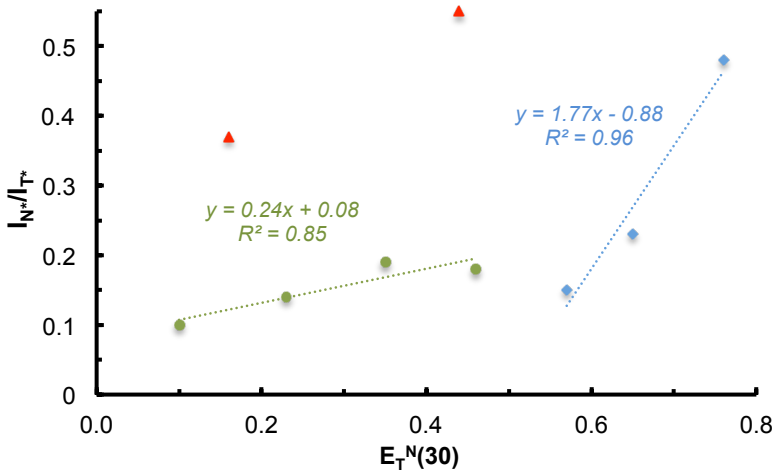

Figure S7. Intensity ratio I_{N*}/I_{T*} of **TCA** (bottom) as a function of the normalized Reichardt's parameter $E_T^N(30)$. The green circles and blue diamonds represent aprotic (toluene, dioxane, THF, EtOAc, acetone, CH_3CN) and protic (MeOH, EtOH, i-PrOH) solvents, respectively. The green and blue dashed lines reflect the corresponding fitting curves. The red triangle displays the result of DMSO and dioxane.

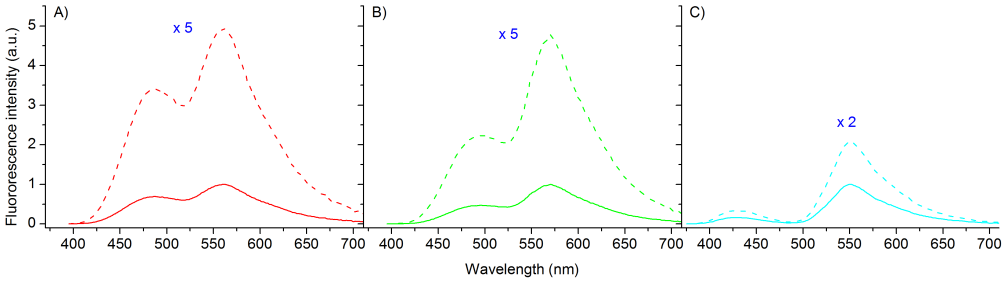

Figure S8. Turn-on emission in MeOH upon TFA addition (1 ‰, *v*/*v*) for A) **FCA** (red), B) **TCA** (green) and C) **revTCA** (cyan) as evidences of the acid-mediated PET inhibition.

2. Calculations of Dipole Moment Differences

2.1 Lippert-Mataga model

Herein, Stokes shift (Δν) *vs.* orientation polarizability function (also called Lippert's parameter, Δ*f*) were plotted for **the considered dyes (FCA**, **TCA**, **angTCA** and **revTCA)**. The linear plots shown were obtained with aprotic solvents (Toluene, Dioxane, EtOAc, Acetone, Acetonitrile) according to the Lippert's equation (orange line and crosses).

$$\textbf{Lippert's equation: } \bar{\nu}_A - \bar{\nu}_F = \frac{2}{hc}\Delta f \frac{(\mu_E - \mu_G)^2}{a^3} + cst$$

In this equation, h (= 6.63 x 10^{-27} ergs) is the Planck's constant, c (= 3.00 x 10^{10} cm.s^{-1}) is the speed of light, and a is the radius of the Onsager's cavity. ν_A and ν_F are the wavenumbers (cm^{-1}) of the absorption and emission, respectively. $\Delta\nu$ is the corresponding Stokes shift (ν_A-ν_F in cm^{-1}). μ_E and μ_G are the dipole moments of the excited and ground states, respectively. Δf is the Lippert's parameter defined as follows, where n is the refractive index and ε is the dielectric constant:

$$\Delta f = \left(\frac{\varepsilon - 1}{2\varepsilon + 1} - \frac{n^2 - 1}{2n^2 + 1} \right)$$

Remark: Exploiting the Lippert's equation to get the difference of the dipole moments (μ_E – μ_G) requires determining the Onsager radius. In the Lippert-Mataga model, the fluorophore is treated as a solute occupying a spherical volume for which the radius corresponds to the Onsager radius. Measuring the distance between both ends of the fluorophore and dividing it then by two, provide the Onsager radius. In general, this distance corresponds to that between the donor and acceptor groups of the fluorophore. Applying this approximation to **FCA**, **TCA**, **angTCA** and **revTCA** is not fully satisfactory because they are extended conjugated fluorophores with the accepting and donating groups (respectively highlighted in red and blue in Figure S8), which are not positioned at the extremities. However, the use of these data remains acceptable for comparative analysis within the compounds of this series because they are structurally close and the same approximation to calculate the Onsager radius has been made for each of them.

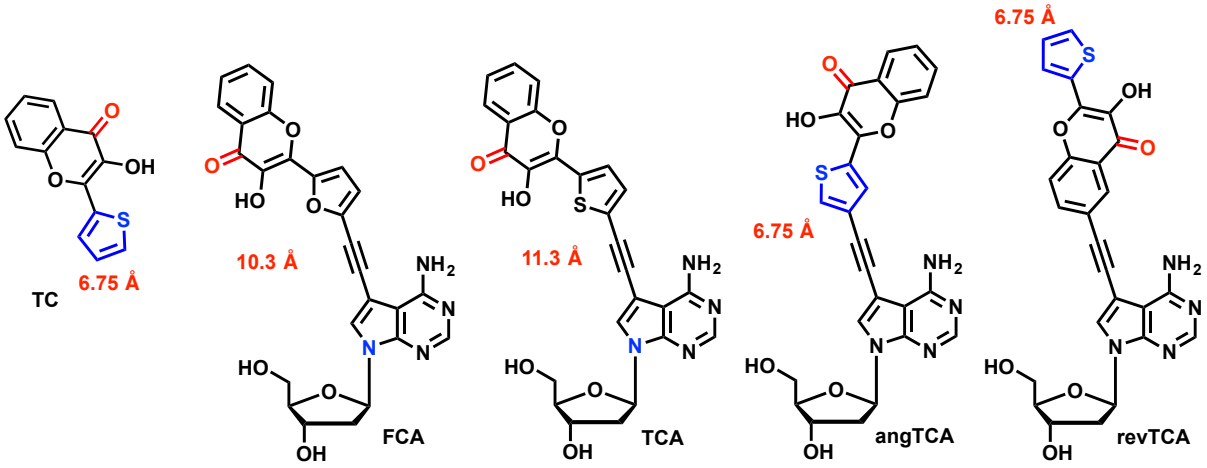

Figure S9. Considered 3HC derivatives with their D-π-A distance corresponding to the Onsager's cavity used for the calculation of the dipole moment differences listed in Table S1. *Donor and acceptor functional groups of the parent 2-aryl-3HC (**TC**) and corresponding dA conjugates (**FCA, TCA, angTCA** and **revTCA**) are depicted in blue and red, respectively.*

2.2 Lippert-Mataga function plots

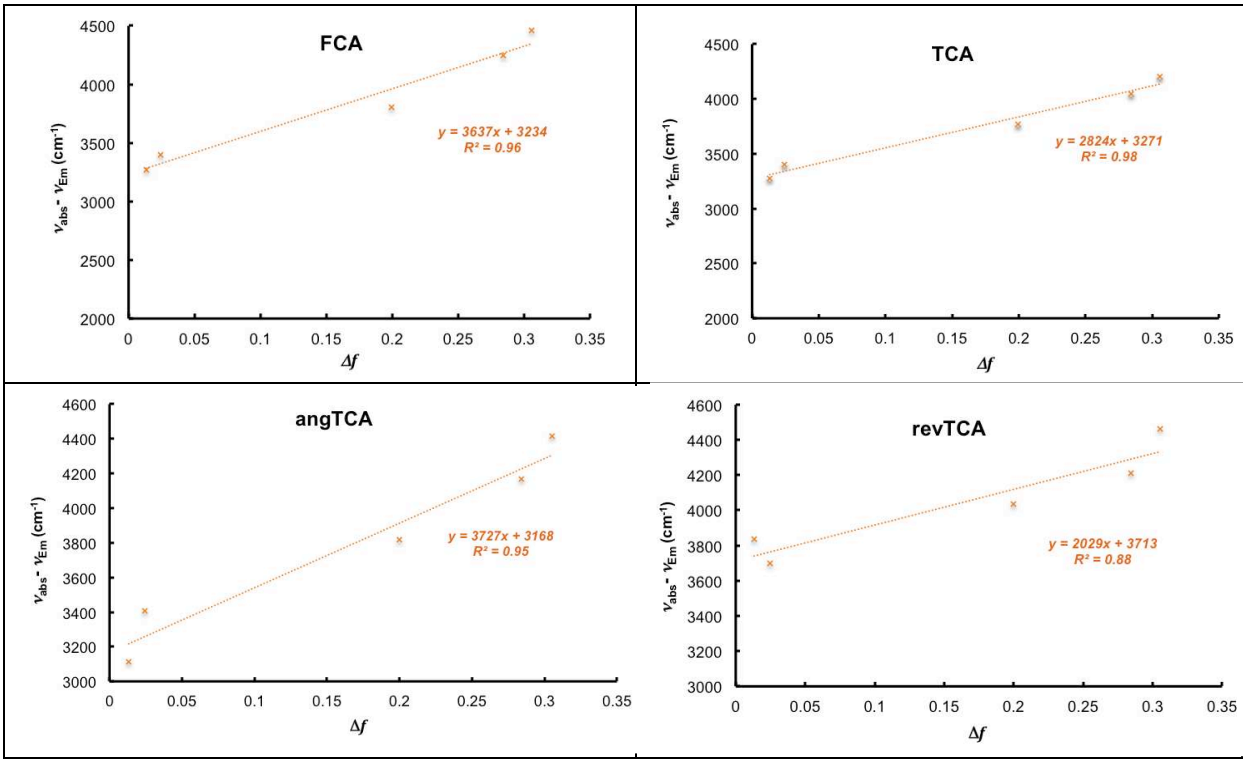

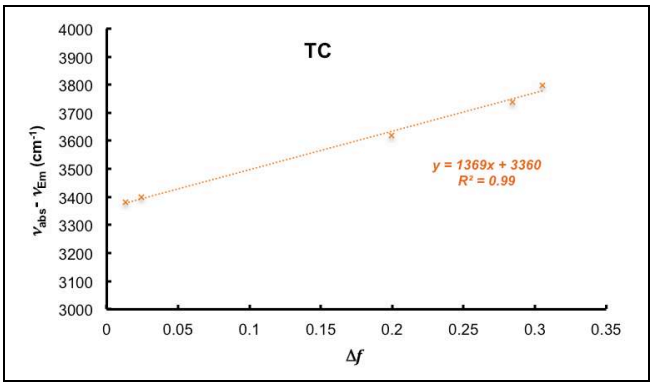

Figure S10. Dependence of the Stokes shift ($\Delta\nu$) on the orientation polarizability function Δf (Lippert's parameter) for the fluorophores considered in this study (**FCA**, **TCA**, **angTCA**, **revTCA**, and **TC**). The linear fits were obtained only with aprotic solvents (Toluene, Dioxane, EtOAc, Acetone, Acetonitrile) according to the Lippert's equation.

Table S1: Dipole Moment Differences (in Debye – D) of the investigated fluorophores:

Parent 3HC:

TC
2.3

3HC-based dA analogs:

FCA	TCA	angTCA	revTCA
7.0	7.1	3.8	2.8

3. Synthetic Procedures

3.1 Preparation of the 3-HC fluorophore 25

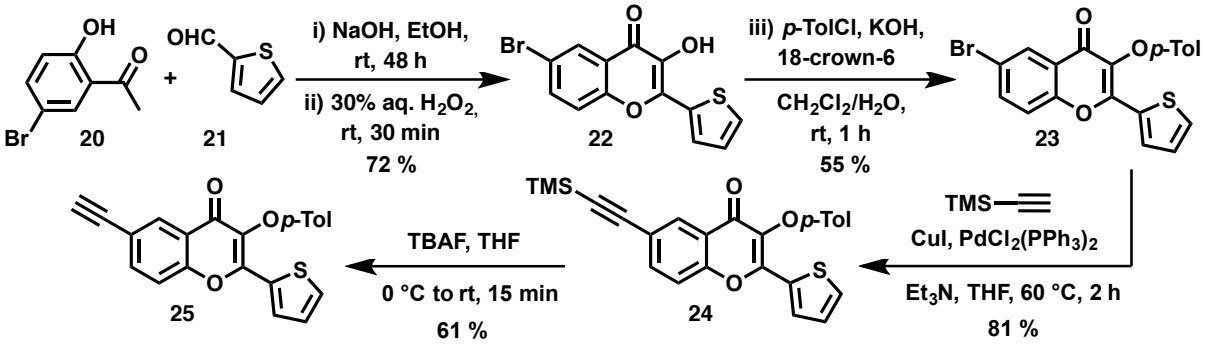

Scheme S1. Synthetic preparation of the 3HC coupling partner **30** for the reversed orientation approach.

6-Bromo-2-(thiophen-2-yl)-3-hydroxychromen-4-one (22): To a stirred solution of **20** (4.00 g, 18.6 mmol) and **21** (2.1 mL, 22.3 mmol) in ethanol (36 mL), was dropwise added a 5 M NaOH solution (12 mL). The reaction mixture was stirred 48 h at rt before a dropwise addition of 30 % aq. hydrogen peroxide solution (5 mL). The resulting mixture was stirred 30 min at rt, and then poured into cold water (200 mL) and acidified with 2 M HCl to pH = 5. The resulting precipitate was filtered and thoroughly washed with water and cyclohexane to provide the desired product **22** as a yellow solid (4.31 g, 72 %). $C_{13}H_7BrO_3S$ (323.16). R_f = 0.5 (toluene/acetone = 9:1). ^{1}H-NMR (400 MHz, CD_2Cl_2 with drops of CD_3OD): δ 8.27 (d, J = 2.4 Hz, 1H), 8.01 (dd, J = 3.8, 1.2 Hz, 1H), 7.77 (dd, J = 8.9, 2.4 Hz, 1H), 7.66 (dd, J = 5.0, 1.2 Hz, 1H), 7.50 (d, J = 9.0 Hz, 1H), 7.23 (dd, J = 5.0, 3.8 Hz, 1H). ^{13}C-NMR (101 MHz, CD_2Cl_2 with drops of CD_3OD): δ 172.1, 154.2, 144.7, 137.4, 136.8, 133.1, 131.0, 129.9, 128.4, 128.0, 123.6, 120.6, 118.1. MS (ESI+, MeOH): *m/z*: 322.9, 325.0 $[M+H]^+$.

6-Bromo-2-(thiophen-2-yl)-3-((methylbenzoyl)oxy)chromen-4-one (23): To a stirred solution of **22** (4.00 g, 12.378 mmol) in pyridine (62 mL), was dropwise added *p*-TolCl (5.58 mL, 3 eq.) at 0 °C. Then, the reaction mixture was stirred overnight under argon at rt. The resulting solution was reduced *in vacuo* by 2/3 of its volume, and CH_2Cl_2 was added for dilution. The organic phase was successively washed with saturated NH_4Cl and $NaHCO_3$ aqueous solutions, brine and dried over $MgSO_4$, filtered and reduced *in vacuo*. The residue was washed with toluene (10 mL) to remove *p*-toluoyl anhydride, and then with petroleum ether (2 x 20 mL) to provide the desired product **23** as a white light yellow (3.00 g, 55 %). $C_{21}H_{13}BrO_4S$ (441.30). R_f = 0.55 (PE/Et_2O = 7:3). ^{1}H-NMR (400 MHz, CD_2Cl_2): δ 8.33 (d, J = 2.4 Hz, 1H, H5), 8.17 (d, J = 7.8 Hz, 2H, H*o*-Tol), 7.96 (d, J = 3.8 Hz, 1H, Hγ), 7.83 (dd, J = 9.2, 2.4 Hz, 1H, H7), 7.64 (d, J = 4.9 Hz, 1H, Hα), 7.54 (d, J = 8.9 Hz, 1H, H8), 7.40 (d, J = 7.9 Hz, 2H, H*m*-Tol), 7.21 (t, J = 4.5 Hz, 1H, Hβ), 2.49 (s, 3H, CH_3). ^{13}C-NMR (101 MHz, CD_2Cl_2): δ 170.6, 163.6, 154.6, 152.5, 146.0, 137.4, 132.8, 132.0, 131.4, 131.3, 131.2, 130.1, 128.9, 128.6, 126.2, 125.5, 120.6, 119.0, 22.1. MS (ESI^+, MeOH) *m/z*: 440.8 $[M+H]^+$. HRMS (ESI^+): *m/z* calcd for $C_{21}H_{14}BrO_4S$: 440.9791 $[M+H]^+$; found 440.9809.

6-((Trimethylsilyl)ethynyl)-2-(thiophen-2-yl)-3-((methylbenzoyl)oxy)chromen-4-one (24): To a stirred solution of **23** (1.890 g, 4.283 mmol, 1 eq) in dry THF (53.5 mL, 0.08 M), previously degased by sonication under argon, were sequentially added TMS-acetylene (1.4 mL, 2.3 eq.), Et_3N (4.8 mL, 8 eq.) and CuI (13 mol%, 108 mg) / $PdCl_2(PPh_3)_2$ (13 mol%, 395 mg) simultaneously. The reaction mixture was refluxed at 70 °C for 3h, and then, kept at 60 °C overnight. The volatiles were reduced *in vacuo*. The residue was dissolved in CH_2Cl_2 (50 mL), filtered to remove solid particles. CH_2Cl_2 was removed under reduced pressure, and the resulting crude was taken out with a minimum amount of toluene (50 mL), then petroleum ether was added (ca. 100 mL) to precipitate the product. After filtration, and washing with PE (3x 20 mL) and cold toluene (2 x 10 mL), the desired compound **24** was obtained as a yellow solid (1.587 g, 81 %). $C_{26}H_{22}O_4SSi$ (458.60). R_f = 0.45 (PE/EtOAc = 4:1). ^{1}H-NMR (400 MHz, $CDCl_3$): δ 8.33 (d, J = 2.1 Hz, 1H, H5), 8.20 (d, J = 8.2 Hz, 2H, H*o*-Tol), 7.89 (dd, J = 3.9, 1.2 Hz, 1H, Hγ), 7.75 (dd, J = 8.7, 2.1 Hz, 1H, H7), 7.56 (dd, J = 5.0, 1.2 Hz, 1H, Hα), 7.51 (d, J = 8.7 Hz, 1H, H8), 7.35 (d, J = 8.0 Hz, 2H, H*m*-Tol), 7.16 (dd, J = 5.1, 3.9 Hz, 1H, Hβ), 2.48 (s, 3H, CH_3), 0.27 (s, 9H, TMS). ^{13}C-NMR (101 MHz, $CDCl_3$): δ 170.9, 163.3, 154.7, 151.8, 145.1, 137.0, 132.1, 131.6, 131.1, 131.0, 130.7, 129.9, 129.6, 128.1, 125.8, 123.6, 120.7, 118.2, 103.2, 96.0, 22.0, 0.0. MS (ESI^+, MeOH) *m/z*: 459.0 $[M+H]^+$. HRMS (ESI^+): *m/z* calcd for $C_{26}H_{23}O_4SSi$: 459.1081 $[M+H]^+$; found 459.1090.

6-Ethynyl)-2-(thiophen-2-yl)-3-hydroxychromen-4-one (25): To a stirred solution of **24** (1.587 g, 3.461 mmol, 1 eq.) in THF (32 mL) at 0 °C, TBAF (3.98 mL, 1.0 M in THF, 1.15 eq.) was added dropwise. The reaction mixture was stirred for 15 min at rt, before quenching with water. The organic phase was extracted with Et_2O (3 x 50 mL) and CH_2Cl_2 (2 x 30 mL), dried over $MgSO_4$, filtered and reduced *in vacuo*. The resulting residue was purified by flash chromatography on silica gel eluted with petroleum ether/Et_2O (100:0 → 50:50, v/v) to provide the desired compound **25** as a yellow solid (811 mg, 61 %). $C_{23}H_{14}O_4S$ (386.42). R_f = 0.6 (toluene/Et_2O = 9:1). ^{1}H-NMR (400 MHz, $CDCl_3$): δ 8.37 (d, J = 2.1 Hz, 1H, H5), 8.21 (d, J = 8.2 Hz, 2H, H*o*-Tol), 7.92 (dd, J = 3.8, 1.2 Hz, 1H, Hγ), 7.79 (dd, J = 8.7, 2.1 Hz, 1H, H7), 7.59 (dd, J = 5.0, 1.2 Hz, 1H, Hα), 7.54 (d, J = 8.7 Hz, 1H, H8), 7.36 (d, J = 8.0 Hz, 2H, H*m*-Tol), 7.18 (dd, J = 5.0, 3.9 Hz, 1H, Hβ), 3.15 (s, 1H, ≡CH), 2.48 (s, 3H, CH_3). ^{13}C-NMR (101 MHz, $CDCl_3$): δ 170.8, 163.3, 155.0, 151.9, 145.2, 137.2, 132.2, 131.7, 131.1, 131.0, 130.8, 130.3, 129.6, 128.1, 125.8, 123.7, 119.6, 118.4, 82.0, 78.7, 22.0. MS (ESI^+, MeOH) *m/z*: 386.80 $[M+H]^+$. HRMS (ESI^+): *m/z* calcd for $C_{23}H_{15}O_4S$: 387.0686 $[M+H]^+$; found 387.0707.

3.2 Preparation of the dual-emissive 7 – revTCA

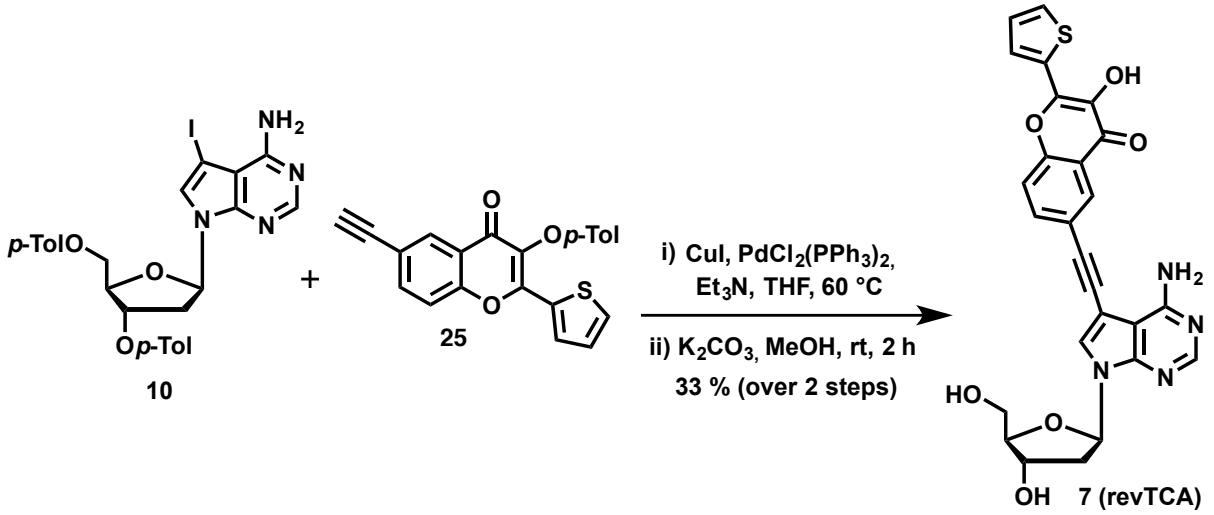

Scheme S2. Synthesis of the two-color dA analog **revTCA**.

7-Deaza-2′-deoxy-7-((3-hydroxy-4-oxo-2-(thiophen-2-yl)chromen-6-yl)ethynyl)adenosine (7 – revTCA): To a stirred solution of **10** (150 mg, 0.245 mmol) in dry THF (7.9 mL), previously degased by sonication under argon, were sequentially added **25** (220 mg, 0.563 mmol, 2.3 eq.), Et_3N (276 μL, 8 eq.), and CuI (3 mg, 7 mol%) / $PdCl_2(PPh_3)_2$ (12 mg, 7 mol%) simultaneously. The reaction mixture was warmed to 60 °C under argon overnight. The resulting solution was diluted with CH_2Cl_2 (10 mL) and the volatiles were removed *in vacuo*. The residue was purified by flash chromatography on silica gel eluted with CH_2Cl_2/MeOH (99:1 → 85:15, v/v) to provide the coupled product as a yellow solid (210 mg, 98 %). $C_{50}H_{38}N_4O_9S$ (870.24). R_f = 0.25 (toluene/acetone = 7:3). MS (ESI^+, MeOH) *m/z*: 871.3 $[M+H]^+$. HRMS (ESI^+): *m/z* calcd for $C_{50}H_{39}N_4O_9S$: 871.2432 $[M+H]^+$; found 871.2435. The latter was considered pure enough, and engaged in the next step. To a stirred solution of this intermediate (200 mg, 0.23 mmol) in CH_2Cl_2/MeOH (5:5 mL) was added a K_2CO_3 saturated methanolic solution (80 mL). The reaction mixture was stirred at rt for 2h, before H_2O (50 mL) was added. The resulting solution was acidified with AcOH until pH = 5 and stored in the fridge overnight, and filtered. The obtained solid was washed with H_2O (3 x 20 mL), CH_2Cl_2 (3 x 20 mL), MeOH (20 mL) and

dissolved in DMF to be purified by flash chromatography on silica gel eluted with $CHCl_3$/MeOH/H_2O (6:1/0.15, v/v) to provide the desired product **7** as a yellowish brown solid (40 mg, 34 %). $C_{26}H_{20}N_4O_6S$ (516.53). R_f = 0.5 (CH_2Cl_2/MeOH = 4:1). ^{1}H-NMR (400 MHz, Pyridine-d^5): δ 13.60 (s, 1H), 8.73 (s, 1H), 8.61 (s, 1H), 8.30 (s, 1H), 8.21 (d, J = 3.6 Hz, 1H), 7.85 (d, J = 4.8 Hz, 1H), 7.77 (d, J = 8.6 Hz, 1H), 7.53 (d, J = 8.3 Hz, 1H), 7.33 (t, J = 4.3 Hz, 1H), 7.27 (t, J = 6.8 Hz, 1H), 5.21 (dt, J = 6.1, 3.1 Hz, 1H), 4.62 (q, J = 3.3 Hz, 1H), 4.29 (dd, J = 11.9, 3.5 Hz, 1H), 4.19 (dd, J = 11.9, 3.5 Hz, 1H), 3.05 (dt, J = 13.1, 6.5 Hz, 1H), 2.78 (ddd, J = 13.0, 6.1, 3.3 Hz, 1H). ^{13}C-NMR (101 MHz, Pyridine-d^5): δ 173.0, 159.5, 154.8, 154.4, 151.1, 144.8, 139.6, 136.1, 134.4, 131.0, 129.3, 129.0, 128.6, 128.3, 123.6, 120.2, 119.3, 104.4, 96.3, 91.1, 89.8, 85.7, 85.1, 72.6, 63.6, 42.4. MS (ESI^+, MeOH) *m/z*: 516.9 $[M+H]^+$. HRMS (ESI^+): *m/z* calcd for $C_{26}H_{21}N_4O_6S$: 517.1176 $[M+H]^+$; found 517.1187.

4. NMR Spectra

3.2. SI of publication 2

Supporting Information To:

Control of intermolecular photoinduced electron transfer in deoxyadenosine-based fluorescent probes

Hoang-Ngoan Le,[†][a] Johanna Brazard,[b, c] Guillaume Barnoin,[a] Steve Vincent,[a] Benoît Y. Michel,*[a] Jérémie Leonard,[b] and Alain Burger*[a]

[a] *Université Côte d'Azur, CNRS, Institut de Chimie de Nice, UMR 7272 − Parc Valrose, 06108 Nice cedex 2, France*
[b] *Université de Strasbourg, CNRS, Institut de Physique et Chimie des Matériaux de Strasbourg and Labex NIE, UMR 7504, F-67200 Strasbourg, France*

[†] Main contributor to these research works

Corresponding authors: benoit.michel@univ-cotedazur.fr, burger@univ-cotedazur.fr

Graphical abstract:

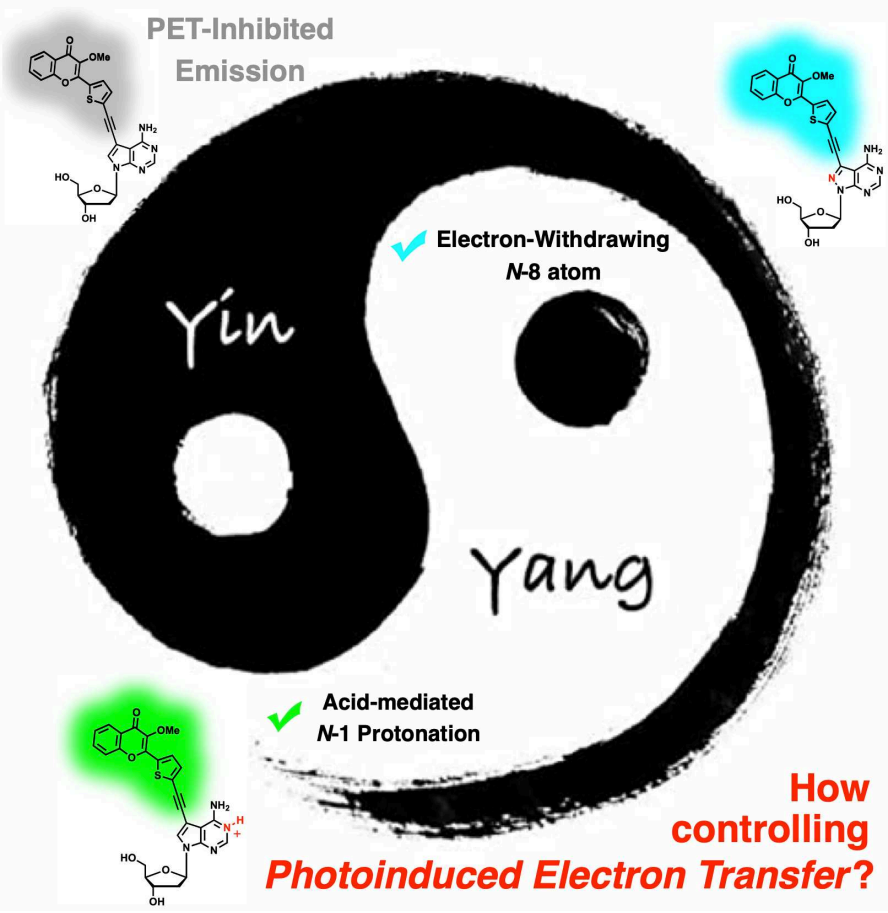

Table of contents

Experimental section

1. General Methods

All reactions involving air- and water-sensitive conditions were performed in oven-dried glassware under argon by using Schlenk techniques employing a dual vacuum/argon manifold system and dry solvents. The synthetic intermediates were initially co-evaporated twice with toluene and dried *in vacuo* before use. All chemical reagents were purchased from commercial sources (Sigma-Aldrich, Acros, Alfa Aesar) and were used as supplied. Anhydrous solvents were obtained according to standard procedures.[1] The reactions were monitored simultaneously by liquid chromatography–mass spectrometry (LC-MS) and thin-layer chromatography (TLC, silica gel 60 F254 plates). Compounds were visualized on TLC plates by both UV radiation (254 and 365 nm) and spraying with a staining agent (Vanillin, PMA, $KMnO_4$ or ninhydrin) followed by subsequent warming with a heat gun. Column chromatography was performed with flash silica gel (40−63 μm) with the indicated solvent system using gradients of increasing polarity in most cases.[2] All NMR spectra (^{1}H, ^{13}C, ^{2}D) were recorded on 200, 400 or 500 MHz Bruker Advance Spectrometers. ^{1}H-NMR (200, 400 and 500 MHz), ^{13}C{^{1}H}NMR (50, 101 and 126 MHz, recorded with complete proton decoupling), and ^{31}P-NMR (80 and 160 MHz, *proton decoupling*) spectra were obtained with samples dissolved in $CDCl_3$, CD_2Cl_2, CD_3OD, DMSO-d^6, acetone-d^6, CD_3CN or C_5D_5N with the residual solvent signals used as internal references: 7.26 ppm for C*H*Cl_3, 5.32 ppm for CD*H*Cl_2, 3.31 ppm for CD_2*H*OD, 2.50 ppm for (CD_3)(CD_2*H*)S(O), 2.05 ppm for (CD_3)(CD_2*H*)C(O), 1.94 ppm for CD_2*H*CN, 8.74 ppm for C_5D_4*H*N regarding ^{1}H-NMR experiments, and 77.2 ppm for $CDCl_3$, 53.8 ppm for CD_2Cl_2, 49.0 ppm for CD_3OD, 39.4 ppm for (CD_3)$_2$S(O), 30.8 ppm for (CD_3)$_2$C(O), 118.7 ppm for CD_3CN, 150.3 ppm for C_5D_5N concerning ^{13}C-NMR experiments.[3,4] Chemical shifts (δ) are given in ppm to the nearest 0.01 (^{1}H) or 0.1 ppm (^{13}C and ^{31}P). The coupling constants (J) are given in Hertz (Hz). The signals are reported as follows: (s = singlet, d = doublet, t = triplet, m = multiplet, br = broad). Assignments of ^{1}H and ^{13}C-NMR signals were achieved with the help of D/H exchange, COSY, DEPT, APT, HMQC, HSQC, TOCSY, NOESY, and HMBC experiments. LC-MS spectra were recorded using an ion trap Esquire 3000 Plus mass spectrometer equipped with an electrospray ionization (ESI) source in both positive and negative modes. High-resolution mass spectrometry (HRMS) was conducted with a hybrid ion trap−Orbitrap Thermo Scientific™ mass spectrometer (combining quadrupole precursor selection with high-resolution and accurate-mass Orbitrap detection) using ESI techniques. Systematic flavone and nucleoside nomenclatures are used below for the assignment of each spectrum. All solvents for absorption and fluorescence experiments were of spectroscopic grade. Absorption spectra were recorded on a Cary 100 Bio UV–Vis spectrophotometer (Varian/Agilent) using Suprasil® quartz cuvettes with 1 cm path length. Stock solutions of dyes **MFCA, MTCA, MFC8A,** and **MTC8A** were prepared using DMSO. The samples used for spectroscopic measurements contained ≈ 0.2 % v/v of solvents of the stock solution. Fluorescence spectra were recorded on a FluoroMax 4.0 spectrofluorometer (Jobin Yvon, Horiba) with a thermostatically controlled cell compartment at 20 ± 0.5 °C with slits open to 2 nm and were corrected for Raman scattering, lamp fluctuations and instrumental wavelength-dependent bias.

Excitation wavelengths correspond to the absorption maxima except when mentioned in the corresponding experiments. Supplementary data associated with the synthesis of intermediates and target compounds, including the experimental protocols, some ^{1}H, ^{13}C, ^{1}H–^{1}H COSY, ^{1}H–^{1}H NOESY, ^{1}H–^{13}C HSQC, and ^{1}H–^{13}C HMBC NMR spectra of derivatives previously mentioned, can be consulted in this *Supporting Information*. Redox potentials were recorded on EG&G Princeton Applied Research Model 273A. A three-electrode cell system was used for the measurements. The working, reference, and auxiliary electrodes were glassy carbon, Ag/AgCl, and platinum foil, respectively.

2. Synthesis

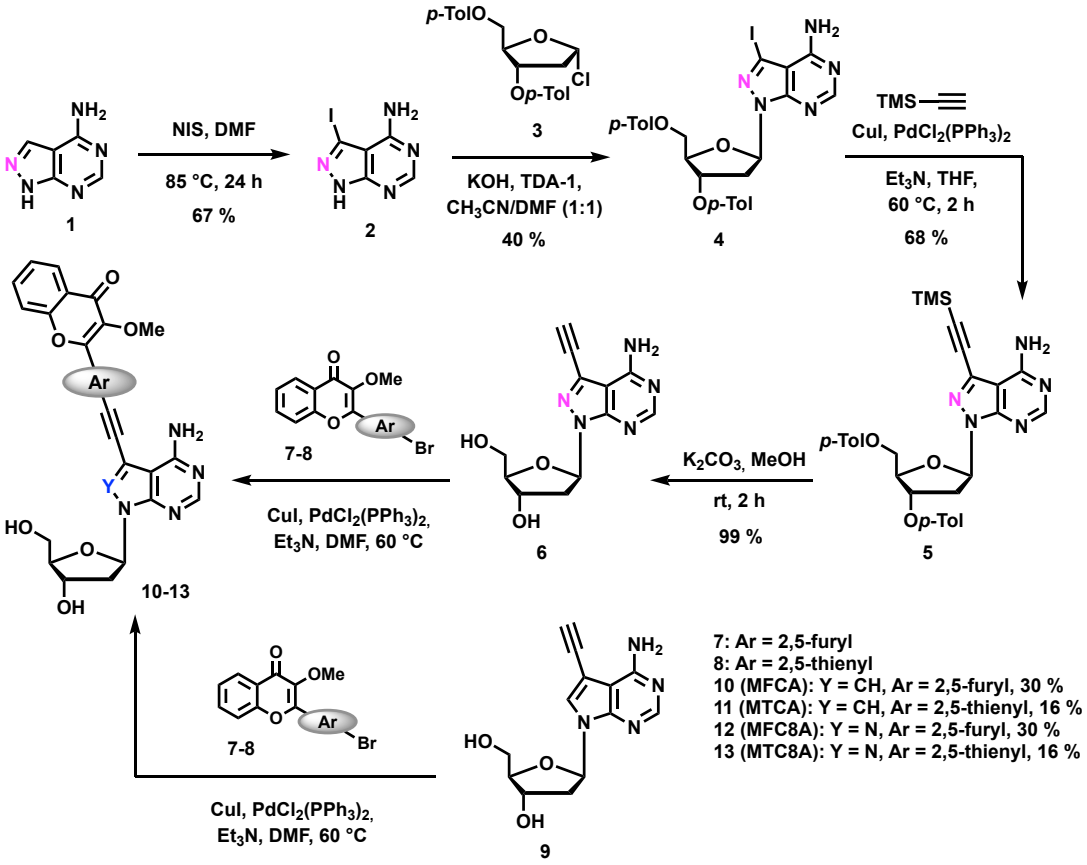

Scheme S1. Synthesis of conjugated systems between 3MC and 7-deaza-dA analogs.

At the glycosylation step, difficulties arose from the very poor solubility of starting material (**2**) combined with a competitive reaction at the exocyclic NH_2 group (checked by LC/MS). Several conditions have been tested (*Table S1*). As a result, we obtained a comparable yield with Seela's procedure[5] while shortcutting one step of amination. Moreover, this approach also simplified the first Sonogashira reaction by ensuring a good solubility of both starting material (**4**) and product (**5**). The first Sonogashira coupling with TMS-acetylene followed by the removal of the silyl ether were proceeded smoothly. However, due to the poor solubility of deprotected product (**6**), the compound was purified by extraction. For that purpose, we used pure starting material (**5**) to avoid

chromatography, which is low-yielding. During the last Sonogashira coupling, although the reactions were stopped after a good conversion (by TLCs), the isolated yields were rather low. This problem was mainly due to the poor solubility of the desired products (**10–13**) that made the purification process difficult and low-yielding. However, the important goal was to obtain products of the highest purity for further photophysical investigations. Starting from **9**, the synthesis of **10** and **11** was previously reported.[6]

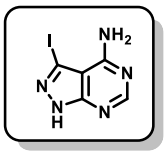

8-Aza-7-deaza-7-iodoadenine (2): A stirred suspension of 4-Amino-1H-pyrazolo[3,4-d]-pyrimidine (2, 5.0 g, 37.0 mmol, 1.0 equiv) and *N*-iodosuccinimide (12.5 g, 55.5 mmol, 1.5 equiv) in DMF (20 mL) was heated at 85 °C for 24 h. The mixture was cooled down to room temperature, filtered and thoroughly washed with cold ethanol until obtaining a white-off solid. The solid was dried *in vacuo* to provide the desired product as a light-yellow solid (6.47 g, 67 %). R_f = 0.47 (CH_2Cl_2/MeOH = 9:1). ^{1}H-NMR (200 MHz, DMSO-d_6) δ 13.81 (s, 1H), 8.17 (s, 1H), 7.15 (br s, 3H). ^{13}C-NMR (101 MHz, DMSO-d_6) δ 157.5, 156.0, 155.0, 102.5, 89.7.

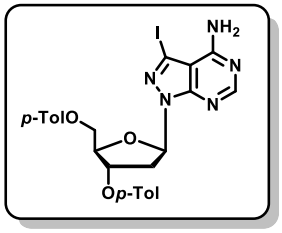

8-Aza-7-deaza-2′-deoxy-7-iodo-3′,5′-di-*O*-*p*-toluoyladenosine (4): To a sonicated (in 1 min) suspension of KOH (645 mg, 11.493 mmol, 1.5 eq) in dry DMF/ACN (153.2 mL, 1:1, v/v) were sequentially added TDA-1 (511 μL, 1.597 mmol), **2** (2.00 g, 7.66 mmol). The suspension was stirred under argon at room temperature for 2 hours *(a hair dryer has been used sometimes to warm up the mixture for better solubility)* to obtain a solution-like *(clear)* suspension. The mixture was cooled down using an ice bath and a solution of the chlorosugar **3** (2.98 g, 7.66 mmol, 1 eq) in dry CH_2Cl_2 (20 mL) was dropwise added over 10 min. Stirring was maintained for 2 hours and the resulting mixture was diluted with H_2O (20 mL) and brine (10 mL). Extraction was performed using Et_2O (3 x 150 mL). The organic layer was washed twice with H_2O (2 x 20 mL) to partially remove DMF and this washing aqueous solution was combined with the above-mentioned aqueous phase for next extraction with Et_2O. All the organic layers were combined, dried over $MgSO_4$ and evaporated under vacuum to remove all the volatiles. The residue was purified by flask chromatography on silica gel using petroleum ether / EtOAc (85:15 → 0:100) to provide the desired product (1.86 g, 40 %) as a light-yellow (or brownish) foam. R_f = 0.45 (toluene/EtOAc = 1:1). R_f = 0.35 (petroleum ether/EtOAc = 3:7). ^{1}H-NMR (400 MHz, CD_2Cl_2-d_2) δ 8.32 (s, 1H), 8.11–7.83 (m, 4H), 7.29 (dd, J = 8.1, 2.6 Hz, 4H), 6.82 (t, J = 6.6 Hz, 1H), 5.94 (s, 2H), 5.81 (dt, J = 6.3, 3.0 Hz, 1H), 4.62–4.48 (m, 3H), 3.43 (dt, J = 13.7, 6.7 Hz, 1H), 2.65 (ddd, J = 14.1, 6.5, 3.3 Hz, 1H), 2.43 (s, 3H), 2.41 (s, 3H). ^{13}C-NMR (101 MHz, CD_2Cl_2-d_2) δ 166.7, 166.4, 158.2, 157.0, 155.4, 144.9, 144.4, 130.3, 130.2, 129.7, 129.7, 127.7, 127.4, 105.0, 89.5, 85.2, 83.1, 75.9, 64.9, 36.4, 22.0, 22.0. MS (ESI$^+$, MeOH) *m/z*: 613.80 [M+H]$^+$.

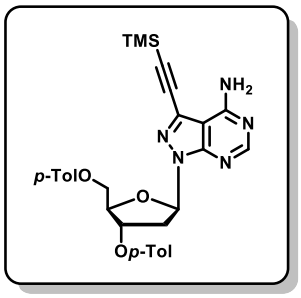

8-Aza-7-deaza-2′-deoxy-3′,5′-di-*O*-*p*-toluoyl-7-((trimethylsilyl)ethynyl)adenosine (5): To a stirred solution of **4** (4.34 g, 7.08 mmol) in dry THF (44 mL) under argon, were sequentially added Et_3N (4.98 mL, 35.38 mmol, 5 eq.), TMS-acetylene (1.52 mL, 10.61 mmol, 1.5 eq.), and CuI (8 mol%, 110 mg) / $PdCl_2(PPh_3)_2$ (8 mol%, 401 mg). The reaction mixture was stirred under argon at 60 °C for 2 h. Then, the resulting mixture was diluted with CH_2Cl_2 (30 mL) and evaporated under reduced pressure. The residue was purified by flash

chromatography on silica gel eluted with toluene/Et_2O (80:20 → 0:100, v/v) to provide the desired compound **5** as a white solid (2.81 g, 68 %). R_f = 0.67 (CH_2Cl_2/MeOH = 9:1); ^{1}H-NMR (400 MHz, CD_2Cl_2-d_2) δ 8.33 (s, 1H), 8.06–7.90 (m, 4H), 7.36–7.19 (m, 4H), 6.86 (t, J = 6.5 Hz, 1H), 6.17 (s, 2H), 5.85 (dt, J = 6.7, 3.4 Hz, 1H), 4.59 (ddd, J = 5.5, 4.2, 3.0 Hz, 1H), 4.56–4.50 (m, 2H), 3.44 (dt, J = 14.0, 6.5 Hz, 1H), 2.67 (ddd, J = 14.0, 6.6, 3.7 Hz, 1H), 2.43 (s, 3H), 2.41 (s, 3H), 0.35 (s, 9H). ^{13}C-NMR (101 MHz, CD_2Cl_2-d_2) δ 166.7, 166.4, 158.4, 157.5, 154.9, 144.9, 144.4, 130.3, 130.2, 129.7, 129.7, 128.2, 127.7, 127.4, 102.9, 102.2, 96.6, 85.3, 83.1, 75.8, 64.9, 36.3, 22.0, -0.1. MS (ESI$^+$, MeOH) *m/z*: 583.93 [M+H]$^+$. HRMS (ESI$^+$): *m/z* calcd for $C_{31}H_{34}N_5O_5Si$: 584.23237 [M+H]$^+$; found 584.23395.

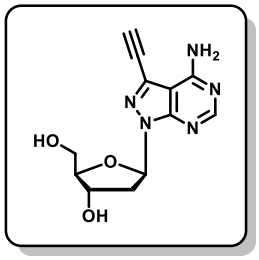

8-Aza-7-deaza-2′-deoxy-7-ethynyladenosine (6): To a stirred solution of **5** (5.39 g, 9.23 mmol) in CH_2Cl_2 (80 mL)/MeOH (20 mL), was added a saturated solution of K_2CO_3 in MeOH (100 mL). The reaction mixture was stirred at rt for 2 h and all the volatiles were removed under reduced pressure. The residue was dissolved in H_2O (100 mL) followed by thorough extractions with EtOAc (10 x 200 mL). All the organic layers were combined, washed with brine (100 mL), dried over $MgSO_4$ and reduced under vacuum. The obtained solid was purified by washing with toluene (3 x 20 mL) and dried under high vacuum to provide the desired product as a white solid (2.52 g, 99 %). R_f = 0.25 (CH_2Cl_2/MeOH = 9:1). ^{1}H-NMR (400 MHz, Pyridine-d_5) δ 9.27 (s, 2H, NH_2), 8.69 (s, 1H), 7.28 (t, J = 6.4 Hz, 1H), 7.23 (s, 1H), 6.63 (t, J = 6.2 Hz, 1H), 5.30 (dq, J = 7.9, 4.1 Hz, 1H), 4.69 (td, J = 4.9, 3.6 Hz, 1H), 4.63 (s, 1H), 4.42–4.12 (m, 2H), 3.37 (dt, J = 12.7, 6.1 Hz, 1H), 2.75 (ddd, J = 13.2, 6.8, 4.3 Hz, 1H). ^{13}C-NMR (101 MHz, Pyridine-d_5) δ 159.5, 158.0, 155.1, 127.4, 103.3, 90.3, 86.7, 85.5, 77.0, 72.7, 64.3, 40.2. MS (ESI$^+$, MeOH) *m/z*: 275.87 [M+H]$^+$.

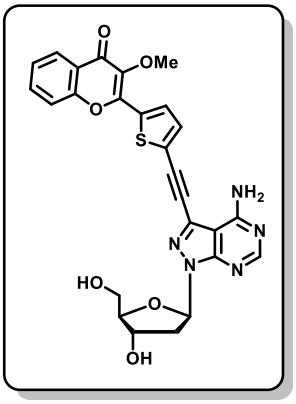

8-Aza-7-deaza-2′-deoxy-7-((5-(3-methoxy-4-oxo-chromen-2-yl)thiophen-2-yl)ethynyl)adenosine (13 – MTC8A): To a stirred solution of **6** (44 mg, 0.16 mmol) and chromone **8** (65 mg, 0.19 mmol, 1.2 eq) in dry DMF (4.0 mL) under argon, were sequentially added Et_3N (113 μL, 0.80 mmol, 5 eq.) and CuI (8 mol%, 2 mg) / $PdCl_2(PPh_3)_2$ (8 mol%, 9 mg). The reaction mixture was stirred under argon at 60 °C for 2 h. Then, the resulting mixture was diluted with CH_2Cl_2 (5 mL) and evaporated under reduced pressure. The residue was purified by flash chromatography on silica gel eluted with CH_2Cl_2/MeOH (100:0 → 85:15, v/v) to provide the desired compound **13** (**MTC8A**) as an orange-yellow solid (72 mg, 85 %). R_f = 0.3 (CH_2Cl_2/MeOH = 9:1); ^{1}H-NMR (400 MHz, DMF-d_7) δ 8.33 (s, 1H), 8.17 (dd, J = 8.0, 1.6 Hz, 1H), 8.09 (d, J = 4.1 Hz, 1H), 7.90 (ddd, J = 8.6, 7.0, 1.7 Hz, 1H), 7.86 (d, J = 4.1 Hz, 1H), 7.83 (dd, J = 8.5, 1.1 Hz, 1H), 7.55 (ddd, J = 8.1, 7.0, 1.2 Hz, 1H), 7.30 (s, 2H), 6.75 (t, J = 6.5 Hz, 1H), 5.43 (d, J = 4.1 Hz, 1H), 4.96 (t, J = 5.4 Hz, 2H), 4.71–4.62 (m, 1H), 4.14 (s, 3H), 4.02 (td, J = 5.4, 3.1 Hz, 1H), 3.72 (dt, J = 10.4, 4.8 Hz, 1H), 3.60 (dt, J = 11.5, 5.6 Hz, 1H), 2.99 (dt, J = 13.2, 6.4 Hz, 1H). ^{13}C-NMR (101 MHz, DMF-d_7) δ 174.2, 159.4, 158.1, 155.9, 155.5, 150.9, 140.1, 135.6, 135.3, 134.6, 130.8, 127.7, 127.5, 126.3, 126.1, 125.3, 119.4, 102.5, 89.8, 88.5, 87.4, 86.4, 72.8, 64.1, 60.5, 39.6. MS (ESI$^+$, MeOH) *m/z*: 531.80 [M+H]$^+$. HRMS (ESI$^+$): *m/z* calcd for $C_{26}H_{22}N_5O_6S$: 532.12853 [M+H]$^+$; found 532.13013.

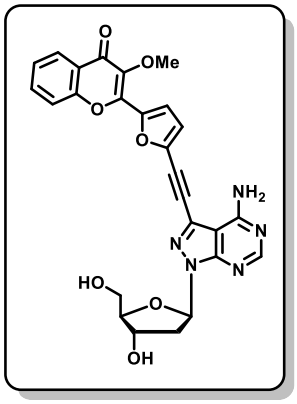

8-Aza-7-deaza-2′-deoxy-7-((5-(3-methoxy-4-oxo-chromen-2-yl)furan-2-yl)ethynyl)adenosine (12 – MFC8A): To a stirred solution of **6** (48 mg, 0.174 mmol) and chromone **7** (68 mg, 0.21 mmol, 1.2 eq) in dry DMF (4.3 mL) under argon, were sequentially added Et_3N (122 μL, 0.87 mmol, 5 eq.) and CuI (8 mol%, 3 mg) / $PdCl_2(PPh_3)_2$ (8 mol%, 10 mg). The reaction mixture was stirred under argon at 60 °C for 2 h. Then, the resulting mixture was diluted with CH_2Cl_2 (5 mL) and evaporated under reduced pressure. The residue was purified by flash chromatography on silica gel eluted with CH_2Cl_2/MeOH (100:0 → 85:15, v/v) to provide the desired compound **12** (**MFC8A**) as a light-orange solid (60 mg, 67 %). R_f = 0.31 (CH_2Cl_2/MeOH = 9:1); ^{1}H-NMR (400 MHz, DMF-d_7) δ 8.36 (s, 1H), 8.18 (dd, J = 8.0, 1.7 Hz, 1H), 7.89 (ddd, J = 8.6, 7.0, 1.7 Hz, 1H), 7.80 (dd, J = 8.5, 1.0 Hz, 1H), 7.60–7.51 (m, 2H), 7.46 (d, J = 3.7 Hz, 1H), 7.28 (s, 2H), 6.76 (t, J = 6.5 Hz, 1H), 5.44 (d, J = 4.4 Hz, 1H), 4.95 (t, J = 6.0 Hz, 1H), 4.67 (dq, J = 7.4, 4.0 Hz, 1H), 4.10 (s, 2H), 4.03 (td, J = 5.4, 3.2 Hz, 1H), 3.73 (dt, J = 11.1, 5.4 Hz, 1H), 3.60 (dt, J = 11.8, 5.9 Hz, 1H), 2.99 (dt, J = 13.3, 6.4 Hz, 1H), 2.45 (ddd, J = 13.3, 6.7, 3.9 Hz, 1H). ^{13}C-NMR (101 MHz, DMF-d_7) δ 174.4, 159.3, 158.2, 155.8, 155.5, 147.4, 146.7, 141.1, 139.0, 135.3, 126.9, 126.4, 126.2, 125.4, 121.5, 119.5, 118.7, 102.8, 89.8, 88.3, 86.4, 84.1, 72.8, 64.1, 60.5, 39.6. MS (ESI$^+$, MeOH) *m/z*: 515.87 [M+H]$^+$. HRMS (ESI$^+$): *m/z* calcd for $C_{26}H_{22}N_5O_7$: 516.15137 [M+H]$^+$; found 516.15302.

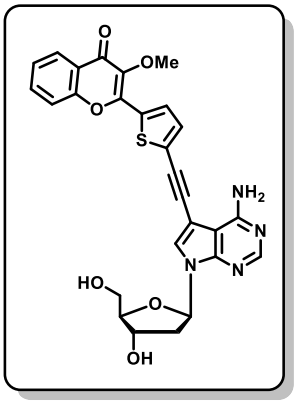

7-Deaza-2′-deoxy-7-((5-(3-methoxy-4-oxo-chromen-2-yl)thiophen-2-yl)ethynyl)adenosine (11 – MTCA): To a stirred solution of **9** (66 mg, 0.24 mmol) and chromone **8** (114 mg, 0.32 mmol, 1.2 eq.) in DMF (4.8 mL) under argon, were sequentially added Et_3N (168 µL, 1.20 mmol, 5 eq.), and CuI (7 mol%, 3 mg) / $PdCl_2(PPh_3)_2$ (7 mol%, 12 mg) all together. The reaction mixture was degassed by sonication under argon and then, warmed to 60 °C for 1 h. The resulting mixture was diluted with CH_2Cl_2 (10 mL) and the volatiles were removed *in vacuo*. The residue was purified by flash chromatography on silica gel eluted with CH_2Cl_2/MeOH (98:2 → 80:20, v/v) to provide the desired compound **3** as an orange-yellow solid (90 mg, 71 %). R_f = 0.38 (CH_2Cl_2/MeOH = 9:1). ^{1}H-NMR (500 MHz DMF-d^7): δ 8.25 (1H, br s), 8.16 (1H, dd, J = 8.0 Hz, J = 2.0 Hz), 8.09 (1H, s), 8.04 (1H, d, J = 4.0 Hz), 7.87 (1H, ddd, J = 8.5 Hz, J = 7.0 Hz, J = 1.5 Hz), 7.81 (1H, d, J = 8.0 Hz), 7.66 (1H, d, J = 4.0 Hz), 7.54 (1H, m), 6.91 (2H, br s), 6.69 (1H, dd, J = 8.0 Hz, J = 6.0 Hz), 5.44 (1H, d, J = 4.0 Hz), 5.36 (1H, t, J = 6.0 Hz), 4.59 (1H, m), 4.03 (1H, d, J = 6.5 Hz, J = 3.5 Hz), 3.80 (1H, m), 3.74 (1H, m), 3.53 (3H, s), 2.69 (1H, m), 2.39 (1H, m). ^{13}C-NMR (125 MHz DMF-d^7): δ 174.1, 159.2, 155.9, 154.2, 151.12, 151.08, 139.7, 135.2, 133.6, 132.8, 131.0, 129.7, 129.1, 126.2, 126.1, 125.2, 119.3, 103.6, 95.6, 91.3, 89.5, 85.4, 85.0, 72.8, 63.6, 60.4, 41.7. HRMS (ESI$^+$): *m/z* calcd for $C_{27}H_{23}O_6N_4S$: 531.13328 [M+H]$^+$; found 531.11367.

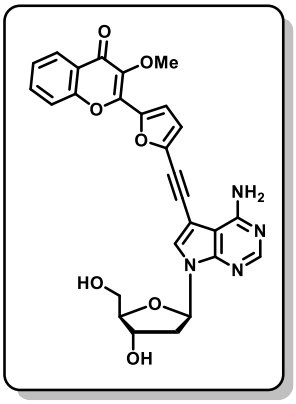

7-Deaza-2′-deoxy-7-((5-(3-methoxy-4-oxo-chromen-2-yl)furan-2-yl)ethynyl)adenosine (10 – MFCA): To a stirred solution of **9** (58 mg, 0.21 mmol) and chromone **7** (91 mg, 0.27 mmol, 1.28 eq.) in DMF (4.2 mL) under argon, were sequentially added Et_3N (147 μL, 1.06 mmol, 5 eq.), and CuI (7 mol%, 3 mg)/ $PdCl_2(PPh_3)_2$ (7 mol%, 10 mg) all together. The reaction mixture was degassed by sonication under argon and then, warmed to 60 °C for 1 h. The resulting mixture was diluted with CH_2Cl_2 (10 mL) and the volatiles were removed *in vacuo*. The residue was purified by flash chromatography on silica gel eluted with CH_2Cl_2/MeOH (98:2 → 80:20, v/v) to provide the desired compound **10** (**MFCA**) as a yellow-orange solid (67 mg, 62 %). R_f = 0.33 (CH_2Cl_2/MeOH = 9:1). ^{1}H-NMR (500 MHz DMF-d^7): δ 8.28 (1H, br s), 8.17 (1H, dd, J = 8.0 Hz, J = 1.5 Hz), 8.15 (1H, s), 8.03 (1H, d, J = 2.5 Hz), 7.88 (1H, ddd, J = 8.5 Hz, J = 7.0 Hz, J = 1.5 Hz), 7.77 (1H, d, J = 8.2 Hz), 7.56 (1H, m), 7.53 (1H, d, J = 3.5 Hz), 7.26 (1H, d, J = 4.0 Hz), 6.94 (2H, br s), 6.69 (1H, dd, J = 8.0 Hz, J = 6.0 Hz), 5.44 (1H, d, J = 4.0 Hz), 5.36 (1H, t, J = 6.0 Hz), 4.59 (1H, m), 4.08 (3H, s), 4.03 (1H, dd, J = 6.0 Hz, J = 3.5 Hz), 3.80 (1H, m), 3.74 (1H, m), 2.40 (1H, m), 2.69 (1H, m). ^{13}C-NMR (125 MHz DMF-d^7): δ 174.3, 159.2, 155.8, 154.3, 151.2, 147.7, 145.6, 140.7, 140.3, 135.2, 129.7, 126.2, 126.1, 125.3, 119.4, 118.9, 103.8, 94.7, 90.9, 89.6, 85.5, 81.8, 72.8, 63.6, 60.4, 41.7. HRMS (ESI$^+$): *m/z* calcd for $C_{27}H_{23}O_7N_4$: 515.1561 $[M+H]^+$; found 515.1566.

Table S1. Screening conditions for the glycosylation reaction.

Solvent	Condition: KOH, TDA-1	Condition: NaH
ACN + Poor solubility + Difficult to scale up + Good selectivity	+ Good conversion in small scale (100 mg); $\beta/\alpha \approx$ 4:1; Bis+tris/mono ≈ 1.6/1	+ Good conversion in small scale (100 mg); $\beta/\alpha \approx$ 5.5/1; Bis+tris/mono ≈ 1/2 + Scalable to 1 g; 32% yield. $\beta/\alpha \approx$ 5.5/1; Bis+tris/mono ≈ 2.5/1
DMF + Good solubility + Poor selectivity	+ Good conversion in small scale (100 mg). $\beta/\alpha \approx$ 3.2/1; Bis+tris/mono ≈ 3.5/1	+ Good conversion in small scale (100 mg); $\beta/\alpha \approx$ 1.5/1; Bis+tris/mono ≈ 2/1
DMF/DCM 1:1 + Fairly soluble + Mediate selectivity	+ Good conversion in small scale (100 mg); $\beta/\alpha \approx$ 3.5:1; Bis+tris/mono ≈ 2/1	+ Good conversion in small scale (100 mg); $\beta/\alpha \approx$ 1:1; Bis+tris/mono ≈ 2/1). A lot of other by-products
DMF/ACN 1:1 + Fairly good solubility + Acceptable selectivity; scalable	+ Good conversion in small scale (100 mg); $\beta/\alpha \approx$ 5:1. Quite good solubility. (Bis+tris/mono = ca. 1.5/1) + Scalable to 500 mg with 38% isolated yield. $\beta/\alpha \approx$ 4/1; Bis+tris/mono ≈ 1/1.5	+ Good conversion in small scale (100 mg). $\beta/\alpha \approx$ 3.5:1; Bis+tris/mono ≈ 0.8/1

3. PET reaction between separated donors and acceptors

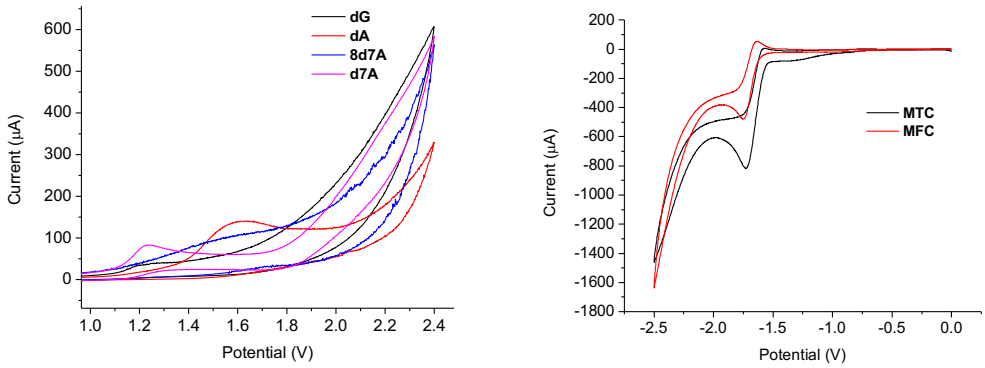

Figure S1. Determination of redox potentials of donors and acceptors by cyclic voltammetry.

Table S2. Comparison of oxidation potential of donors in acetonitrile with reported values.

Compound	$E^{ox}(D)^{a}$ *vs* NHE	Reported value
dG	+1.42	+1.49[b]
d7A	+1.46	+1.48[c]
8d7A	+1.81	+1.91[d]
dA	+1.85	+1.96[b]

[a] CV measurements were conducted in acetonitrile with a typical concentration in nucleosides and fluorescent dyes of 1 mM and as electrolyte, a solution of 0.1 M tetra-*n*-butylamonium hexafluorophosphate (TBA PF_6). Records were against Ag/AgCl (KCl saturated) as a reference and converted into normal hydrogen electrode (NHE) for comparison. The scan speed was 100 $mV \cdot s^{-1}$; [b] Ref[7]; [c] Ref[8]; [d] Ref[9]

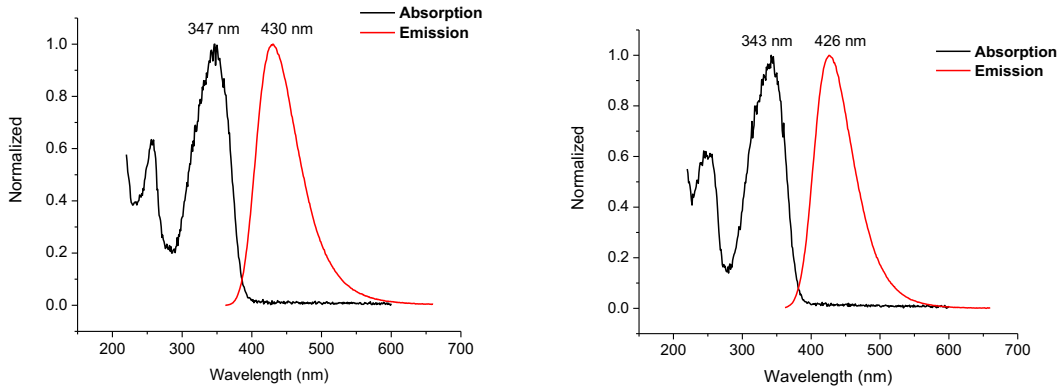

Figure S2. Normalized absorption and emission spectra in water of **MTC** *(left)* and **MFC** *(right)*.

4. General photophysics

4.1. Absorption and emission spectra in different protic solvents

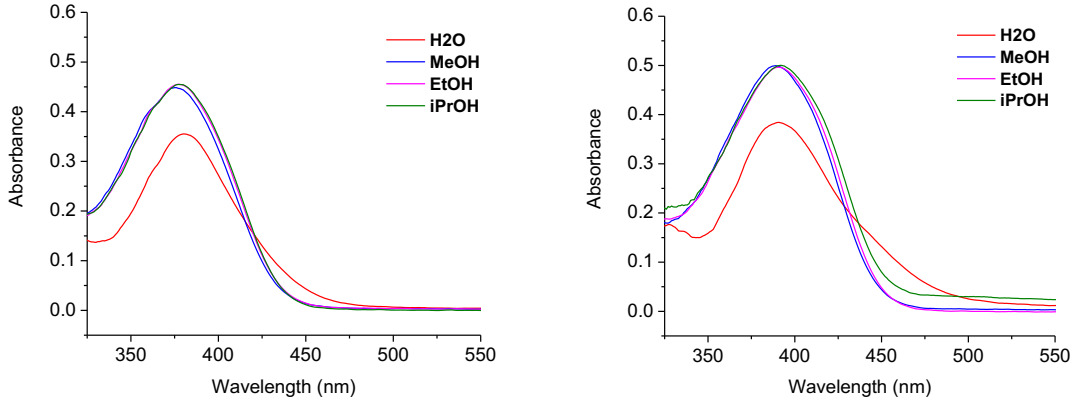

Figure S3. Absorption spectra of d7A-3MC conjugates at 11 μM, in a set of protic solvents of increasing polarity: **MFCA** *(left)* and **MTCA** *(right)*.

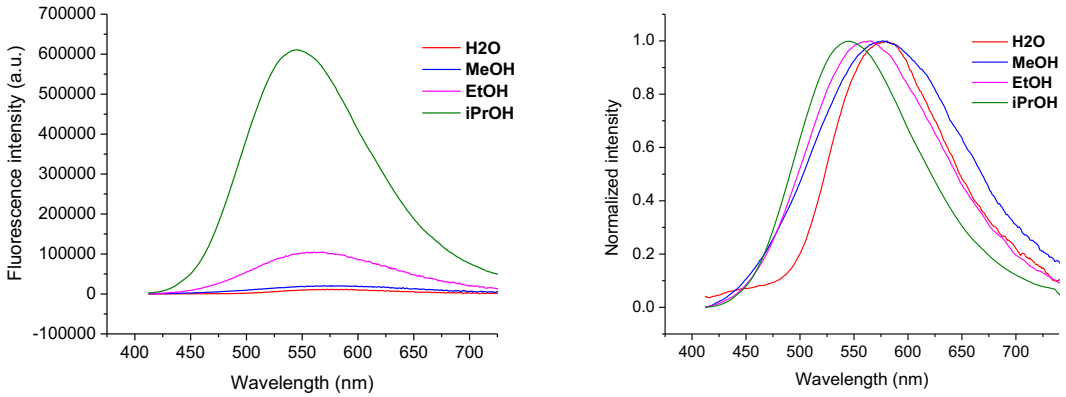

Figure S4. Emission spectra of **MTCA** at 1.1 μM, in protic solvents: raw data *(left)* and normalized on emission maximum *(right)*.

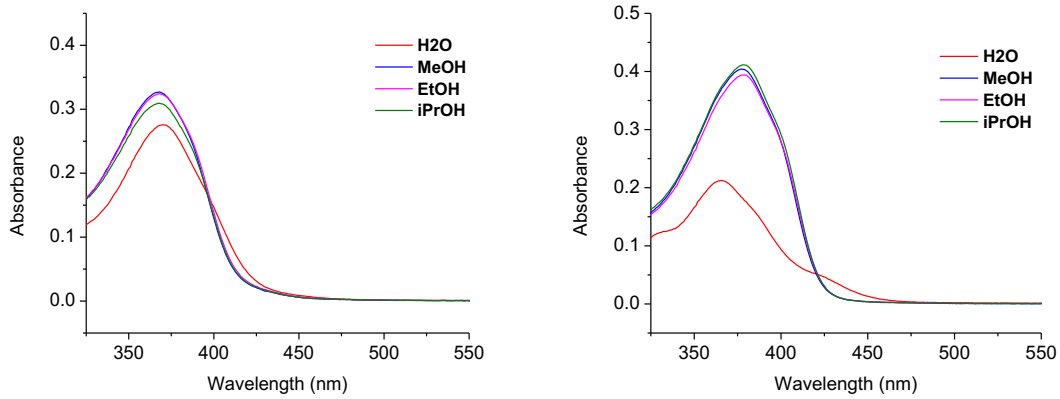

Figure S5. Absorption spectra of **MFC8A** *(left)* and **MTC8A** *(right)* at 11 μM, in a set of protic solvents of increasing polarity.

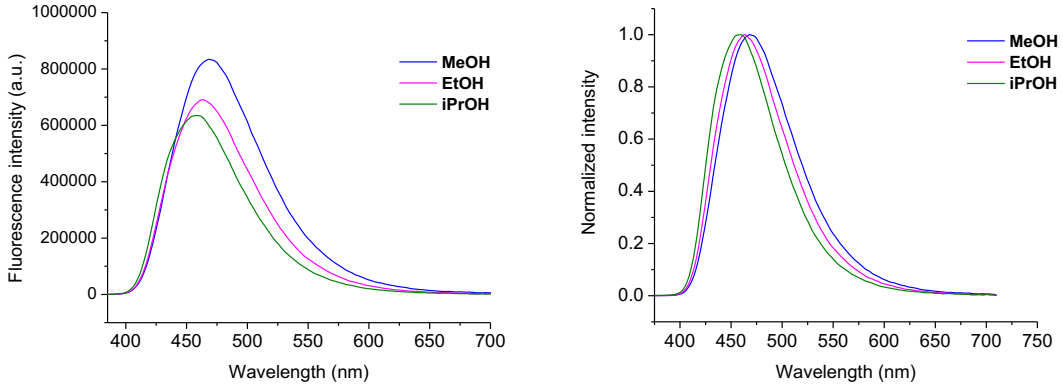

Figure S6. Emission spectra of **MTC8A** at 1.1μM, in protic solvents: raw data *(left)* and normalized on emission maximum *(right)*.

4.2. Ground-state complex favoring PET

4.2.1. MTCA

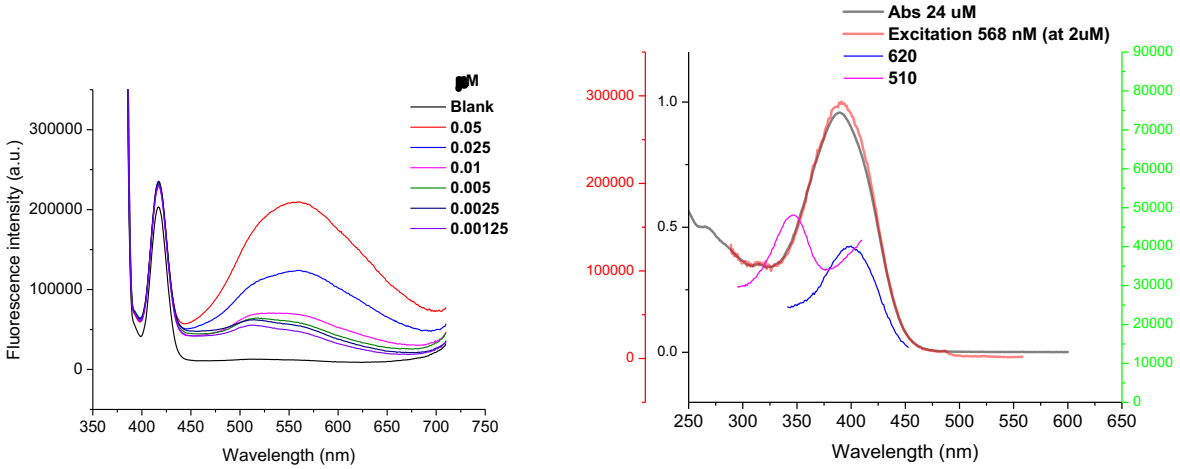

Figure S7. *(Left)* emission spectra of **MTCA**, raw data corresponding to *Figure 4*: the 1.25 nM and 2.5 nM spectra are clearly blue-shifted and distinct from the blank. *(Right)* absorption *(black at 24 μM)* and excitation spectra of **MTCA** in MeOH recorded at different wavelengths (*red at 2 μM, blue and magenta curves at 10* nM*).*

4.2.2. MFCA

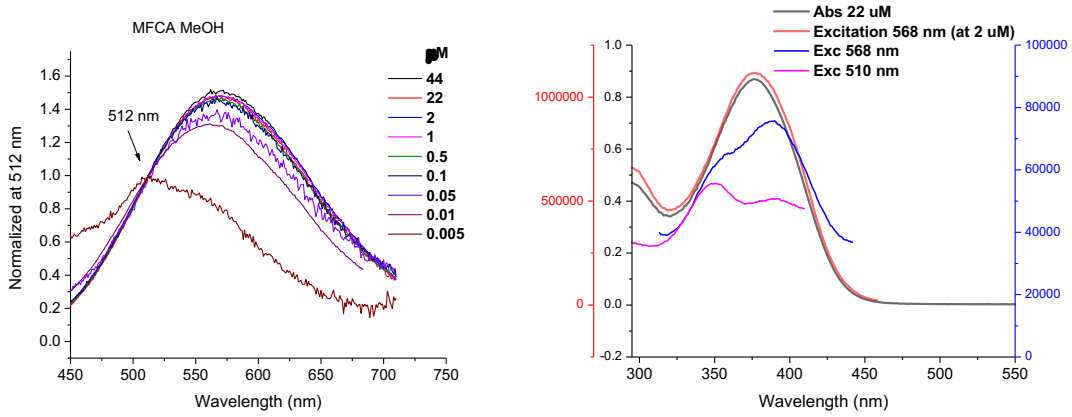

Figure S8. *(Left)* normalized emission spectra of **MFCA** in MeOH at different concentrations. *(Right)* absorption *(black at 22 μ*M*)* and excitation spectra of **MFCA** in MeOH recorded at different wavelengths (*red at 2 μ*M*, blue and magenta curves at 50 n*M*).*

4.2.3. MTCA in MeOH with TFA

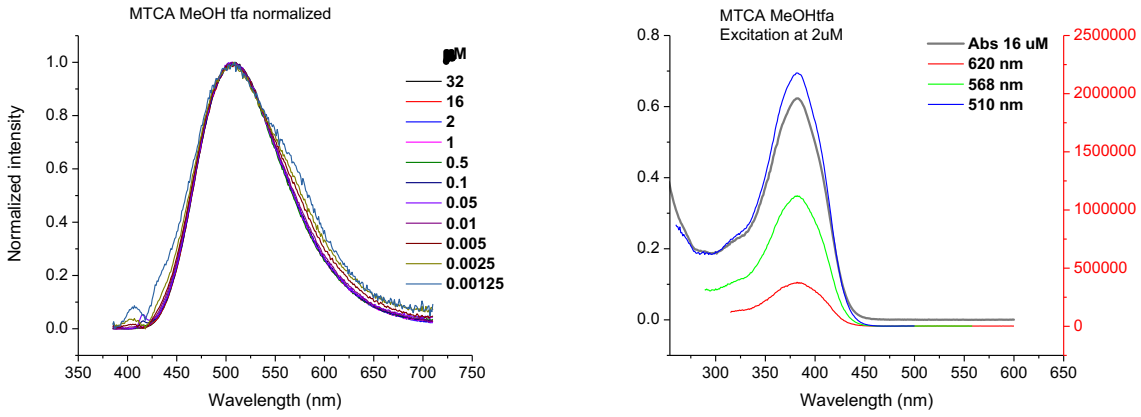

Figure S9. *(Left)* normalized emission spectra of **MTCA** in MeOH + TFA (5 ‰ *v/v*) at different concentrations. *(Right)* absorption *(black)* and excitation spectra of **MTCA** in MeOH + TFA (5 ‰ *v/v*) recorded at different wavelengths (*red, green, and blue curves were measured at 5 n*M*).*

4.2.4. MFCA in MeOH with TFA

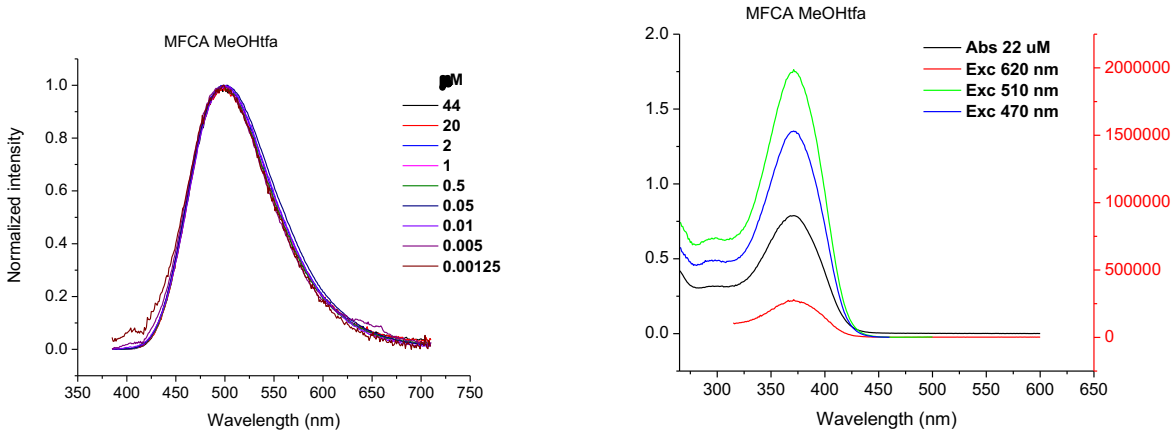

Figure S10. *(Left)* normalized emission spectra of **MFCA** in MeOH + TFA (5 ‰ *v/v*) at different concentrations. *(Right)* absorption *(black)* and excitation spectra of **MTCA** in MeOH + TFA (5 ‰ *v/v*) recorded at different wavelengths (*red, green, and blue curves were measured at 5 n*M*).*

4.2.5. MTC8A

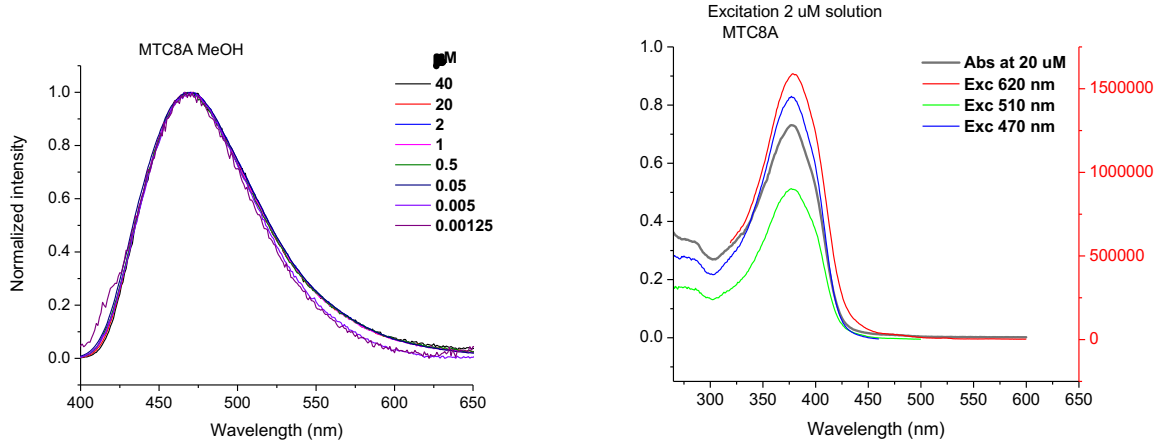

Figure S11. *(Left)* normalized emission spectra of **MTC8A** in MeOH at different concentrations. *(Right)* absorption *(black)* and excitation spectra of **MTC8A** in MeOH recorded at different wavelengths (*red, green, and blue curves were measured at 5 n*M*).*

4.2.6. MFC8A

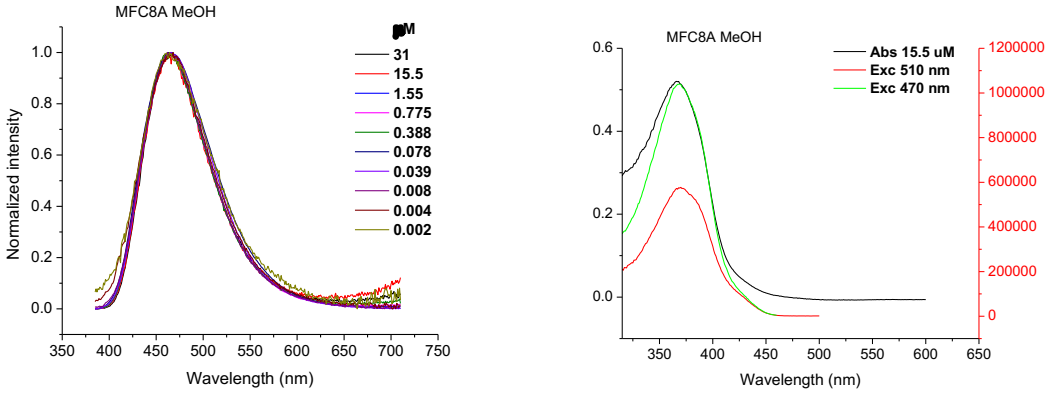

Figure S12. *(Left)* normalized emission spectra of **MFC8A** in MeOH at different concentrations. *(Right)* absorption *(black)* and excitation spectra of **MFC8A** in MeOH recorded at different wavelengths (*red and green curves were measured at 5 n*M*).*

5. Acid-mediated complex inhibition and fluorescence turn-on

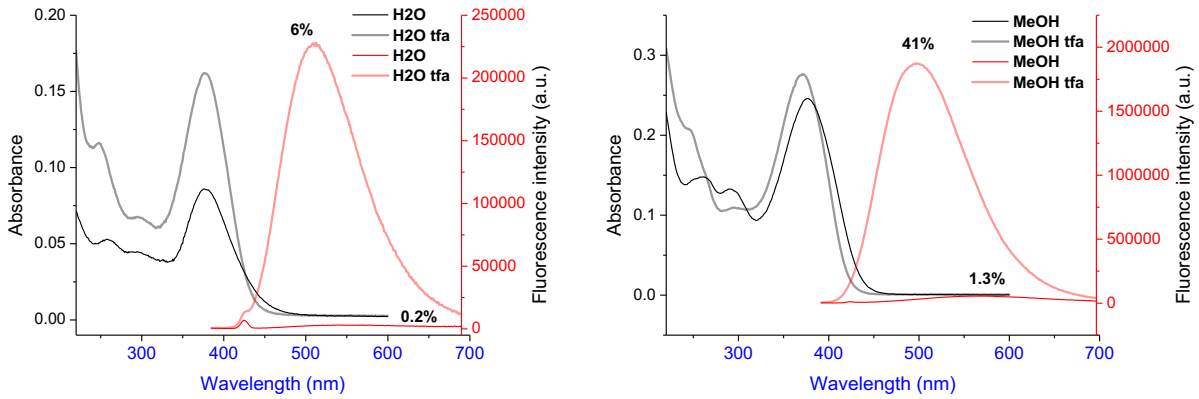

Figure S13. Acid-mediated inhibition of PET on **MFCA** recorded in H_2O (*left*) and MeOH (*right*). Absorption *(grey & black)* and emission *(pink & red)* spectra recorded at 6 and 2 μM, respectively. Quantum yields (in %), mentioned above the emission maxima, take into account the change in absorbance at the excitation wavelength of 370 nm.

6. Transient Absorption experiments

The pump probe setup for transient absorption (TA) spectroscopy and data analysis methods have already been described elsewhere.[10-13] In brief, a 40fs pulses of a Ti: sapphire regenerative amplifier (5 kHz) is used to pump a commercial optical parametric amplifier (TOPAS; Light Conversion) followed by 4th harmonic generation to produce pulses at 370 nm. The probe white-light continuum is generated in a 2mm thick CaF_2 crystal. The polarization of the pump beam is

set at the magic angle (54.7°) with respect to that of the probe. The samples were circulated through a 0.5-mm-path-length, fused silica, flow cell using a peristaltic pump. Data sets were acquired displaying the spectrally resolved (350 to 700 nm) pump-induced absorbance change ΔA as a function of pump probe delay. All TA data presented here are post-processed in order to *(i)* subtract the "solvent" signal around time-zero resulting from the coherent interaction of pump and probe laser fields, and *(ii)* compensate for the group velocity dispersion in the probe beam – independently determined from the pure solvent signal – so as to define time-zero accurately (within ~20 fs) at all wavelengths. Singular Value Decomposition (SVD) was used for data reduction and noise filtering. Global fitting of the dominant 5 singular traces was performed. The fitting function was a sum of exponential decaying functions convolved with a normalized Gaussian curve of standard deviation σ standing for the temporal Instrument Response Function (IRF). The residuals of the fits of the 5 dominating singular transients were structureless, and of amplitude similar to or larger than that of the 6th and 7th singular transients, justifying that only the first five singular transients were considered as significant in this global analysis. The result of the global fitting was analyzed by computing and displaying the Decay-Associated Spectra (DAS). Each decay time constant is associated to a DAS representing the spectral dependence of the prefactor of this decay component in the original 2D data set. The DAS reveal the spectral evolution occurring within their associated time constant, along the course of the molecule photoreaction.

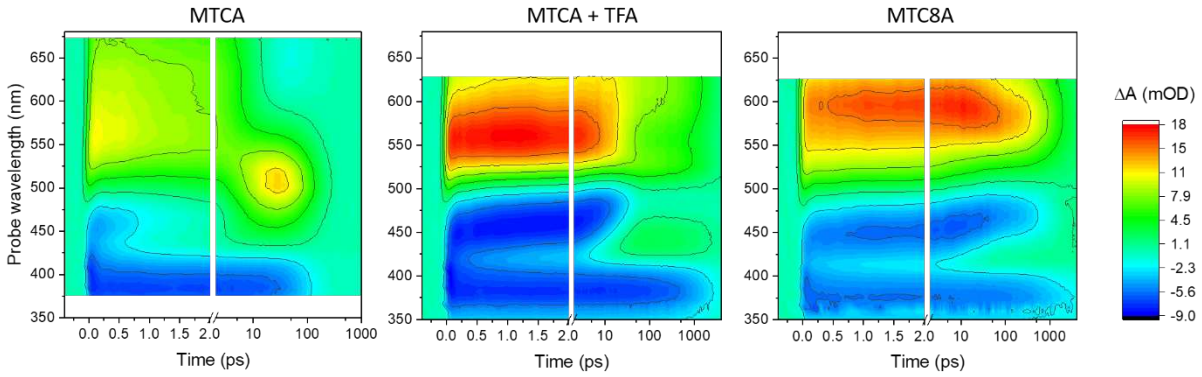

Figure S14. 2D map representations of the TA signal (false-color scale) of **MTCA** (*left*), **MTCA**+TFA (*middle*), and **MTC8A** (*right*) as a function of probe wavelength (vertical scale in nm) and pump-probe delay (horizontal scale in ps). *Notice the break at 2 ps.*

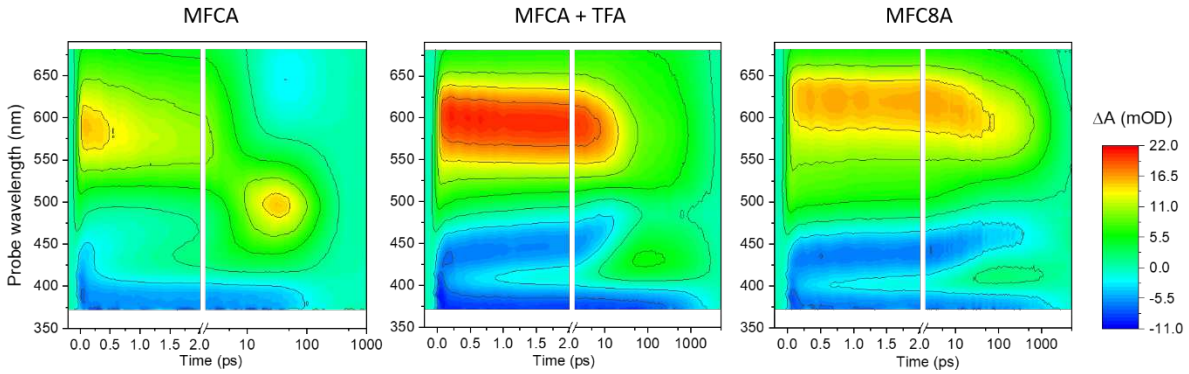

Figure S15. Same as *Figure S14* for **MFCA** (*left*), **MFCA**+TFA (*middle*), and **MFC8A** (*right*).

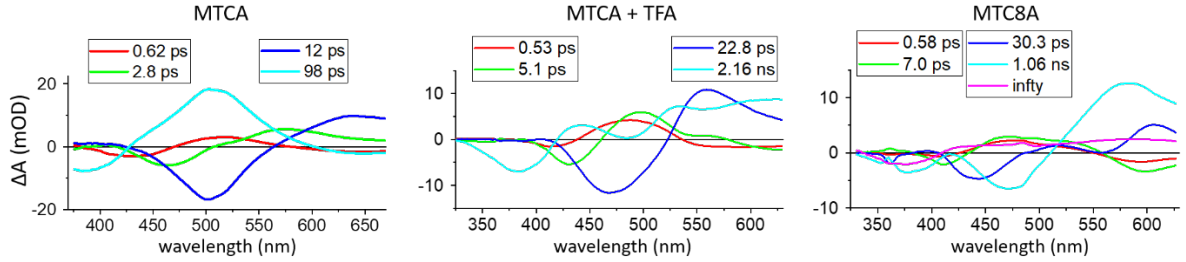

Figure S16. Decay-Associated Spectra (DAS) obtained from the global analysis of **MTCA**, **MTCA+TFA** and **MTC8A** datasets.

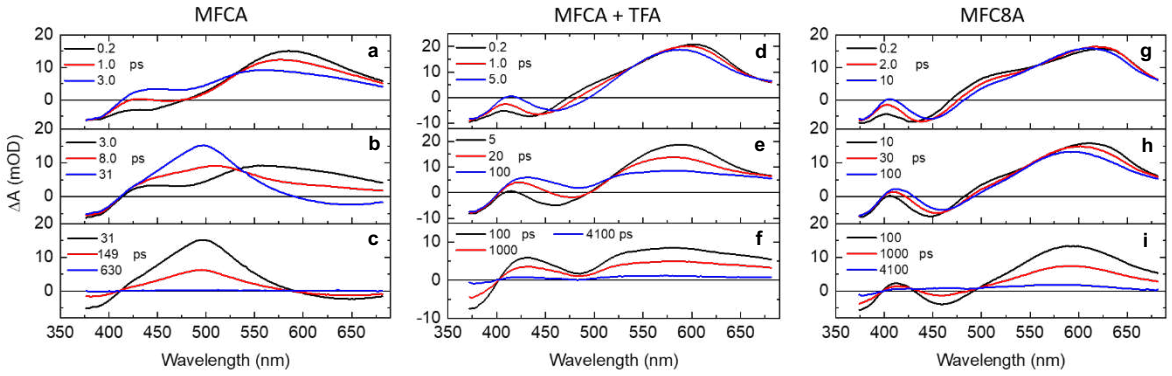

Figure S17. TA data *(ΔA)* measured upon 370nm excitation of methanolic solutions of **MFCA** *(left)*, **MFCA**+TFA *(middle)*, and **MFC8A** *(right)*. A selection of transient spectra at early *(first line: panels a, d, & g)*, intermediate *(second line: panels b, e, & h)* and later *(third line: panels c, f, & i)* pump-probe time delays are displayed to illustrate the spectral evolutions observed on different times.

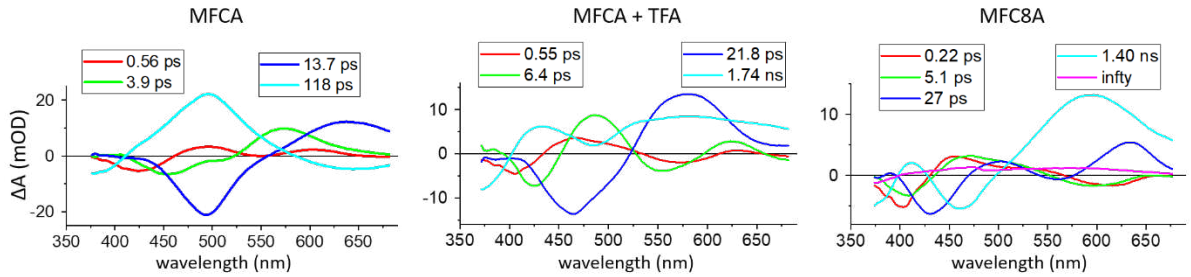

Figure S18. Decay-Associated Spectra (DAS) obtained from the global analysis of **MFCA**, **MFCA**+TFA and **MFC8A** datasets.

7. References

[1] W. L. F. Armarego, C. L. L. Chai in *Purification of Laboratory Chemicals* (7th ed.), Butterworth–Heinemann: Oxford; **2012**, p. 1024.

[2] W. C. Still, M. Kahn, A. Mitra, *J. Org. Chem.* **1978**, *43*, 2923–2925.

[3] H. E. Gottlieb, V. Kotlyar and A. Nudelman, *J. Org. Chem.*, **1997**, *62*, 7512–7515.

[4] G. R. Fulmer, A. J. M. Miller, N. H. Sherden, H. E. Gottlieb, A. Nudelman, B. M. Stoltz, J. E. Bercaw, K. I. Goldberg, *Organometallics* **2010**, *29*, 2176–2179.

[5] F. Seela, M. Zulauf, *J. Chem. Soc., Perkin Trans. 1* **1998**, 3233–3240.

[6] H.-N. Le, C. Zilio, G. Barnoin, N. P. F. Barthes, J.-M. Guigonis, N. Martinet, B. Y. Michel, A. Burger, *Dyes Pigm.* **2019**, *170*, 107553.

[7] C. A. M. Seidel, A. Schulz, M. H. M. Sauer, *J. Phys. Chem.* **1996**, *100*, 5541–5553.

[8] F. Seela, S. S. Pujari, *Bioconjug. Chem.* **2010**, *21*, 1629–1641.

[9] T. Aso, K. Saito, A. Suzuki, Y. Saito, *Org. Biomol. Chem.* **2015**, *13*, 10540–10547.

[10] J. Briand, O. Bräm, J. Réhault, J. Léonard, A. Cannizzo, M. Chergui, V. Zanirato, M. Olivucci, J. Helbing, S. Haacke, *Phys. Chem. Chem. Phys.* **2010**, *12*, 3178–3187.

[11] C. García-Iriepa, M. Gueye, J. Léonard, D. Martínez-López, P. J. Campos, L. M. Frutos, D. Sampedro, M. Marazzi, *Phys. Chem. Chem. Phys.* **2016**, *18*, 6742–6753.

[12] M. Paolino, M. Gueye, E. Pieri, M. Manathunga, S. Fusi, A. Cappelli, L. Latterini, D. Pannacci, M. Filatov, J. Léonard, et al., *J. Am. Chem. Soc.* **2016**, *138*, 9807–9825.

[13] A. I. Skilitsi, D. Agathangelou, I. Shulov, J. Conyard, S. Haacke, Y. Mély, A. Klymchenko, J. Léonard, *Phys. Chem. Chem. Phys.* **2018**, *20*, 7885–7895.

8. NMR spectra of synthesized products

3.3. SI of part 2.3

Dual-emissive analog of 8-aza-7-deazadeoxyadenosine with the capability to report hydration and electron transfer in DNA

Graphical abstract:

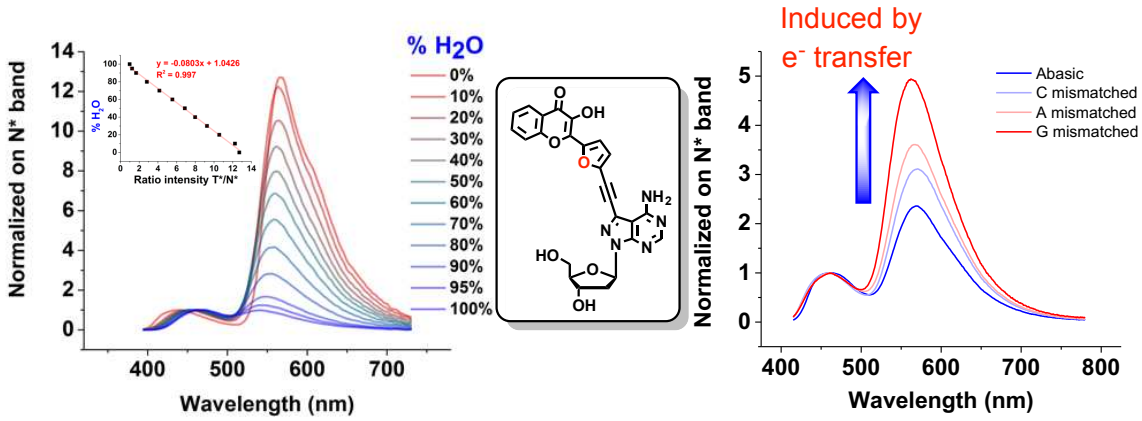

Table of contents

Supporting information *Pages*

Table of Contents

1. Synthesis

1.1. Synthesis of modified nucleosides

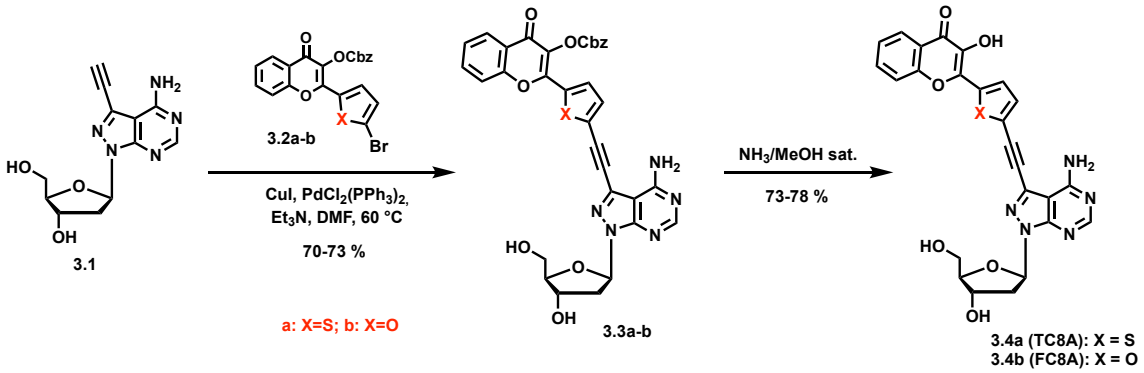

Scheme S1. Synthesis of the modified nucleosides used in this study.

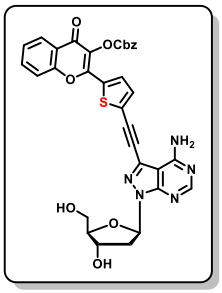

1.1.1. Synthesis of 8-aza-7-((5-(3-benzyloxycarbonyloxy-4-oxochromen-2-yl)thiophen-2-yl)ethynyl)-7-deaza-2′-deoxyadenosine (3a): To a stirred solution of **3.1** (49 mg, 0. 178 mmol) and chromone **3.2a** (99 mg, 0.214 mmol, 1.2 eq) in dry DMF (4.5 mL) under argon, were sequentially added Et_3N (125 µL, 0.890 mmol, 5 eq.) and CuI (8 mol%, 3 mg) / $PdCl_2(PPh_3)_2$ (8 mol%, 10 mg). The reaction mixture was stirred under argon at 60 °C for 2 h. Then, the resulting mixture was diluted with CH_2Cl_2 (5 mL) and evaporated under reduced pressure. The residue was purified by flash chromatography on silica gel eluted with CH_2Cl_2/MeOH (100:0 → 85:15, v/v) to provide the desired compound **3.3a** as a light orange solid (81 mg, 70%). R_f = 0.35 (CH_2Cl_2/MeOH = 9/1); ^{1}H NMR (400 MHz, DMF-d_7) δ 8.34 (s, 1H), 8.18 (dd, *J* = 7.9, 1.6 Hz, 1H), 8.13 (d, *J* = 4.1 Hz, 1H), 7.98 (ddd, *J* = 8.6, 7.0, 1.7 Hz, 1H), 7.94 – 7.85 (m, 2H), 7.68 – 7.61 (m, 1H), 7.61 – 7.55 (m, 2H), 7.54 – 7.46 (m, 2H), 7.45 – 7.38 (m, 1H), 7.28 (s, 2H), 6.77 (t, *J* = 6.5 Hz, 1H), 5.49 (s, 2H), 5.45 (d, *J* = 4.3 Hz, 1H), 4.97 (t, *J* = 6.0 Hz, 1H), 4.67 (dq, *J* = 7.3, 4.0 Hz, 1H), 4.03 (td, *J* = 5.3, 3.1 Hz, 1H), 3.73 (dt, *J* = 11.1, 5.4 Hz, 1H), 3.61 (dt, *J* = 11.5, 5.8 Hz, 1H), 3.01 (dt, *J* = 12.9, 6.2 Hz, 1H), 2.46 (ddd, *J* = 13.2, 6.7, 4.0 Hz, 1H). ^{13}C NMR (101 MHz, DMF-d_7) δ 171.9, 159.3, 158.1, 156.2, 155.5, 152.8, 151.3, 136.2, 136.2, 136.1, 133.2, 132.9, 132.6, 129.9, 129.7, 129.5, 128.8, 127.2, 127.0, 126.2, 124.3, 119.7, 102.5, 89.7, 89.2, 86.7, 86.3, 72.8, 72.3, 64.1, 39.6. MS (ESI$^+$, MeOH) *m/z*: 651.93 [M+H]$^+$. HRMS (ESI$^+$): *m/z* calcd for $C_{33}H_{26}N_5O_8S$: 652.14966 [M+H]$^+$; found 652.14948.

1.1.2. Synthesis of 8-aza-7-deaza-2′-deoxy-7-((5-(3-hydroxy-4-oxochromen-2-yl)thiophen-2-yl)ethynyl)adenosine (3.4a – TC8A): To a stirred solution of **3.3a** (51 mg, 0.08 mmol) in DMF (6 mL) was added a solution of saturated NH_3 in MeOH (1 mL). After 5 min, all the volatiles were removed under reduced pressure, and the residue was washed thoroughly with toluene (3 x 5 mL), CH_2Cl_2 (3 x 5 mL), MeOH (3 x 5 mL), and pentane (3 x 5 mL). The obtained solid was recrystallized two times with DMF/H_2O/AcOH and dried under high vacuum to provide the desired product (30 mg, 73%) as an orange solid. R_f = 0.35 (AcOEt/MeOH/H_2O = 20/1/1). ^{1}H NMR (400 MHz, DMSO-d_6) δ 10.83 (s, 2H), 8.28 (s, 1H), 8.11 (dd, *J* = 8.0, 1.6 Hz, 1H), 7.98 – 7.88 (m, 1H), 7.87 – 7.69 (m, 2H), 7.47 (t, *J* = 7.5 Hz, 1H), 7.02 (s, 2H), 6.59 (t, *J* = 6.4 Hz, 1H), 5.31 (d, *J* = 4.5 Hz, 1H), 4.80 (t, *J* = 5.7 Hz, 1H), 4.45 (t, *J* = 4.9 Hz, 1H), 3.83 (td, *J* = 5.7, 3.5 Hz, 1H), 3.54 (dt, *J* = 11.2, 5.4 Hz, 1H), 3.44 – 3.36 (m, 1H), 2.82 (dt, *J* = 12.7, 6.1 Hz, 1H), 2.29 (ddd, *J* = 13.2, 6.8, 4.2 Hz, 1H). ^{1}H NMR (500 MHz, DMSO-d_6) δ 10.49 (s, 1H), 8.28 (s, 1H), 8.12 (dd, *J* = 8.0, 1.6 Hz, 1H), 7.95 (d, *J* = 4.1 Hz, 1H), 7.81 (ddd, *J* = 8.6, 7.0, 1.7 Hz, 1H), 7.76 (d, *J* = 4.1 Hz, 1H), 7.72 (d, *J* = 8.4 Hz, 1H), 7.48 (ddd, *J* = 8.0, 6.9, 1.0 Hz, 1H), 7.32 (s, 2H), 6.61 (t, *J* = 6.4 Hz, 1H), 5.31 – 4.99 (m, 1H), 4.60 (s, 1H), 4.52 – 4.39 (m, 1H), 3.87 (td, *J* = 5.6, 3.5 Hz, 1H), 3.57 (dd, *J* = 11.5, 5.3 Hz, 1H), 3.44 (dd, *J* = 11.5, 5.9 Hz, 1H), 2.86 (dt, *J* = 13.3, 6.2 Hz, 1H), 2.30 (ddd, *J* = 13.3, 6.8, 4.2 Hz, 1H). ^{13}C NMR (126 MHz, DMSO-d_6) δ 171.8, 157.5, 156.4, 154.1, 153.7, 141.8, 137.4, 134.6, 134.3, 133.6, 127.7, 125.9, 124.6, 124.4, 124.1, 121.7, 117.8, 100.7, 87.7, 86.8, 86.5, 84.3, 70.8, 62.1, 37.9. MS (ESI$^+$, MeOH) *m/z*: 517.80 [M+H]$^+$. HRMS (ESI$^+$): *m/z* calcd for $C_{25}H_{20}N_5O_6S$: 518.11288 [M+H]$^+$; found 518.11511.

1.1.3. Synthesis of 8-aza-7-((5-(3-benzyloxycarbonyloxy-4-oxochromen-2-yl)furan-2-yl)ethynyl)-7-deaza-2′-deoxyadenosine (3.3b): To a stirred solution of **3.1** (56 mg, 0.20 mmol) and chromone **3.2b** (109 mg, 0.22 mmol, 1.2 eq) in dry DMF (5.1 mL) under argon, were sequentially added Et_3N (143 µL, 1.02 mmol, 5 eq.) and CuI (8 mol%, 3 mg) / $PdCl_2(PPh_3)_2$ (8 mol%, 12 mg). The reaction mixture was stirred under argon at 60 °C for 2 h. Then, the resulting mixture was diluted with CH_2Cl_2 (5 mL) and evaporated under reduced pressure. The residue was purified by flash chromatography on silica gel eluted with CH_2Cl_2/MeOH (100:0 → 85:15, v/v) to provide the desired compound **3.3b** as a light orange solid (95 mg, 73%). R_f = 0.33 (CH_2Cl_2/MeOH = 9/1); ^{1}H NMR (400 MHz, DMF-d_7) δ 8.35 (s, 1H), 8.19 (dd, *J* = 7.9, 1.7 Hz, 1H), 7.97 (ddd, *J* = 8.7, 7.1, 1.7 Hz, 1H), 7.87 (dd, *J* = 8.5, 1.0 Hz, 1H), 7.63 (ddd, *J* = 8.1, 7.1, 1.1 Hz, 1H), 7.56 (d, *J* = 3.8 Hz, 1H), 7.58 – 7.50 (m, 2H), 7.47 (d, *J* = 3.8 Hz, 1H), 7.44 – 7.30 (m, 3H), 7.27 (s, 2H), 6.76 (t, *J* = 6.5 Hz, 1H), 5.46 (s, 2H), 5.45 (d, *J* = 4.4 Hz, 1H), 5.05 – 4.89 (m, 1H), 4.66 (dq, *J* = 7.8, 3.8 Hz, 1H), 4.03 (td, *J* = 5.4, 3.1 Hz, 1H), 3.72 (dt, *J* = 11.1, 5.4 Hz, 1H), 3.59 (dt, *J* = 11.8, 6.3 Hz, 1H), 2.99 (dt, *J* = 12.9, 6.2 Hz, 1H), 2.45 (ddd, *J* = 13.3, 6.7, 3.9 Hz, 1H). ^{13}C NMR (101 MHz, DMF-d_7) δ 172.1, 159.2, 158.1, 156.1, 155.4, 153.2, 147.8, 145.6, 140.4, 136.2, 136.2, 132.9, 129.7, 129.3, 127.1, 126.6, 126.3, 124.5, 121.3, 119.7, 119.3, 99.7, 89.8, 88.5, 86.5, 83.5, 72.8, 72.1, 64.1, 39.6. MS (ESI$^+$, MeOH) *m/z*: 635.93 [M+H]$^+$. HRMS (ESI$^+$): *m/z* calcd for $C_{33}H_{26}N_5O_9$: 636.17250 [M+H]$^+$; found 636.17291.

1.1.4. Synthesis of 8-aza-7-deaza-2′-deoxy-7-((5-(3-hydroxy-4-oxochromen-2-yl)furan-2-yl)ethynyl)adenosine (3.4b – FC8A): To a stirred solution of **3.3b** (70 mg, 0.08 mmol) in DMF (8.3 mL) was added a solution of saturated NH_3 in MeOH (1.4 mL). After 5 min, all the volatiles were removed under reduced pressure, and the residue was washed thoroughly with toluene (3 x 5 mL), CH_2Cl_2 (3 x 5 mL), MeOH (3 x 5 mL), and pentane (3 x 5 mL). The obtained solid was recrystallized two times from DMF/H_2O/AcOH and dried under high vacuum to provide the desired product (43 mg, 78%) as an orange solid. R_f = 0.3 (AcOEt/MeOH/H_2O = 20/1/1). ^{1}H NMR (400 MHz, DMF-d_7) δ 10.64 (s, 1H), 8.37 (s, 1H), 8.17 (d, J = 7.7 Hz, 1H), 7.87 (t, J = 7.4 Hz, 1H), 7.80 (d, J = 8.5 Hz, 1H), 7.54 (t, J = 7.4 Hz, 1H), 7.50 (d, J = 3.6 Hz, 1H), 7.43 (d, J = 3.6 Hz, 1H), 7.27 (s, 2H), 6.76 (t, J = 6.5 Hz, 1H), 5.45 (d, J = 4.4 Hz, 1H), 4.96 (t, J = 6.1 Hz, 1H), 4.67 (s, 1H), 4.03 (td, J = 5.3, 3.0 Hz, 1H), 3.73 (dt, J = 10.4, 4.8 Hz, 1H), 3.67 – 3.55 (m, 1H), 3.00 (dt, J = 12.8, 6.2 Hz, 1H), 2.45 (ddd, J = 13.1, 6.6, 3.9 Hz, 1H). (NH_2 shows a very broad singlet from 6.9-8.9 ppm). ^{13}C NMR (101 MHz, DMF-d_7) δ 173.3, 159.3, 158.1, 155.8, 155.4, 147.5, 140.0, 139.3, 138.2, 135.0, 127.0, 126.0, 125.8, 123.3, 121.4, 119.5, 117.2, 102.8, 89.8, 88.2, 86.3, 84.3, 72.8, 64.1, 39.6. MS (ESI$^+$, MeOH) *m/z*: 501.87 $[M+H]^+$. HRMS (ESI$^+$): *m/z* calcd for $C_{25}H_{20}N_5O_7$: 502.13572 $[M+H]^+$; found 502.13675.

1.2. Synthesis of phosphoramodite

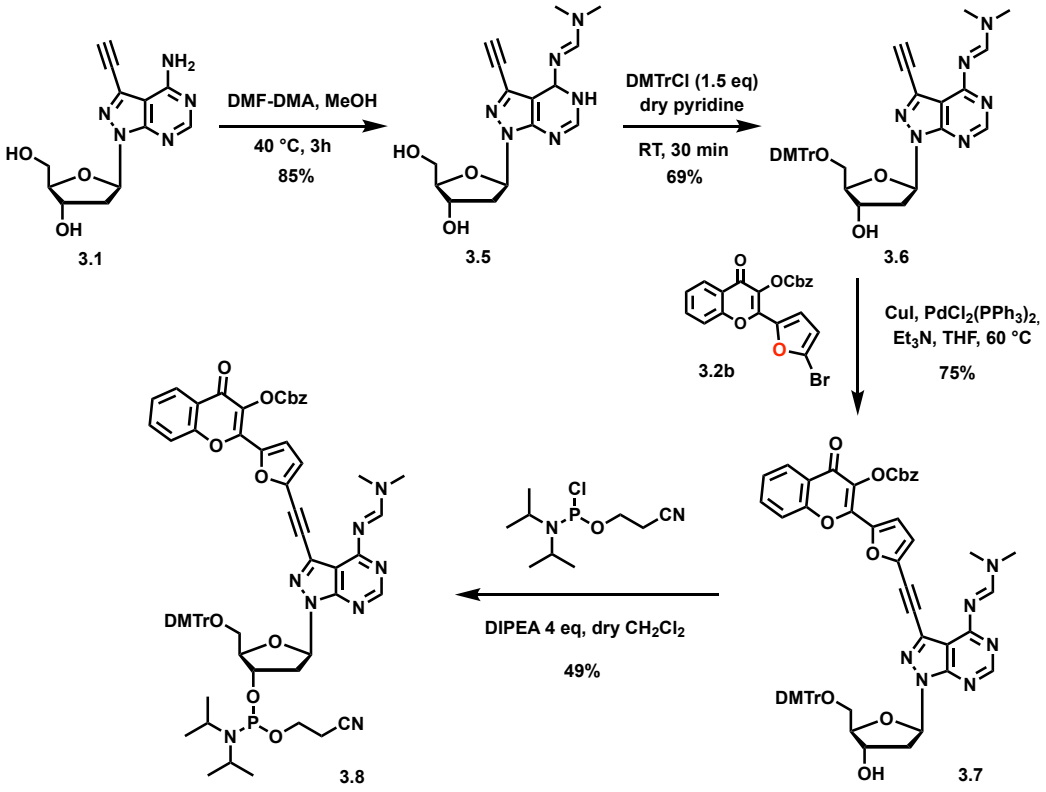

Scheme S2. Synthesis of phosphoramidite, a building block for oligonucleotides synthesis.

1.2.1. Synthesis of 8-aza-7-deaza-2′-deoxy-6-*N*-(dimethylformamidine)-7-ethynyladenosine (3.5): To a stirred suspension of **3.1** (503 mg, 1.827 mmol) in dry MeOH (26 mL), was added DMF-DMA (2.91 mL, 12 eq). The reaction mixture was stirred at 40 °C under argon atmosphere for 3 h. Then all the volatiles were removed under reduced pressure, and the residue was purified by flash chromatography on silica gel eluted with CH_2Cl_2/MeOH (100:0 → 85:15, v/v) to provide the desired compound (**3.5**) as a white solid (515 mg, 85%). R_f = 0.35 (CH_2Cl_2/MeOH = 9/1); ^{1}H NMR (400 MHz, Methylene Chloride-d_2) δ 8.85 (s, 1H), 8.39 (s, 1H), 6.67 (t, *J* = 6.9 Hz, 1H), 5.18 (s, 1H), 4.76 (dt, *J* = 5.6, 2.6 Hz, 1H), 4.14 (q, *J* = 2.7 Hz, 1H), 3.86 (dd, *J* = 12.5, 2.6 Hz, 1H), 3.80 – 3.66 (m, 2H), 3.44 (s, 1H), 3.23 (s, 3H), 3.21 (s, 3H), 2.92 (ddd, *J* = 13.4, 7.4, 5.8 Hz, 1H), 2.42 (ddd, *J* = 13.6, 6.5, 2.8 Hz, 1H). ^{13}C NMR (101 MHz, Methylene Chloride-d_2) δ 163.4, 158.2, 156.3, 154.3, 128.5, 110.0, 89.4, 88.6, 81.7, 76.4, 73.1, 63.8, 41.8, 40.8, 35.6. MS (ESI$^+$, MeOH) *m/z*: 330.93 [M+H]$^+$.

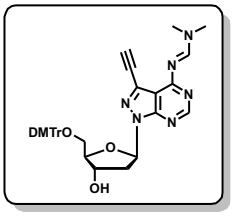

1.2.2. Synthesis of 8-aza-7-deaza-2′-deoxy-5′-*O*-(4,4′-dimethoxytrityl)-6-*N*-(dimethylformamidine)-7-ethynyladenosine (3.6): Compound **3.1** (253 mg, 0.766 mmol) was co-evaporated 3 times with dry pyridine (3 x 2 mL) and then dissolved in dry pyridine (3 mL). To the resulting solution, DMTrCl (389 mg, 1.5 eq) was added portionwise. The reaction mixture was stirred under argon atmosphere at RT for 30 minutes. Then, the resulting mixture was diluted with MeOH (1 mL) and evaporated under reduced pressure. The residue was purified by flash chromatography on silica gel eluted with CH_2Cl_2/AcOEt (50:50 → 0:100, v/v) to provide the desired compound (**3.6**) as a white foam solid (332 mg, 69%). R_f = 0.55 (CH_2Cl_2/MeOH = 9/1); ^{1}H NMR (400 MHz, Methylene Chloride-d_2) δ 8.90 (s, 1H), 8.46 (s, 1H), 7.43 – 7.35 (m, 2H), 7.31 – 7.23 (m, 4H), 7.27 – 7.18 (m, 2H), 7.22 – 7.10 (m, 1H), 6.81 – 6.72 (m, 4H), 6.71 (dd, *J* = 7.1, 4.7 Hz, 1H), 4.78 (q, *J* = 5.7 Hz, 1H), 4.03 (q, *J* = 5.3 Hz, 1H), 3.76 (s, 3H), 3.75 (s, 3H), 3.39 (s, 1H), 3.24 (s, 3H), 3.24 – 3.22 (m, 2H), 3.20 (s, 3H), 3.03 (ddd, *J* = 13.3, 6.6, 4.7 Hz, 1H), 2.39 (ddd, *J* = 13.1, 7.1, 5.8 Hz, 1H), 2.25 (s, 1H). ^{13}C NMR (101 MHz, Methylene Chloride-d_2) δ 163.1, 159.1, 159.0, 158.0, 156.7, 155.5, 145.6, 136.6, 136.5, 130.6, 130.5, 129.5, 128.6, 128.3, 127.2, 113.6, 109.6, 86.6, 86.2, 84.7, 81.2, 77.0, 73.2, 64.9, 55.7, 41.7, 38.8, 35.5. HRMS (ESI$^+$): *m/z* calcd for $C_{36}H_{37}N_6O_5$: 633.28199 [M+H]$^+$; found 633.28369.

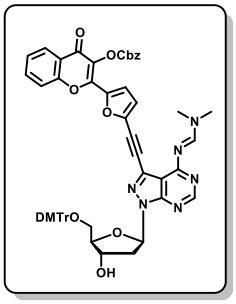

1.2.3. Synthesis of 8-aza-7-((5-(3-benzyloxycarbonyloxy-4-oxochromen-2-yl)furan-2-yl)ethynyl)-7-deaza-2′-deoxy-5′-*O*-(4,4′-dimethoxytrityl)-6-*N*-(dimethylformamidine)adenosine (3.7): A suspension of chromone **3.2b** (266 mg, 0.597 mmol, 1.2 eq), Et_3N (350 µL, 2.489 mmol, 5 eq.) and CuI (5 mol%, 5 mg) / $PdCl_2(PPh_3)_2$ (5 mol%, 18 mg) in dry THF (10 mL) was degassed under argon for 1 minute. The mixture was refluxed under argon atmosphere at 60 °C and was added dropwise during 30 minutes a solution of **3.6** (315 mg, 0.498 mmol) in dry THF (2 mL). The reaction mixture was stirred under argon at 60 °C for 2 h. Then, the resulting mixture was diluted with CH_2Cl_2 (10 mL) and evaporated under reduced pressure. The residue was purified by flash chromatography on silica gel eluted with CH_2Cl_2/AcOEt (80:20 → 0:100, v/v) to provide the desired compound (**7**) as a yellow foam (373 mg, 75%). R_f = 0.4 (cyHex/AcOEt = 8/2); ^{1}H NMR (400 MHz, Methylene Chloride-d_2) δ 8.87 (s, 1H), 8.52 (s, 1H), 8.23 (dd, *J* = 8.0, 1.7 Hz, 1H), 7.77 (ddd, *J* = 8.7, 7.2, 1.7 Hz, 1H), 7.60 (dd, *J* = 8.5, 1.0 Hz, 1H), 7.48 (ddd, *J* = 8.1, 7.1, 1.1 Hz, 1H), 7.40 (ddt, *J* = 5.8, 4.2, 1.7 Hz, 4H), 7.35 – 7.24 (m, 8H), 7.28 – 7.19 (m, 2H), 7.19 – 7.14 (m, 1H), 6.94 (d, *J* = 3.7 Hz, 1H), 6.83 – 6.66 (m, 5H), 5.31 (s, 2H), 4.82 (d, *J* = 4.4 Hz, 1H), 4.10 – 4.01 (m, 1H), 3.72 (s, 3H), 3.71 (s, 3H), 3.29 (s, 3H), 3.26 (d, *J* = 5.3 Hz, 2H), 3.17

(s, 3H), 3.07 (ddd, *J* = 13.3, 6.6, 4.5 Hz, 1H), 2.44 (dt, *J* = 13.1, 6.5 Hz, 1H), 2.27 (s, 1H). ^{13}C NMR (101 MHz, Methylene Chloride-d_2) δ 171.9, 163.1, 159.1, 159.1, 157.9, 157.0, 155.7, 155.7, 152.6, 147.5, 145.6, 144.7, 140.6, 136.6, 136.5, 135.2, 134.9, 132.5, 130.6, 130.5, 129.2, 129.1, 128.8, 128.7, 128.3, 127.2, 126.3, 126.1, 124.4, 119.0, 118.6, 118.4, 113.6, 110.0, 89.9, 86.7, 86.3, 84.9, 81.9, 73.2, 71.8, 64.8, 55.7, 41.8, 38.9, 35.7. HRMS (ESI$^+$): *m/z* calcd for $C_{57}H_{49}N_6O_{11}$: 993.34538 [M+H]$^+$; found 993.34735.

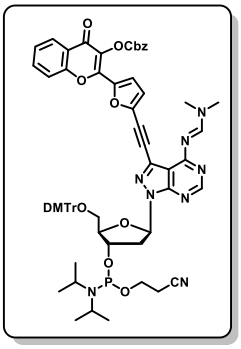

1.2.4. Synthesis of 8-aza-7-((5-(3-benzyloxycarbonyloxy-4-oxochromen-2-yl)furan-2-yl)ethynyl)-7-deaza-2′-deoxy-5′-*O*-(4,4′-dimethoxytrityl)-6-*N*-(dimethylformamidine)adenosine, 3′-[(2-cyanoethyl)-*N*,*N*-diisopropyl]phosphoramidite (3.8): Compound **3.7** (381 mg, 0.384 mmol) was co-evaporated with toluene (3 x 5 mL) and was dissolved in dry CH_2Cl_2 (7 mL). The solution was cooled down to 0 °C and was sequentially added DIPEA (267 µL, 4 eq) and 2-cyanoethyl-*N*,*N*-diisopropylchlorophosphoramidite (134 µL, 1.5 eq) in dry CH_2Cl_2 (2 mL). The reaction mixture was stirred under argon at RT for 2 h. The volatiles were removed in vacuo, and the residue was purified by flash chromatography on silica gel eluted with toluene/AcOEt (90:10 → 0:100, v/v) to provide the desired product as an orange foam (223 mg, 49%). R_f = 0.45 (CH_2Cl_2/AcOEt = 3/7); ^{1}H NMR (400 MHz, Methylene Chloride-d_2) δ 8.87 (s, 1H), 8.52 (s, 1H), 8.23 (dd, *J* = 8.0, 1.7 Hz, 1H), 7.78 (ddd, *J* = 8.7, 7.1, 1.7 Hz, 1H), 7.60 (dd, *J* = 8.6, 1.1 Hz, 1H), 7.49 (ddd, *J* = 8.1, 7.1, 1.1 Hz, 1H), 7.45 – 7.36 (m, 4H), 7.33 – 7.22 (m, 8H), 7.27 – 7.19 (m, 2H), 7.22 – 7.11 (m, 1H), 6.94 (d, *J* = 3.7 Hz, 1H), 6.82 – 6.69 (m, 5H), 5.30 (s, 2H), 4.94 – 4.81 (m, 1H), 4.29 – 4.19 (m, 1H), 3.93 – 3.75 (m, 1H), 3.71 (t, *J* = 3.0 Hz, 6H), 3.71 – 3.51 (m, 3H), 3.35 – 3.24 (m, 1H), 3.28 (s, 3H), 3.24 – 3.11 (m, 2H), 3.17 (s, 3H), 2.69 – 2.55 (m, 1H), 2.48 (t, *J* = 6.4 Hz, 2H), 1.20 (d, *J* = 6.7 Hz, 12H). ^{31}P NMR (162 MHz, Methylene Chloride-d_2) δ 148.6, 148.5. HRMS (ESI$^+$): *m/z* calcd for $C_{66}H_{66}N_8O_{12}P$: 1193.45323 [M+H]$^+$; found 1193.45496.

2. Photophysics of nucleosides

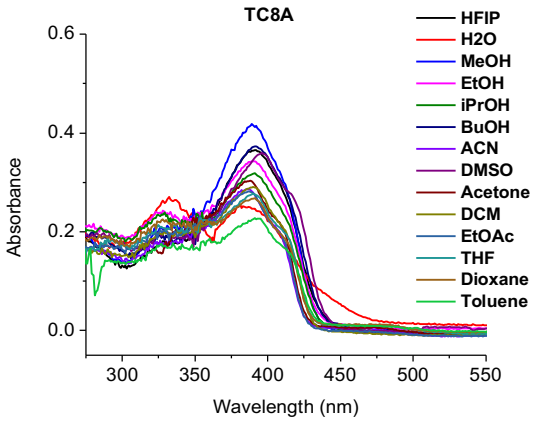

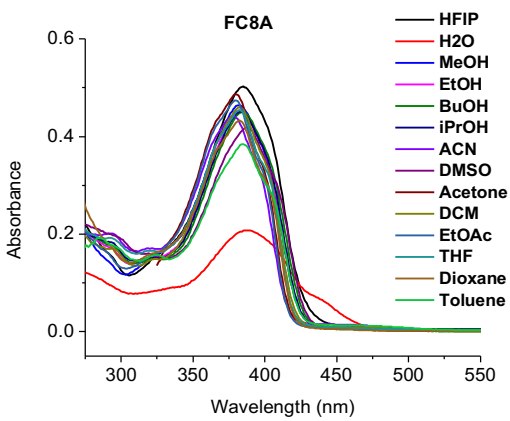

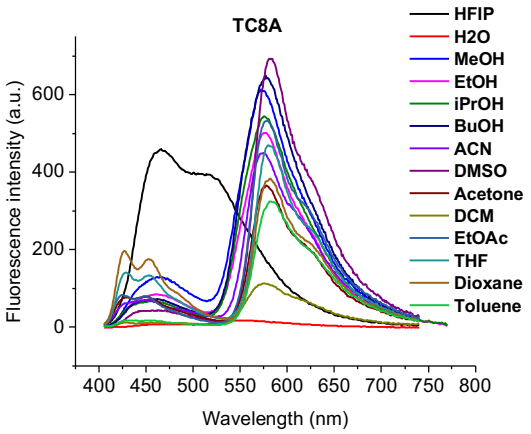

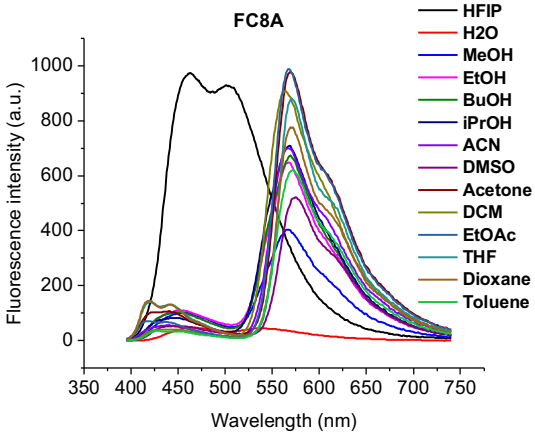

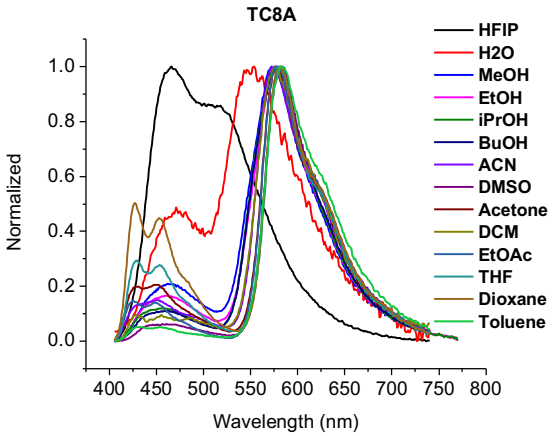

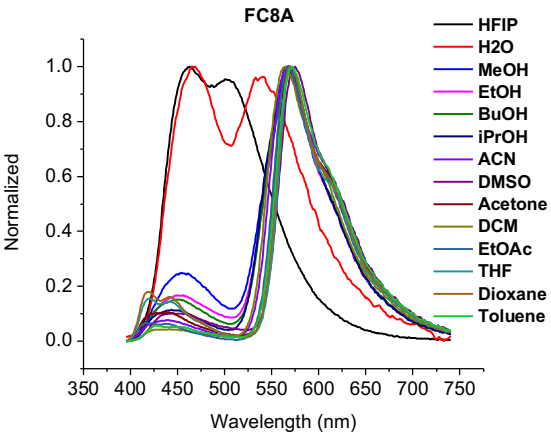

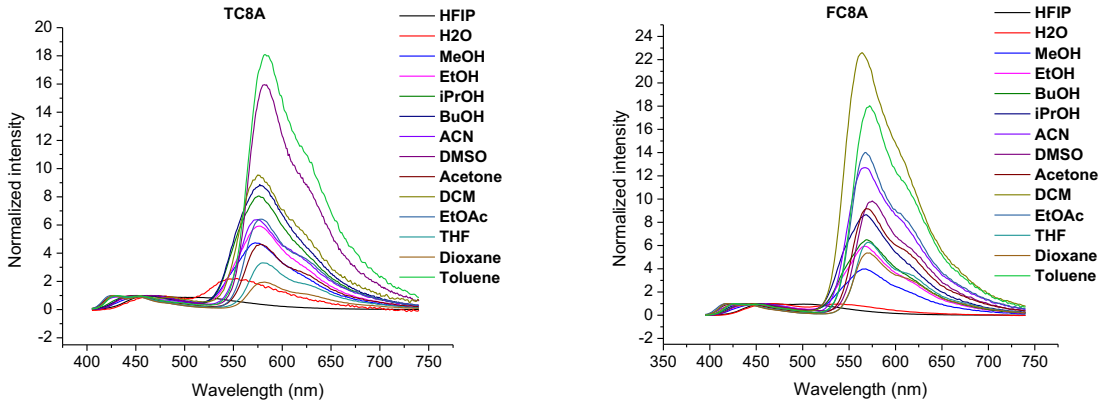

Figure S1. Absorption and emission spectra of the two nucleosides in different solvents: **TC8A** (Left panel, **LH_30**); **FC8A** (Right panel, **LH_32**).

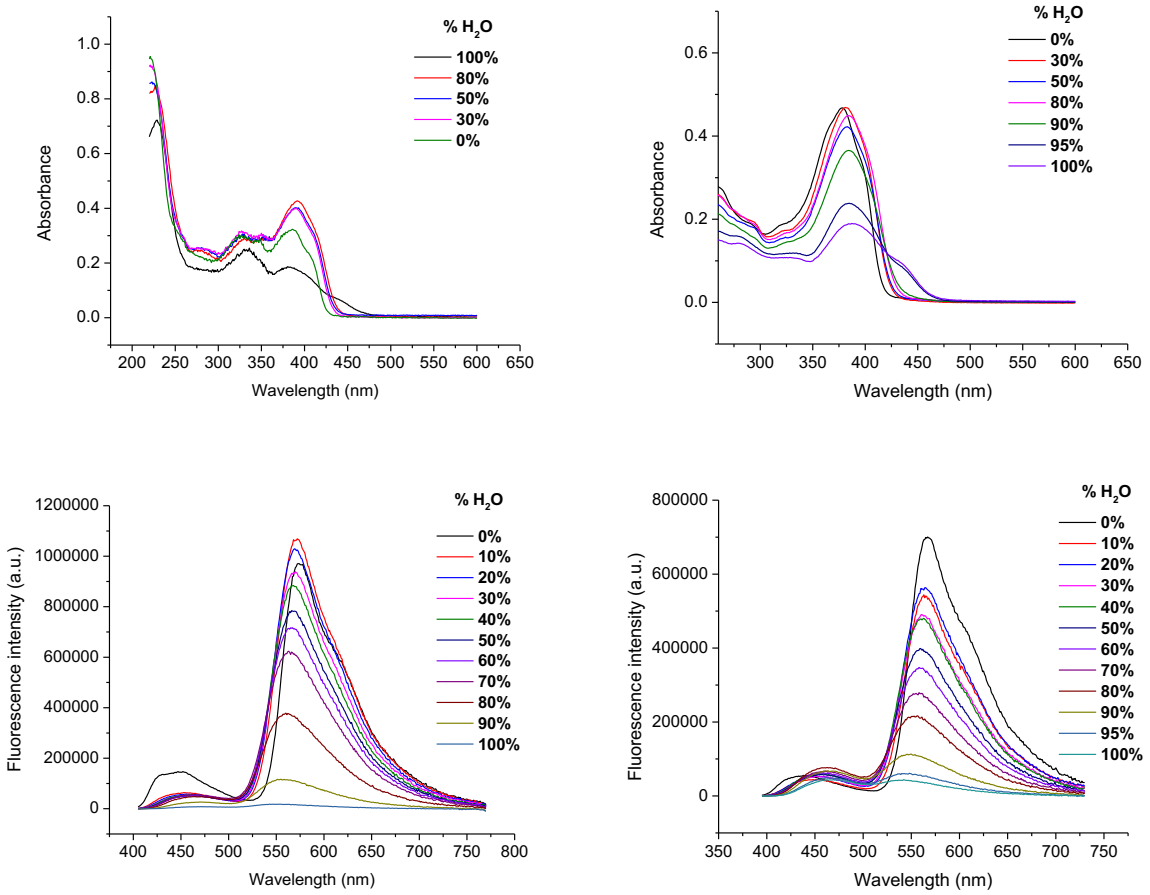

Figure S2. Absorption and emission spectra of the two nucleosides in different mixture between ACN/water: **TC8A** (left panel), **FC8A** (right panel). Excitation wavelengths were 390 and 380 nm, respectively.

Table S1. Photophysical properties of the two nucleosides at different concentration of water.

%H_2O	$\lambda Absc$		λN^*		λT^*		I_{T^*}/I_{N^*}		Φ	
	TC8A	*FC8A*	*TC8A*	*FC8A*	*TC8A*	*FC8A*	*TC8A*	*FC8A*	*TC8A*	*FC8A*
0	387	377	452	438	572	566	6.60	12.71	25	23
10	388	380	453	449	570	562	16.65	12.24	29	19
20	390	381	456	449	568	565	17.81	10.56	31	19
30	390	382	458	448	567	561	17.07	9.25	28	17
40	391	382	460	456	566	563	16.01	7.98	25	17
50	391	383	461	454	564	559	15.32	6.88	24	15
60	391	383	462	456	563	559	13.61	5.55	21	14
70	391	384	464	458	561	559	11.15	4.16	19	12
80	391	384	467	461	558	554	7.87	2.82	14	11
90	386	387	470	460	553	549	4.35	1.67	8	8
95		387		462		545		1.24		6
100	384	387	471	468	541	542	2.15	0.98	1.3	5

3. ODNs characterization

3.1. Analytical HPLC

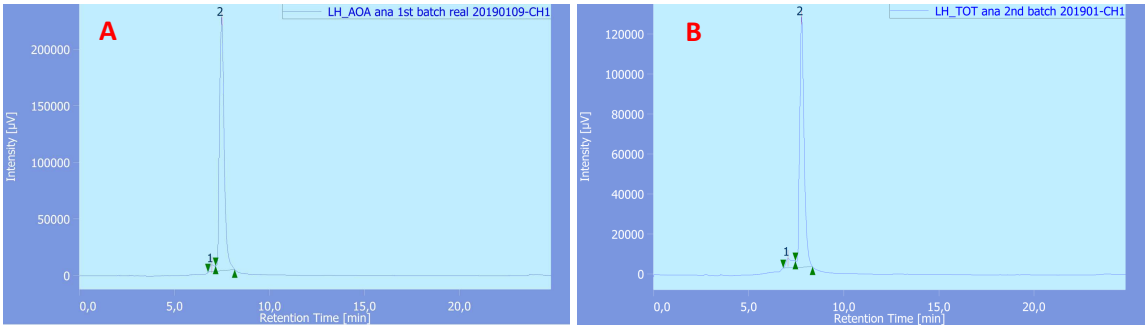

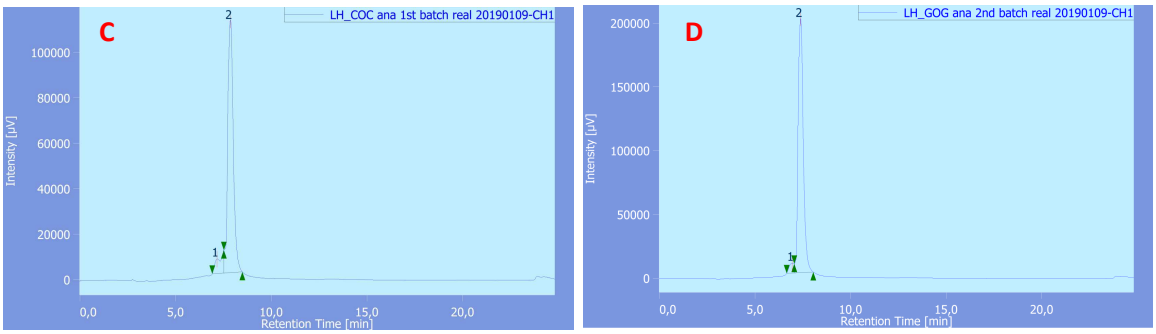

Figure S3. Analytical HPLC of purified ODNs sequences: **ssAOA** (A), **ssTOT** (B), **ssCOC** (C), and **ssGOG** (D). The detector was set at 260 nm.

3.2. HRMS of labeled ODNs sequences

Table S2. HRMS characterization of synthesized sequences **ssAOA** (A), **ssTOT** (B), **ssCOC** (C), and **ssGOG** (D).

A m/z	z	Exact mass	Calc. AOA
684.1102	7	4795.82621	4795.80974
798.2961	6	4795.82358	
958.1572	5	4795.82515	
1197.9474	4	4795.82092	
1597.5965	3	4795.81299	

B m/z	z	Exact mass	Calc. TOT
681.5356	7	4777.80401	4777.7866
795.293	6	4777.80498	
954.5516	5	4777.79715	
1193.4454	4	4777.81292	
1591.5912	3	4777.79709	

C m/z	z	Exact mass	Calc. COC
677.2495	7	4747.80131	4747.78727
790.2929	6	4747.80438	
948.5537	5	4747.80765	
1185.9433	4	4747.80452	
1581.5879	3	4747.78719	

D m/z	z	Exact mass	Calc. GOG
688.6802	7	4827.81621	4827.79957
803.6209	6	4827.77238	
964.5557	5	4827.81765	
1205.9434	4	4827.80492	
1608.2593	3	4827.80139	

3.3. Duplex melting temperature (Tm)

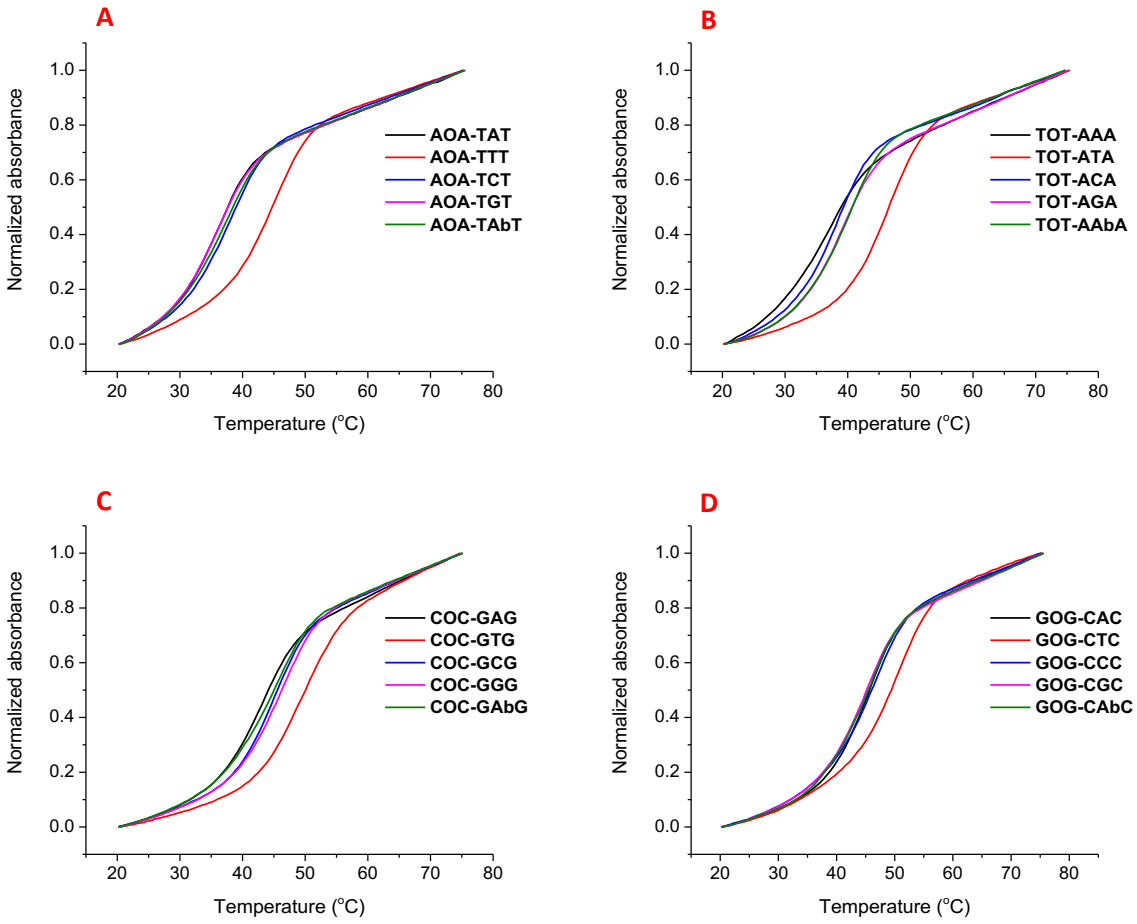

Figure S4. Duplex melting temperature of labeled sequences: **AOA** contexts (A); **TOT** contexts (B); **COC** contexts (C); and **GOG** contexts (D).

4. Absorption and emission spectra of labeled ODN sequences

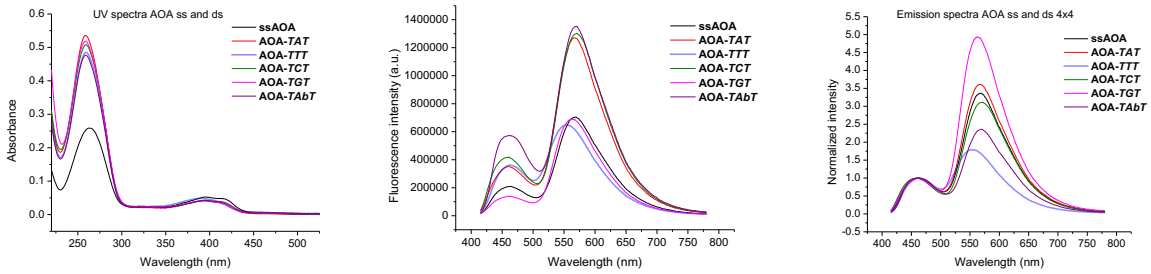

Figure S5. Absorption and emission spectra (at 2 μM) of ss and ds ODN sequences with **AOA** context. Excitation wavelength was 400 nm.

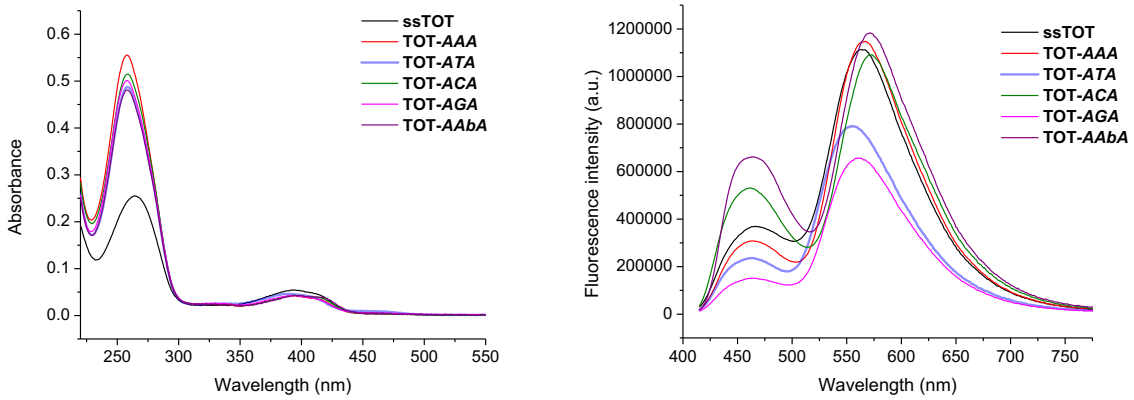

Figure S6. Absorption and emission spectra (at 2 μM) of ss and ds ODN sequences with **TOT** context. Excitation wavelength was 400 nm.

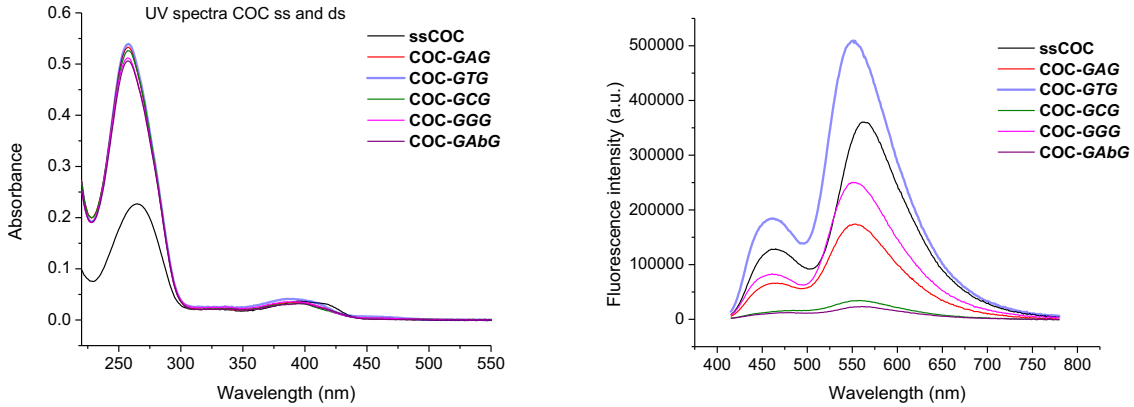

Figure S7. Absorption and emission spectra (at 2 μM) of ss and ds ODN sequences with **COC** context. Excitation wavelength was 400 nm.

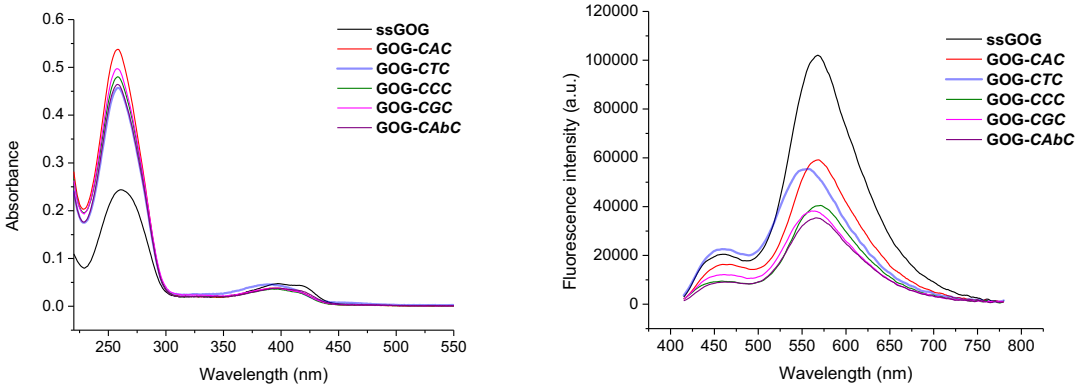

Figure S8. Absorption and emission spectra (at 2 μM) of ss and ds ODN sequences with **GOG** context. Excitation wavelength was 400 nm.

5. NMR spectra

References

[1] H. F. Lodish, *Molecular Cell Biology 6 Ed*, W. H. Freeman and Company, **2008**.
[2] J. D. Watson, F. H. C. Crick, *Nature* **1953**, *171*, 737–738.
[3] N. B. Leontis, E. Westhof, *RNA* **2001**, *7*, 499–512.
[4] E Stofer, A. C Chipot, R. Lavery, *J. Am. Chem. Soc.* **1999**, *121*, 9503–9508.
[5] K. Hoogsteen, *Acta Crystallogr.* **1959**, *12*, 822–823.
[6] K. Hoogsteen, *Acta Crystallogr.* **1963**, *16*, 907–916.
[7] H. Zhou, B. J. Hintze, I. J. Kimsey, B. Sathyamoorthy, S. Yang, J. S. Richardson, H. M. Al-Hashimi, *Nucleic Acids Res.* **2015**, *43*, 3420–3433.
[8] L. C. Sowers, G. V. Fazakerley, R. Eritja, B. E. Kaplan, M. F. Goodman, *Proc. Natl. Acad. Sci. U. S. A.* **1986**, *83*, 5434–5438.
[9] L. C. Sowers, M. F. Goodman, R. Eritja, B. Kaplan, G. V. Fazakerley, *J. Mol. Biol.* **1989**, *205*, 437–447.
[10] W. Saenger, *Principles of Nucleic Acid Structure*, Springer New York, New York, NY, **1984**.
[11] R. R. Sinden, *DNA Structure and Function*, Elsevier Science, **2012**.
[12] R. R. Sinden, in *DNA Structure and Function*, Elsevier, San Diego, **1994**, pp. 1–57.
[13] N. M. Luscombe, R. A. Laskowski, J. M. Thornton, *Nucleic Acids Res.* **2001**, *29*, 2860–2874.
[14] W. Saenger, in *Principles of Nucleic Acid Structure*, Springer, New York, NY, New York, NY, **1984**, pp. 368–384.
[15] R. E. Franklin, R. G. Gosling, *Nature* **1953**, *172*, 156–157.
[16] R. E. Franklin, R. G. Gosling, *Nature* **1953**, *171*, 740–741.
[17] R. E. Franklin, R. G. Gosling, *Acta Crystallogr.* **1953**, *6*, 673–677.
[18] M. Kulkarni, A. Mukherjee, *Prog. Biophys. Mol. Biol.* **2017**, *128*, 63–73.
[19] M. J. B. Tunis, J. E. Hearst, *Biopolymers* **1968**, *6*, 1345–1353.
[20] H. M. Berman, *Curr. Opin. Struct. Biol.* **1991**, *1*, 423–427.
[21] J. J. Howard, G. C. Lynch, B. M. Pettitt, *J. Phys. Chem. B* **2011**, *115*, 547–556.
[22] M. L. McDermott, H. Vanselous, S. A. Corcelli, P. B. Petersen, *ACS Cent. Sci.* **2017**, *3*, 708–714.
[23] M. H. Moore, W. N. Hunter, B. L. d'Estaintot, O. Kennard, *J. Mol. Biol.* **1989**, *206*, 693–705.
[24] A. H. Wang, G. Ughetto, G. J. Quigley, A. Rich, *Biochemistry* **1987**, *26*, 1152–1163.
[25] D. G. Brown, M. R. Sanderson, J. V. Skelly, T. C. Jenkins, T. Brown, E. Garman, D. I. Stuart, S. Neidle, *EMBO J.* **1990**, *9*, 1329–1334.
[26] T. A. Larsen, D. S. Goodsell, D. Cascio, K. Grzeskowiak, R. E. Dickerson, *J. Biomol. Struct. Dyn.* **1989**, *7*, 477–491.
[27] P. VN, S. RR, in *Madame Curie Bioscience Database Internet. Austin TX Landes Bioscience; 2000-2013*, pp. 1–24.
[28] N. P. F. Barthes, K. Gavvala, D. Dziuba, D. Bonhomme, I. A. Karpenko, A. S. Dabert-Gay, D. Debayle, A. P. Demchenko, R. Benhida, B. Y. Michel, et al., *J. Mater. Chem. C* **2016**, *4*, 3010–3017.
[29] V. N. Potaman, R. R. Sinden, in *DNA Conformation and Transcription*, Springer, Boston, MA, Boston, MA, **2005**, pp. 3–17.
[30] T. E. Cheatham III, P. A. Kollman, *Structure* **1997**, *5*, 1297–1311.
[31] M. Egli, *Chem. Biol.* **2002**, *9*, 277–286.

[32] M. Feig, B. M. Pettitt, *Biopolymers* **1998**, *48*, 199–209.
[33] W. Fuller, M. H. Wilkins, H. R. Wilson, L. D. Hamilton, *J. Mol. Biol.* **1965**, *12*, 60–76.
[34] L. Fairall, S. Martin, D. Rhodes, *EMBO J.* **1989**, *8*, 1809–1817.
[35] J. C. García-Ramos, R. Galindo-Murillo, F. Cortés-Guzmán, L. Ruiz-Azuara, *J. Mex. Chem. Soc.* **2013**, *57*, 245–259.
[36] A. Herbert, A. Rich, *Genetica* **1999**, *106*, 37–47.
[37] P. Khuu, M. Sandor, J. DeYoung, P. S. Ho, *Proc. Natl. Acad. Sci. U. S. A.* **2007**, *104*, 16528–16533.
[38] A. Herbert, J. Alfken, Y.-G. Kim, I. S. Mian, K. Nishikura, A. Rich, *Proc. Natl. Acad. Sci. U. S. A.* **1997**, *94*, 8421–8426.
[39] D.-B. Oh, Y.-G. Kim, A. Rich, *Proc. Natl. Acad. Sci. U. S. A.* **2002**, *99*, 16666–16671.
[40] S. Zhang, C. Lockshin, A. Herbert, E. Winter, A. Rich, *EMBO J.* **1992**, *11*, 3787–3796.
[41] J. R. Bothe, K. Lowenhaupt, H. M. Al-Hashimi, *J. Am. Chem. Soc.* **2011**, *133*, 2016–2018.
[42] J. Choi, T. Majima, *Chem. Soc. Rev.* **2011**, *40*, 5893–18.
[43] E. P. Wright, H. A. Day, A. M. Ibrahim, J. Kumar, L. J. E. Boswell, C. Huguin, C. E. M. Stevenson, K. Pors, Z. A. E. Waller, *Sci. Rep.* **2016**, 1–7.
[44] T. A. Brooks, S. Kendrick, L. Hurley, *FEBS J.* **2010**, *277*, 3459–3469.
[45] M. Guéron, J.-L. Leroy, *Curr. Opin. Struct. Biol.* **2000**, *10*, 326–331.
[46] J.-L. Mergny, L. Lacroix, X. Han, J.-L. Leroy, C. Hélène, *J. Am. Chem. Soc.* **1995**, *117*, 8887–8898.
[47] S. Kendrick, Y. Akiyama, S. M. Hecht, L. H. Hurley, *J. Am. Chem. Soc.* **2009**, *131*, 17667–17676.
[48] J. Zhou, C. Wei, G. Jia, X. Wang, Z. Feng, C. Li, *Mol. Biosyst.* **2010**, *6*, 580–586.
[49] S. R. Shin, K. S. Jin, C. K. Lee, S. I. Kim, G. M. Spinks, I. So, J. H. Jeon, T. M. Kang, J. Y. Mun, S. S. Han, et al., *Adv. Mater.* **2009**, *21*, 1907–1910.
[50] X. Li, Y. Peng, J. Ren, X. Qu, *Proc. Natl. Acad. Sci. U. S. A.* **2006**, *103*, 19658–19663.
[51] O. Y. Fedoroff, A. Rangan, V. V. Chemeris, L. H. Hurley, *Biochemistry* **2000**, *39*, 15083–15090.
[52] S. Robidoux, R. Klinck, K. Gehring, M. J. Damha, *J. Biomol. Struct. Dyn.* **1997**, *15*, 517–527.
[53] M. Debnath, K. Fatma, J. Dash, *Angew. Chem. Int. Ed. Engl.* **2019**, *58*, 2942–2957.
[54] J. T. Davis, *Angew. Chem. Int. Ed. Engl.* **2004**, *43*, 668–698.
[55] J. L. Huppert, *FEBS J.* **2010**, *277*, 3452–3458.
[56] A. T. Phan, V. Kuryavyi, D. J. Patel, *Curr. Opin. Struct. Biol.* **2006**, *16*, 288–298.
[57] V. Víglaský, K. Tlučková, L. Bauer, *Eur. Biophys. J.* **2011**, *40*, 29–37.
[58] J. B. Chaires, *FEBS J.* **2009**, *277*, 1098–1106.
[59] N. Smargiasso, F. Rosu, W. Hsia, P. Colson, E. S. Baker, M. T. Bowers, E. De Pauw, V. Gabelica, *J. Am. Chem. Soc.* **2008**, *130*, 10208–10216.
[60] T. A. Brooks, L. H. Hurley, *Nat. Rev. Cancer.* **2009**, *9*, 849–861.
[61] D. Hanahan, R. A. Weinberg, *Cell* **2000**, *100*, 57–70.
[62] J. Spiegel, S. Adhikari, S. Balasubramanian, *Trends Chem.* **2020**, *2*, 123–136.

[63] P. Pandey, S. Hasnain, S. Ahmad, in *Encyclopedia of Bioinformatics and Computational Biology*, Elsevier, Oxford, **2019**, pp. 142–154.
[64] N. M. Luscombe, S. E. Austin, H. M. Berman, J. M. Thornton, *Genome Biol.* **2000**, *1*, 1–37.
[65] J. F. Thompson, A. Landy, *Nucleic Acids Res.* **1988**, *16*, 9687–9705.
[66] T. T. Paull, M. J. Haykinson, R. C. Johnson, *Genes Dev.* **1993**, *7*, 1521–1534.
[67] J. E. Masse, B. Wong, Y.-M. Yen, F. H. T. Allain, R. C. Johnson, J. Feigon, *J. Mol. Biol.* **2002**, *323*, 263–284.
[68] M. Andrabi, K. Mizuguchi, S. Ahmad, *Proteins: Struct., Funct., Bioinf.* **2014**, *82*, 841–857.
[69] M. Fuxreiter, I. Simon, S. Bondos, *Trends Biochem. Sci.* **2011**, *36*, 415–423.
[70] R. Rohs, S. M. West, A. Sosinsky, P. Liu, R. S. Mann, B. Honig, *Nature* **2009**, *461*, 1248–1253.
[71] S. Ahmad, H. Kono, M. J. Arauzo-Bravo, A. Sarai, *Nucleic Acids Res.* **2006**, *34*, W124–W127.
[72] S. C. Schultz, G. C. Shields, T. A. Steitz, *Science* **1991**, *253*, 1001.
[73] N. Shimamoto, *J. Biol. Chem.* **1999**, *274*, 15293–15296.
[74] S. E. Halford, J. F. Marko, *Nucleic Acids Res.* **2004**, *32*, 3040–3052.
[75] A. Esadze, C. A. Kemme, A. B. Kolomeisky, J. Iwahara, *Nucleic Acids Res.* **2014**, *42*, 7039–7046.
[76] B. Wardle, *Principles and Applications of Photochemistry*, John Wiley & Sons, **2009**.
[77] N. J. Turro, V. Ramamurthy, J. C. Scaiano, *Principles of Molecular Photochemistry: an Introduction*, University Science Books, **2009**.
[78] M. Kasha, *Discuss. Faraday Soc.* **1950**, *9*, 14–19.
[79] A. P. Demchenko, V. I. Tomin, P.-T. Chou, *Chem. Rev.* **2017**, *117*, 13353–13381.
[80] H.-W. Tseng, J.-Y. Shen, T.-Y. Kuo, T.-S. Tu, Y.-A. Chen, A. P. Demchenko, P.-T. Chou, *Chem. Sci.* **2016**, *7*, 655–665.
[81] J. R. Lakowicz, *Principles of Fluorescence Spectroscopy*, Springer Science & Business Media, **2013**.
[82] **2007**, 1–960.
[83] L. M. Wilhelmsson, *Q. Rev. Biophys.* **2010**, *43*, 159–183.
[84] U. Asseline, *Curr. Org. Chem.* **2006**, *10*, 491–518.
[85] S. G. Srivatsan, M. Famulok, *Comb. Chem. High Throughput Screening* **2007**, *10*, 698–705.
[86] X. Shi, D. Herschlag, in *Methods in Enzymology*, Elsevier, **2009**, pp. 287–302.
[87] B. Juskowiak, *Anal. Bioanal. Chem.* **2011**, *399*, 3157–3176.
[88] S. H. Weisbrod, A. Marx, *Chem. Commun.* **2008**, 5675–5685.
[89] F. Wachowius, C. Höbartner, *ChemBioChem* **2010**, *11*, 469–480.
[90] O. Khakshoor, E. T. Kool, *Chem. Commun.* **2011**, *47*, 7018–7024.
[91] J. Peon, A. H. Zewail, *Chem. Phys. Lett.* **2001**, *348*, 255–262.
[92] E. Nir, K. Kleinermanns, L. Grace, Mattanjah S de Vries, *J. Phys. Chem. A* **2001**, *105*, 5106–5110.
[93] R. T. Ranasinghe, T. Brown, *Chem. Commun.* **2005**, *22*, 5487–16.
[94] A. A. Martí, S. Jockusch, N. Stevens, J. Ju, N. J. Turro, *Acc. Chem. Res.* **2007**, *40*, 402–409.
[95] T. Ha, *Biochemistry* **2004**, *43*, 4055–4063.
[96] R. Zhao, D. Rueda, *Methods* **2009**, *49*, 112–117.
[97] S. Tyagi, D. P. Bratu, F. R. Kramer, *Nat. Biotechnol.* **1998**, *16*, 49–53.

[98] A. Jenne, J. S. Hartig, N. Piganeau, A. Tauer, D. A. Samarsky, M. R. Green, J. Davies, M. Famulok, *Nat. Biotechnol.* **2001**, *19*, 56–61.
[99] M. Dorywalska, S. C. Blanchard, R. L. Gonzalez Jr, H. D. Kim, S. Chu, J. D. Puglisi, *Nucleic Acids Res.* **2005**, *33*, 182–189.
[100] M. Hafner, A. Schmitz, I. Grüne, S. G. Srivatsan, B. Paul, W. Kolanus, T. Quast, E. Kremmer, I. Bauer, M. Famulok, *Nature* **2006**, *444*, 941–944.
[101] M. Stoop, C. J. Leumann, *Chem. Commun.* **2011**, *47*, 7494–7496.
[102] A. A. Tanpure, M. G. Pawar, S. G. Srivatsan, *Isr. J. Chem.* **2013**, *53*, 366–378.
[103] D. C. Ward, E. Reich, L. Stryer, *J. Biol. Chem.* **1969**, *244*, 1228–1237.
[104] W. Xu, K. M. Chan, E. T. Kool, *Nat. Chem.* **2017**, *9*, 1043–1055.
[105] M. Segal, B. Fischer, *Org. Biomol. Chem.* **2012**, *10*, 1571–1580.
[106] N. J. Greco, Y. Tor, *J. Am. Chem. Soc.* **2005**, *127*, 10784–10785.
[107] G. T. Crisp, B. L. Flynn, *J. Org. Chem.* **1993**, *58*, 6614–6619.
[108] D. E. Bergstrom, J. L. Ruth, *J. Am. Chem. Soc.* **1976**, *98*, 1587–1589.
[109] V. Kumar, J. Yap, A. Muroyama, S. V. Malhotra, *Synthesis* **2009**, *2009*, 3957–3962.
[110] Y. Liang, S. F. Wnuk, in *Palladium-Catalyzed Modification of Nucleosides, Nucleotides and Oligonucleotides*, Elsevier, **2018**, pp. 197–246.
[111] R. Rayala, S. F. Wnuk, *Tetrahedron Lett.* **2012**, *53*, 3333–3336.
[112] J. Maity, R. Stromberg, *Molecules* **2013**, *18*, 12740–12750.
[113] N. Pottabathini, S. Bae, P. Pradhan, H.-G. Hahn, H. Mah, M. K. Lakshman, *J. Org. Chem.* **2005**, *70*, 7188–7195.
[114] Y. Li, Y. Xiong, G. Zhang, L. Zhang, W. Yang, J. Yang, L. Huang, Z. Qiao, Z. Miao, G. Lin, et al., *J. Med. Chem.* **2018**, *61*, 11398–11414.
[115] F. Seela, K. Xu, *Org. Biomol. Chem.* **2007**, *5*, 3034–3045.
[116] F. Seela, M. Zulauf, *J. Chem. Soc., Perkin Trans. 1* **1998**, 3233–3240.
[117] A. Fin, A. R. Rovira, P. A. Hopkins, Y. Tor, in *Modified Nucleic Acids*, Springer, **2016**, pp. 1–26.
[118] K. Nakatani, Y. Tor, Eds., *Modified Nucleic Acids*, Springer International Publishing, Cham, **2016**.
[119] C. R. Guest, R. A. Hochstrasser, L. C. Sowers, D. P. Millar, *Biochemistry* **1991**, *30*, 3271–3279.
[120] E. L. Rachofsky, R. Osman, J. A. Ross, *Biochemistry* **2001**, *40*, 946–956.
[121] J. T. Stivers, *Nucleic Acids Res.* **1998**, *26*, 3837–3844.
[122] B. W. Allan, N. O. Reich, *Biochemistry* **1996**, *35*, 14757–14762.
[123] S. O. Kelley, J. K. Barton, *Science* **1999**, *283*, 375–381.
[124] E. Freese, *J. Mol. Biol.* **1959**, *1*, 87–105.
[125] L. C. Sowers, Y. Boulard, G. V. Fazakerley, *Biochemistry* **2000**, *39*, 7613–7620.
[126] N. Ben Gaied, N. Glasser, N. Ramalanjaona, H. Beltz, P. Wolff, R. Marquet, A. Burger, Y. Mély, *Nucleic Acids Res.* **2005**, *33*, 1031–1039.
[127] A. Nadler, J. Strohmeier, U. Diederichsen, *Angew. Chem. Int. Ed. Engl.* **2011**, *50*, 5392–5396.
[128] D. Shin, R. W. Sinkeldam, Y. Tor, *J. Am. Chem. Soc.* **2011**, *133*, 14912–14915.
[129] P. G. Wu, T. M. Nordlund, B. Gildea, L. W. McLaughlin, *Biochemistry* **1990**, *29*, 6508–6514.
[130] N. J. Greco, Y. Tor, *Tetrahedron* **2007**, *63*, 3515–3527.
[131] A. Okamoto, K. Tanaka, T. Fukuta, I. Saito, *J. Am. Chem. Soc.* **2003**, *125*, 9296–9297.
[132] A. Okamoto, K. Tanaka, T. Fukuta, I. Saito, *ChemBioChem* **2004**, *5*, 958–963.

[133] N. J. Leonard, M. A. Sprecker, A. G. Morrice, *J. Am. Chem. Soc.* **1976**, *98*, 3987–3994.
[134] B. Y. Michel, D. Dziuba, R. Benhida, A. P. Demchenko, A. Burger, *Front. Chem.* **2020**, *8*, 14757–23.
[135] A. T. Krueger, E. T. Kool, *J. Am. Chem. Soc.* **2008**, *130*, 3989–3999.
[136] S. K. Jarchow-Choy, A. T. Krueger, H. Liu, J. Gao, E. T. Kool, *Nucleic Acids Res.* **2010**, *39*, 1586–1594.
[137] S. J. O. Hardman, S. W. Botchway, K. C. Thompson, *Photochem. Photobiol.* **2008**, *84*, 1473–1479.
[138] Y. Sato, T. Moriguchi, K. Shinozuka, *Chem. Lett.* **2012**, *41*, 420–422.
[139] S. S. Bag, R. Kundu, K. Matsumoto, Y. Saito, I. Saito, *Bioorg. Med. Chem. Lett.* **2010**, *20*, 3227–3230.
[140] A. Okamoto, K. Kanatani, I. Saito, *J. Am. Chem. Soc.* **2004**, *126*, 4820–4827.
[141] Y. Saito, Y. Miyauchi, A. Okamoto, I. Saito, *Chem. Commun.* **2004**, *0*, 1704–1705.
[142] A. Dumas, G. Mata, N. W. Luedtke, in *Fluorescent Analogues of Biomolecular Building Blocks: Design and Applications*, John Wiley & Sons, Ltd, Hoboken, NJ, USA, **2016**, pp. 242–275.
[143] K. Tainaka, K. Tanaka, S. Ikeda, K.-I. Nishiza, T. Unzai, Y. Fujiwara, I. Saito, A. Okamoto, *J. Am. Chem. Soc.* **2007**, *129*, 4776–4784.
[144] U. Förster, K. Lommel, D. Sauter, C. Grünewald, J. W. Engels, J. Wachtveitl, *ChemBioChem* **2010**, *11*, 664–672.
[145] C. Wagner, M. Rist, E. Mayer-Enthart, H.-A. Wagenknecht, *Org. Biomol. Chem.* **2005**, *3*, 2062–2063.
[146] S. De Ornellas, J. M. Slattery, R. M. Edkins, A. Beeby, C. G. Baumann, I. J. S. Fairlamb, *Org. Biomol. Chem.* **2015**, *13*, 68–72.
[147] H. Cahová, R. Pohl, L. Bednárová, K. Nováková, J. Cvačka, M. Hocek, *Org. Biomol. Chem.* **2008**, *6*, 3657–4.
[148] A. Matarazzo, J. Brow, R. H. E. Hudson, *Can. J. Chem.* **2018**, *96*, 1093–1100.
[149] C. Grünewald, T. Kwon, N. Piton, U. Förster, J. Wachtveitl, J. W. Engels, *Bioorg. Med. Chem.* **2008**, *16*, 19–26.
[150] V. A. Korshun, I. A. Prokhorenko, S. V. Gontarev, M. V. Skorobogatyi, K. V. Balakin, E. V. Manasova, A. D. Malakhov, Y. A. Berlin, *Nucleosides, Nucleotides Nucleic Acids* **2006**, *16*, 1461–1464.
[151] M. Segal, E. Yavin, P. Kafri, Y. Shav-Tal, B. Fischer, *J. Med. Chem.* **2013**, *56*, 4860–4869.
[152] P. Herdewijn, *Oligonucleotide Synthesis: Methods and Applications*, Springer Science & Business Media, **2005**.
[153] R. W. Sinkeldam, N. J. Greco, Y. Tor, *Chem. Rev.* **2010**, *110*, 2579–2619.
[154] J. C. Schulhof, D. Molko, R. Teoule, *Tetrahedron Lett.* **1987**, *28*, 51–54.
[155] H. Vu, C. McCollum, K. Jacobson, P. Theisen, R. Vinayak, E. Spiess, A. Andrus, *Tetrahedron Lett.* **1990**, *31*, 7269–7272.
[156] F. Seela, S. S. Pujari, *Bioconjugate Chem.* **2010**, *21*, 1629–1641.
[157] M. K. Schlegel, E. Meggers, *J. Org. Chem.* **2009**, *74*, 4615–4618.
[158] V. Vongsutilers, J. Daft, K. Shaughnessy, P. Gannett, *Molecules* **2009**, *14*, 3339–3352.
[159] A. Weller, *Naturwissenschaften* **1955**, *42*, 175–176.
[160] J. Zhao, S. Ji, Y. Chen, H. Guo, P. Yang, *Phys. Chem. Chem. Phys.* **2012**, *14*, 8803–8817.
[161] V. S. Padalkar, S. Seki, *Chem. Soc. Rev.* **2016**, *45*, 169–202.

[162] J. E. Kwon, S. Y. Park, *Adv. Mater.* **2011**, *23*, 3615–3642.
[163] J. Wu, W. Liu, J. Ge, H. Zhang, P. Wang, *Chem. Soc. Rev.* **2011**, *40*, 3483–3495.
[164] P.-T. Chou, Y.-C. Chen, W.-S. Yu, Y.-H. Chou, C.-Y. Wei, Y.-M. Cheng, *J. Phys. Chem. A* **2001**, *105*, 1731–1740.
[165] M. T. Ignasiak, C. Houée Levin, G. Kciuk, B. Marciniak, T. Pedzinski, *Chemphyschem* **2015**, *16*, 628–633.
[166] P. K. Sengupta, M. Kasha, *Chem. Phys. Lett.* **1979**, *68*, 382–385.
[167] D. McMorrow, M. Kasha, *J. Phys. Chem.* **1984**, *88*, 2235–2243.
[168] S. J. Schmidtke, D. F. Underwood, D. A. Blank, *J. Am. Chem. Soc.* **2004**, *126*, 8620–8621.
[169] M. J. Paterson, M. A. Robb, L. Blancafort, A. D. DeBellis, *J. Am. Chem. Soc.* **2004**, *126*, 2912–2922.
[170] E. Hadjoudis, I. M. Mavridis, *Chem. Soc. Rev.* **2004**, *33*, 579–588.
[171] Y. Nakane, T. Takeda, N. Hoshino, K.-I. Sakai, T. Akutagawa, *J. Phys. Chem. A* **2015**, *119*, 6223–6231.
[172] A. C. Sedgwick, L. Wu, H.-H. Han, S. D. Bull, X.-P. He, T. D. James, J. L. Sessler, B. Z. Tang, H. Tian, J. Yoon, *Chem. Soc. Rev.* **2018**, *47*, 8842–8880.
[173] C.-L. Chen, Y.-T. Chen, A. P. Demchenko, P.-T. Chou, *Nat. Rev. Chem.* **2018**, 1–13.
[174] M. H. Lee, J. S. Kim, J. L. Sessler, *Chem. Soc. Rev.* **2015**, *44*, 4185–4191.
[175] A. P. Demchenko, *Advanced Fluorescence Reporters in Chemistry and Biology I: Fundamentals and Molecular Design*, Springer, Berlin, Heidelberg, **2010**.
[176] W.-S. Yu, C.-C. Cheng, Y.-M. Cheng, P.-C. Wu, Y.-H. Song, Y. Chi, P.-T. Chou, *J. Am. Chem. Soc.* **2003**, *125*, 10800–10801.
[177] V. Shvadchak, *Theses* **2009**, 1–263.
[178] A. S. Klymchenko, V. G. Pivovarenko, A. P. Demchenko, *Spectrochim. Acta, Part A* **2003**, *59*, 787–792.
[179] P.-T. Chou, M. L. Martinez, J. H. Clements, *J. Phys. Chem.* **1993**, *97*, 2618–2622.
[180] S. M. Ormson, R. G. Brown, F. Vollmer, W. Rettig, *J. Photochem. Photobiol., A* **1994**, *81*, 65–72.
[181] V. I. Tomin, A. P. Demchenko, P.-T. Chou, *J. Photochem. Photobiol., C* **2015**, *22*, 1–18.
[182] A. S. Klymchenko, A. P. Demchenko, *Phys. Chem. Chem. Phys.* **2003**, *5*, 461–468.
[183] V. V. Shynkar, A. S. Klymchenko, E. Piémont, A. P. Demchenko, Y. Mély, *J. Phys. Chem. A* **2004**, *108*, 8151–8159.
[184] A. S. Klymchenko, C. Kenfack, G. Duportail, Y. Mély, *J. Chem. Sci.* **2007**, *119*, 83–89.
[185] S. Ameer-Beg, S. M. Ormson, R. G. Brown, P. Matousek, M. Towrie, E. T. J. Nibbering, P. Foggi, F. V. R. Neuwahl, *J. Phys. Chem. A* **2001**, *105*, 3709–3718.
[186] A. J. G. Strandjord, S. H. Courtney, D. M. Friedrich, P. F. Barbara, *J. Phys. Chem.* **1983**, *87*, 1125–1133.
[187] A. J. Strandjord, P. F. Barbara, *J. Phys. Chem.* **1985**, *89*, 2355–2361.
[188] V. V. Shynkar, Y. Mély, G. Duportail, E. Piémont, A. S. Klymchenko, A. P. Demchenko, *J. Phys. Chem. A* **2003**, *107*, 9522–9529.
[189] Y.-M. Cheng, S.-C. Pu, Y.-C. Yu, P.-T. Chou, Huang, C.-T. Chen, T.-H. Li, W.-P. Hu, *J. Phys. Chem. A* **2005**, *109*, 11696–11706.
[190] A. D. Roshal, J. A. Organero, A. Douhal, *Chem. Phys. Lett.* **2003**, *379*, 53–59.

[191] A. P. Demchenko, K.-C. Tang, P.-T. Chou, *Chem. Soc. Rev.* **2013**, *42*, 1379–1408.
[192] A. S. Klymchenko, T. Ozturk, V. G. Pivovarenko, A. P. Demchenko, *Can. J. Chem.* **2011**, *79*, 358–363.
[193] T. C. Swinney, D. F. Kelley, *J. Chem. Phys.* **1993**, *99*, 211–221.
[194] P.-T. Chou, M. L. Martinez, J. H. Clements, *J. Phys. Chem.* **1993**, *97*, 2618–2622.
[195] A. S. Klymchenko, V. G. Pivovarenko, T. Ozturk, A. P. Demchenko, *New J. Chem.* **2003**, *27*, 1336–8.
[196] A. S. Klymchenko, T. Ozturk, V. G. Pivovarenko, A. P. Demchenko, *Tetrahedron Lett.* **2001**, *42*, 7967–7970.
[197] A. P. Demchenko, A. S. Klymchenko, V. G. Pivovarenko, S. Ercelen, in *Fluorescence Spectroscopy, Imaging and Probes*, Springer Berlin Heidelberg, Berlin, Heidelberg, **2002**, pp. 101–110.
[198] A. S. Klymchenko, Y. Mély, *Tetrahedron Lett.* **2004**, *45*, 8391–8394.
[199] O. M. Zamotaiev, V. Y. Postupalenko, V. V. Shvadchak, V. G. Pivovarenko, A. S. Klymchenko, Y. Mély, *Org. Biomol. Chem.* **2014**, *12*, 7036–7044.
[200] V. V. Shvadchak, A. S. Klymchenko, H. de Rocquigny, Y. Mély, *Nucleic Acids Res.* **2009**, *37*, e25–e25.
[201] A. V. Strizhak, V. Y. Postupalenko, V. V. Shvadchak, N. Morellet, E. Guittet, V. G. Pivovarenko, A. S. Klymchenko, Y. Mély, *Bioconjugate Chem.* **2012**, *23*, 2434–2443.
[202] O. M. Zamotaiev, V. Y. Postupalenko, V. V. Shvadchak, V. G. Pivovarenko, A. S. Klymchenko, Y. Mély, *Bioconjugate Chem.* **2011**, *22*, 101–107.
[203] A. S. Klymchenko, A. P. Demchenko, *New J. Chem.* **2004**, *28*, 687–692.
[204] A. Suzuki, N. Nemoto, I. Saito, Y. Saito, *Org. Biomol. Chem.* **2013**, *12*, 660–666.
[205] A. Suzuki, T. Yanaba, I. Saito, Y. Saito, *ChemBioChem* **2014**, *15*, 1638–1644.
[206] Y. Saito, A. Suzuki, T. Yamauchi, I. Saito, *Tetrahedron Lett.* **2015**, *56*, 3034–3038.
[207] M. Spadafora, V. Y. Postupalenko, V. V. Shvadchak, A. S. Klymchenko, Y. Mély, A. Burger, R. Benhida, *Tetrahedron* **2009**, *65*, 7809–7816.
[208] D. Dziuba, I. A. Karpenko, N. P. F. Barthes, B. Y. Michel, A. S. Klymchenko, R. Benhida, A. P. Demchenko, Y. Mély, A. Burger, *Chem. Eur. J.* **2014**, *20*, 1998–2009.
[209] D. Dziuba, V. Y. Postupalenko, M. Spadafora, A. S. Klymchenko, V. Guérineau, Y. Mély, R. Benhida, A. Burger, *J. Am. Chem. Soc.* **2012**, *134*, 10209–10213.
[210] V. Kilin, K. Gavvala, N. P. F. Barthes, B. Y. Michel, D. Shin, C. Boudier, O. Mauffret, V. Yashchuk, M. Mousli, M. Ruff, et al., *J. Am. Chem. Soc.* **2017**, *139*, 2520–2528.
[211] L. Zargarian, A. Ben Imeddourene, K. Gavvala, N. P. F. Barthes, B. Y. Michel, C. A. Kenfack, N. Morellet, B. René, P. Fossé, A. Burger, et al., *J. Phys. Chem. B* **2017**, *121*, 11249–11261.
[212] N. P. F. Barthes, I. A. Karpenko, D. Dziuba, M. Spadafora, J. Auffret, A. P. Demchenko, Y. Mély, R. Benhida, B. Y. Michel, A. Burger, *RSC Adv.* **2015**, *5*, 33536–33545.
[213] K. Gavvala, N. P. F. Barthes, D. Bonhomme, A. S. Dabert-Gay, D. Debayle, B. Y. Michel, A. Burger, Y. Mély, *RSC Adv.* **2016**, *6*, 87142–87146.
[214] F. Seela, M. Zulauf, *Synthesis* **1996**, *1996*, 726–730.

[215] C. A. M. Seidel, A. Schulz, M. H. M. Sauer, *J. Phys. Chem.* **1996**, *100*, 5541–5553.
[216] M. Torimura, S. Kurata, K. Yamada, T. Yokomaku, Y. Kamagata, T. Kanagawa, R. Kurane, *Anal. Sci.* **2001**, *17*, 155–160.
[217] V. Pogenberg, M. H. Ogmundsdottir, K. Bergsteinsdottir, A. Schepsky, B. Phung, V. Deineko, M. Milewski, E. Steingrimsson, M. Wilmanns, *Genes Dev.* **2012**, *26*, 2647–2658.